

12-2014

Development of a Transport System for Advancing Tissue Engineering and Cell Identification

Suzanne Mae Tabbaa
Clemson University

Follow this and additional works at: https://tigerprints.clemson.edu/all_dissertations



Part of the [Biomedical Engineering and Bioengineering Commons](#)

Recommended Citation

Tabbaa, Suzanne Mae, "Development of a Transport System for Advancing Tissue Engineering and Cell Identification" (2014). *All Dissertations*. 1806.

https://tigerprints.clemson.edu/all_dissertations/1806

This Dissertation is brought to you for free and open access by the Dissertations at TigerPrints. It has been accepted for inclusion in All Dissertations by an authorized administrator of TigerPrints. For more information, please contact kokeefe@clemson.edu.

DEVELOPMENT OF A TRANSPORT SYSTEM FOR ADVANCING TISSUE
ENGINEERING AND CELL IDENTIFICATION

A Dissertation
Presented to
the Graduate School of
Clemson University

In Partial Fulfillment
of the Requirements for the Degree
Doctor of Philosophy
Bioengineering

by
Suzanne Mae Tabbaa
December 2014

Accepted by:
Dr. Karen J.L. Burg, Committee Chair
Dr. Melinda K. Harman
Dr. Kyle J. Jeray
Dr. Julia Sharp
Dr. Dan Simionescu

ABSTRACT

This work centers on the development of a novel passive transport system for two tissue engineering applications – cell distribution and cell separation. This approach relies on a wicking fiber-based system, derived from the textile field that functions by directing and maintaining transport of cells as well as fluids and biomolecules. This system has the ability to enhance cell movement for both the purpose of cell seeding distribution as well as to isolate specific cell types from heterogeneous cell populations.

The success of spinal fusions and large bone defects is often limited by the decreased surrounding vasculature and the ability of cells to penetrate and proliferate both the surface and interior regions of large scaffolds. Therefore, the transport system was tested for improved mass transport, distribution of bone-forming cells, and infiltration of biomolecules in a commonly used spinal fusion scaffold. Heterogeneous cell solutions containing cancerous and benign cell types were used as the proof-of-concept isolation system, where the transport system rapidly and efficiently identifies and isolates cancer cells. Methods to identify cancer cells rely considerably on biomarker detection and analysis of gene expression, with biomarker detection often unreliable and limited. The transport system distinguishes and isolates cancer cells of varying metastatic potential. An integrated, interactive hands-on learning module was developed to introduce middle school female students to transport and tissue engineering principles. The hands-on activity introduces the engineering design process and promotes engineering problem solving.

DEDICATION

I would like to dedicate this work to my family. My parents and four siblings are an incredible support system. To my parents for not only providing me love and encouragement, but also for constantly believing in me. To my big brother, Omar, for always motivating me to be the best I can be, and showing me an incredible work ethic to live up to. He set the bar high and taught me to dream big and work hard. To my sisters, Lena, Serena, and Jenna, for being my best friends and always making me smile and laugh no matter what we are doing. Finally, I would also like to dedicate this to a few of the special people I met at Clemson: Matt Rusin, Bryan Thurston, Natalie Patzin, Dick Pace, Meghan McCoy, and especially Olsen Horton for being my family away from home. A special thank you to Olsen Horton, for helping me revise the document and constantly encouraging me along the way.

ACKNOWLEDGMENTS

I would like to thank Dr. Karen J.L. Burg for her constant encouragement and guidance and providing me the opportunities and resources in IBIOE. I would also like to thank all my committee members, Dr. Kyle Jeray, Dr. Julia Sharp, Dr. Dan Simionescu, and Dr. Melinda Harman.

I also would like to acknowledge all the members of Institute for Biological Interfaces of Engineering for their support and help along the way, especially Olsen Horton, Dick Pace, and Jordon Gilmore for helping me trouble shoot and always being excited about science. I would also like to thank our staff Kerri Kwist and Chris Moody for always assisting me when I need help and providing a fun and positive atmosphere. I also would like to thank Chad MaMahan for help with histology and all of the other bioengineering students and faculty for their support and help with various problems along the way.

I would like to thank the department administrative staff, Maria Torres, Maranda Arnold, Sherri Morrison, and Leigh Humphries for always smiling and willing to help whenever I ask.

Finally, I would like to acknowledge funding sources for this work: Clemson University Hunter Endowment Fund and Avon Foundation.

TABLE OF CONTENTS

	Page
ABSTRACT.....	ii
DEDICATION.....	iii
ACKNOWLEDGMENTS.....	iv
LIST OF TABLES.....	viii
LIST OF FIGURES.....	x
PREFACE.....	1
CHAPTER	
I. LITERATURE REVIEW.....	8
Introduction.....	8
Anatomical Background.....	14
Spinal Fusion Procedures.....	21
Vascularity and Bone Regeneration.....	31
Review of Bone Tissue Engineering and Bone Substitutes.....	48
Summary.....	66
References.....	68
II. EFFECT OF WICKING FIBERS IN TISSUE ENGINEERED SCAFFOLDS.....	80
Fluid Transport of Fibers.....	82
Effect of Wicking Fibers on Biomolecule Transport.....	88
Enhanced Cell Transport Using Wicking Fibers.....	93
Discussion.....	103
Conclusion.....	110
References.....	111
III. IMPROVING TRANSPORT LIMITATIONS OF LARGE SCAFFOLDS.....	114
Introduction.....	114
Scaffold Characterization with Fibers.....	120

Table of Contents (Continued)

	Page
Assessment of Progenitor Cell Recruitment into ChronOS strip	127
Cell Viability and Proliferation in ChronOS	133
Effect of Wicking Fibers on Bone Formation.....	142
Discussion.....	159
References.....	163
IV. IMPROVING CELL SEEDING OF LARGE SCAFFOLDS.....	166
Introduction.....	166
Characterizing the Modified Wicking Fiber Bundle	170
Discussion.....	208
Conclusion	213
References.....	214
V. DEVELOPMENT OF AN ANTIBIOTIC RELEASE SYSTEM.....	216
Introduction.....	216
Gentamicin Release Profile from Fiber Bundles and Alginate Caps.....	217
Results.....	229
Discussion.....	242
References.....	245
VI. DEVELOPMENT AND TESTING OF THE MODIFIED WICKING BUNDLE FOR CELL SEPARATION AND ISOLATION	246
Introduction.....	246
Cell Separation along Single and Wicking Fiber Bundles.....	252
Cell Separation and Isolation along Modified Wicking Bundle	266
Discussion.....	296
Conclusion	301
References.....	302
VII. INVESTIGATING THE CELLULAR SEPARATION MECHANISM OF WICKING FIBERS.....	306
Introduction.....	306

Table of Contents (Continued)

	Page
Impact of Cell Size and Fiber Geometry on Cell Type Separation	309
Investigating Cytoskeletal Arrangement and Protein Expression along the Modified Wicking Bundles	327
Discussion	352
Conclusions	361
References	362
VIII. DEVELOPMENT OF A BONE TISSUE ENGINEERING LEARNING MODULE FOR MIDDLE SCHOOL STUDENTS	365
Introduction.....	365
Teaching Modules.....	367
Discussion.....	383
Conclusion	385
References.....	386
IX. CONCLUSIONS AND RECOMMENDATIONS FOR FUTURE WORK	387
Conclusions.....	387
Future Work	394
APPENDICES	398
A: Educational Surveys and Activities	399

LIST OF TABLES

Table	Page
1.1: Soft tissue contribution to fracture repair and spinal fusion (Table was also published in Tabbaa et al. Critical Reviews in Biomedical Engineering ⁸²).....	44
1.2: Osteogenic Cell Contributions. (Also published in Tabbaa et al. (2014) Critical Reviews in Biomedical Engineering ⁸²)	47
1.3: A summary of bone grafts used in posterolateral fusions provides examples of commercially available bone grafts and their potential use as a bone substitute or bone graft extender. (Also published in Tabbaa et al. (2014) Critical Reviews in Biomedical Engineering ⁸²).....	62
1.4: Characteristics of bone grafts used for posterolateral fusion.	63
1.5: Comparison of current tissue engineering methods to improve vasculature. (Also published in Tabbaa et al. (2014) Critical Reviews in Biomedical Engineering ⁸²).....	66
2.1: Experimental groups of fiber configuration for vertical test investigating wicking height	84
3.1: Experimental setup	134
3.2: Primer Sequences for RT-PCR.....	146
3.3: Phosphate substrate dilutions for standard curve	148
3.4: H & E procedures for frozen sections	151
3.5: Antibodies used for IHC staining.....	152
4.1: Limitations of various cell seeding strategies	167
4.2: Experimental groups of twisted bundle configurations for round and wicking fibers.....	173
4.3: Experimental set-up.....	191
5.1: Loading Mechanisms	220
5.2: Standard curve concentrations for gentamicin detection assay	227

List of Tables (Continued)

	Page
5.3: Results from DSC showing T_g and T_m for each polylactide wicking fiber experimental group	240
6.1: Summarizes the cell lines used in this chapter	250
6.2: Summarizes the type of wicking fiber construct used to cell wicking, the cell types analyzed, and the type of analysis.....	252
7.1: Cell lines investigated	329
8.1: Grading Scale	375
8.2: Pre Survey responses. Table depicts the percentage of students who agree or disagree for each survey question	376
8.3: Post survey questions depicts similar responses to pre survey questions.....	377
8.4: Significant positive change between pre and post survey responses, no negative changes were seen	378

LIST OF FIGURES

Figure	Page
1.1: Graph depicts the rate of common surgical procedures in past decade (Adapted from Rajaei et al. (2012) Spine) ²⁷	12
1.2: Indicates three components of intervertebral discs. Red arrows indicate vascular channels in endplates supplying the disc (Adapted from Ullrich et al. (2004) Spine-Health) ⁴⁵	20
1.3: Spinal fusion surgeries. A: posterolateral spinal fusion. B: Anterior lumbar interbody spinal fusion. C: Transforaminal lumbar interbody fusion (Adapted from Ullrich et al. (2004) Spine- Health) ⁴⁵	30
1.4: Schematic A shows the furthest cell supported by a capillary vessel is 0.1 mm. Red arrows in Image B depict the flow of nutrients from a vascular network on the transverse processes. This supply must span the entire length of fusion (30 mm) ⁷⁸	32
1.5: Diffusion distances of vasculature; (A) depicts the flow of nutrients from a vascular network on the transverse processes, this supply must span the entire length of fusion, 30mm ⁷⁸ ; (B) major vascular supply for interbody fusions, must span the intervertebral distance of 10mm. (Also published in Tabbaa et al. (2014) Critical Reviews in Biomedical Engineering ⁸²)	34
1.6: Surrounding vascular supply of tibia. Contributing factors are the surrounding musculature as well as the highly vascularized periosteum, the anterior tibial artery, and the bone marrow. (Also published in Tabbaa et al. (2014) Critical Reviews in Biomedical Engineering ⁸²).....	35
1.7: Depicts the central and outer regions. The central region forms bone later than outer regions and is often a cause for fusion failure. (Adapted from Boden et al. (2000) Tissue Engineering ⁸⁹)	37
1.8: Faster cancellous bone formation in the outer zones compared to the central zone. (Adapted from Boden et al. (2000) Tissue Engineering ⁸⁹)	37
1.9: Location of posterolateral placement of bone graft and paraspinal muscle tissue. (Figure was also published in Tabbaa et al. Critical Reviews in Biomedical Engineering, 2014 ⁸²).....	40

List of Figures (Continued)

	Page
1.10. Bone fracture healing concepts. Schematic shows an additional apex for vascularity, revealing the star concept model (Also published in Tabbaa et al. (2014) Critical Reviews in Biomedical Engineering ⁸²).....	51
1.11. Functionality of various bone grafts based on the strength of the start concept attributes. (Also published in Tabbaa et al. (2014) Critical Reviews in Biomedical Engineering ⁸²).....	55
2.1: Scanning electron microscope (SEM) image of a wicking fiber. Adapted with permission from Elsevier (Marcus RK et al. 2005). Image shows non-circular grooved cross-section and parallel channels of the wicking fiber, which facilitate strong wicking action and greatly increase surface area.	81
2.2: (A) Vertical test apparatus to evaluate the rate of the fluid front in various fiber configurations. (B) Vertical test set-up to assess the amount of fluid wicked through the fiber over a time interval.....	83
2.3: Results from vertical wicking test. Left image shows the vertical test apparatus. (A) Bundled and (C) single wicking fiber samples depict greater vertical movement of the dye-solution than (B) bundled and (D) single round fiber samples	86
2.4: Wicking behavior of round and wicking fibers (A) Plot of wicking height vs time for round and wicking fibers (B) The wicking rate (cm/min) of single, bundle, and braided round and wicking fibers (C) The maximum height reached for each fiber type (D) Wicking rate (mg/min) of round and wicking twisted bundles (*) signifies significant difference between round and wicking fiber types, $p < 0.05$	88
2.5: Schematics of experimental set-up of collage-agarose gel containing fibers. (A) Digital image of the rotated chamber well to create a hydrogel in half the well and with inserted fibers. (B) The sample was then laid back on its side and tested and then imaged using fluorescent confocal imaging of the FITC albumin along the horizontal axis with laser confocal microscopy	90

List of Figures (Continued)

	Page
2.6: (A) Schematic of an individual well in a 2-well chamber slide filled partially containing with collagen-agarose gel containing either round or wicking fibers. The other portion of the well is filled with medium containing the BSA-FITC solution. (B) Image frame from confocal real-time video of the BSA-FITC diffusion diffusing into the collagen-agarose gel.	91
2.7: (A) Schematic indicates interface between hydrogel and FITC-albumin solution and the region of interest locations. (B) The rate of BSA-FITC in the collagen-agarose gel at various distances into the hydrogel. The hydrogel samples containing wicking fibers have a significantly greater rate than the samples with round fibers; * $p < 0.001$. The rate of BSA-FITC is consistent for various distances from the interface for both fiber types into the sample. (also published in Tabbaa et al. 2004 JTERM ²³)	92
2.9: Schematic depicts experimental set-up to assess progenitor cells wicking in round or wicking fibers. The purple cylinders depict the holding mechanism of the fibers	94
2.10: Schematic illustrates the arrangement for double-layered collagen hemispheres (A) without fibers and (B) with round or wicking fibers. The pink sphere corresponds to the first hemisphere layer containing fluorescently tracked D1 mouse progenitor cells. The blue sphere depicts the second larger collagen hemisphere containing a chemotactic growth factor encapsulating the first hemisphere with or without fibers.	96
2.11: Two 8-well chamber slides were used to make two-layered collagen hemispheres samples (n=4) with and without fibers.	98
2.12: Depicts images after image J processing methods. (A) The initial fluorescent image captured, (B) the split red channel image, and (C) the converted binary image.....	99

List of Figures (Continued)

	Page
2.13: (A) Schematic illustrating the location of the captured fluorescent images shown in (B) along wicking or round fibers. Measurements of progenitor cell movement quantified through imaging software and shown in the chart (C). The vertical displacement and cell density along the wicking fibers is significantly greater than the round fibers; * $p < 0.001$	101
2.14: Qualitative fluorescent and binary images of collagen hydrogel hemisphere samples containing no fibers and samples with round or wicking fibers. Images show greatest cell expansion with wicking fibers compared to samples with round fibers or no fibers.....	102
2.15: Results of progenitor cell expansion in double-layered collagen hydrogels. Samples with wicking fibers showed greatest cell distribution compared to all other experimental groups. (* represents significantly different groups with $p < 0.05$)	103
3.1: (A) The model developed by Muschler and coworkers shows the highest concentration of oxygen is at the surface of the graft and decreases towards the center of the graft ² . (B) The minimum oxygen concentration occurs at the center of the graft. Depending on the number of cells seeded and their metabolic activity necrosis can occur.	115
3.2: (A) Illustrates placement of chronOS strip during posterolateral fusion (B) Dimensions of chronOS strip (C) and (D) depict the two major sources of vasculature to the fusion site, transverse processes and paraspinal muscles, respectively. (Also published in Tabbaa et al. 2014 ⁴)	118
3.3: Experimental set-up to assess porosity in chronOS strip scaffolds with and without fibers.....	121
3.4: (A) Initial time point of chronOS strips scaffolds with (Right) and without fibers (Left) (B) Horizontal test initial time point	123
3.5: The wicking fibers increase the porosity of the chronOS strip samples by ~10%. The asterisk (*) represents statistically significant differences with $p < 0.05$	124

List of Figures (Continued)

	Page
3.6: (A) Digital image of vertical test after 5 minutes (B) Digital image of vertical test after 30 minute. Images depict wicking fibers enhance fluid transport in scaffolds	125
3.7: Results from horizontal test. (A) Scaffolds prior to directly seeding dye-solution to top face of scaffolds (B) Interior cross-sectional images of chronOS strips with and without fibers. Scaffolds with fibers show more homogenous distribution of dye-solution.....	126
3.8: Experimental set-up assessing if wicking fibers improve cellular penetration and distribution in chronOS strip scaffolds.....	128
3.9: Schematic illustrating experimental set-up to assess the horizontal test of green labeled cells in scaffolds with and without fibers	129
3.10: The schematic illustrates the vertical wicking of cells into scaffolds with and without fibers. (A) Fluorescent cross-section of densely populated green-tracked cells distributed homogeneously in the center region of the scaffold with fibers (B) Fluorescent cross-section of fewer green-tracked cells unevenly distributed in the center region of the scaffold without fibers (C) Data associated with the fluorescent images comparing the percentage of cells in the center region of the scaffolds with and without fibers using image J software	131
3.11: Fluorescent images of central region of cross-sectional regions of chronOS strips with and without fibers. (A) Scaffolds with fibers depict greater green-labeled cell penetration and distribution (B) Unmodified chronOS strip scaffolds shows fewer cells and less spread. (C) and (D) show significant cell penetration of the polylactide wicking fiber bundles.....	132
3.12: Top image shows an overlay of composite live/dead fluorescent images for chronOS strip samples with and without wicking fibers. Bottom chart illustrates percentage of dead cells in both scaffold types	138
3.13: Calibration line that relates a known number of D1 cells to the DNA concentration found by using PicoGreen. Determined lysing a known number of cells placed in microvials.....	139

List of Figures (Continued)

	Page
3.14: Results of the PicoGreen assay. ChronOS strips with fibers show more D1 cell proliferation on Days 4 and 7	140
3.15: Flow cytometry analysis indicate significantly more viable cells after days 3, 7, and 10 in scaffolds containing wicking fibers; *p<0.05.	141
3.16: Experimental set-up for each endpoint (Days 0, 7, and 14). Each 24-well plate includes both experimental groups (chronOS with and without fibers) and a control group with no scaffold	144
3.17: ALP activity of chronOS strips with and without fibers normalized by amount of DNA. Day 0 and Day 7 show chronOS samples with fibers had significantly higher ALP activity than chronOS without fibers. Day 14 showed significantly higher ALP activity for chronOS samples without fibers; *p<0.05.	153
3.18: qRT-PCR results for osteoblastic differentiation markers: osteocalcin (A), Runx2 (B), ALP (C), and BMP2 (D). Modified chronOS showed significantly higher Runx2 expression than unmodified chronOS, *p<0.05.....	154
3.19: H&E staining for chronOS strip samples with fibers after Day 0 (A), Day 7 (C), and Day 14 (E), as well as chronOS strip samples without fibers after Day 0 (B), Day 7 (D) and Day 14 (F). Images show more cells in samples containing fibers. Day 14 samples with fibers show the aligned cells and formation of collagen.	156
3.20: IHC staining for BMP-2 (green), osteopontin (red), and nuclei (blue) for Day 0 time point. Top row and bottom row depict chronOS with fibers and without, respectively. (A) Overlaid images of BMP-2, osteopontin, and nuclei. (B) Osteopontin expression and nuclei staining (C) BMP-2 and nuclei staining. ChronOS containing fibers shows greater expression of BMP-2. Both scaffold types show low expression of osteopontin.	157

List of Figures (Continued)

	Page
3.21 IHC staining for BMP-2 (green), osteopontin (red), and nuclei (blue) for Day 7 time point. Top row and bottom row depict modified and unmodified chronOS, respectively. The modified chronOS scaffolds show significantly more (B) osteopontin expression and (C) BMP-2 expression compared to the unmodified scaffolds.....	158
3.22: IHC staining for BMP-2 (green), osteopontin (red), and nuclei (blue) for Day 14 time point. Top row and bottom row depict modified and unmodified chronOS, respectively. The modified chronOS scaffolds show significantly more (B) osteopontin expression and (C) BMP-2 expression compared to the unmodified scaffolds.....	159
4.1: Synthes developed perfusion pack for chronOS strip (www.synthes.com).....	168
4.2: Results from Synthes in vitro assessment of the perfusion pack seeding. (A) Top surface of scaffold shows significantly more cells than the central region (B) and bottom surface of the scaffold (C).....	169
4.3: Modified wicking bundle comprised of 1.4% alginate hydrogel cap and a wicking fiber bundle.....	171
4.4: Wicking behavior tests. (A) Assessing the change in mass over various time intervals. (B) Measuring fluid absorbed after 12 and 24 hours in modified and unmodified fiber bundles (C) Measuring fluid height front every minute for a 10 minute interval.....	172
4.5: (A) The modified wicking bundle depicts the greatest change in fluid front height over a 10 minute interval (B) Modified wicking bundles on left depicts significantly greater fluid absorption and fluid height than unmodified wicking fiber bundles on the right.....	175

List of Figures (Continued)

	Page
4.6: (A) Modified wicking bundles absorb significantly more fluid after 12 and 24 hours than unmodified (*) indicates significant difference of $p < 0.05$ (B) Qualitatively illustrates enhanced fluid absorption by modified wicking bundles after 5 minutes and 12 hours.....	176
4.7: Plot of the change in wicking rate over a 3 minute time interval. Modified wicking bundles show an increasing wicking rate over time.....	177
4.8: Schematic of experimental set-up of collagen-agarose hydrogel containing modified or unmodified wicking bundles. (A) Digital image of rotated chamber well to apply hydrogel to half the well (B) Fluorescent microscopy to image diffusion of FITC-albumin into hydrogel using time-lapse.....	178
4.9: (A) Schematic of an individual well in a 2-well chamber slide filled partially containing with collagen-agarose gel containing either modified or unmodified wicking fiber bundles. The other portion of the well is filled with medium containing the BSA-FITC solution. (B) Image frame from time-lapse video of the BSA-FITC diffusion into the collagen-agarose gel. Average intensity was measured from labeled ROI adjacent to interface.....	179
4.10: Schematic represents experimental set-up evaluating cell wicking in modified and unmodified wicking bundles.....	181
4.11: Schematic illustrating cell isolation from top and bottom regions of unmodified and modified wicking bundles.....	182
4.12: Experimental set-up to assess cellular infiltration in a submerged system. Modified and unmodified bundles were submerged in growth media in a 6-well culture plate. Cell solution was added to the wells after the samples were submerged. After 12 hours, the cellular recruitment was assessed by imaging various regions of the modified and unmodified bundles, depicted in schematic.....	184

List of Figures (Continued)

	Page
4.13: (A) Plot depicts the modified wicking fiber constructs show greatest increase in intensity over 30 minute time interval (B) Hydrogel containing modified wicking fiber constructs have significantly greater rate than samples with unmodified wicking fibers and samples without fibers; *p<0.05.	185
4.14: (A) Shows significantly more cells isolated from top regions of the modified wicking bundle than unmodified, *p<0.05. (B) No significant cell count in bottom regions of bundles (C) Illustrates greater cell penetration in the top region of the modified wicking bundle (D) Qualitatively shows no significant difference in cell count in bottom regions.....	186
4.15: (A and B) Ends of unmodified wicking bundle show less cellular infiltration than (C) Modified wicking bundle end and (D) Alginate component	187
4.16: (A) Modified chronOS strip sample vacuum sealed with absorbent cap positioned distal the inlet valve (B) Unmodified chronOS strip vacuum sealed	189
4.17: (A) Injected progenitor cell solution into vacuum-sealed perfusion pack through inlet valve (B) Incubated perfused samples with cell solution for 60 minutes at room temperature	191
4.18: The interior cross-section of the modified and unmodified chronOS strip samples. Schematic illustrates central and peripheral regions along the cross-section	196
4.19: Composite images of viable (green) and dead (red) cells in modified and unmodified chronOS strip scaffolds. Illustrates more viable cells in modified chronOS strip samples.....	197
4.20: Unmodified chronOS scaffolds depict greater numbers of dead cells and fewer viable cells than modified chronOS strip samples	198

List of Figures (Continued)

	Page
4.21: Schematic illustrations location of Live/Dead images along the modified wicking bundles in the chronOS strip scaffolds. The Live/Dead composite images illustrate significant cell penetration into the construct and high numbers of viable cells along the wicking fiber and alginate component.	199
4.22: (A) Modified chronOS strip samples contained significantly more viable cells and total cell than unmodified samples, *p<0.05. (B) Modified samples contained four times the amount of DNA isolated from unmodified samples, *p<0.05	200
4.23: Central regions of the modified chronOS strip scaffolds depict greater cell penetration.....	201
4.24: Peripheral regions of modified and unmodified chronOS strips show similar cell densities and distribution	202
4.25: Depicts cell recruitment in modified wicking bundles of modified chronOS strips. Images depict cells along the twisted fiber bundle embedded in the chronOS scaffold.	203
4.26: Actin and nuclei staining of progenitor cells shows high cell penetration and proliferation in the peripheral regions of both modified and unmodified chronOS strip scaffolds	204
4.27: Cell distribution and proliferation in central regions of modified and unmodified chronOS strip scaffolds. Modified samples show significantly more cell penetration and proliferation, as well as cell infiltration along the modified wicking bundle component.....	205
4.28: Images show significant cell infiltration along the wicking fiber - alginate construct. Images depict high cell densities along the wicking fiber bundle component.....	206

List of Figures (Continued)

	Page
4.29: (A) Normalized glucose consumption after 2 hours, 48 hours, and 72 hours. No statistical significance was observed on any time point. (B) Normalized lactic acid production in modified and unmodified chronOS strip samples. Both scaffolds show increase in lactic acid production after 72 hours. The modified scaffolds show greater production than unmodified but are statistically significant after 1 hour.	207
5.1: Schematic shows the extruding process of polymer fibers. Polylactide beads are inserted through a funnel into a hopper with a screw that transport the polymer through a heating cylinder. The pump pushes the melted polymer through a die to form the cross-section shape of the fiber	219
5.2: Depicts the feeding of the polymer monofilament from the outlet through the water bath and along the rollers	221
5.3: (A) Long and short axis dimension of the die used for extruding the wicking fibers. (B) Cross-sectional image of the PLA extruded wicking monofilament	222
5.4: Depicts third approach for incorporating antibiotic into extruded polymer fibers by mixing the gentamicin powder and polylactide pellets prior to loading the extruder	224
5.5: (A) Gentamicin release from round or wicking fiber bundles loaded with gentamicin from mechanism 1 or 2. At the initial time point all the experimental groups show a significantly different concentration of gentamicin (#,\$,*,+) signify each group is significantly different within the initial time point (p<0.05). After 15 minutes the wicking fiber group loaded by mechanism 1 is significantly greater than the round fiber group loaded by the same mechanism, (*) signifies statistical differences between these groups with p<0.05. The red dotted line indicates the target elution concentration. (B) Depicts the cumulative release of gentamicin from each experimental group	231

List of Figures (Continued)

	Page
5.6: (A) Release of gentamicin from wicking fiber bundles after longer time intervals. Gentamicin was undetectable in early time points for all experimental groups. No significant difference in gentamicin elution was found at any of the time points (B) Cumulative release profile of the gentamicin elution from each experimental group shows the wicking fiber loaded by mechanism 2 has the greatest cumulative elution over this time interval.....	233
5.7: Release profile of gentamicin loaded by mechanism 3. (A) Elution profile of small bundled wicking fiber and a single large wicking fiber (B) Cumulative release of both wicking fiber types over a 14 day time period.	235
5.8: The amount of gentamicin incorporated into the PLA fibers from loading mechanisms 2 and 3	236
5.9: (A) Elution from alginate caps shows an initial burst and steady release of gentamicin. The total amount of gentamicin loaded in the alginate is depicted in both graphs. The red dotted line indicates MIC. The release from the alginate cap reaches the target concentration until Day 7. (B) The cumulative release profile shows that all of the gentamicin loaded was completely eluted by day 14.	238
5.10: (A) DSC plot after first heating cycle of the experimental and control group. The control group and Mechanism 2 show different heat flow curves at the T_g value. Control group and Mechanism 2 show the same T_m values. Mechanism 3 depicts a different T_m value with two melting temperatures. All the groups show a varying crystallinity curve (B) DSC curve after second heat cycle shows similar T_g and T_m values but different crystallinity curves than the control polylactide group	241
6.1: Schematic shows cell vertical wicking test set-up. The wells contain 1 mL of media consisting of equal densities of normal and cancer cells. The fiber is vertically placed into the cell solution so only 3 mm of the fiber is submerged. The cell movement is analyzed at various time points	254

List of Figures (Continued)

	Page
6.2: Left schematic shows the vertical test set-up of human cancer and benign cells. The right schematic shows the isolation of cells from the top and bottom regions of the wicking fiber bundle for analysis.....	258
6.3: (A) Depicts compiled fluorescent images of the vertical displacement of MMTV-neu-RFP, cancer cells, along the length of the fiber. (B) Shows NMuMG-GFP, normal cells, progressed significantly less than the cancer cells. (C) Graph shows quantitative analysis of the vertical displacement of cancer cells (2759 ± 928.9 (SD), n=4) and mouse normal cells (2219 ± 940.6 (SD), n=4) after various time points. After 24 hours there was significantly greater vertical displacement of MMTV-neu-RFP (14380 ± 1192 (SD), n=4) than displacement of NMuMG-RFP (6220 ± 994.2 (SD), n=4) ($p < 0.05$), indicated by (*) in graph.....	261
6.4: (Left) Approximately equal densities of red and green fluorescently labeled cancer and normal cells depicted in bottom region of the fiber. (Right) Mostly fluorescently labeled red cells in top region indicating cancer cells displace the entire wicking fiber bundle.....	262
6.5: Schematic of the fiber regions and data depicting percentage of each cell type in fiber regions. Left image illustrates axial slicing of fiber bundle to extract cells from top and bottom regions. Graph exhibits quantitative analysis of top and bottom region of the fiber bundle, demonstrating significantly higher concentration of MCF-7-RFP cells in the top region of the fiber bundle (82.4 ± 4.3 (SD), n=3) than the bottom region of the fiber bundle (61.6 ± 3.04 (SD), n=3) The graph indicates a significantly lower concentration of MCF-10A-GFP cells in top region (17.6 ± 4.3 (SD), n=3) than bottom region (38.4 ± 3.04 (SD), n=3), (*) indicates significant difference, $p < 0.05$	263
6.6: (A) Fluorescent image shows vertical displacement of RAW and D1 cells along the bottom region of the wicking fiber bundle. Image shows higher densities of red fluorescently labeled D1 cells. (B) D1 cells show increased vertical displacement after 1 hour and 24 hours.....	265

List of Figures (Continued)

	Page
6.7: Set-up to analyze cell separation and isolation	269
6.8: Schematic depicts fluorescent microscopy analysis and regions of interest images.....	270
6.9: Schematic shows regions cancer and normal cells were isolated from along the modified wicking bundle.....	272
6.10: (A) Experimental set-up investigating vertical displacement of metastatic cancer cells and benign epithelial cells (B) Qualitative analysis using fluorescent microscopy (C) Flow cytometry analysis.....	274
6.11: Schematic depicting experimental set-up to analyze a tri-culture of benign and of cancer cells of varying metastatic potential	278
6.12: Fluorescent images of the cancerous MCF-7 (red) and benign MCF-10A (green) epithelial cell displacement along the modified wicking bundles. (A) Depicts more MCF-10A cells in the bottom region of the fiber bundle where the cell solution contacts the fiber bundle. (B) Similar cell densities of MCF-7 and MCF-10A cells in the middle region of the fiber bundle. (C) Depicts primarily MCF-7 cells along the top region of the fiber in the alginate cap. (D) Reveals significantly more cancer cells in the alginate cap.....	281
6.13: Scatter plots of control groups from flow cytometry analysis. Depicts the forward and side-scattering plots of MCF-7 (Top Row) and MCF-10A (Bottom Row. The red and green fluorescent intensity plots show the MCF-7 cells are labeled with red fluorescence and the MCF-10A cells are labeled with green fluorescence.....	283
6.14: Flow cytometry results investigating the number of cancer and benign cells in each region. Chart illustrates significantly higher percentage of MCF-7 in alginate cap (A) and in top region of wicking fiber bundle (*) indicates significant difference of $p < 0.05$ (B). No comparable difference in percentage of MCF-7 and MCF-10A cells in bottom region of the wicking fiber bundle.....	284

List of Figures (Continued)

	Page
6.15: Forward scatter plots and fluorescence intensity of MCF-10A and MCF-7 cells in each region. The forward scatter plot shows greater numbers of both cell types in the bottom region compared to the top fiber region and the alginate cap. The bottom region depicts similar red and green fluorescent intensities. The top fiber region and alginate cap show high red fluorescent intensity counts correlating to mainly cancer cells in these regions.....	285
6.16: Fluorescent images analyzing the vertical displacement of metastatic breast cancer cells (red) and benign breast epithelial cells (green). Comparable cell densities are depicted in the bottom or seeded region of the fiber (A). Greater numbers of metastatic cancer cells (red) wick to the middle (B) and top (C) regions of the fiber. (D) The alginate cap consists of greater numbers of the metastatic cancer cells.....	286
6.17: (A) Scatter and fluorescent intensity plots confirming the red-label of the MDA-MB-231 metastatic cancer cells. (B) Scatter and fluorescent intensity plots of green-labeled benign cells. (C) Depicts separation of the metastatic cells, MDA-MB-231 from MCF10A cells in each region of the fiber bundle and alginate cap.	287
6.18: (A) and (B) depict similar cell densities of metastatic cancer cells (MDA-MB-231) labeled green and non-metastatic cancer cells (MCF-7) labeled red. (C) Top region of the wicking fiber bundle shows more metastatic cancer cells and (D) alginate cap depicts both metastatic and non-metastatic cancer cells.....	289

List of Figures (Continued)

	Page
6.19: (A) Scatter plot of MDA-MB-231 metastatic cells. Red and green fluorescence intensity plots shows high green intensity and low red intensity confirming labeling procedure. (B) Scatter plot of MCF-7 non-metastatic cancer cells shows variation in size and shape of cells within cell line. The fluorescence intensity plots show high red intensity confirming the cells are fluorescently tagged red. (C) Comparable amounts of metastatic and non-metastatic cells in bottom region of the fiber bundle and the alginate cap. The top region depicts significantly more MDA-MB-231 cells than MCF-7 cells, (*) indicates significant difference, $p < 0.05$	290
6.20: Scatter and fluorescent intensity plots depict low amounts of cell removal from the top fiber region and the alginate cap	291
6.21: Cell displacement of metastatic cancer cells, MDA-MB-231 (blue), non-metastatic cancer cells, MCF-7 (red), and benign breast epithelial cells (green). The bottom (A) and middle (B) region of the fiber bundle depict all cancer cell types along the fiber. High densities of MDA-MB-231 are depicted in the top region of the fiber bundle (C) and the alginate cap (D).	293
6.22: (A) and (B) Bottom and middle regions of the wicking fiber bundle show similar cell densities of D1 cells (green) and MC3T3E1 cells (red). (C) and (D) depict more D1 progenitor cells in top region and alginate cap.....	295
6.23: (A) Scatter and fluorescent intensity plots for MC3T3-E1 cells show cells were labeled with red tracker. (B) Scatter and fluorescent intensity plot for green fluorescently labeled D1 cells. (C) Quantifies the wicking displacement of D1 cells and MC3T3E1 cells. Depicts significantly more D1 cells ($p < 0.05$) in the alginate cap and fiber bundle regions than MC3T3E1 cells.	296
7.1: Experimental set-up investigating cell separation of benign and cancerous cells in modified wicking bundles containing small or large fibers.....	316

List of Figures (Continued)

	Page
7.2: Fluorescently green labeled MCF-10A cells (A) and red labeled MCF-7 cells (B) suspended in growth media. (C) The average diameter of the benign MCF-10A cells is significantly larger than the cancerous MCF-7 cells, (*) indicate significant difference, $p < 0.05$	319
7.3: Fluorescently red labeled MC3T3E1 cell and green labeled D1 cells suspended in cell solution (C) The average cell diameter of D1 cells is significantly smaller than the MC3T3E1 cells.....	320
7.4: (A) Section of polylactide wicking fiber bundle depicts a range of inter- and intra- fiber spaces (B) and (C) depicts cross-sectional images of two different sized polylactide fibers	322
7.5: Bead wicking analysis with flow cytometry (A) Scatter plots showing the regions of the 6 μm (right) and 20 μm beads.....	324
7.6: Flow cytometry analysis of 6 μm and 20 μm diameter beads in alginate modified fibers containing small or large individual fibers. (A) Both constructs showed significantly more 6 μm diameter beads in each region than the 20 μm beads. The modified fiber bundle containing the smaller bundles contained significantly more 6 μm beads in the top and bottom regions of the fiber bundle than the modified construct containing larger cross-sectional fibers. (B) The modified large and small fiber constructs showed comparable percentages of both bead types in each region of the fiber bundle and the alginate cap.....	325

List of Figures (Continued)

Page

7.7 (A) Cell count in each region of the modified small and large wicking bundles. The alginate cap and bottom region of the wicking fiber bundle show similar cell counts of both cell types. The top region of the smaller fiber depicted significantly less MCF-10A and MCF-7 cells than the top region of the modified large fiber construct. (B) Percentage of each cell type in each region of the modified small and large wicking fiber constructs. The alginate cap and bottom fiber region show similar percentages of benign and cancer cells for both large and small fiber bundles. The percentage of MCF-10A cells in the top region of the large fiber bundle is significantly greater than the small fiber bundle..... 326

7.8: Scatter and fluorescent intensity plots of benign and cancer cells in each region of the alginate modified construct. (A) Bottom region of modified small bundles (left) shows comparable amounts of benign and cancer cells as the modified large bundles (right). (B) Top region of modified small bundles (Left) show less cell penetration and less green labeled benign cells than the modified large bundle construct (Right). (C) Alginate cap from modified small bundle construct shows comparable amounts of cancer and benign cell in large bundle construct. 327

7.9: Actin cytoskeletal and vinculin arrangement of the various cancer types (A) MCF-7 non-metastatic cancer cells show weak actin cytoskeleton lacking fiber arrangement (B) MCF-10A benign cells show actin fibril arrangement with alignment along the periphery of the cell. Benign cells depict vinculin expression concentrated in central region of cells. (C) MDA-MB-231 cells depict more actin fiber arrangement compared to the other cell lines. Images show distinct actin fibers along the periphery and central regions of the cell. 335

7.10: The actin and vinculin arrangement of MCF-7 and MCF-10A cells along the modified wicking fiber construct (A) Bottom region of the wicking fiber bundle shows the actin fibers are arranged along the periphery forming an outer shell. (B) Middle region of the wicking fiber bundle shows clumps of cells with round morphology (C) Top region of wicking fiber bundle depicts the same rounded morphology of the cells 336

List of Figures (Continued)

	Page
7.11: Cytoskeletal architecture of MDA-MB-231 cells along the modified wicking fiber construct. (A) Cells in bottom region of construct depict rounded morphology with actin concentrated along the periphery. The middle region (B) and top region (C) of the modified construct shows the same rounded morphology.....	337
7.12: (A) Actin arrangement of D1 mouse mesenchymal stem cells show fibroblast-like morphology with actin fiber formation predominantly on the periphery of the cell. (B) MC3T3E1 pre-osteoblast cells depicts a less spindle shaped morphology with more actin fiber formation within the cell.....	339
7.13: (A) Pre-osteoblast cells and (B) D1 cells along the top region of the wicking fiber bundle show the pre-osteoblasts have a less rounded morphology and more spread-out along the fiber. (C) Pre-osteoblast and (D) D1 cells in the middle region depict the pre-osteoblast have adhered more to the fiber compared to the rounded shape of the D1 cells. The pre-osteoblasts (E) and D1 cells (F) both show more rounded morphology in the top regions of the fiber	340
7.14: EpCAM expression (Green fluorescence) of each cancer cell line (A) MCF-7 cells show high expression of EpCAM (B) MCF-10A cells and (C) MDA-MB-231 show low expression of EpCAM	342
7.15: EpCAM expression (Tagged with red-fluorescent secondary antibody) of MCF-7 and MCF-10A cells in the bottom region of the wicking fiber bundle.....	343
7.16: EpCAM expression of MCF-7 and MCF-10A cells along central region of wicking fiber bundle.....	344
7.17: Depicts high percentage of EpCAM expression in top region of the wicking fiber bundle	345
7.18: Flow cytometry analysis (A) Percentage of cells expressing EpCAM (B) Scatter and intensity plots of EpCAM expression from each region	346

List of Figures (Continued)

	Page
7.19: Depicts low EpCAM expression (tagged with green fluorescent secondary antibody) of MCF-10A and MDA-MB-231 cells in bottom (A), middle (B), and top regions (C) of the wicking fiber bundle.....	349
7.20: Flow cytometry analysis of EpCAM expression along top and bottom regions of wicking fiber bundle (A) Percentage of cells expressing EpCAM in top and bottom regions of wicking fiber (B) MCF10A control group shows low expression of EpCAM (C) MDA-MB-231 group depicts almost no EpCAM expression	350
7.21: Levels of CD44 expression of the various cancer cell lines (A) MCF-7 show low CD44 expression (B) MCF10A and (C) MDA-MB-231 cells show high levels of CD44 expression	351
8.1: Demos presented to students to illustrate diffusion and osmosis (A) Diffusion of smell (B) Osmosis in an egg in a hypertonic or hypotonic solution after the shell is removed with vinegar (C) Osmosis in gummy bears in hypertonic or hypotonic solutions	368
8.2: (A) Different materials with varying stiffness to represent muscle, fat, and bone tissues (B) The group activity where students determine the rate of movement of the dye solution in various agarose stiff gels.....	370
8.3: Demonstration of water moving through capillaries or xylem in the celery stalks by capillary action	371
8.4: (A) Designing and testing capillary action in various yarn materials (B) Architecture of the paper towel will affect capillary action	373
8.5: Student responses to the open-ended question "What is engineering?"	379
8.6: Student responses to second open-ended question: "What does an engineer do?".....	380
8.7: Categorizes the drawings of pre and post surveys. The categories include people, actions, and themes.....	381

List of Figures (Continued)

	Page
8.8: The post quiz grade percentages were significantly greater than the pre quiz grade percentages, (*) signifies $p < 0.05$	383

PREFACE

Wicking systems are commonly used in the textile industry. Wicking is a passive mode of transport using capillary action to move fluids. The purpose of this work involves the development and optimization of novel wicking fiber bundles to sustain transport of nutrients and biomolecules, as well as direct and identify particular cell types. In one application, wicking fiber bundles were applied to large tissue engineered scaffolds to increase cellular distribution throughout the scaffold. Another application involved the development of a wicking fiber system to separate and identify cell types. Different cells move through the fiber bundles at varying rates and distances based on cell characteristics, providing a means of isolating and analyzing pathological and multipotent cells.

The first application of the wicking fiber system involved improving the transport limitations of bone grafts that are used for large bone defects, specifically in spinal fusions. Spinal fusions are the standard treatment for lower back pain, as well as spinal deformities and trauma. In the past 3 decades, there has been a significant increase in number and cost of spinal fusions compared to other common surgical procedure[2]. Bone graft material is an essential component used in spinal fusions and are also used in other large defect fracture repair procedures. Successful bone formation can be controlled by the properties of the bone graft. Alternate bone grafts such as allograft or synthetic substitutes lack the bone-forming qualities of autologous bone graft. Due to availability limitations of autologous grafts, there is a need and competitive market to improve bone substitutes that augment bone formation in spinal fusion procedures[1]. The environment of the fusion site

also greatly impacts the success of the fusion. The environment surrounding the implant provides vasculature and the essential bone-forming factors. The success of bone formation is highly dependent on the surrounding vasculature and is often overlooked when designing tissue engineered constructs[4]. The current tissue engineering methods used to create vascularity and improve transport of the bone construct have had very limited success. Researchers have discovered non-homogeneous bone formation within the spinal fusion site[5, 6]. Regions closer to the source of vasculature form bone more rapidly than regions further away. The regions lacking vascular supply are more susceptible to pseudarthrosis, which causes the fusion to fail. The first part of the work involved developing and testing the novel non-biological wicking fiber approach to improve vascularity and direct transport of essential bone-forming biomolecules and cells to all regions of the bone graft in the implant site.

The second application of the wicking fiber bundles involved the development of a wicking fiber system to separate and identify particular cell types, specifically cancer and normal cells. The National Cancer Institute estimates 1 in 30 Americans have or have had some form of cancer, with an annual cost of \$126 billion[7]. This high incidence rate drives the need for reliable and accurate testing. The occurrence of diagnostic error, including failure to diagnose the existing cancer and delayed diagnosis, can be as frequent as 1 in 5 cancer cases[8]. A major contributing factor for this error is the extensive oncologic pathology testing process. This extensive process provides frequent opportunities to switch or contaminate samples, as well as to inadequately prepare, analyze, or interpret specimens[9]. The gold standard for cancer detection involves histological analysis using

phenotypic and genotypic biomarkers. A major limitation of biomarkers in the identification of cancer is the absence of a universal tumorigenic marker. The complexity and heterogeneity of a tumor create a challenge for researchers to characterize the tumor based on phenotypic and genotypic biomarkers alone. Tumors are reported to have different subpopulations of cancer cells with varying phenotypes and degrees of tumor-initiating capabilities [12]. The transient phenotypes of these cells create complexities for current detection methods and treatments[19]. For instance, cancer stem cells have the potential to be dormant or aggressive[20]. This ability to phenotypically change may cause resistance to treatment and recurrence[21].

An emerging field for oncology diagnostics involves the use of non-invasive liquid biopsy tests. This involves testing blood, urine, or other bodily fluids for cancer cells or oncologic related proteins and biomolecules. Again, these liquid biopsy samples are typically analyzed using conventional methods for identifying progenitor or cancer cells, which involve detecting phenotypic biomarkers and analyzing gene expression[13]. The use of phenotypic and genotypic biomarkers to identify progenitors is unreliable, lacks specificity, and provides limited information regarding the cancer cell potential. This work involved the development of new physical biomarkers based on cell behavior through the wicking fiber system. The goal of this application was to establish a method to better capture and characterize cancer cells of different metastatic capabilities.

The goal of this work was to develop a novel approach using a wicking fiber system that can achieve sufficient transport of biomolecules and cells throughout the entirety of

the scaffold as well efficiently identify pathological cell types from heterogeneous samples or tissues. To accomplish these overall goals the following specific aims were recognized:

Specific Aim 1 – Evaluate the effects of wicking fibers on the transport of biomolecules and progenitor cells in tissue engineered scaffolds

- *Phase A* – Characterize wicking fluid properties of wicking bundles
- *Phase B* – Evaluate the effects of wicking fibers on recruitment of progenitor cells and biomolecule transport in 3-dimensional scaffolds

Specific Aim 2 – Investigate the use of a wicking fiber system to improve the success rates of bone graft used for spinal fusion

- *Phase A*– Determine if wicking fibers improve cellular viability, proliferation, and distribution of large bone scaffolds
- *Phase B* – Evaluate if incorporating wicking fibers in large bone scaffolds improve cellular differentiation and bone formation

Specific Aim 3 – Develop and assess a passive transport system to improve large tissue engineered constructs

- *Phase A* - Develop and assess the capabilities of the passive transport system to sustain movement and direct cell and biomolecule movement
- *Phase B* - Investigate the effectiveness of the passive transport system as an antibiotic eluting system and assess the release of antibiotic

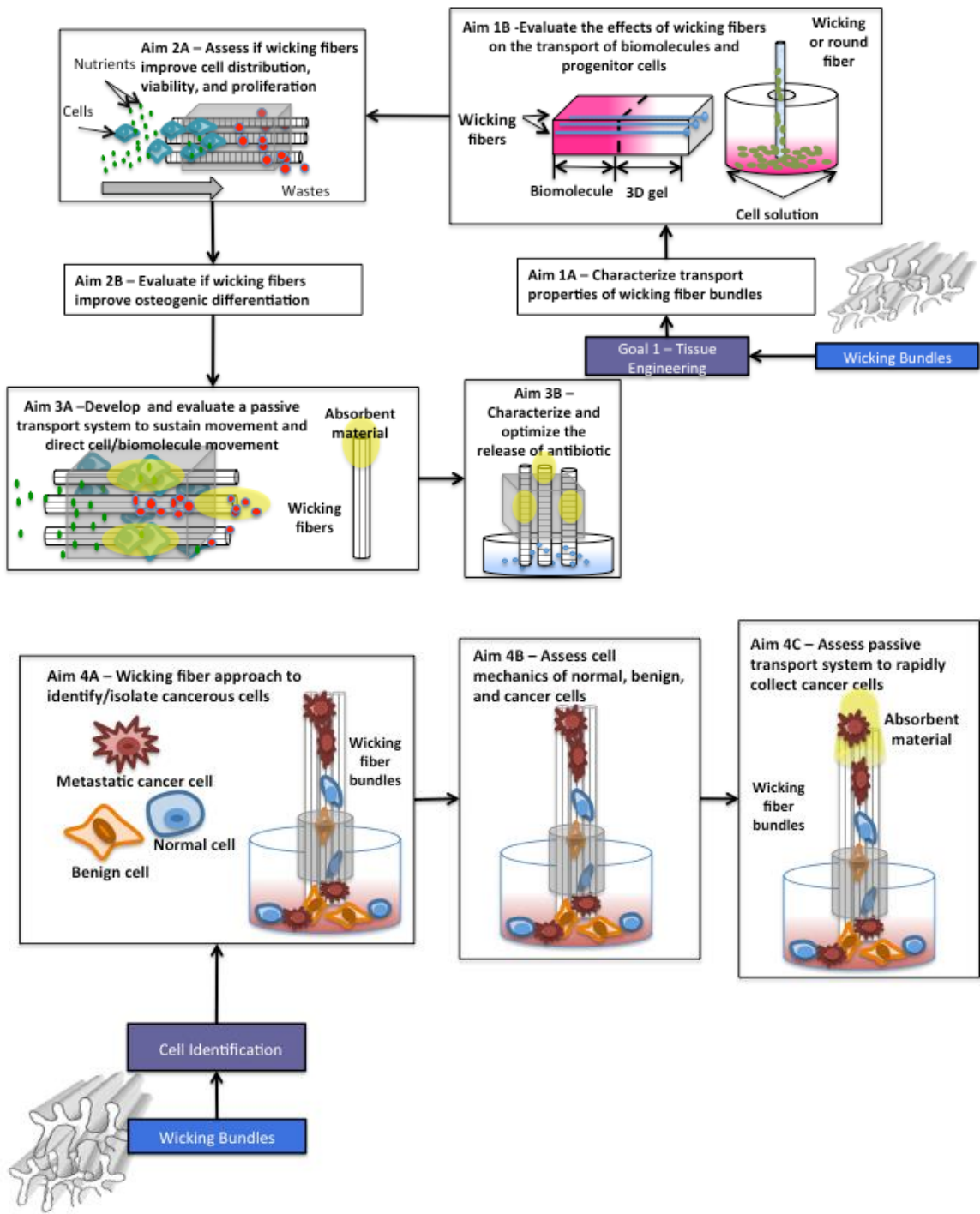
Specific Aim 4 – Assess the ability of the wicking fibers to identify and isolate subpopulations of cancer cell with different metastatic capabilities

- *Phase A* – Optimize the wicking fiber approach to identify cancerous cells from a mixture of benign and more aggressive cancer cells
- *Phase B* – Investigate the distribution of cancer cells of varying metastatic potential and changes in cells mechanical properties
- *Phase C* – Assess the efficiency of the wicking fiber and absorbent construct to rapidly collect cancer cells of high metastatic potential

Specific Aim 5 – Develop and assess an interactive learning module that introduces middle school female students to tissue engineering and related transport phenomena

Chapter 1 provides an overall literature review of the topic; various sections published in *Critical Reviews in Biomedical Engineering*, 2014. Studies supporting the first aim, described in chapter 2, investigated fluid transport properties of various configurations of wicking fibers, and the ability of wicking fibers to transport biomolecules and progenitor cells; work published in the *Journal of Tissue Engineering & Regenerative Medicine*, 2014. Studies supporting the second aim, presented in chapter 3, explored the effects of wicking fiber bundles on cell viability, proliferation, and distribution in all regions of the scaffold, predominately in regions in the center of the scaffold or furthest from the vascular source. The final study in chapter 3 determined the effect of wicking fiber on osteoblastic differentiation. Studies building toward the third aim (Chapter 4) involved the development of a passive transport system using the wicking fiber bundles and evaluation of whether the system can sustain transport longer and more efficiently direct the movement of progenitor cells and biomolecules to the center of the scaffold where necrosis or delayed bone formation occurs. In Chapter 5, the cross-sectional effects of the fiber bundles on antibiotic elution were explored, as well as, various mechanisms to load the antibiotic into the system. Experiments supporting the final technical aim, presented in chapters 6, investigated the ability of the wicking fiber transport system to identify and isolate cancer cells of different stages of aggressiveness. This chapter further explores the use of the wicking system to separate progenitor cells of varying differentiation potential. The factors affecting cell of cell type separation were investigated in Chapter 7. The final chapter reviews the development of an educational module designed to effectively introduce young middle school students to tissue engineering and the impacts

of tissue engineering on advancing the medical field; the module impact was evaluated using pre- and post- quizzes to assess if there is an improvement in the understanding of tissue engineering. Survey assessments were implemented to evaluate if the module influenced a change in interest in the field of science and engineering. The following flow chart illustrates the specific aims of this work.



CHAPTER ONE

LITERATURE REVIEW

Introduction

Bone grafting is required in sites where bone formation will not spontaneously occur, to bridge a large bone defect or fusion site. These grafts are used to improve the formation of bone in critical defect sites that can result from trauma, complex non-unions, fusions, or resections from pathologies^{1,2}. In the United States, 1.5 million bone grafting procedures are conducted annually and are increasing at an annual growth rate of 13%^{3,4}. Spinal fusions are the most common grafting procedure, constituting half of all bone graft orthopaedic procedures⁵. Even with the use of bone grafts to augment bone regeneration, non-unions or impaired bone formation occur in both critical bone defects and fusions. Delayed bone formation or non-union occurs in 5-10% of all fracture cases and in 20% of high-energy trauma fractures^{1,6}. Non-union rates in spinal fusions are reported at a relative frequency of 5-40% based on the location, surgical technique, type of graft used, and patient indications⁷.

The cause of pseudoarthrosis, or non-unions, can be related to both patient and surgical factors, including metabolic abnormalities, smoking, infection, fracture location and pattern, soft tissue damage, and excessive motion at the fusion or defect site^{8,9}. Regardless of which surgical approach is used to treat a patient with a large critical bone defect, there are necessary contributing factors that result in successful bone formation. These contributing factors include the use and choice of instrumentation, the amount and type of graft material, the surgical technique, and the surrounding environment^{7,10-13}.

Successful bone formation in spinal fusion and fracture repair procedures can, in part, be controlled by the properties of the bone graft. Even with advancements in tissue engineering and the development of composite grafts, autologous bone grafts remain the gold standard for bone grafting procedures^{14,15}. Due to availability and limited amounts of autologous bone graft, there is a need and competitive market to develop bone substitutes that enhance bone formation in fusion procedures and critical size bone defects¹⁶. Currently, no alternative bone grafts, including allograft, synthetic, and composite substitutes, have stimulated comparable bone forming qualities to autologous bone graft. In fact, only 10% of the bone grafting procedures globally are performed with synthetic bone graft¹⁷. Vast research has been conducted to identify the critical cellular and molecular events during the well-orchestrated bone formation process^{18,19}. By understanding the local and systemic molecular and cellular factors, synthetic bone grafts can be improved.

The local surrounding environment of the implant site influences the bone healing process and plays a critical role in the success of the graft. The implant environment varies based on location, fracture pattern, patient indication, quality and loss of bone, as well as surgical technique. Therefore, it is critical to understand the interactions and effects of the surrounding tissue environment with bone grafts to improve success rates. Critically important to this implant environment is the presence of vasculature. The success of bone formation is highly dependent on the surrounding vasculature and is often overlooked when designing tissue engineered constructs²⁰. Many tissue engineering methods fail to account for the contribution of the surrounding environment. By understanding the interaction

between the surrounding tissue of the fusion or defect site and the bone graft, tissue engineered constructs can be better tailored to lower rates of non-unions.

Critical defects and fusions require large amounts of bone formation to successfully repair or fuse the bone. Hence, a large bone graft is desired to fill the region and stimulate bone formation. The intrinsic limitation of large bone scaffolds is their inability to promote mass transport and encourage penetration of bone-forming cells and biomolecules into the scaffold's interior²¹. Bone formation is directly impacted by the vascularity of the scaffold and the surrounding implant site. Researchers have shown that lack of vasculature in the central region results in high risk for pseudoarthrosis and failure of complete fusion²²⁻²⁵. Likewise, avascular regions in critical fracture defects have led to necrosis of cells in the interior of large scaffolds, as well as heterogeneous formation of bone²⁶.

This first section of this chapter will provide background information on the anatomy and physiology of the spine as well as clinical information regarding the types of spinal fusion procedures and their limitations. The second section of this chapter will assess the importance of vasculature and related environmental factors during the bone healing process both for spinal fusions and for large fracture defects. This next section will focus on the vascular, cellular, and biomolecular contribution of local surrounding tissue, including the adjacent muscle and periosteum, to bone formation. The final sections will evaluate currently available bone substitutes and bone tissue engineering approaches to improve transport and vascularity within large bone scaffolds for critical defects.

Market for Spinal Fusion Surgeries

Spinal fusion procedures are standard treatments for lower back pain caused by disc degeneration, spinal deformities, or trauma²⁷. The worldwide market for spinal devices totals 3-5 billion in revenue and is growing approximately 25% each year²⁸. A recent article in *Spine* analyzed the frequency and trends of spinal fusions in the United States from 1998 to 2008²⁷. Figure 1.1 shows the frequency of spinal fusion surgeries in this decade compared to other common surgical techniques, which include: total knee replacement (TKR), total hip replacement (THR), laminectomy, coronary artery bypass graft (CABG), and percutaneous transluminal coronary angioplasty (PTCA)²⁷. In the past three decades, there has been a significant increase in the number and cost of spinal fusion surgeries in contrast with other surgical procedures with lumbar fusions experiencing the largest increase in number of procedures performed this decade.²⁷

Fusion procedures require the use of a bone graft. Over 500,000 orthopedic procedures are conducted with the use of bone grafts in the United States. Spinal fusions make up roughly 50% of these procedures²⁸. The increase in prevalence of lower back pain and, subsequently, the increase in spinal fusion procedures show there is a need and competitive market to improve bone substitutes that augment bone formation in spinal fusion procedures¹⁶.

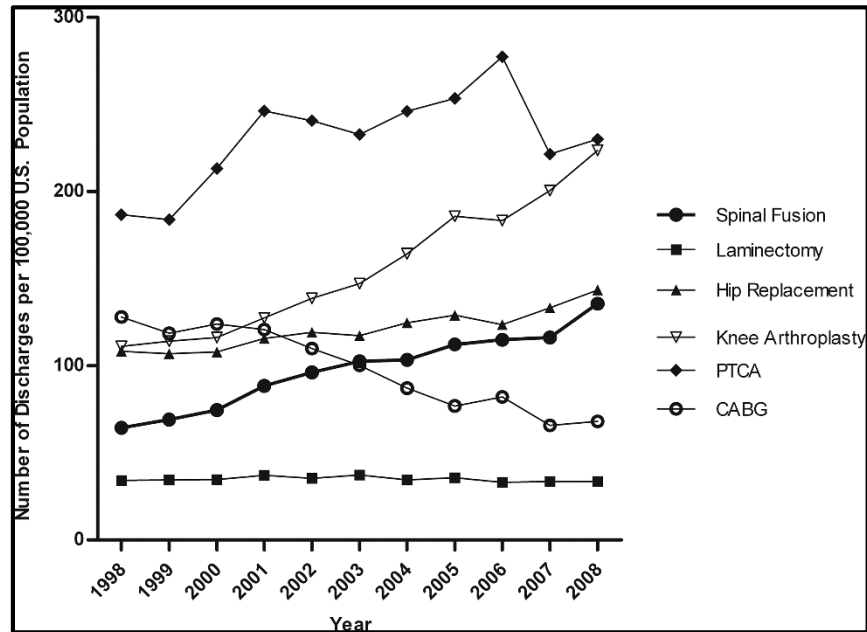


Figure 1.1: Graph depicts the rate of common surgical procedures in past decade (Adapted from Rajae et al. (2012) Spine)²⁷.

Problems with Spinal Fusion Procedures

Spinal fusion treats lower back pain and other spinal deformities by restoring stability²⁹. A non-successful spinal fusion indicates pseudoarthrosis, or the formation of a “false joint” caused from failure of bone formation, union, or remodeling. Pseudoarthrosis can result in pain, instability, and disability. A 2013 review article from *Journal of the American Academy of Orthopaedic Surgeons* have reported non-unions to occur at a relative frequency between 5-40% based on the location, surgical technique, type of graft used, and patient indications. Posterolateral spine fusion (PLS) is the most common spinal fusion procedure and involves placing the bone graft in the posterolateral portion of the spine, where fusion occurs. The incidence rate of pseudoarthrosis for this procedure has a similar relative frequency between 5-44%⁷. The cause of pseudoarthrosis, or non-unions,

in spinal fusion surgeries can be related to a number of factors, including metabolic abnormalities, smoking, infection, and excessive motion at the fusion site. Regardless of which surgical treatment is used to treat a patient with a degenerative spinal disorder, there are necessary contributing factors that result in a successful spinal fusion. These contributing factors include the use and choice of instrumentation, the amount and type of graft material, and the surgical technique^{7,10-12}. Like most implanted tissue engineered constructs, the surrounding environment and its interaction with the construct plays a critical role in the success of the graft. The environment of the fusion site is unique in that bone forms where it normally does not. Therefore, understanding the contributing factors from surrounding tissue and interaction with the bone graft is essential for improving fusion rates. The surrounding environment of the implant provides vasculature. The success of bone formation is highly dependent on the surrounding vasculature and is often overlooked when designing tissue engineered constructs²⁰. Although tissue engineering advancements have resulted in synthetic bone substitutes with attributes that contribute to bone formation, autologous bone graft is still the gold standard. Many of the tissue engineering methods fail to emphasize the contribution of the surrounding environment. By understanding the interaction between the surrounding tissue of the fusion site and effect on the bone graft, and using this knowledge for tissue engineering constructs, the success of bone grafts will increase, ultimately resulting in lower rates of pseudoarthrosis.

Anatomical Background

Bone

Bone regeneration is a multifaceted intrinsic process involved predominately in bone healing and skeletal remodeling³⁰. This process can be compromised in bone conditions such as large bone defect, tumor resection, or skeletal abnormalities. Often in orthopaedic surgeries, such as oral and maxillofacial surgery or spinal fusions, bone regeneration and formation is required in large quantities that the body cannot generate normally. When bone regeneration is compromised, bone substitutes and other bone tissue engineering solutions are critical for improving bone repair and bone formation³⁰. Understanding the components of bone, the dynamic processes, and the factors that maintain bone, will greatly contribute to developing a bone tissue engineering solution when bone regeneration and formation is compromised.

Bone is a dynamic, specialized connective tissue with the inherent ability to remodel and renew itself. The dynamic processes of bone are controlled by physiological stimuli, such as hormones, external mechanical loads, and pathological conditions³¹. Bone contains both mineralized and nonmineralized content. The mineralized content comprises mostly hydroxyapatite. This component of bone provides support and a storage site for calcium and phosphate. The organic component, or nonmineralized content, of bone is produced by osteoblasts and consists of collagen type 1 and ground substance of proteoglycans and noncollagenous glycoproteins^{31,32}.

Bone tissue can be characterized by the porosity or volume fraction of soft tissue. There are two types of bone tissue: cortical or trabecular (cancellous). Cortical bone

comprises dense and compact bone, with 5%-10% porosity. Cortical bone is formed from densely packed osteons, or Haversian systems, the functional unit of bone³³. Cortical bone is found primarily on the diaphysis of long bones, such as the femur³¹. This type of bone forms a rather thick cortex, which provides essential strength for the mechanical loading conditions of the femur. Low vasculature found in cortical bone is a result of the dense packing, and is supplied by the Haversian canal system³¹. Trabecular, or cancellous, bone is less dense than cortical bone and is most abundant in cuboidal bone, such as vertebrae. Trabecular bone has a much higher porosity, 75%-95%, than cortical bone. The bone matrix of trabecular bone is formed by trabeculae, which are plates or struts. The porous interlocking structure of trabeculae provides compressive strength for the tissue³³. In comparison to cortical bone, trabecular bone is greatly vascularized as a result of its highly porous structure and abundant vascular complexes between trabeculae³¹. Trabecular bone responds quicker to metabolic alterations due to the high vascularity. As a result, bone tissue composed of trabecular bone, such as vertebral bodies, is more susceptible to processes, such as osteoporosis, that can increase bone resorption³¹.

The four types of bone cells include osteoclasts, osteoblasts, osteocytes, and bone-lining cells. The primary functions of these bone cells are to form and maintain bone matrix. These cells either form or resorb bone in response to mechanical or physiological stimuli. Osteoclasts are multinuclear cells related to macrophages that resorb bone. In contrast, osteoblasts are mononuclear cells that differentiate from mesenchymal cells. These cells are involved in bone formation by producing osteoid. Osteoblasts that are surrounded by bone matrix are considered osteocytes, and housed in cavities called

lacunae. However, osteoblasts that remain quiescent on the surface are bone-lining cells. These cells function to transfer mineral, sense mechanical strain, and initiate bone remodeling³³. Bone cells play an essential role in physiological remodeling, which occurs throughout life and consists of bone resorption and bone formation. Adaptive remodeling will occur in response to alterations in physiological and mechanical conditions, also described in Wolff's Law³⁴.

Understanding the processes associated with maintaining and forming bone tissue provides a foundation for solutions when bone regeneration and formation is compromised. Spinal fusion surgeries require the formation of a large quantity of bone between vertebrae. Bone substitutes are necessary to augment and accelerate the bone forming process required for fusion. Understanding the biology of spinal fusions and the bone forming process can help improve the bone substitutes needed for spinal fusions.

Anatomy and Physiology of the Spine

Vertebrae are classified as irregular bones due to the complexity of their shape. Vertebrae contain both cortical and cancellous bone tissue. The micro-architecture of the bone tissue dictates the strength and functionality of the vertebrae. The vertebral column consists of thirty-three vertebrae connected by intervertebral discs. The three distinct regions of vertebrae include: the cervical spine, the thoracic spine, and the lumbar spine³⁵⁻³⁷. There are typically seven cervical vertebrae, twelve thoracic vertebrae, five lumbar vertebrae, five fused vertebrae to form the sacrum, and four fused vertebrae to form the coccyx^{36,37}. Lower back pain targets the lumbar region of the spine and, consequently, most spinal fusion surgeries are performed in this region. The lumbar vertebrae are the largest

moveable vertebrae in the spine, supporting more weight than any other region of the spine³⁶.

Structure of Vertebrae

As shown in Figure 1.2, the lumbar vertebrae contain a large vertebral body, which forms the anterior element of the vertebrae. The vertebral body comprises primarily trabecular bone. The micro-architecture of the trabecular bone dictates the strength and mechanical properties of the vertebral body. The trabecular bone is highly dense and organized along the peripheral and the posterior region. The center and anterior regions of the vertebral body contain smaller, irregular, and less dense trabeculae, which contribute to the reduced compressive strength of these regions³⁸.

The posterior arch is composed of two pedicles and laminae, which join to form the spinous process^{31,36}. Superior and inferior articulating processes form the bilateral facet joints. Transverse processes attach on both lateral sides of the arch. The vertebral body and posterior arch form the vertebral foramen as a triangular opening. The cauda equine, a system of spinal nerves, transverse this opening. Compression of these nerves by spinal abnormalities or disc herniation can result in lower back pain³⁵. Muscle tissue attaches to the transverse and spinous processes^{31,39}. The lumbar ligaments function to prevent anterior separation of vertebral bodies and provide stability³⁵. The transverse processes, which are located on either side of the arch, play a role in supplying vasculature for posterolateral spinal fusion surgeries.

Intervertebral Disc Anatomy and Function

The intervertebral disc is a complex fibrocartilaginous tissue located between the vertebral bodies of the spine and plays a significant role in spinal support, flexibility, and durability^{40,41}. The intervertebral disc is the largest avascular tissue in the human body, with essentially no repair capabilities. Furthermore, there is a sensitive and multifaceted interaction between the small local cell population within the discs and the surrounding matrix^{40,42}. The normal highly heterogeneous tissue micro-architecture of the intervertebral disc is intricately and precisely constructed to provide the spine optimal support and stability. These factors contribute to the challenges and difficulties for tissue engineering solutions.

The intervertebral discs are defined by three structures: the nucleus pulposus (NP), the annulus fibrosus (AF), and the vertebral end-plates⁴². The nucleus pulposus, located in the central region of the intervertebral disc, contains collagenous and noncollagenous proteins, which include: collagen types III, V, IV, IX, elastin, fibronectin, and laminin⁴⁰. This region is highly mechanically loaded in compression. The high density of proteoglycans located in this region maintains a large amount of water content in the intervertebral disc to resist the compressive loads. Proteoglycans are core proteins, with at least one hydrophilic, negatively charged glycosaminoglycan (GAG) attached. This hydrophilic component causes osmotic pressure or interstitial swelling pressure, which maintains the hydration of the disc³⁷.

The concentration of proteoglycans and water content decreases toward the periphery of the disc. The inhomogeneous radial distribution of proteoglycans contributes

to even distribution of forces within the spine, resulting in spine stability. The low cell density of chondrocytes in the NP primarily functions to maintain synthesis of the surrounding extracellular matrix^{40,42}. The balance of matrix synthesis and degradation is controlled by cytokines and growth factors released from surrounding cells and matrix⁴³. This balance maintains the normal function and structure of the disc. Alterations of growth factor and cytokine concentrations can lead to structural changes that will potentially disrupt normal function. In comparison to the NP, the annulus fibrosus is composed primarily of collagen with much less proteoglycan content. The outer region of the AF is formed by densely packed collagen oriented in concentric arrays. Toward the central region of the AF, the collagen is less dense and organized. In contrast to the cellular components of the NP, the AF contains fibroblast-like cells that are thin and elongated. The concentric arrangement of collagen fibers and radial composition changes contribute to anisotropic mechanical properties to resist complex mechanical loads³⁷.

Vertebral Endplates

The vertebral end plates are located between the vertebral bodies and intervertebral disc. The endplates consist of a uniform layer of hyaline cartilage and cortical bone, which provide even distribution of loads. The blood supply for the end plates and vertebral bodies is the segmental artery⁴¹. The end plates are semipermeable and facilitate diffusion of water, solute, and wastes, through marrow channels, to the intervertebral disc⁴⁴. The red arrows in Figure 3 indicate the supply of nutrients from the vertebral endplates to the nucleus pulposus and annulus fibrosus. The mechanical properties of the end plates vary radially as well³⁷. The thickness is largest in the periphery and smallest in the center.

Understanding the biomechanics of normal vertebral components and how they are altered with age and other abnormal spinal conditions is essential for developing tissue engineering solutions³⁸.

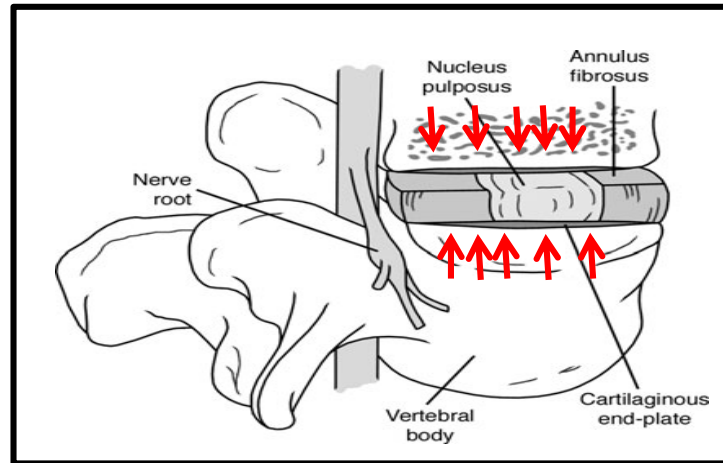


Figure 1.2: Indicates three components of intervertebral discs. Red arrows indicate vascular channels in endplates supplying the disc (Adapted from Ullrich et al. (2004) Spine-Health)⁴⁵.

Most of the vertebral components are innervated. The dorsal root ganglion and branches innervate most of the lumbar region. The nerve endings and mechanoreceptors located in these components can contribute to lower back pain. The annulus fibrosus and posterior longitudinal ligament contain nociceptive fibers, which are branches from the sino-vertebral nerve. In addition, facet joints contain sensory autonomic nerve fibers in the capsule. Abnormal spinal conditions, aging, and disc degeneration can influence the innervated components of the lumbar region, triggering pain.

Spinal Fusion Procedures

Causes of Spine Instability and Altered Environment

The spinal segments of intervertebral disc and vertebral components influence each other. The mechanical stability of the intervertebral disc is dependent on the integrity of the nucleus pulposus and annulus fibrosus. The normal intervertebral disc main function is to create stability in the spine by redistributing compressive stresses. Degeneration to the disc will alter the ability of the disc to distribute stresses⁴⁶⁻⁴⁸. Load alterations of the disc will also affect bone density distribution in the vertebral body and load alterations in the vertebral component, especially the facet joints⁴⁶. These spinal abnormalities can lead to altered spinal motion and cancellous bone architecture, which have adverse consequences, including back pain and segmental instability.

The natural aging process alters the vertebral micro-architecture, cell interplay, and overall function of essentially every anatomical structure in the spine. Intervertebral disc degeneration and lower back pain is linked with age. The frequency of lower back pain and disc alterations increases with age. Miller and coworkers used data from published reports regarding cadavers and disc degeneration incidence. They found that 97% of the individuals had developed some level of disc degeneration by age 49^{42,49}. The natural aging process of the spine includes bone mass reduction and degenerative changes. The effects of normal aging and degenerative disc disease are difficult to differentiate⁵⁰. It has been suggested that disc degeneration disease is a result of accelerating this aging process, however, the exact causes are unknown^{50,51}. The aging process will result in a continuous loss of bone mass, alterations in architecture of the spine components, and degeneration of

the disc^{33,38}. Disc degeneration results when the intervertebral disc goes through degenerative changes that cause a loss or destruction of tissue, ultimately altering the load transfer which affects the mechanical properties and tissue composition of the vertebral components^{42,50}. Disc degeneration can result due to abnormal components of the matrix or abnormal concentrations of growth factors that promote matrix degradation; for example, IL-1 or TNF- α will lead to structural changes and impaired function of the disc⁴³. Understanding the effects of age and disc degeneration on the mechanical properties of the vertebral endplates and vertebrae is imperative for developing spinal treatments that include instrumentation and tissue engineered bone scaffolds.

Aging and disc degeneration alter the environment and vasculature of the spine and surrounding tissue. Age and other conditions, such as atherosclerosis, reduce the blood supply by altering vertebral capillaries that supply the lumbar vertebrae components. As a result, there is a significant decrease in blood perfusion of the vertebral bone marrow, which supplies nutrients to the intervertebral disc. In one particular study, dynamic contrast-enhanced MRI was used to evaluate two vertebral bodies from 25 patients. The vertebral bodies evaluated were either between two adjacent normal discs or between two adjacent degenerated discs. This study found a 14% decrease in blood perfusion between two degenerated intervertebral discs compared to the perfusion between two normal discs, suggesting there is a relationship between insufficient vertebral marrow perfusion and degenerative disc disease^{41,52}.

Aging affects the composition of the vertebral endplates and causes both calcification of the cartilage and vertebral bone sclerosis. The architecture and alterations

in calcification of the vertebral end plates will affect transport of nutrients into the nucleus pulposus. Consequently, there is a reduction in blood flow and transport into the disc^{53,54}. In another study, the diffusion and temporal pattern of paramagnetic contrast medium in regions of vertebral bone and intervertebral disc were evaluated in 96 normal discs and 54 degenerative discs using magnetic resonance. The temporal pattern of enhancement between the vertebral bone and intervertebral disc was evaluated throughout both regions. This study determined the diffusion into the nucleus pulposus is related to the amount of perfusion in the bone and endplate. Furthermore, endplate changes due to age or degenerative disc resulted in altered diffusion patterns. Vertebrae with intact cartilage showed no changes in response to the diffusion pattern, while vertebral endplates containing damaged tissue or alterations changed the diffusion pattern⁵³.

Cell function in the intervertebral disc is altered due to the reduction in blood flow from vertebral end plate alterations and from local vasculature changes. This reduction will initiate or enhance degeneration⁵⁵. Other factors shown to influence degeneration include nerve and vessel ingrowth into the nucleus pulposus as well as cytokine alterations⁵⁵. An increased level of inflammatory mediators and cytokines has been shown to affect disc degeneration and cause lower back pain. Understanding the environmental changes due to these factors will affect the design of tissue engineering solutions and therapeutics. The environment and surrounding vasculature plays an essential role in bone formation. The degenerative environment of the vertebrae and interaction with native cell populations must be taken into account when developing tissue engineering solutions, such as scaffolds, to

promote bone formation. The complexity of the intervertebral disc and the environment provide major challenges for developing tissue engineering solutions for the spine⁵⁶.

Spinal Indications for Lumbar Fusion Treatment

Spinal fusion surgery was originally used to treat infectious conditions. In later years, these surgeries were used to treat deformities and traumatic injuries. With better surgical techniques, instrumentations, and understanding of the pathology, these treatments are frequently used and are currently standard treatment for degenerative spinal conditions¹¹.

Spinal fusion treatment is a procedure performed to generate stability in painful spinal segments by immobilizing the region. Panjabi describes the stability of the spine as a system consisting of three subsystems: the spinal column, the spinal muscles surrounding the column, and the neural control unit coordinating and evaluating responses. Panjabi developed a mathematical model evaluating the contribution of each of these components to the biomechanical stability of the spine. This model evaluated changes in these components due to degenerative disorders or spinal abnormalities. It also provides a basis for spinal treatment and the rationale to recreate biomechanical stability by limiting mobility. Instability defined by Panjabi is the loss of the ability of the spine to maintain normal patterns and distributions of physiological loads¹¹. Degenerative disorders and spinal deformities alter intervertebral motion, which can lead to lower back pain. Therefore, treatments such as spinal fusions decrease intervertebral motion to treat the pain. The intervertebral disc and components of vertebral bone, if causing pain, can be removed.

There are various types of spinal fusion procedures; however, in general a fusion procedure immobilizes painful segments of vertebral bone by generating new bone between the segments⁵⁷. Spinal fusion can be performed in combination with other procedures such as discectomy, decompression, and laminectomy. The type of spinal fusion and treatment is governed by a number of indications presented by the patient. These factors include the spinal disorder or disease, the quality of bone, and the patient's age. The most common spinal conditions treated with fusions include scoliosis, spondylolisthesis, disc degeneration, spinal stenosis, spinal instability due to trauma, or adverse changes to vertebrae due to infection or malignancy. Spondylolysis is a defect such as a fracture in the pars interarticularis, which is a vertebral structure between the inferior and superior articular processes. Spondylolisthesis is the forward displacement of one vertebra over the other. In some spondylolysis cases, a slip may occur and the situation progresses to spondylolisthesis; this is also known as isthmic or spondylolytic spondylolisthesis⁵⁸. In fact, 50-81% of individuals with spondylolysis also have spondylolisthesis⁵⁹. Patients can be affected by multiple conditions or the development of one condition can initiate and progress to another. For example, a patient with degenerative disease can subsequently have narrowing of the spinal canal or spinal stenosis. Spinal stenosis can also develop with degenerative spondylolisthesis and degenerative scoliosis. The alterations in biomechanical loading due to one spinal abnormality can alter the structure of the vertebrae leading to progressive degeneration.

Degenerative disc disease in the lumbar region is the most common indication of spinal fusion treatment. From the years 1998 to 2008, it is important to note the significant

increase in degenerative disc disease and spinal stenosis of the lumbar region correlates with the increase in average age of patients receiving spinal fusions. In 1998, the average age of patients was 48.8 years and increased to 54.2 years in 2008. Due to the increasing average age of our population, degenerative spinal disorders are more frequently diagnosed⁶⁰⁻⁶². A study evaluated a Medicare population of patients 65 years of age and older who had surgical procedures for lumbar stenosis. From 2002 to 2007, the analysis of Medicare recipients showed a decrease in treatments that include only decompression or simple fusion. However, the surgical rate employing complex fusion procedures increased approximately 15-fold. Complex fusion involves both anterior fusion with posterior or transverse fusion³³.

Spondylolisthesis is the most recognized indication for spinal fusion in the lumbar spine. This condition is defined by the forward translation of the superior vertebrae on the inferior vertebrae. There are five different types of spondylolisthesis. However, type III or degenerative spondylolisthesis is most often treated with spinal fusion surgeries. This type of spondylolisthesis occurs due to chronic disc degeneration with vertebral segment instability from facet joint arthritis. Disc degeneration causes the narrowing of the disc space and instability in the ligamentum flavum, which leads to instability in the sagittal plane, which can progress to spondylolisthesis¹¹. Degenerative scoliosis is another indication for fusion, primarily in the lumbar spine. Scoliosis is a structural disorder to the spine that results in a lateral curvature. This spinal abnormality is caused by disc degeneration that results in instability in the frontal plane. There are various types and degrees of scoliosis⁶³; however, degenerative scoliosis is directly related to disc

degeneration. Spinal fusion can also be employed to treat instability caused by other spinal treatments. This includes patients who had an extensive laminectomy, which is the removal of vertebrae on the posterior arch to alleviate pain by reducing pressure on the nerve roots.

Types of Spinal Fusions

One of the first types of fusions in the early 20th century was a posterior fusion performed by placing bone graft on lamina. Major complications resulted due to placement of bone graft. These included pseudoarthrosis and overgrowth of bone into the spinal canal, a condition called stenosis⁵⁷. This posterior fusion surgery was improved by placing bone graft on the side of the vertebrae between the transverse processes, a procedure known as posterolateral fusion. This technique remains is still the gold standard of posterior fusion⁵⁷.

Spinal fusion can augment other procedures such as decompression, which can involve laminectomy and or discectomy procedures. A laminectomy involves the removal of lamina, ligamentum flavum, and portions of the facet joints that are causing pressure on nerve roots, resulting in pain. This procedure and foraminectomies, which are frequently performed with laminectomies, typically approach the spine posteriorly⁶⁴. Similarly, a discectomy is a removal of disc material adversely affecting nerve roots, or the removal of the annulus if the patient indicates discogenic pain, or stimulated nociceptors in the outer annulus. Discectomies are typically performed to treat herniated discs. Decompression is somewhat controversial. Studies suggest this treatment to cause instability and contribute disc degeneration. However, there is evidence in literature supporting treatments of decompression and fusion for certain indications, such as degenerative spondylolisthesis. Instrumentation is typically recommended with fusion surgeries; however, depending on

the diagnosis of the patient before fusion, this may not always be the case⁶⁵. Spinal instrumentation augments the spinal fusion by straightening and stabilizing the spine. Typically, hooks, rods and wires are used to redistribute stresses and align the bones⁶⁶. One of the first methods of using instrumentation, developed by Dr. Harrington, used hooks placed under lamina and connected by rods. This led to further advances using bone screws attached through facet joints and then to screw plate fixation. Screw-plate fixation remains an important method for augmenting a fusion. This technique involves the placement of screws through the pedicle and the screws are connected with rods^{57-65,67}.

Numerous spinal fusion procedures implemented are based on the spinal condition. Each surgery incorporates the use of a bone graft to promote bone growth between the vertebral bodies and generate fusion⁴⁵. The most common lumbar spinal fusion surgeries include posterolateral fusions and lumbar interbody fusions⁶⁸. These procedures are typically approached from the posterior or anterior. The standard method for approach is posterior, which allows direct decompression of neural structures. However, an advantage to the anterior approach is better restoration of the disc height and ability to prepare the site for graft material.

Posterolateral spine fusion is the most common procedure and involves placing the bone graft, usually autologous bone graft from the iliac crest, in the posterolateral portion of the spine. This procedure does not always remove the intervertebral disc, as shown in Figure 1.3a. Furthermore, instrumentation such as pedicle screws and rods are used for greater stability^{69,70}. One study found the addition of instrumentation to posterolateral spine fusion has improved spinal fusion rates from roughly 60% to 90%⁴⁵. However, the

use of this instrumentation is still controversial due to the increased complication rates and inconsistent clinical outcomes⁷¹. Posterolateral spinal fusions are frequently used to treat degenerative conditions such as degenerative spondylolisthesis and spinal stenosis. This surgery has high clinical success rates with degenerative spondylolisthesis patients^{50,72}. A study involving a long-term follow up of patients of various spinal degenerative conditions and abnormalities that were treated with posterolateral fusion with instrumentation found that patients with degenerative spondylolisthesis had the greatest improvement overall with the treatment.

Interbody fusions each involve the removal of the intervertebral disc, which is replaced by bone graft and stabilized with hardware⁶⁸. Four types of interbody fusion surgeries include posterior lumbar interbody fusion (PLIF), anterior lumbar interbody fusion (ALIF), transforminal lumbar interbody fusion (TLIF), and circumferential interbody fusion. Posterior lumbar interbody fusion is also used to treat degenerative disc disease and chronic back pain. This treatment first involves a laminectomy, which is the removal of bone and disc to relieve the pressure from a pinched nerve. A spinal cage containing a bone graft can be incorporated into the empty disc space. The addition of the bone graft will promote a bone bridge, or fusion, between the vertebral bodies⁴⁵. Anterior lumbar interbody fusion parallels the PLIF technique but is approached from the anterior region of the spine, as shown in Figure 1.3b. This approach is less frequently used to treat degenerative conditions because of the difficulty in performing decompression⁷³. Transforminal lumbar interbody fusion surgery, shown in Figure 1.3c, is similar to the posterior lumbar interbody fusion, but only requires one insertion site from the side to perform the procedure, which enhances

recovery time. Laminectomy and implantation of bone graft in the empty disc space still occurs. Additional instrumentation, such as pedicle screws and rods are often used for more stability⁴⁵. Anterior/posterior or circumferential lumbar fusion is a type of spinal fusion surgery that fuses the vertebral bodies from both the anterior and posterior. Circumferential fusion typically involves anterior lumbar interbody fusion and posterolateral fusion with instrumentation⁷⁴. Several clinical studies showed better clinical results and pseudoarthrosis rates with circumferential fusion in comparison to posterolateral fusion with instrumentation^{74,75}. Although the additional fusion technique results in better outcomes, there are supplementary complications. These include operation time, cost, and neurological issues⁷⁵.

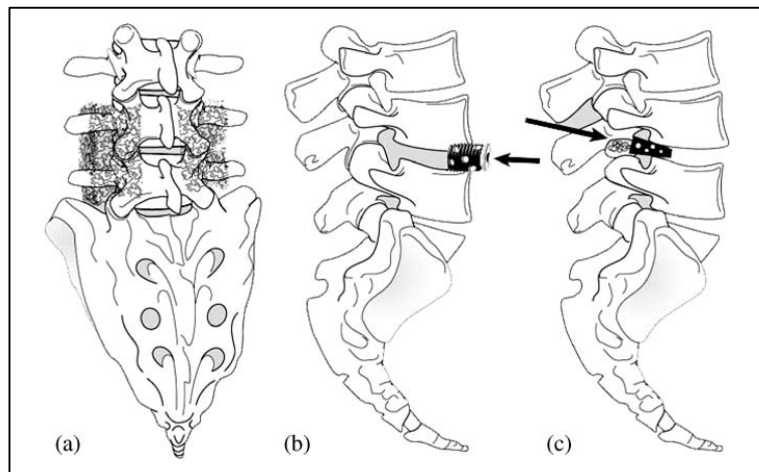


Figure 1.3: Spinal fusion surgeries. A: posterolateral spinal fusion. B: Anterior lumbar interbody spinal fusion. C: Transforaminal lumbar interbody fusion (Adapted from Ullrich et al. (2004) Spine-Health)⁴⁵

Vascularity and Bone Regeneration

The amount of bone formation is directly related to the amount of vasculature, which provides the mass transport of oxygen and nutrients, and a mode of delivery for cells and growth factors that contribute to bone formation^{21,76,77}. In general, large-area bone defects require large scaffolds that promote the transport of oxygen and nutrients through vascularization⁷⁷. This transport is essential for bone tissue constructs that include mesenchymal stem cells or other osteogenic cell types. Oxygen diffusion is limited to 200µm from the blood vessel. Mesenchymal cells in a large tissue construct will not proliferate, differentiate, and ultimately lead to ontogenesis without a transport of oxygen, nutrients, and essential growth factors that promote bone formation²⁴. Non-unions and pseudoarthrosis may occur due to poor blood supply, which is essential for the bone healing process¹². Spinal fusions require large bone grafts. For successful fusions, sufficient vascular supply must be incorporated and maintained. For example, cervical fusions have a higher success rate compared to fusions of the lumbar region due to increased vascularity to the cervical region^{12,67}. The cervical region of the spine, the abundance of vertical source arteries, anastomoses, and segmental branches provides considerably more blood flow, resulting in bone fusion even when the site is not sufficiently prepared⁶⁷. In posterolateral lumbar spinal fusion, bone formation is needed in a space greater than the critical size defect. As shown in Figure 1.4, this treatment requires large amounts of bone regeneration and therefore a large quantity of bone graft that promotes transport of nutrients and oxygen.

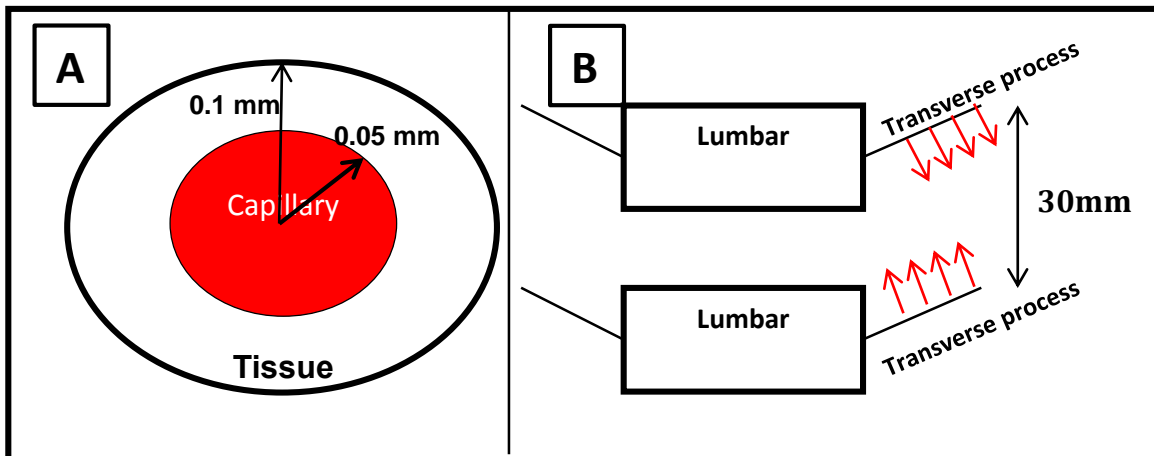


Figure 1.4: Schematic A shows the furthest cell supported by a capillary vessel is 0.1 mm. Red arrows in Image B depict the flow of nutrients from a vascular network on the transverse processes. This supply must span the entire length of fusion (30 mm)⁷⁸.

Vascular supply and types of tissue surrounding a defect will vary based on anatomical location and impact bone formation accordingly. Spinal fusions of the cervical region have a higher success rate compared to fusions of the lumbar region, due to increased vascularity to the cervical region^{12,79}. In the cervical region of the spine, the abundance of vertical source arteries, anastomoses, and segmental branches provides considerably more blood flow, resulting in bone fusion even when the site is not sufficiently prepared⁷⁹. In posterolateral fusion of the lumbar spine, bone formation is needed in a region comparable to a critical size defect. The lumbar spine does not have

the vascular supply of the cervical region, increasing the susceptibility for non-unions.

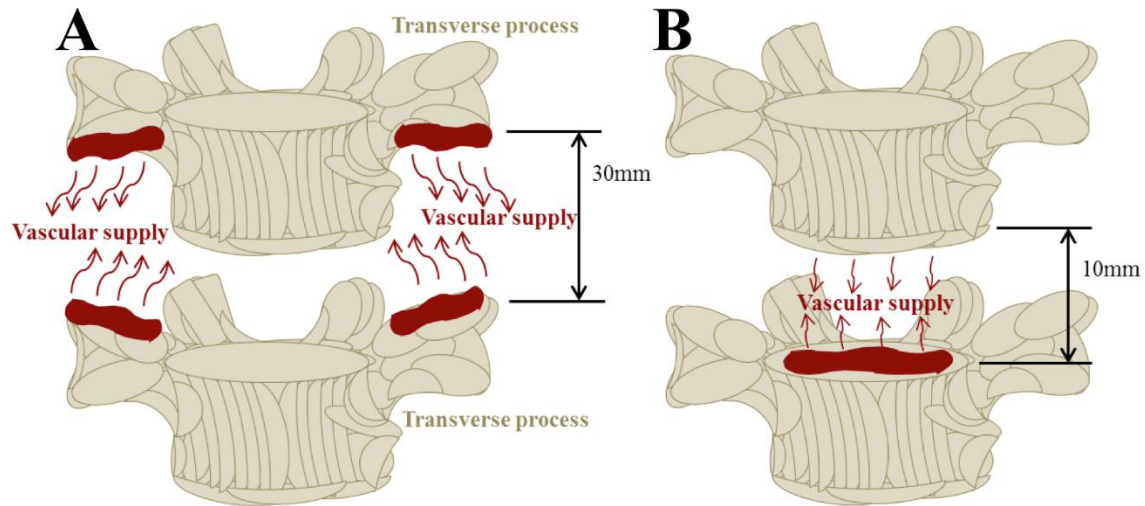


Figure 1.5A indicates the transverse processes as the major blood supply of posterolateral fusion⁸⁰. This type of spinal fusion involves high surrounding muscle tissue coverage, as compared to interbody fusion which involve the formation of bone in the intervertebral disc space between adjacent vertebral bodies⁸⁰. In contrast, interbody fusion has a greater supply of blood and osteoprogenitor cells from the high surface area of the perforated inferior and superior vertebral endplates⁸¹, seen in Figure 1.5.

Generally interbody fusion procedures have successful fusion rates due to the enhanced vascularity and access to bone marrow⁸⁰. The design of a large bone graft for fusion procedures should not only consider the amount and orientation of vascular supply but the contribution of biomolecules and osteoprogenitor cells from the surrounding tissues.

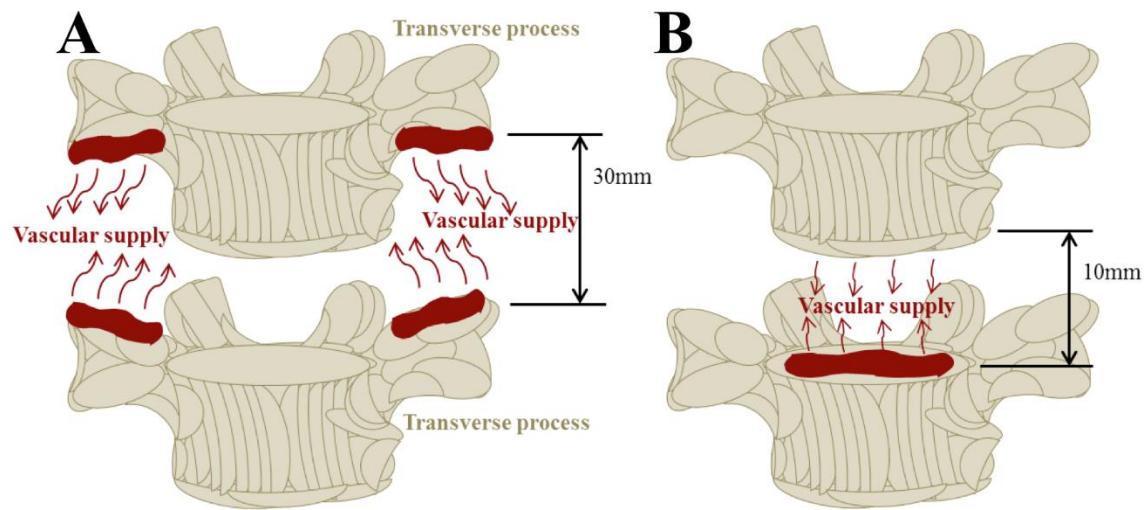


Figure 1.5. Diffusion distances of vasculature; (A) depicts the flow of nutrients from a vascular network on the transverse processes, this supply must span the entire length of fusion, 30mm⁷⁸; (B) major vascular supply for interbody fusions, must span the intervertebral distance of 10mm. (Also published in Tabbaa et al. (2014) Critical Reviews in Biomedical Engineering⁸²)

Similarly, in long bone defects the vascular supply and soft tissue coverage of the bone segment will contribute to the success of the fracture repair. Figure 1.6 indicates the major blood supplies to long bone, including blood vessels, periosteum, bone marrow, and other surrounding soft tissues. Fractures in the tibia, especially in the distal shaft, have the highest rate of non-unions compared to other long bone fractures. The limited vascular supply to the tibia is a significant factor for the high rates of non-unions⁸³. The tibia is supplied by nutrient, periosteal, and epiphyseal-metaphyseal vascular systems. The periosteal blood supply can support the entire tibia. A traumatic fracture to the tibia will typically result in stripping of the periosteum, resulting in loss of major vasculature supply

and high risk for non-union⁸⁴. Long bone defects like femoral diaphyseal fractures have much lower rates of non-unions. In contrast to tibia fracture sites, diaphyseal fracture sites have increased vascular supply and significantly greater soft tissue coverage⁸³.

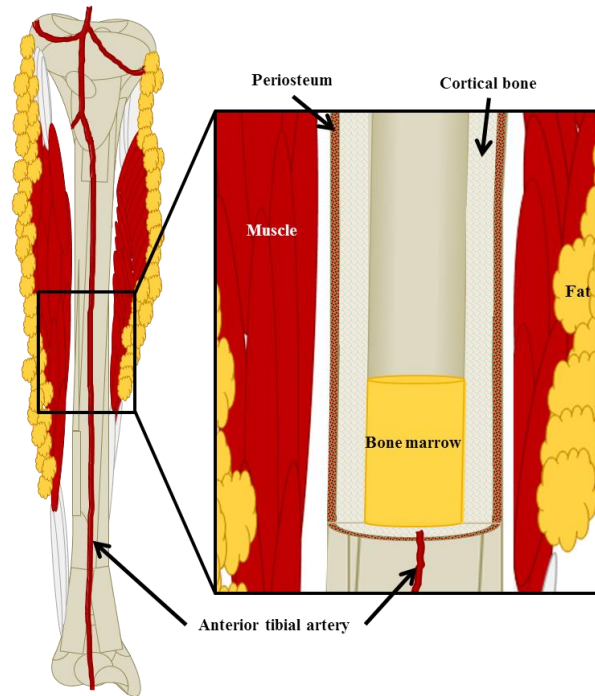


Figure 1.6. Surrounding vascular supply of tibia. Contributing factors are the surrounding musculature as well as the highly vascularized periosteum, the anterior tibial artery, and the bone marrow. (Also published in Tabbaa et al. (2014) Critical Reviews in Biomedical Engineering⁸²)

Vascularity and Tissue Contribution in Posterolateral Spinal Fusions

Bone formation in spinal fusion occurs through two different mechanisms based on the region in the spine. Intramembranous formation is one mechanism, where bone forms by direct ossification of fibrous tissue. Endochondral formation is the other mechanism, where bone replaces a cartilaginous intermediate⁸⁵. The process of bone formation in posterolateral spinal fusion begins with the migration of osteoprogenitor cells from

decorticated transverse processes and marrow cavity of autologous bone graft. Osteoinductive factors and osteoclast resorption promote the differentiation of osteoprogenitor cells into osteoblasts. These bone-forming cells deposit bone matrix, which is remodeled. The bone forming process begins at the decorticated surfaces⁸⁶.

Boden and coworkers developed an intertransverse process arthrodesis model using New Zealand white rabbits to simulate the human environment better than previous models—demonstrating a nonunion rate similar to that in humans. This model provides insight into the biology of the bone-forming process in posterolateral fusion^{17,24,80,87–89}. The technique included an intermuscular posterolateral approach, decortication of transverse processes, and the use of autologous bone graft to augment bone formation. The bone healing process was analyzed through various methods, including manual palpation, x-ray, light microscopy, quantitative histology, and molecular biology.

The manual palpation and macroscopic imaging revealed a nonunion rate comparable to that in humans. The results of quantitative histology demonstrated three temporal phases of spine fusion healing in posterolateral fusion, which occur at different times in the different regions of the fusion. These phases include inflammatory, reparative, and remodeling. In regions near the decorticated transverse processes, also called the “outer zones”, bone formation was most advanced. Quantitative histology in these regions demonstrated bone was formed through intramembranous formation. Conversely, in the “central zone”, or region furthest away from the transverse processes, bone formed via an endochondral bone-forming mechanism. Figure 1.7 indicates the location of outer and central zones in relation to adjacent vertebrae (V) and fusion mass (FM)⁸⁸.

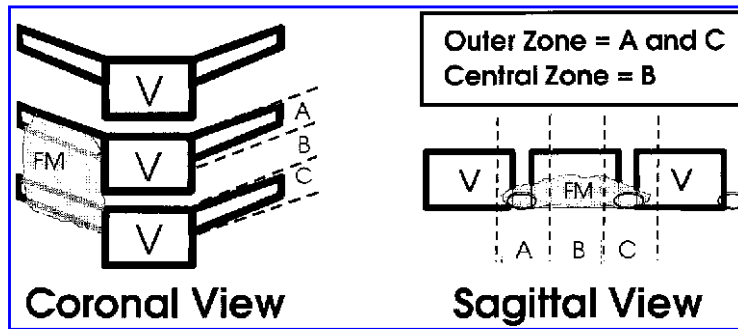


Figure 1.7: Depicts the central and outer regions. The central region forms bone later than outer regions and is often a cause for fusion failure. (Adapted from Boden et al. (2000) *Tissue Engineering*⁸⁹)

This central region experienced a lag effect, where the formation of bone was delayed with a cartilage intermediate. The lag effect, shown in Figure 1.8 below, correlates to non-unions occurring in the central zone. The lack of inadequate blood supply and increased mechanical motion resulted in lack of remodeling and ossification in this region and rendered it susceptible to nonunions^{24,80,88-90}.

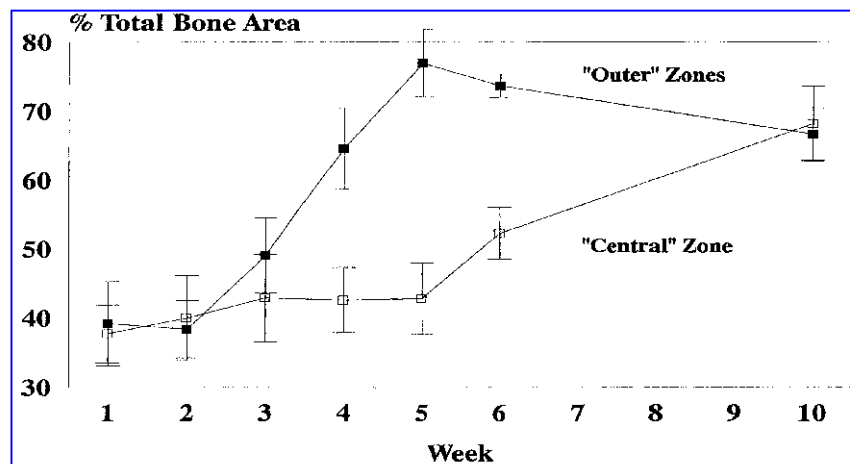


Figure 1.8: Faster cancellous bone formation in the outer zones compared to the central zone. (Adapted from Boden et al. (2000) *Tissue Engineering*⁸⁹)

Bone formation in this posterolateral fusion model was further characterized by gene expression, which was analyzed by real-time polymerase chain reaction from ribonucleic acid (RNA) in both the central and outer zones. Osteoblast-related gene expression demonstrated a temporal and spatial pattern. Osteocalcin peak expression in the central zone occurred 2 weeks later than in the outer zone, which agrees with the delayed bone formation depicted via histology. The temporal patterns of mRNA expression of bone morphogenetic proteins were analyzed in the outer and central zones. BMP-2, BMP-4, and BMP-6 depicted different levels of expression at various time points. BMP-6 was expressed in the outer zones the earliest and had the greatest increase over time. The expression of BMP-6 in the central zone showed a different temporal pattern, with delayed expression, which corresponds to the smaller bone formation and susceptibility of nonunion in this region^{22,24,26,80,88,90,91}.

The delayed bone formation in the central zone of posterolateral fusion is a result of less vascularization. In another study, Giannicola and coworkers showed that neovasculature is essential to support osteogenic potential cells and bone formation⁹². In this study, the rabbit posterolateral fusion model was employed. The neovasculature in the interapophyseal zone (central zone) and periapophyseal zone (outer zone) were evaluated using immunostained histology sections with α -smooth muscle actin antiserum. The number of blood vessels per surface area (VD) was calculated in both regions. Giannicola and coworkers found a significant difference in VD between central and outer zones of posterolateral fusion. VD was significantly higher in the periapophyseal region than in the

interapophyseal region, reflecting a gradient of VD across the regions. The most significant source of blood supply is from the transverse processes. As a result, the central or interapophyseal region is furthest from the blood supply and contains the least amount of new blood vessel formation. Similar to critical bone defects, the area of bone formation in the central region is a critical size⁹². In a similar study, Toribatake and coworkers evaluated the extent of vascularization using microangiograms in solid fusions, cartilaginous cleft type fusions, and nonunion type fusions in New Zealand white rabbits²⁶. This study related the success of posterolateral fusion to the amount of area vascularized on the transverse processes. Area of vasculature on transverse processes and fusion mass were greatest for solid fusion. The cartilaginous cleft area of vascularization was greatest along the edges but did not penetrate the fusion mass. Nonunion type fusions had no vessels along the transverse processes. This study confirmed that adequate decortication is necessary for branches of the transverse process blood vessels to penetrate the fusion mass. These studies are consistent with trends shown by Boden and coworkers^{22-24,80,88,91}. Both bone formation and BMP temporal expression lagged in the central region because this region is the furthest from the decorticated transverse processes, the major source of vasculature and osteogenic potential factors and cells.

In addition to adequate decortication, the integrity and quality of the surrounding soft tissue also plays an important role in bone formation. In posterolateral fusion, the paraspinal muscles comprise most of the surrounding soft tissue. Part of the surgical procedure involves placement of the muscles to secure the graft material as shown in Figure 1.9 below. The surrounding soft tissue, including the paraspinal muscles, must support

osteogenic potential cells in the graft, as well as the migration of bone-forming cells and inflammatory cells into the fusion mass. The effect of the surrounding soft tissue on bone formation was evaluated using a dog posterior spinal fusion model. In one group, a plastic porous membrane permeable to tissue fluids but not to cells was placed between the site of the fusion mass and the surrounding muscle tissue. Another group contained a membrane between the fusion site and muscle tissue that was impermeable to tissue fluids and cells. The latter of the two groups resulted in nonunions. This study suggests the surrounding soft tissue provides nutrition and osteogenic factors and cells necessary for fusion⁹³⁻⁹⁵.

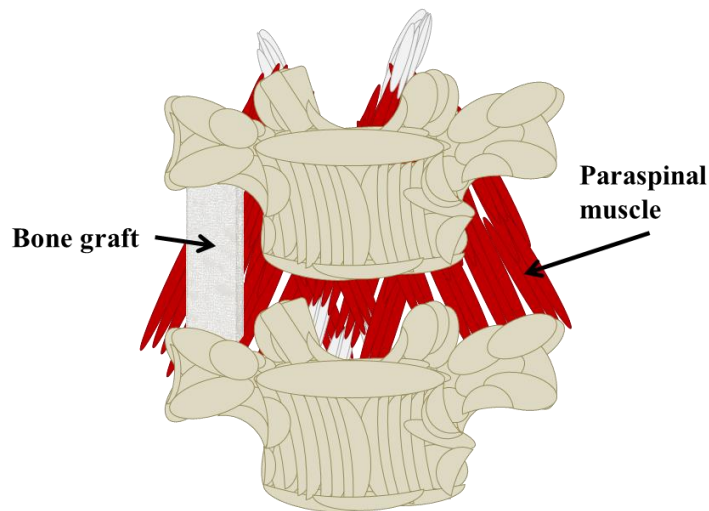


Figure 1.9. Location of posterolateral placement of bone graft and paraspinal muscle tissue. (Figure was also published in Tabbaa et al. Critical Reviews in Biomedical Engineering, 2014⁸²)

Bawa and coworkers evaluated whether the paraspinal muscles have any adverse effects on the fusion mass. Muscle tissue becomes incorporated into the bone graft, resulting in formation of fibrous tissue and inhibits bone formation. To further evaluate the

role of paraspinal muscles on posterolateral fusion, Bawa and coworkers used a rabbit posterolateral fusion model, where the animal was treated with iliac crest autologous bone graft with and without a porous or nonporous barrier sheet. The computed tomography (CT) scans and histological results demonstrated the group with a porous polymer barrier sheet between the fusion site and paraspinal muscles had the highest rate of fusion (90%). The nonporous barrier group and control group had fusion rates of 40% and 55%, respectively. This study suggests the porous barrier improves the fusion rate by preventing interposition of the muscle tissue and providing local growth factors and cells that result in bone formation and vessel ingrowth. Histology samples of the bone-muscle interaction revealed vascular ingrowth into the fusion mass in the group with the porous barrier sheets. The nonporous group contained no neovessel formation from the muscle tissue to the fusion mass. The control group had vascular ingrowth from both muscle and transverse processes. However, the increased numbers of cases of pseudarthrosis are thought to be a result of muscle interposition or migration of bone graft from the fusion site. Although the mechanism and specific factors regarding the contribution of surrounding muscle to spinal fusion is unknown, the surrounding soft tissue significantly contributes to the spinal fusion^{96,97}. Tissue engineering should evaluate the mechanism soft tissue contributes to spinal fusions to develop new tissue engineering solutions to improve the success rates of fusions⁹³.

Tissue Contribution to Fracture Repair

Similar to fusions, the composition of tissues surrounding the defect site will influence healing and susceptibility for nonunion. The loss of tissue and soft tissue damage

of a fracture plays a critical role in the successful bone repair. The tissue surrounding a fracture will vary depending on the type of fracture and anatomical location. For example, high-energy fractures typically lose bone marrow and periosteum and are supported by the vasculature of the local muscle and soft tissues. In closed fracture cases, the main sources of tissue that promote healing include bone marrow and periosteum—experimentally shown to enhance fracture healing. Both sources are accepted as the major contributors of osteoprogenitor cells, vasculature, and bone forming biomolecules. The role of surrounding soft tissue, including muscle and fat, is less established. Muscle tissue coverage has been shown to increase vasculature and bone formation in both fusion and long bone defect animal models⁹⁸. Non-unions are more prevalent in defects or fusions lacking muscle tissue and an intact periosteum. The degree of soft tissue damage will influence the activity of the periosteum, blood flow, and rate of bone formation^{99,100}. Landry and coworkers showed that moderate soft-tissue damage of the muscle tissue will actually enhance the periosteum, suggesting that injury to the muscle will not impair fracture healing. However, muscle resection has been shown to adversely affect bone healing of a trauma defect¹⁰⁰.

The fracture healing process is generally described with cellular and vascular contribution from the periosteum and bone marrow. Also of importance are the cellular, biomolecular, and vascular contributions from surrounding soft tissues including muscle and fasciocutaneous tissue. Harry and coworkers investigated the role of muscle or fasciocutaneous tissue in a murine mouse open tibia fracture model with stripped periosteum and soft tissue disruption. The outcomes indicated the group with muscle tissue

coverage had faster bone formation, 50% higher bone mineral content, and three-fold stronger union¹⁰¹. Harris and colleagues suggested the rich vascular supply from the muscle tissue enhanced the bone formation in the tibia defect¹⁰¹. In a follow-up study, Harry and coworkers investigated the amount of vasculature in muscle and fasciocutaneous tissue when in contact with the open tibia fracture site¹⁰². The vascular density was determined using immunohistochemistry post fracture at various time points throughout the fracture healing process. The outcomes showed the fasciocutaneous tissue coverage of the tibia fracture contained higher vascular density at each time point throughout the fracture healing process.¹⁰² However, the muscle tissue coverage indicated accelerated bone formation. This study suggests other factors from the muscle tissue are enhancing the bone healing process.¹⁰²

To investigate potential contributing factors from muscle tissue, other researchers have explored the osteogenic potential of myogenic cells^{103,104}. Studies have demonstrated the ability of isolated muscle-derived progenitor cells to differentiate towards osteoblast lineages, both *in vitro* and *in vivo*¹⁰⁵. Liu and colleagues investigated the contribution of muscle progenitor cells (MyoD- lineage cells) *in vivo* using a MyoD-Cre+: Z/AP+ conditional reporter mouse with MyoD-lineage cells labeled with a human alkaline phosphatase (hAP) reporter¹⁰⁶. The contribution of the MyoD-lineage cells were assessed in both open and closed mouse tibia fracture models. The closed fracture model consisted of an intact periosteum, whereas the open fracture model simulated a high-energy fracture with tissue trauma and a stripped periosteum. Although the outcomes from the closed fracture group showed no significant contribution of the MyoD-lineage cells to the fracture

callus, the open fracture group contained approximately 50% of the MyoD-lineage cells. The outcomes suggest the muscle acts a “secondary periosteum”, as described by Liu and coworkers. In cases such as closed fractures where the periosteum is intact, the muscle demonstrated limited contribution. The periosteum can directly supply the fracture with vasculature and mesenchymal progenitor cells as well as other bone forming growth factors. In fracture cases where the periosteum is stripped or damaged the muscle will directly impact the fracture healing contribute significant amounts of progenitor cells¹⁰⁷. This work suggests that muscle supplies vasculature as well as muscle-derived progenitors, which play a critical role in the bone repair process in addition to the conventional contributors, periosteum and bone marrow.

Table 1.1: Soft tissue contribution to fracture repair and spinal fusion (Table was also published in Tabbaa et al. Critical Reviews in Biomedical Engineering⁸²)

Soft tissue evaluation	Animal model	Experimental groups	Outcomes	Comments	Authors
Posterolateral fusion					
Paraspinal muscle	Rabbit posterolateral fusion model	Control - autograft in one side of rabbit; Group 1 - autograft contained in porous barrier sheet; Group 2 - autograft contained in nonporous barrier	Control - graft in contact with muscle, 55% fusion; Group 1 - porous sheet allows blood vessel and cell penetration, 90% fusion; Group 2 - nonporous sheet prevented muscle contact, 40% fusion	The porous sheet allowed vasculature and cell penetration, creating fusion rates. The porous barrier prevents muscle interposition that can lead to pseudoarthrosis	Bawa et al. 2006 ⁹³
Paraspinal muscle	Canine posterior fusion model	Group 1 - posterolateral fusion with autograft; Group 2 - posterior fusion with paraspinal muscle flap	Group 1 – 50% fusion rate after 16 weeks; Group 2 – 87.5% fusion rate after 16 weeks	Outcomes suggest the blood supply and muscle derived factors contribute to the enhanced fusion rates	Xi et al. 2010 ⁹⁴
Tibial fracture					

Fasciocutaneous and muscle tissue coverage	Murine open tibial fracture model with stripped periosteum and soft tissue disruption	Group 1 - tibial fracture covered with muscle tissue; Group 2 - tibial fracture covered with fasciocutaneous tissue	Muscle coverage group: faster bone formation, higher bone mineral content, stronger union Fasciocutaneous coverage: Greater vascular density	The fasciocutaneous revealed slower bone formation than muscle tissue coverage group, however, the tissue did not impair callus formation	Harry et al. 2008
Fasciocutaneous and muscle tissue contact	Murine open tibial fracture model	Control - no fracture with soft tissue and periosteum dissected; Group 1 - fracture covered with muscle; Group 2 - fracture covered with fasciocutaneous tissue	Fasciocutaneous tissue resulted in higher vascular density than muscle throughout the fracture healing, muscle showed accelerated bone formation	Outcomes imply factors other than vascularity are contributing to the accelerated bone formation with muscle tissue coverage	Harry et al. 2009
Myogenic progenitor cells	Murine tibial fracture model	Group 1 - closed fracture; Group 2 - open fracture	Group 1 - muscle-derived progenitor cells had no significant contribution Group 2 - 50% of muscle-derived progenitor cells contributed to fracture callus	Suggests muscle directly affects repair in fractures with damaged periosteum; intact periosteum is the major contributor in cases such as closed fractures	Liu et al. 2011 ¹⁰⁶
Injured muscle on periosteum	Rat tibial bone defect	Group 1 - Bone defect with muscle injury Group 2 - Bone defect without injury	The bone defect with muscle injury resulted in increased proliferation of the periosteum and increased osteoblast activity	Moderate soft tissue damage to the muscle initiates the inflammatory response and increases periosteum activity	Landry et al. 2000 ⁹⁹

Cellular Contribution in Fracture Site from Surrounding Tissues

In addition to vascular contribution, the surrounding connective tissues may also supply osteogenic progenitor cells and bone initiating biomolecules critical for bone formation. Researchers have investigated the osteogenic cellular contribution from surrounding tissues, including the periosteum, local bone, bone marrow, muscle, fat, soft tissues, as well as homing through the systemic circulation¹⁰⁸.

Vascular pericytes are considered multipotent osteoprogenitor cells that penetrate the fusion or defect site through invading capillaries and other microvessels^{109,110}. Several research groups have investigated the osteogenic potential of vascular pericytes isolated from aortic intima. The studies found, both *in vitro* and *in vivo*, that vascular pericytes are osteogenic and capable of differentiation into functional osteoblasts¹¹¹.

Muschler and coworkers investigated the osteoprogenitor cells in the systemic circulation and their ability to migrate through the systemic circulation to contribute to bone formation of the defect¹¹². This study used a mouse parabiotic murine model with transgenic green fluorescent mice (GFP+) and wild type mice (GFP-). The outcomes indicated the GFP+ cells from the donor mouse home through the peripheral blood and contribute to the fracture. Furthermore, the results showed an increase in GFP+ cells between 7-14 days post fracture, suggesting the osteoprogenitor circulating cells coincide with revascularization and hard callus formation¹¹². The outcomes of this study support the outcomes of earlier investigations, finding the fracture site may provide a homing signal for circulating progenitor cells^{112,113}.

Shirley and coworkers used New Zealand rabbits to study the systemic transport of bone marrow-derived stem cells in an osteotomy model¹¹³. Bone marrow mesenchymal stem cells were isolated and fluorescently tagged to allow image analysis. After osteotomy, cells were transplanted into the fracture site intravenously, or into a remote tibial bone marrow cavity. Interestingly, general systemic MSCs implanted intravenously did not relocate to the site of the osteotomy, while both the directly implanted MSCs and remotely located MSCs within the tibial remained and migrated to the site, respectively. Not only are stem cells recruited from the adjacent tissue during fracture repair, but also they are recruited systemically from locations of higher mesenchymal stem cell reservoirs.

Table 1.2: Osteogenic Cell Contributions. (Also published in Tabbaa et al. (2014) Critical Reviews in Biomedical Engineering⁸²)

Stem cell	Source	Plastic potential	Procedural notes	Outcomes	Author
Mesenchymal	Human adipose tissue	Proangiogenic	Hind limb ischemic model of nude mice using human adipose-derived stem cells (ADSC); isolated by collagenase-I	Increased blood perfusion in the injury model; potential for improved neovascular support	Kim et al. 2007 ¹¹⁴
Muscle	Rat hind-limb muscle	Osteogenic	Rat muscle; cell isolation by collagenase-XI digestion and plating onto collagen-coated flasks	Potential for highly osteogenic source of stem cells for tissue engineering applications	Kim et al. 2008 ¹⁰⁵
Muscle	Human skeletal muscle	Myogenic, adipogenic, osteogenic, chondrogenic	Cells isolated by modified pre-plate technique and subjected to immunomagnetic separation	Demonstrates muscle stem cells as a potential multipotent stem cell, needs further testing to demonstrate osteogenic potential	Lu et al. 2010 ¹¹⁵
Pericyte	Bovine retina	Chondrogenic, adipogenic	Pericytes identified by morphology, expression of α -smooth muscle actin, and cell-surface ganglioside	Preliminary evaluation demonstrating the potential for these two lineage cell maturation; further studies needed to confirm	Farrington-Rock et al.

					2004 ¹⁰ 9
Pericyte	Human gracilis and semitendinosus muscle		Isolation by collagenase-I and plating onto collagen-coated flasks	Adult skeletal muscle could be an important source of multipotent stem cells; isolated cells do not express endothelial cell surface markers	Levy et al. 2001 ¹¹ 6
Periosteal	Mouse hind-limb periosteum	Adipogenic, osteogenic	Tissue explants cultured on fibronectin-coated flasks	MC3T3-E1 preosteoblast cells exhibited higher levels of ALP activity; fibroblasts demonstrated higher levels of Oil Red O over periosteal cells; periosteal stem cells have potential but potentially limited	Arnsdorf et al. 2009 ¹¹ 7
Mesenchymal	Rat bone marrow		Bone marrow of femora, centrifuged through cell strainer and adherent cells used	Had lower colony forming units but demonstrated highest levels of osteogenic potential	Hayashi et al. 2008 ¹¹ 8
	Rat periosteum	Osteogenic	Diaphyseal areas of femora and tibiae; collagenase and centrifuged through cell strainer, adherent cells used	Periosteal cells demonstrated osteogenic potential, only slightly lower than MSC; differs from other literature potentially due to passage levels of cells evaluated	
	Rat adipose tissue		Inguinal adipose tissue; collagenase	Demonstrated lower osteogenic potential than bone marrow and periosteal stem cells; should be considered when investigating sources for bone tissue engineering	

Review of Bone Tissue Engineering and Bone Substitutes

Bone Tissue Engineered Scaffolds

The field of tissue engineering is based on understanding normal tissue formation and regeneration and applying this knowledge to produce new functional tissue when normal repair process is impaired and there is a need for new tissue formation. The design of tissue engineered constructs incorporates skills from the fields of cell biology, medicine, and engineering. The goal of tissue engineering is to generate functional tissue; one

approach encompasses incorporating progenitor cells and growth factors on a scaffold (also termed “matrix” or “construct”) designed for a specific anatomical region or purpose. One typical approach for developing a tissue engineering construct involves isolating cells from the patient, differentiating cells on a 3-dimensional matrix with growth factors, and culturing the composite to form an *in vitro* tissue construct that can be implanted into the patient¹⁵. When designing constructs for tissue engineering it is essential to understand the pathological environment and anatomical location of the defect or area where bone regeneration is required. The location for bone regeneration will vary in terms of mechanical load, type of bone, and degree of vascularity. Furthermore, the altered environment due to the patient’s condition will affect the fixation, vascularization, and integration of the construct^{30,34,76,119–122}. In comparison to organ transplants, tissue engineered bone grafts lack pre-existing vascular networks. This avascularity is a considerable problem for spinal fusion, where a large amount of bone formation is needed. The tissue engineered construct depends on diffusion from surrounding tissue for nutrient supply and waste removal as well as essential growth factors and osteoprogenitor cells^{21,123,124}. Designing tissue-engineered scaffolds that promote transport or stimulate vasculature is essential for the success of bone grafts in areas requiring large amounts of bone formation.

Bone tissue engineered scaffolds or bone grafts are defined by three main attributes: osteogenic, osteoinductive, and osteoconductive. Osteogenic is defined as the ability of the construct to form bone tissue by containing and supporting cells that can differentiate into functional osteoblasts. Osteoinduction is defined as the recruitment and stimulation of local

bone-forming cells, typically through growth factor signaling, such as bone morphogenic proteins (BMPs). Osteoconduction describes the ability of the bone graft to act as a scaffold and generate new bone by allowing infiltration of osteogenic cells and neovasculature. The diamond concept of bone tissue engineering describes four essential factors for bone formation. These factors necessary for optimal bone formation include the biological attributes of osteoinduction, osteoconduction, and osteogenesis as well as the mechanical environment^{77,125,126}. In spinal fusion treatments, mechanical stability is a significant factor in contributing to successful fusion. Mechanical stability can be achieved using instrumentation, which has increased the fusion rates. The significant impact of mechanical stability in the success of spinal fusion is reflected by fusions in the lumbosacral junction. This region is disposed to instability due to excessive motion. As a result, this region of the spine in particular has elevated rates of spinal failure^{124,127,128}.

The diamond concept of bone tissue engineering describes four essential factors for bone formation, including the biological attributes of osteoinduction, osteoconduction, and osteogenesis as well as a proper mechanical environment^{77,126,129}. Although these four factors are critical for bone formation, a fifth element of sufficient vascularization is critical for optimizing bone formation.

depicts an additional apex to the diamond shaped model, thus establishing the star concept for bone healing. That is, successful tissue engineering bone grafts should not only incorporate the diamond concept attributes, but should also factor in principles of vascularization^{76,120}. For successful bone formation, the principles of vascularization

include preparation of the recipient site, the vascular supply from surrounding tissue, and vascularization of the bone graft.

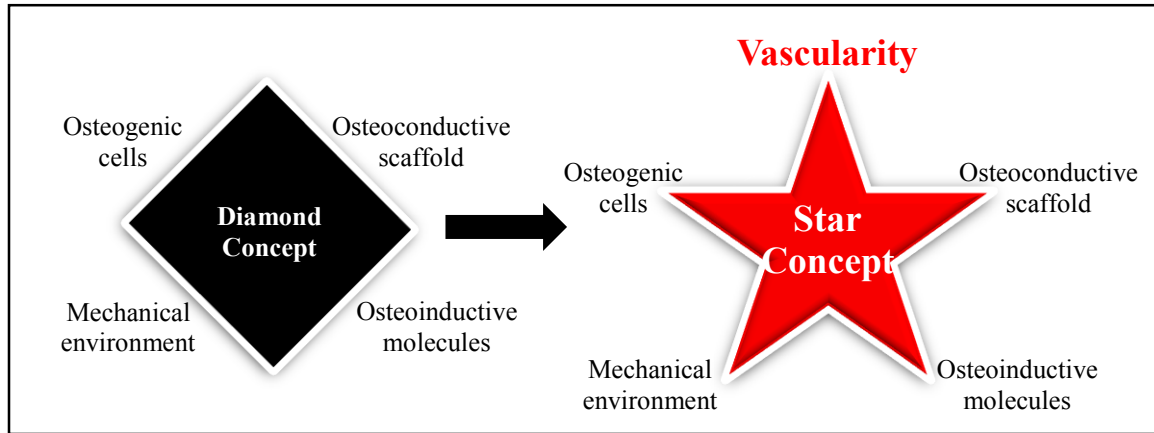


Figure 1.10. Bone fracture healing concepts. Schematic shows an additional apex for vascularity, revealing the star concept model (Also published in Tabbaa et al. (2014) Critical Reviews in Biomedical Engineering⁸²)

Types of Bone Grafts for Spinal Fusion

Autologous Grafts

Autologous bone, or autograft, is the clinical gold standard for bone repair and spinal fusions. Autografts contain the necessary attributes for promoting bone formation, including osteoinduction, osteoconduction, osteogenesis, and vascular elements.

Autografts are obtained by a secondary surgical procedure, commonly derived from the iliac crest or intramedullary canal. The most common and successful autograft in spinal fusion surgery is corticocancellous bone harvested from the iliac crest. Cancellous bone contains marrow that the cortical bone lacks, and provides osteogenic cells and inductive proteins. Furthermore, the porosity of the cancellous bone promotes neovasculature at the fusion site and an influx of osteogenic cells⁹¹. Disadvantages of autografts include tissue

morbidity at the bone graft harvest site, lack of structural integrity, increased operative time, and increased blood loss. Most importantly, autografts are limited by the total amount available. This drawback is especially an issue in spinal fusion surgeries, where large amounts of bone grafts are needed for fusion, or patients require multiple levels of fusion^{6,17,85,129,130}.

Allografts

Allografts incorporate the necessary attributes to some degree but do not revascularize or remodel as well as autografts^{15,30,34,120,123}. Allografts are mostly osteoconductive, somewhat osteoinductive, and are not osteogenic. In comparison to autografts, allografts are more available but have a higher failure rate in spinal fusion surgeries. Slower fusion rate and higher graft resorption were also observed with allografts¹³⁰. Other associated problems include the risk of disease transmission. Demineralized bone matrix (DBM) can be allografts or xenografts. DBM contains growth factors, proteins, and a portion of the mineral phase; the major disadvantage of DBM is variability between grafts. The macrostructure and mechanical properties significantly vary and are challenging to control.

Synthetic Grafts

The shortcomings of allografts and autografts led to the use of synthetic materials and composites of materials from natural and synthetic origin. Synthetic bone substitutes include the use of ceramics, polymers, metals, and cements^{8,131,132}. Polymer materials used as osteoconductive scaffolds include polyglycolide, poly-L-lactide, and polylactide-co-

glycolide. Ceramics are the most commonly used synthetic material in surgery. Ceramics include calcium phosphates that incorporate hydroxyapatite (HA) and tricalcium phosphate (TCP). Various ratios of HA and TCP are used to obtain optimal bone fusions. HA biodegrades slowly, which increases the mechanical strength but hinders remodeling. On the other hand, TCP biodegrades too fast to support bone fusion¹³⁰.

Ceramics are strongly osteoconductive but lack the osteoinductive and osteogenic capabilities of autologous bone. This has led to the use of composite bone substitutes, which include osteoinductive factors coupled with osteogenic potential cells to augment an osteoconductive material¹⁷. Bone morphogenetic proteins, in native (BMP) and recombinant forms (rhBMP), are the most effective inductive agents for bone-forming applications. BMP, in combination with a biodegradable osteoconductive polymer or ceramic, has been reported to increase union rate and has been shown to be effective in spinal fusion treatment. However, more recent literature shows BMP use in the clinic to have adverse effects on patients and complications¹³³. The addition of osteogenic progenitor cells, ranging from sources such as bone marrow aspirate to a synthetic osteoconductive material that contains osteoinductive agents, creates a composite that encompasses all of the bone-forming properties similar to autologous bone grafts. Composite synthetic bone grafts, as an alternative to autologous bone grafts, have huge potential since these grafts incorporate the bone-forming attributes but do not have the limitations of autologous grafts^{22,91,134}. Other inductive growth factors, including transforming growth factor-beta (TGF- β), fibroblast growth factor (FGF), and growth differentiation factor 5 (GDF-5), augment the bone forming process⁹¹. Autologous bone

marrow aspirate is used to augment synthetic bone grafts. The marrow is typically obtained from the posterior iliac crest and contains progenitor cells that can be isolated and expanded^{17,89,127}. Tissue engineering techniques are employed to produce composites that are effective and assist the natural bone-forming process.

The ideal bone graft should incorporate all the bone-forming attributes of the star concept to some degree. Most bone grafts used in the clinic lack one or multiple properties essential for promoting spinal fusions. Figure 1.11 depicts the attributes various bone grafts possess and quantifies the strength of each attribute. Most bone grafts contain some degree of osteoconductive and osteoinductive properties while very few bone grafts incorporate vascularity via factors that promote angiogenesis or neovessel formation. Vascularized autografts and cancellous autografts are the only bone grafts that incorporate all five attributes to some degree. The inclusion and strength of each bone-forming property is directly related to the functionality of the bone graft. Autografts are the only type containing each of the five attributes to some degree and, as a result, have the most success in spinal fusions and remain the gold standard. This further illustrates the need for a bone graft to promote vascularity for bone regeneration.

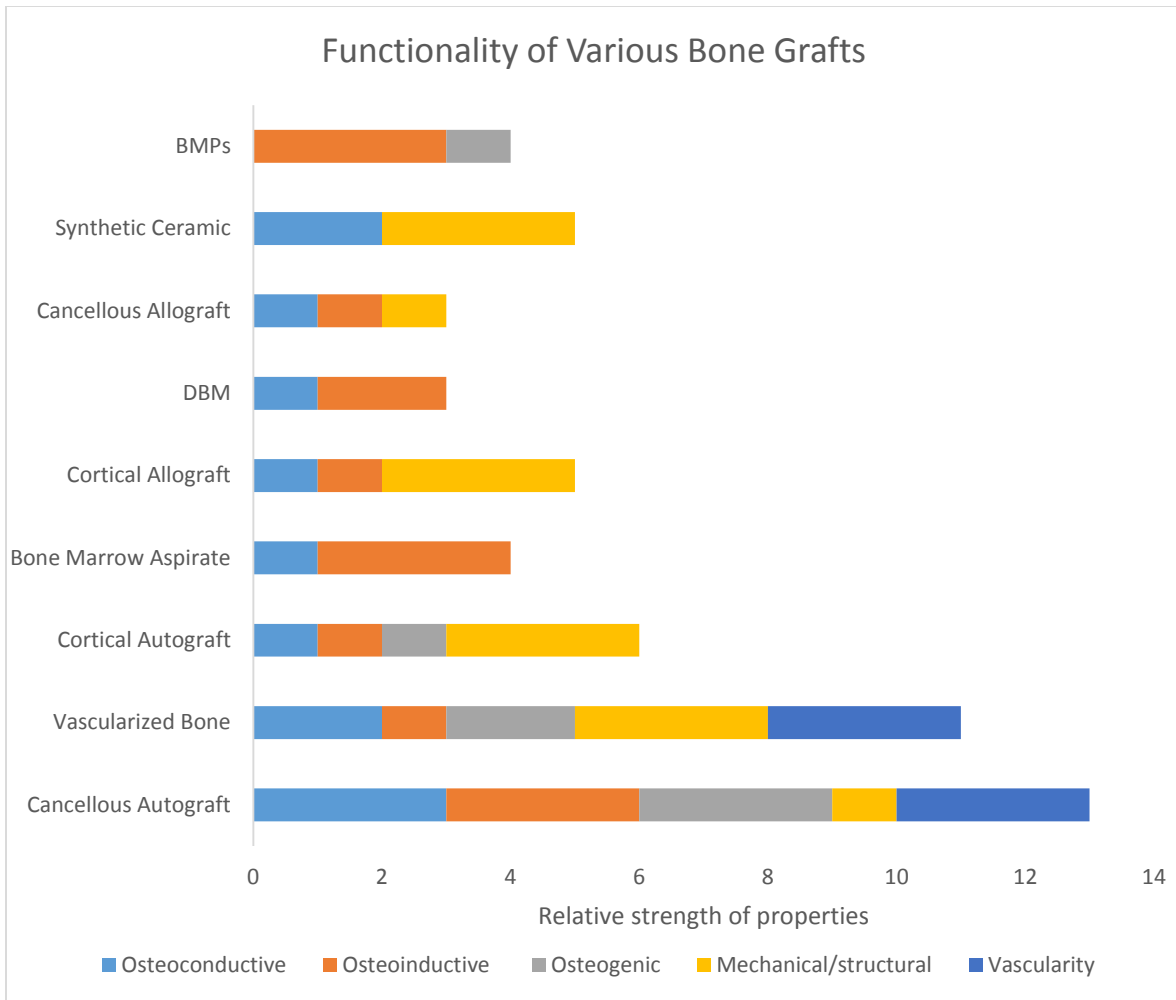


Figure 1.11. Functionality of various bone grafts based on the strength of the start concept attributes. (Also published in Tabbaa et al. (2014) Critical Reviews in Biomedical Engineering⁸²)

Bone Substitutes in the Clinic

Autologous iliac crest bone graft is the most commonly used bone substitute and is still today the gold standard for lumbar fusion. The complications involved with using this bone substitute are still present¹³⁵. Graft alternatives, in addition to bone substitutes, include graft enhancers and graft extenders. Graft extenders are used in combination with

autologous bone graft and provide a comparable fusion rate to autologous bone alone. Graft extenders are employed when there is a limited supply of autologous bone graft, predominantly for patients who require multiple levels of fusion¹³⁶. Graft enhancers function to improve the fusion rates of autologous bone used in adequate amounts. Graft extenders and enhancers are both used in the clinics.

Animal Studies to Test the Efficacy of Bone Substitutes

Relevant animal studies must allow simulation of the surgical procedure of posterolateral fusion and replication of similar bone formation as in humans. During the surgical technique of posterolateral fusion, the surgeon must extensively prepare the site for fusion by decortication; instrumentation is frequently employed. The animal models used to study posterolateral fusion do not accurately replicate all the aspects of this surgical technique nor the pathology and spinal abnormalities the patient indicates. An animal model must not only simulate fusion from the surgical technique but must also create a pathological environment that demonstrates the instability of spinal conditions¹³⁴.

In the rabbit model, no instrumentation is used and decortication is limited to the transverse processes. Dog and sheep models are anatomically better in size. A sheep model allows decortication and use of instrumentation; however, the model does not replicate the human environment better than rabbits¹²⁷. The canine models use posterior thoracic fusions, which do not correlate well to lumbar posterolateral intertransverse fusions. Another issue with the canine model is the 100% autologous bone graft fusion rate, which is not analogous to humans⁹¹. The evolutionary complexity of the species will affect the biological factors affecting spinal fusions. Animals with lower complexity, such as rats,

used in studies exhibits a much higher spinal fusion rate compared to other, more complex, species. Furthermore, the chronology of fusion will differ between species. For example, rabbit lumbar intertransverse spinal fusion develops after 4-6 weeks, whereas this process in humans and primates take months. Several animal studies are used to demonstrate the efficacy of a bone substitute for posterolateral fusion. The athymic nude rat muscle pouch assay can demonstrate the concept. The rabbit posterolateral fusion model can demonstrate the feasibility. The nonhuman primate spinal fusion model is used as an efficacy study. However, due to the cost and ethical issues associated with experimenting with primates, this type of study is only performed when the feasibility models are highly successful¹³⁴.

Clinical Studies and the Efficacy of Bone Substitutes in Posterolateral Spinal Fusion

The effectiveness of ceramics in posterolateral spinal fusions has been studied in animals and in clinical trials. In some studies, the ceramic bone substitutes showed comparable fusion rates to autologous bone. Other researchers have demonstrated that ceramics are a successful graft extender for autologous bone^{130,135,137}.

The clinical use of ceramics in spinal fusion procedures involves the use of bone marrow aspirate (BMA), which contains osteoprogenitor cells and osteoinductive factors¹³⁸. The success rate of ceramics and BMA in the clinic for spinal fusions has had varied results. Several researchers have claimed ceramic and BMA composites have comparable results to autologous bone graft, whereas other studies have shown less successful fusions. The contribution of BMA in improving fusion is not well understood. BMA is highly cellular, containing hematopoietic and mesenchymal cells that both contribute to bone formation. However, only the mesenchymal-derived cells can lead to

bone forming cells. The osteoprogenitor cells within the BMA are a very small sub-fraction of the cellular component. In fact, one mesenchymal cell is present in 100,000 cells of the BMA. The lack of mesenchymal or osteoprogenitor cells in the BMA is a major limitation^{139,140}. Other limitations include variability between patients and loss of osteoinductive cells and factors from the site through migration or diffusion^{135,137}. The cellular composition of the bone marrow aspirate will affect its success in spinal fusion and contribution to bone formation. This is reflected in the variability of BMA in efficacy trials for spinal fusion procedures.

Researchers have proven platelets to provide an ample amount of growth factors. Activated growth factor (AGF) platelet gel consists of ultraconcentrated growth factors. AGF platelet gel is suggested to improve fusions by stimulating pathways that promote osteogenesis, reducing postoperative blood loss by initiating clot formation, and stabilizing the site^{141,142}. Multiple clinical studies have demonstrated the addition of platelet gel to autologous bone graft to decrease the fusion rate has no benefit as a graft extender in posterolateral spinal fusions. Rihn and coworkers suggests the platelet gel may dissolve via fibrinolysis, reducing the amount of growth factors in the site and reducing the fusion rate. This article suggests platelet gel is inadequate as a bone graft enhancer due to the potential reduction in concentration of growth factors and because the specific types of growth factors in the platelet gel may inhibit osteogenesis¹⁴³.

Demineralized bone matrix (DBM) contains osteoinductive glycoproteins that contribute to bone formation. Similar to BMPs, several animal studies have evaluated if DBM increases the success rate for spinal fusions when combined with autologous bone

graft. Boden and coworkers suggested the use of DBM as an extender for autologous bone graft. The researchers performed bilateral posterolateral lumbar spinal fusion on 47 New Zealand white rabbits. Groups were evaluated based on the ratio of autograft to DB with which they were treated. The results of this study suggest that DB combined with autologous bone graft is comparable to using only autologous bone graft. The fusion rates were similar for each group and were determined by manual palpation²². The results of this study are comparable to a study evaluating DBM in dogs, which had similar findings.

A review of DBM to augment spinal fusion treatments found significant inconsistencies between animal studies and efficacy in spinal treatments. A major contributing factor to these inconsistencies is the variability in DBM. The osteogenic potential of this bone substitute is dependent on the type, the donor, and how the DBM is prepared. These factors in DBM contribute to the inconsistencies of the results in animal studies and clinical trials^{22,144}. Wang and coworkers evaluated the osteoinductive potential of three commercially available DBM bone grafts. This study found each product contained various amounts of DBM, with different osteoinductive potential between products, altering the efficacy of the products. The author suggests the processing procedures, the donor quality, and the sterilizing techniques alter the quality of DBM products. Bae and coworkers evaluated the amount of BMP in commercially available DBM products using enzyme-linked immunosorbent assay. Interestingly, this study determined there were varying amounts of BMPs in DBM from different lots of the same manufacturer. DBM quality and osteopotential is inconsistent between DBM products and between lots within the commercial products^{145,146}.

Molecular biology analysis of posterolateral spinal fusion shows bone morphogenic proteins (BMP-2, BMP-4, BMP-6) play a critical role in formation of bone. In a review by Boden and coworkers, the effect of recombinant human morphogenetic protein-2 (rhBMP-2) combined with autologous bone used in posterolateral fusions in rabbits was analyzed. Histology and CT scans showed the fusion mass formed from the composite had greater volume and more contact with host bone than that formed with just autograft. Histology, and analysis of gene expression of rhBMP-2 and other bone related genes, showed rhBMP-2 recruited bone-forming cells and expressed bone forming genes more homogeneously in both zones, indicating no delay in bone formation of the central zone. The use of rhBMP-2 with autologous bone graft in rabbits resulted in 100% success rate of fusion. In general, bone formation in lower vertebrae is much faster and requires less of a dose compared to nonhuman primates. This success rate was further replicated in a primate model, however, at a significantly higher dose and after a much longer fusion time. The incorporation of this osteoinductive factor with autologous bone resulted in local production of BMPs, migration of osteoprogenitor cells from surrounding muscle, and similar rates of bone formation in the central and outer zones. Human clinical trials of rhBMP-2 combined with HA and tricalcium phosphate granules showed the ability of rhBMP-2 to induce bone on an appropriate carrier. Generating large doses of recombinant and extracted BMP is not feasible or cost-effective. Furthermore, a delivery system is required to maintain levels of BMP expression corresponding to the unimpaired natural bone healing process^{24,88,91}.

The US Food and Drug Administration (FDA) approved two recombinant human bone morphogenetic proteins (rhBMP-2 and rhBMP-7) for specific spinal fusion

procedures. Infuse, a bone substitute containing rhBMP-2 (Medtronic; Memphis, Tennessee), is a commercially available product approved for 1-level anterior lumbar interbody fusion. Osteogenic protein-1 (OP-1), BMP-7 (Stryker Biotech; Hopkinton, Massachusetts), is also a commercially available product approved for revision posterolateral fusion. All other uses are off-label and not approved¹³⁵. Numerous clinical studies were conducted to evaluate the efficacy of BMPs. Based on these studies, the efficacy of BMPs is difficult to define. The indications of the patients, the surgical techniques, the outcome measures, and varying types of bone grafts used with BMPs were all varying factors between studies. Major disadvantages of BMPs are the possible complications, which include: heterotopic bone formation, resorption or osteolysis, seromas or hematomas, antibody formation, inflammatory reaction, and adverse effect on neural elements^{135,140}. Table 2 provides a list of various commercially available bone grafts and evaluates the use of various commercially available products.

Table 1.3: A summary of bone grafts used in posterolateral fusions provides examples of commercially available bone grafts and their potential use as a bone substitute or bone graft extender. (Also published in Tabbaa et al. (2014) *Critical Reviews in Biomedical Engineering*⁸²)

Graft Material	Commercial name	Discrepancies	Efficacy of graft material	References
Ceramic + BMA	Bonograft (India)	Radiographically cannot determine quality of fusion, cannot be assessed with histology	Studies have suggested both comparable and poorer fusion rates with the use BMA	Bansal et al.
Ceramic + BMA	osteoset, Wright Medical Technologies, Arlington, TN	Range of patients degenerative or spondylolytic spondylolisthesis, smokers and nonsmokers	TCP and HA ceramic can be used as an effective graft extender	Niu et al.
DBM	Grafton, DBM (Osteotech Eatontown, NJ)	Variability between DBM products	DBM can be used as graft extender. Several studies have shown comparable fusion rates to autologous bone graft	Vaccaro et al.
DBM	Acela Connexus (IsoTis OrthoBiologics Inc., Irvine, CA)	Low patient number	Results suggest can be used as extender with comparable fusion rates	Schizas et al.
Activating growth factor (AGF) platelet gel	Interpore Cross International (Irvine, CA)	Controversial use in spinal fusions	Activated growth factor platelet gel is not an effective graft extender	Rihn et al.
rhBMP-2	Infuse (Medtronic, Memphis, Tennessee)	Off-label use, uncertain dosages, and possible complications	BMP use is effective in spinal fusions however adequate dosages and complications are unclear	Taghavi et al.

In summary, autografts are the most effective bone substitute for posterolateral surgery. However, the amount available is limited and donor site morbidity may result as a complication. Allografts are more available and cost effective than autografts but are not effective bone substitutes in posterolateral fusion due to their variability and loss of osteoinductive factors and cells. DBM, however, demonstrate comparable fusion rates to autografts when used as a graft extender. BMPs are also effective graft extenders. However, the cost is high and there are complications such as adverse effects to neural elements. Ceramics, similar to DBM, have proven to be effective graft extenders when combined with BMA or BMPs. Currently, there is no effective replacement for autologous bone grafts.

Table 1.4: Characteristics of bone grafts used for posterolateral fusion.

	Efficacy as substitute	Efficacy as extender	Donor site morbidity	Cost	Disease transmission	Availability	Limitations
Autograft	High	High	High	Low	None	Low	Yes
Allograft	Low	Moderate	None	Moderate	Low	High	None
rhBMPs	Moderate	Moderate	None	High	None	Moderate	Yes
BMA	Low	Moderate	None	Low	Low	Low	None
Ceramic	Low	Moderate	None	Moderate	None	Moderate	None

Bone Tissue Engineering Strategies to Improve Vascularity

The design of tissue-engineered constructs incorporates skills from the fields of cell biology, medicine, and engineering. The goal of tissue engineering is to generate functional tissue, specifically in an environment that is indicated for poor healing. Conceptually, tissue engineering has focused on the potential of using a patient's progenitor cells and a

biologically indicative scaffold to develop an active and healthy tissue construct through *in vitro* culture techniques that could then be implanted into a patient¹⁵. When designing constructs for tissue engineering it is essential to understand the pathological environment and anatomical location of the defect or area where bone regeneration is required. The location for bone regeneration will vary in terms of mechanical load, type of bone, and degree of vascularity. Furthermore, the altered environment due to the patient's condition will affect the fixation, vascularization, and integration of the construct^{30,34,76,119,120,122}. In comparison to organ transplants, tissue engineered bone grafts currently lack pre-existing vascular networks. This avascularity is a considerable problem for spinal fusions and critical bone defects, where a large amount of bone formation is needed. Tissue-engineered constructs depend on diffusion from surrounding tissue for nutrient supply and waste removal as well as essential growth factors and osteoprogenitor cells^{21,123,124}. Designing tissue-engineered scaffolds that promote transport or stimulate vasculature is essential for the success of bone grafts in areas requiring large amounts of bone formation.

Tissue engineering provides tools to develop vascularity in bone grafts to improve the overall functionality and success of critical defects. Table 1.5 summarizes various tissue engineering methods to improve vasculature and the complexities that parallel the benefits. A major limitation is often the slow rate of vasculature formation. This rate hinders cellular proliferation, recruitment, and osteoblastic differentiation. Other limitations of current tissue engineering techniques to improve vasculature are predominately seen in large or thick tissue constructs. Tissue engineering methods, where progenitor cells such as endothelial progenitor cells are seeded to promote and develop

vasculature or new vessels prior to implantation, often fail because the cells and neovasculature are not supported from surrounding vasculature and compete for limited supplies of nutrients and oxygen.

Current tissue engineering methods to develop or accelerate vasculature formation in bone grafts overlook the support of the surrounding vasculature. The anatomical location of the defect, composition of surrounding soft tissues, and degree of tissue damage will influence the bone formation process. Tissue engineered bone grafts should be designed specifically to the intended application area. The design of a tissue engineered scaffold should consider optimization of the transport of osteogenic factors, nutrients, and cells from surrounding tissue. Current bone substitutes on the market are comparable or less efficient than autologous bone graft. However, without a mode of transport, such as vascularization, the transplanted or recruited osteogenic cells will not be supported and osteoinductive factors will not be spatially or temporally present to contribute to cell recruitment and differentiation. Due to the environment of many spinal fusions and trauma fractures, the damage to or lack of surrounding vascular supply requires development of tissue engineered constructs to specifically address transport characteristics to improve bone regeneration.

Table 1.5: Comparison of current tissue engineering methods to improve vasculature. (Also published in Tabbaa et al. (2014) *Critical Reviews in Biomedical Engineering*⁸²)

Tissue engineering method to improve vasculature	Potential Benefits	Shortcomings	References
Modify scaffold architecture	Improve mass transport by adjusting porosity, pore size, and scaffold filaments	Provides limited mass transport in large scaffolds and may decrease mechanical strength	Liu et al. 2012
Use angiogenic factors	Enhance and accelerate vascularization	Causes slow rate of vascularization, can cause necrosis	Muschler et al. 2004
Transplant vasculogenic cells such as endothelial progenitor cells	Form new vessels within the scaffold	Creates competition of oxygen and nutrients inside the scaffold, limiting cell proliferation and viability	Tsigokou et al. 2009
Genetically modify cells to secrete factors that promote vasculature	Produce proteins that promote vasculature	Creates biological risk with genetic manipulation	Shen et al. 2005
Generate <i>in vitro</i> vasculature prior to implantation	Develop new vessels within the scaffold that can be anastomosed with host vasculature	Forms vessels requiring vasculature from surrounding tissue	Johnson et al. 2011
Implant construct into subcutaneous region prior to implanting in implantation site	Minimize cost using existing vasculature to form new vasculature networks in the scaffold	Forms random blood vessels in the bone, limiting vasculature; injury may result in surrounding vascular network and new network	Safak et al. 2000 Kneser et al. 2006
Stimulate electrically	Upregulate osteoinductive factors necessary for vascular formation, improves vascularity	Generates expense and lack of evidence for efficacy in spinal fusion surgeries	Gan et al. 2006

Summary

Bone grafts should be designed specifically to the area they are implemented. The design of the tissue engineered scaffold should ideally consider how to optimize the transport of osteogenic potential factors and cells from surrounding tissue. Current bone substitutes on the market are comparable or less efficient than autologous bone graft. The substitutes are designed to incorporate attributes of osteoconduction, osteoinduction, and

osteogenesis. However, without a mode of transport, such as vascularization, the transplanted or recruited osteogenic cells will not be supported and osteoinductive factors will not be spatially or temporally present to contribute to cell recruitment and differentiation. Due to the environment of posterolateral fusion and lack of vascular supply, the improvement of transport characteristics of the bone graft is essential for improving fusion rates.

References

1. Calori GM, Mazza E, Colombo M, Ripamonti C: The use of bone-graft substitutes in large bone defects: Any specific needs? *Injury* 2011; 42 Suppl 2:S56–63
2. Park J, Ries J, Gelse K, Kloss F, Mark K von der, Wiltfang J, Neukam FW, Schneider H: Bone regeneration in critical size defects by cell-mediated BMP-2 gene transfer: A comparison of adenoviral vectors and liposomes. *Gene Ther.* 2003; 10:1089–98
3. Brounts SH, Lee JS, Weinberg S, Lan Levengood SK, Smith EL, Murphy WL: High affinity binding of an engineered, modular peptide to bone tissue. *Mol. Pharm.* 2013; 10:2086–90
4. Jahangir AA, Nunley RM, Mehta S, Sharan A: Bone-graft substitutes in orthopaedic surgery. *AAOS Now* 2008:5–9
5. Delawi D, Kruyt MC, Huipin Y, Vincken KL, Bruign JD de, Oner FC, Dhert WJ: Comparing autograft, allograft, and tricalcium phosphate ceramic in a goat instrumented posterolateral fusion model. *Tissue* 2013; 19:821–8
6. Brydone A, Meek D, Maclaine S: Bone grafting, orthopaedic biomaterials, and the clinical need for bone engineering. *Proc. Inst. Mech. Eng. Part H J. Eng. Med.* 2010; 224:1329–43
7. Grabowski G, Cornett C: Bone Graft and Bone Graft Substitutes in Spine Surgery. *Am. Acad. Orthop. Surg.* 2013; 21:51–61
8. Brown CR, Boden SD: Fracture Repair and Bone Grafting, Orthopaedic Knowledge Update 9. Edited by Fischgrund JS. Rosemont, IL, American Academy of Orthopaedic Surgeons, 2008, pp 13–22
9. Hak DJ, Fitzpatrick D, Bishop JA, Marsh JL, Tilp S, Schnettler R, Simpson H, Alt V: Delayed union and nonunions: Epidemiology, clinical issues, and financial aspects. *Injury* 2014; 45 Suppl 2:S3–7
10. Hamrick MW, McNeil PL, Patterson SL: Role of muscle-derived growth factors in bone formation. *J. Musculoskelet. Neuronal Interact.* 2010; 10:64–70
11. Panjabi MM: Clinical spinal instability and low back pain. *J. Electromyogr. Kinesiol.* 2003; 13:371–9

12. Reid JJ, Johnson JS, Wang JC: Challenges to bone formation in spinal fusion. *J. Biomech.* 2011; 44:213–20
13. Reichert JC, Saifzadeh S, Wullschleger ME, Epari DR, Schütz MA, Duda GN, Schell H, Griensven M van, Redl H, Hutmacher DW: The challenge of establishing preclinical models for segmental bone defect research. *Biomaterials* 2009; 30:2149–63
14. Giannoudis PV, Dinopoulos H, Tsiridis E: Bone substitutes: An update. *Injury* 2005; 36 Suppl 3:20–7
15. Burg KJL, Porter S, Kellam JF: Biomaterial developments for bone tissue engineering. *Biomaterials* 2000; 21:2347–59
16. An H, Phillips F: The future of spinal fusion. *Orthopedics* 2006; 29:1–3
17. Kolk A, Handschel J, Drescher W, Rothamel D, Kloss F, Blessmann M, Heiland M, Wolff K-D, Smeets R: Current trends and future perspectives of bone substitute materials - From space holders to innovative biomaterials. *J. Cranio-Maxillo-Facial Surg.* 2012:1–13
18. Fazzalari NL: Bone remodeling: A review of the bone microenvironment perspective for fragility fracture (osteoporosis) of the hip. *Semin. Cell Dev. Biol.* 2008; 19:467–72
19. Schindeler A, McDonald MM, Bokko P, Little DG: Bone remodeling during fracture repair: The cellular picture. *Semin. Cell Dev. Biol.* 2008; 19:459–66
20. Johnson EO, Troupis T, Soucacos PN: Tissue-engineered vascularized bone grafts: Basic science and clinical relevance to trauma and reconstructive microsurgery. *Microsurgery* 2011; 31:176–82
21. Amini AR, Adams DJ, Laurencin CT, Nukavarapu SP: Optimally porous and biomechanically compatible scaffolds for large-area bone regeneration. *Tissue Eng. Part A* 2012; 18:1376–88
22. Morone M, Boden SD: Experimental posterolateral lumbar spinal fusion with a demineralized bone matrix gel. *Spine.* 1998; 23:159–67
23. Louis-Ugbo J, Boden SD: Biology of Spinal Fusion, *Essentials in Orthopaedics: Spine.* Edited by Bono C, Garfin S. Lippincott Williams and Wilkins, 2004, pp 297–306

24. Boden SD: The biology of posterolateral lumbar spinal fusion. *Orthop. Clin. North Am.* 1998; 29:1–20
25. Ames CP, Smith JS, Preul MC, Crawford NR, Kim GE, Nottmeier E, Chamberlain R, Speiser B, Sonntag VKH, Dickman CA: Effect of recombinant human bone morphogenetic protein-2 in an experimental model of spinal fusion in a radiated area. *Spine.* 2005; 30:2585–92
26. Toribatake Y, Hutton WC, Tomita K, Boden SD: Vascularization of the fusion mass in a posterolateral intertransverse process fusion. *Spine.* 1998; 23:1149–54
27. Rajae SS, Bae HW, Kanim LEA, Delamarter RB: Spinal fusion in the United States: analysis of trends from 1998 to 2008. *Spine.* 2012; 37:67–76
28. Brydone a S, Meek D, Maclaine S: Bone grafting, orthopaedic biomaterials, and the clinical need for bone engineering. *Proc. Inst. Mech. Eng. Part H J. Eng. Med.* 2010; 224:1329–43
29. Kato S, Sangadala S, Tomita K, Titus L, Boden SD: A synthetic compound that potentiates bone morphogenetic protein-2-induced transdifferentiation of myoblasts into the osteoblastic phenotype. *Mol. Cell Biochem.* 2011; 349:97–106
30. Dimitriou R, Jones E, McGonagle D, Giannoudis PV: Bone regeneration: Current concepts and future directions. *BMC Med.* 2011; 9:66
31. Gunzburg R, Szpalski M, Passuti N, Aebi M: The aging spine. *Eur. Spine J.* 2003; 12 Suppl 2:1–21
32. Ross M, Romrell L, Kaye G: *Histology: A Text and Atlas, Third.* Baltimore, Williams and Wilkins, 1995, pp 150–70
33. Martin B, Burr D, Sharkey N: *Skeletal Tissue Mechanics.* New York, Springer, 1998, pp 29–77
34. Reichert J, Hutmacher D: Bone Tissue Engineering, *Bone.* 2011, pp 431–56
35. Middleditch A, Oliver J: *Functional Anatomy of the Spine, Second.* Edited by Harrison H, Campbell S, Fleming D, Wright J. Elsevier Butterworth Heinemann, 2005, pp 1–86
36. Chen K: *Spinal fusion cages: The LT-Cage® team Bursley.* 2010, pp 1–37

37. Benzel E: Spine Surgery: Techniques, Complication, Avoidance, and Management, Second. Edited by Benzel EC. Philadelphia, Elsevier Inc, 2005, pp 109–35
38. Papadakis M, Sapkas G, Papadopoulos EC, Katonis P: Pathophysiology and biomechanics of the aging spine. *Open Orthop. J.* 2011; 5:335–42
39. Strayer A: Lumbar Spine Surgery: A Guide to Preoperative and Postoperative Patient Care. 2009, pp 4–41
40. Setton LA, Bonassar L, Masuda K: Chapter 58: Regeneration and replacement of the intervertebral disc, *Principles of Tissue Engineering*, Third. Edited by Lanza, Langer, Vacanti. Elsevier Inc, 2007, pp 875–94
41. Shankar H, Scarlett JA, Abram SE: Anatomy and pathophysiology of intervertebral disc disease. *Tech. Reg. Anesth. Pain Manag.* 2009; 13:67–75
42. Whatley BR, Wen X: Intervertebral disc (IVD): Structure, degeneration, repair and regeneration. *Mater. Sci. Eng.* 2012; 32:61–77
43. Hadjipavlou AG, Tzermiadianos MN, Bogduk N, Zindrick MR: The pathophysiology of disc degeneration: a critical review. *J. Bone Joint Surg. Br.* 2008; 90:1261–70
44. Woods BI, Sowa G, Vo N, Kang JD: A change in strategy: the use of regenerative medicine and tissue engineering to augment the course of intervertebral disc degeneration. *Oper. Tech. Orthop.* 2010; 20:144–53
45. Ullrich P: Lumbar Spinal Fusion Surgery 2004
46. O’Connell GD, Vresilovic EJ, Elliott DM: Human intervertebral disc internal strain in compression: the effect of disc region, loading position, and degeneration. *J. Orthop. Res.* 2011; 29:547–55
47. Modic T, Carter R, Masaryk J, Ross S: State of the disk. *Radiology* 177–86
48. Pfirrmann CW, Metzdorf A, Zanetti M, Hodler J, Boos N: Magnetic resonance classification of lumbar intervertebral disc degeneration. *Spine.* 2001; 26:1873–8
49. Cassinelli EH, Kang JD: Current understanding of lumbar disc degeneration. *Oper. Tech. Orthop.* 2000; 10:254–62
50. Guerin H, Elliot D: Spine Technology Handbook. Edited by Kurtz S, Edidin A. Elsevier Inc, 2006, pp 35–62

51. Hsieh A: Update on the pathophysiology of degenerative disc disease and new developments in treatment strategies. *Open Access J. Sport. Med.* 2010; 1:191–9
52. Liu Y-J, Huang G-S, Juan C-J, Yao M-S, Ho W-P, Chan WP: Intervertebral disk degeneration related to reduced vertebral marrow perfusion at dynamic contrast-enhanced MRI. *AJR. Am. J. Roentgenol.* 2009; 192:974–9
53. Rajasekaran S, Babu JN, Arun R, Armstrong BRW, Shetty AP, Murugan S: ISSLS prize winner: A study of diffusion in human lumbar discs: a serial magnetic resonance imaging study documenting the influence of the endplate on diffusion in normal and degenerate discs. *Spine.* 2004; 29:2654–67
54. Rodriguez AG, Rodriguez-Soto AE, Burghardt AJ, Berven S, Majumdar S, Lotz JC: Morphology of the human vertebral endplate. *J. Orthop. Res.* 2012; 30:280–7
55. Freemont AJ: The cellular pathobiology of the degenerate intervertebral disc and discogenic back pain. *Rheumatology* 2009; 48:5–10
56. Kandel R, Roberts S, Urban JPG: Tissue engineering and the intervertebral disc: the challenges. *Eur. Spine J.* 2008; 17 Suppl 4:480–91
57. Tehranzadeh J, Ton JD, Rosen CD: Advances in spinal fusion. *Semin. Ultrasound, CT, MRI* 2005; 26:103–13
58. Freeman BJC, Debnath UK: The Management of Spondylolysis and Spondyloisthesis, Surgery for Low Back Pain. Edited by Szpalski M, Gunzburg R, Rydevik BL, Huec J-C Le, Mayer HM. Berlin, Heidelberg, Springer, 2010, pp 137–45doi:10.1007/978-3-642-04547-9
59. Syrmou E, Tsitsopoulos PP, Marinopoulos D, Tsonidis C, Anagnostopoulos I, Tsitsopoulos PD: Spondylolysis: a review and reappraisal. *Hippokratia* 2010; 14:17–21
60. Martin BI, Kreuter W, Goodman DC, Jarvik JG: Trends, major medical complications, and charges associated with surgery for lumbar spinal stenosis in older adults. *Am. Med. Assoc.* 2012; 303:1259–69
61. Goulding M: Public Health and Aging: Trends in Aging—US and Worldwide. *Mortal. Wkly. Rep.* 2003; 56:101–6
62. Park SB, Chung CK: Strategies of spinal fusion on osteoporotic spine. *J. Korean Neurosurg. Soc.* 2011; 49:317–22

63. Dickson RA: Spinal Deformities, Children's Orthopaedics and Fractures. Edited by Benson M, Fixsen J, Macnicol M, Parsch K. London, Springer, 2009, pp 599–637doi:10.1007/978-1-84882-611-3
64. Eliyas JK, Karahalios D: Surgery for degenerative lumbar spine disease. *Disease-a-Month* 2011; 57:592–606
65. Hu S: Spondylolisthesis and Spondylolysis. *J. Bone Jt. Surg.* 2008; 90-A:655–71
66. Schizas C, Triantafyllopoulos D, Kosmopoulos V, Tzinieris N, Stafylas K: Posterolateral lumbar spine fusion using a novel demineralized bone matrix: A controlled case pilot study. *Arch. Orthop. Trauma Surg.* 2008; 128:621–5
67. Constance JA: Minimally Invasive Spinal Surgery: A Market Briefing. New York, 2005, pp 1–47
68. Shelly CE: Effects of fusion mass density and fusion location on the strength of a lumbar interbody fusion 2004:pp 1–72
69. Freemont AJ, Peacock TE, Goupille P, Hoyland JA, Brien JO, Jayson MI V: Early report: Nerve ingrowth into diseased intervertebral disc in chronic back pain. *Lancet* 1997; 350:178–81
70. Mardjetko S: Degenerative lumbar spondylolisthesis: A meta-analysis of literature 1970-1993. *Spine.* 1993; 19:2256S – 2265S
71. Sengupta DK, Herkowitz HN: Degenerative spondylolisthesis: review of current trends and controversies. *Spine.* 2005; 30:S71–81
72. Berven SH, Herkowitz HN: Evidence-based medicine for the spine: degenerative spondylolisthesis. *Semin. Spine Surg.* 2009; 21:238–45
73. Gelalis I, Kang J: Thoracic and lumbar fusions for degenerative disorders: Rationale for selecting the appropriate fusion. *Orthop. Clin. North Am.* 1998; 29:829–34
74. Ohtori S, Koshi T, Yamashita M, Takaso M, Yamauchi K, Inoue G, Suzuki M, Orita S, Eguchi Y, Ochiai N, Kishida S, Kuniyoshi K, Aoki Y, Ishikawa T, Arai G, Miyagi M, Kamoda H, Suzuki M, Nakamura J, Furuya T, Toyone T, Yamagata M, Takahashi K: Single-level instrumented posterolateral fusion versus non-instrumented anterior interbody fusion for lumbar spondylolisthesis: a prospective study with a 2-year follow-up. *J. Orthop. Sci.* 2011; 16:352–8

75. Periasamy K, Shah K, Wheelwright EF: Posterior lumbar interbody fusion using cages, combined with instrumented posterolateral fusion: a study of 75 cases. *Acta Orthop. Belg.* 2008; 74:240–8
76. Kneser U, Schaefer D, Polykandriotis E, Horch R: Tissue engineering of bone: the reconstructive surgeon's point of view. *J. Cell. Mol. Med.* 2006; 10:7–19
77. Muschler GF, Nakamoto C, Griffith LG: Engineering principles of clinical cell-based tissue engineering. *J. Bone Jt. Surg.* 2004; 86-A:1541–58
78. Ledsome J, Lessoway V, Susak L, Gagnon F, Gagnon R, Wing P: Diurnal changes in lumbar intervertebral distance, measuring using ultrasound. *Spine.* 1996; 21:1671–5
79. Constance J: Minimally invasive spinal surgery. 2005, pp 1–123
80. Brown CR, Boden SD: Fracture repair and bone grafting, *Principles of Orthopaedics.* 2011, pp 13–22
81. Shen FH, Samartzis D, An HS: Cell technologies for spinal fusion. *Spine J.* 2005; 5:231S – 239S
82. Tabbaa SM, Horton CO, Jeray K, Burg K: Role of vascularity in successful bone formation and repair. *Crit. Rev. Biomed. Eng.* 2014; 42:1–29
83. Schindeler A, Liu R, Little DG: The contribution of different cell lineages to bone repair: exploring a role for muscle stem cells. *Differentiation.* 2009; 77:12–8
84. Phieffer LS, Goulet JA: Delayed unions of the tibia. *Instr. Course Lect.* 2006; 55:389–401
85. Bohner M: Resorbable biomaterials as bone graft substitutes. *Mater. Today* 2010; 13:24–30
86. Canto FRT, Garcia SB, Issa JPM, Marin A, Bel E Del, Defino HL: Influence of decortication of the recipient graft bed on graft integration and tissue neof ormation in the graft-recipient bed interface. *Eur. Spine J.* 2008; 17:706–14
87. Szpalski C, Wetterau M, Barr J, Warren SM: Bone tissue engineering: Current strategies and techniques - Part I: Scaffolds. *Tissue Eng.* 2012; 18:246–57
88. Boden SD: Overview of the biology of lumbar spine fusion and principles for selecting a bone graft substitute. *Spine.* 2002; 27:26–31

89. Boden SD: Biology of lumbar spine fusion and use of bone graft substitutes: Present, future, and next generation. *Tissue Eng.* 2000; 6:383–99
90. Kang J, An H, Hilibrand A, Yoon ST, Kavanagh E, Boden S: Grafton and local bone have comparable outcomes to iliac crest bone in instrumented single-level lumbar fusions. *Spine.* 2012; 37:1083–91
91. Ludwig SC, Boden SD: Osteoinductive bone graft substitutes for spinal fusion: A basic science summary. *Orthop. Clin. North Am.* 1999; 30:1–14
92. Giannicola G, Ferrari E, Citro G, Sacchetti B, Corsi A, Riminucci M, Cinotti G, Bianco P: Graft vascularization is a critical rate-limiting step in skeletal stem cell-mediated posterolateral spinal fusion. *J. Tissue Eng. Regen. Med.* 2010; 4:273–83
93. Bawa M, Schimizzi AL, Leek B, Bono CM, Massie JB, Macias B, Chung CB, Hargens AR, Garfin SR, Kim CW: Paraspinal muscle vasculature contributes to posterolateral spinal fusion. *Spine.* 2006; 31:891–6
94. Xi C, Li Y, Chi Z, Pei L, Ji Y, Wang X, Yan J: The influence of orthotopic paraspinal muscle-pediculated bone flaps on posterior spinal fusion in a canine model. *Spine.* 2011; 36:E20–6
95. Sun J-S, Wu SY-H, Lin F-H: The role of muscle-derived stem cells in bone tissue engineering. *Biomaterials* 2005; 26:3953–60
96. Qu-Petersen Z, Deasy B, Jankowski R, Ikezawa M, Cummins J, Pruchnic R, Mytinger J, Cao B, Gates C, Wernig A, Huard J: Identification of a novel population of muscle stem cells in mice: potential for muscle regeneration. *J. Cell Biol.* 2002; 157:851–64
97. Wu X, Wang S, Chen B, An X: Muscle-derived stem cells: isolation, characterization, differentiation, and application in cell and gene therapy. *Cell Tissue Res.* 2010; 340:549–67
98. Schaser KD, Zhang L, Haas NP, Mittlmeier T, Duda G, Bail HJ: Temporal profile of microvascular disturbances in rat tibial periosteum following closed soft tissue trauma. *Langenbecks. Arch. Surg.* 2003; 388:323–30
99. Landry PS, Marino AA, Sadasivan KK, Albright JA: Effect of soft-tissue trauma on the early periosteal response of bone to injury. *J. Trauma* 2000; 48:479–83
100. Claes L, Maurer-Klein N, Henke T, Gerngross H, Melnyk M, Augat P: Moderate soft tissue trauma delays new bone formation only in the early phase of fracture healing. *J. Orthop. Res.* 2006; 24:1178–85

101. Harry LE, Sandison A, Paleolog EM, Hansen U, Pearse MF, Nanchahal J: Comparison of the healing of open tibial fractures covered with either muscle or fasciocutaneous tissue in a murine model. *J. Orthop. Res.* 2008; 26:1238–44
102. Harry LE, Sandison A, Pearse MF, Paleolog EM, Nanchahal J: Comparison of the vascularity of fasciocutaneous tissue and muscle for coverage of open tibial fractures. *Plast. Reconstr. Surg.* 2009; 124:1211–9
103. Shah K, Majeed Z, Jonason J, O’Keefe RJ: The role of muscle in bone repair: The cells, signals, and tissue responses to injury. *Curr. Osteoporos. Rep.* 2013; 11:130–5
104. Glass GE, Chan JK, Freidin A, Feldmann M, Horwood NJ, Nanchahal J: TNF-alpha promotes fracture repair by augmenting the recruitment and differentiation of muscle-derived stromal cells. *Proc. Natl. Acad. Sci.* 2011; 108:1585–90
105. Kim KS, Lee JH, Ahn HH, Lee JY, Khang G, Lee B, Lee HB, Kim MS: The osteogenic differentiation of rat muscle-derived stem cells in vivo within in situ-forming chitosan scaffolds. *Biomaterials* 2008; 29:4420–8
106. Liu R, Birke O, Morse A, Peacock L, Mikulec K, Little DG, Schindeler A: Myogenic progenitors contribute to open but not closed fracture repair. *BMC Musculoskelet. Disord.* 2011; 12:288
107. Liu R, Schindeler A, Little DG: The potential role of muscle in bone repair. *J. Musculoskelet. Neuronal Interact.* 2010; 10:71–6
108. Patterson TE, Kumagai K, Griffith L, Muschler GF: Cellular strategies for enhancement of fracture repair. *J. Bone Joint Surg. Am.* 2008; 90 Suppl 1:111–9
109. Farrington-Rock C, Crofts NJ, Doherty MJ, Ashton BA, Griffin-Jones C, Canfield AE: Chondrogenic and adipogenic potential of microvascular pericytes. *Circulation* 2004; 110:2226–32
110. Bianco P, Riminucci M, Gronthos S, Robey PG: Bone marrow stromal stem cells: Nature, biology, and potential applications. *Stem Cells* 2001; 19:180–92
111. Doherty MJ, Ashton BA, Walsh S, Beresford JN, Grant ME, Canfield AE: Vascular pericytes express osteogenic potential in vitro and in vivo. *J. Bone Miner. Res.* 1998; 13:828–38
112. Kumagai K, VasANJI A, Drazba JA, Butler RS, Muschler GF: Circulating cells with osteogenic potential are physiologically mobilized into the fracture healing site in the parabiotic mice model. *J. Orthop. Res.* 2008; 26:165–75

113. Shirley D, Marsh D, Jordan G, McQuaid S, Li G: Systemic recruitment of osteoblastic cells in fracture healing. *J. Orthop. Res.* 2005; 23:1013–21
114. Kim YJ, Kim HK, Cho HH, Bae YC, Suh KT, Jung JS: Direct comparison of human mesenchymal stem cells derived from adipose tissues and bone marrow in mediating neovascularization in response to vascular ischemia. *Cell. Physiol. Biochem.* 2007; 20:867–76
115. Lu S-H, Yang A-H, Wei C-F, Chiang HS, Chancellor MB: Multi-potent differentiation of human purified muscle-derived cells: Potential for tissue regeneration. *BJU Int.* 2010; 105:1174–80
116. Levy MM, Joyner CJ, Viridi AS, Reed A, Triffitt JT, Simpson AH, Kenwright J, Stein H, Francis MJ: Osteoprogenitor cells of mature human skeletal muscle tissue: an in vitro study. *Bone* 2001; 29:317–22
117. Arnsdorf EJ, Jones LM: The periosteum as a cellular source for functional tissue engineering. *Tissue Eng. Part A* 2009; 15:2637–42
118. Hayashi O, Katsube Y, Hirose M, Ohgushi H, Ito H: Comparison of osteogenic ability of rat mesenchymal stem cells from bone marrow, periosteum, and adipose tissue. *Calcif. Tissue Int.* 2008; 82:238–47
119. Lichte P, Pape HC, Pufe T, Kobbe P, Fischer H: Scaffolds for bone healing: Concepts, materials and evidence. *Injury* 2011; 42:569–73
120. Healy KE, Guldberg RE: Bone tissue engineering. *J. Musculoskelet. Neuronal Interact.* 2007; 7:328–30
121. Hutmacher DW: Scaffolds in tissue engineering bone and cartilage. *Biomaterials* 2000; 21:2529–43
122. Salgado PC: Bone remodeling, biomaterials and technological applications: revisiting basic concepts. *J. Biomater. Nanobiotechnol.* 2011; 02:318–28
123. Logeart-Avramoglou D, Anagnostou F, Bizios R, Petite H: Engineering bone: Challenges and obstacles. *J. Cell. Mol. Med.* 2005; 9:72–84
124. Lienau J, Schell H, Duda GN, Seebeck P, Muchow S, Bail HJ: Initial vascularization and tissue differentiation are influenced by fixation stability. *J. Orthop. Res.* 2005; 23:639–45
125. Diwan AD, Girardi FP, Lane JM: The biology of bone grafting functions of bone grafts. *J. Am. Acad. Orthop. Surg.* 2005; 13:77–86

126. Giannoudis PV, Einhorn TA, Marsh D: Fracture healing: The diamond concept. *Injury* 2007; 38 Suppl 4:3–6
127. Kruyt M, Gaalen S van, Oner F, Verbout A, Bruijn J de, Dhert W: Bone tissue engineering and spinal fusion: The potential of hybrid constructs by combining osteoprogenitor cells and scaffolds. *Biomaterials* 2004; 25:1463–73
128. Babis GC, Soucacos PN: Bone scaffolds: the role of mechanical stability and instrumentation. *Injury* 2005; 36 Suppl 4:S38–44
129. Khan SN, Cammisa FP, Sandhu HS, Diwan AD, Girardi FP, Lane JM: The biology of bone grafting. *J. Am. Acad. Orthop. Surg.* 2005; 13:77–86
130. Marchesi DG: Spinal fusions: Bone and bone substitutes. *Eur. Spine J.* 2000; 9:372–8
131. Cutter CS, Mehrara BJ: Bone grafts and substitutes. *J. Long. Term. Eff. Med. Implants* 2006; 16:249–60
132. Baroli B: From natural bone grafts to tissue engineering therapeutics: Brainstorming on pharmaceutical formulative requirements and challenges. *J. Pharm. Sci.* 2009; 98:1317–75
133. Carragee EJ, Hurwitz EL, Weiner BK: A critical review of recombinant human bone morphogenetic protein-2 trials in spinal surgery: Emerging safety concerns and lessons learned. *Spine J.* 2011; 11:471–91
134. Sandhu HS, Khan SN: Animal models for preclinical assessment of bone morphogenetic proteins in the spine. *Spine.* 2002; 27:32–8
135. Arner JW, Daffner SD: Bone graft extenders and substitutes in thoracolumbar spine. *Am. J. Orthop.* 2012
136. Aghdasi B, Montgomery SR, Daubs MD, Wang JC: A review of demineralized bone matrices for spinal fusion: the evidence for efficacy. *Surg.* 2013; 11:39–48
137. Bansal S, Chauhan V: Evaluation of hydroxyapatite and beta-tricalcium phosphate fixed with bone marrow aspirate as a bone graft substitute for posterolateral spinal fusion. *Indian J. Orthop.* 2009; 43:234–9
138. Niu C-C, Tsai T-T, Fu T-S, Lai P-L, Chen L-H, Chen W-J: A comparison of posterolateral lumbar fusion comparing autograft, autogenous laminectomy bone with bone marrow aspirate, and calcium sulphate with bone marrow aspirate: a prospective randomized study. *Spine.* 2009; 34:2715–9

139. Mummaneni P V, Meyer SA, Wu J-C: Biological approaches to spinal instrumentation and fusion in spinal deformity surgery. *Clin. Neurosurg.* 2011; 58:110–6
140. Taghavi CE, Lee K-B, Keorochana G, Tzeng S-T, Yoo JH, Wang JC: Bone morphogenetic protein-2 and bone marrow aspirate with allograft as alternatives to autograft in instrumented revision posterolateral lumbar spinal fusion: a minimum two-year follow-up study. *Spine.* 2010; 35:1144–50
141. Weiner BK, Walker M: Efficacy of autologous growth factors in lumbar intertransverse fusions. *Spine.* 2003; 28:1968–70; discussion 1971
142. Castro FP: Role of activated growth factors in lumbar spinal fusions. *J. Spinal Disord. Tech.* 2004; 17:380–4
143. Rihn JA, Kirkpatrick K, Albert TJ: Graft options in posterolateral and posterior interbody lumbar fusion. *Spine.* 2010; 35:1629–39
144. Lee KJH, Roper JG, Wang JC: Demineralized bone matrix and spinal arthrodesis. *Spine J.* 2005; 5:217S – 223S
145. Bae HW, Zhao L, Kanim LEA, Wong P, Delamarter RB, Dawson EG: Intersubject variability and intrasubject variability of bone morphogenetic proteins in commercially available demineralized bone matrix products. *Spine.* 2006; 31:1299–306
146. Vaccaro AR, Stubbs HA: Demineralized bone matrix composite grafting for posterolateral lumbar spinal fusion. *Orthopedics* 2007; 30:567–70

CHAPTER TWO

EFFECT OF WICKING FIBERS IN TISSUE ENGINEERED SCAFFOLDS

Introduction

Large fracture defect sites and spinal fusions require large amounts of additional bone tissue; therefore, bone substitutes (commonly referred to as scaffolds) are used to augment bone tissue reformation¹⁻⁴. These large tissue-engineered scaffolds are limited by a diminished capacity to transport nutrients, oxygen, large biomolecules, and osteoprogenitor cells^{5,6}. Conventional approaches to improve the transport properties in large bone tissue-engineered scaffolds involve the inclusion of biomolecules that promote angiogenesis and of co-cultured endothelial progenitor cells and other vasculogenic cells that stimulate neovasculature⁷⁻⁹. These approaches have shown limited success due to the slow rate of angiogenesis and the formation of nonfunctional vessels; requiring substantial improvement before consideration for clinical trials¹⁰.

A novel approach to improve transport involves incorporating polymeric wicking fibers into a tissue-engineered construct. A wicking fiber has a grooved cross-section and parallel continuous channels that run the length of the fiber. The fiber configuration, shown in Figure 2.1, has been geometrically optimized by Eastman Chemical Company to enhance capillary action along the channels, resulting in enhanced transport properties. It is well established that the proprietary wicking fiber shape provides highly efficient transport in textile and chromatographic separations¹¹⁻¹⁶. The fibers were later introduced by our research team, to the field of tissue engineering¹⁷.

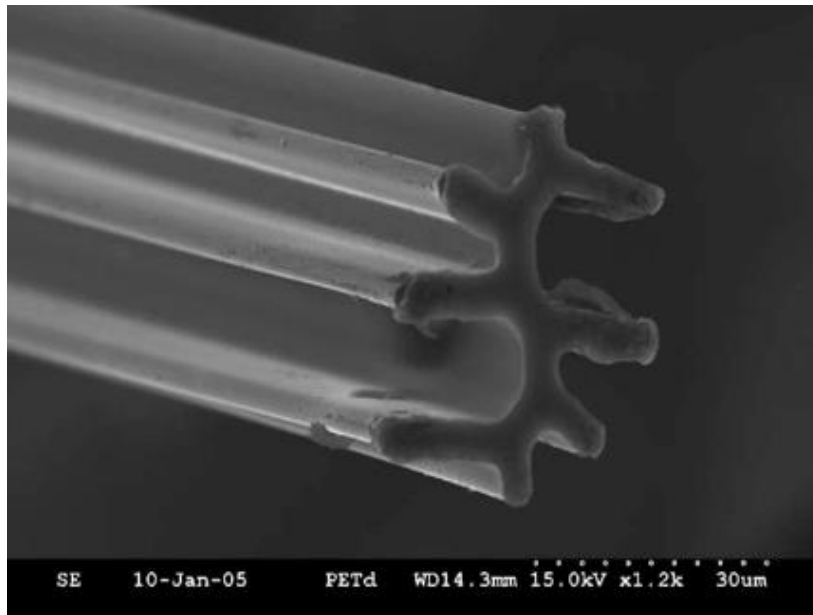


Figure 2.1: Scanning electron microscope (SEM) image of a wicking fiber. Adapted with permission from Elsevier (Marcus RK et al. 2005). Image shows non-circular grooved cross-section and parallel channels of the wicking fiber, which facilitate strong wicking action and greatly increase surface area.

The increased transport properties of the wicking fiber is achieved through geometrically optimized intra-fiber spaces or grooves that combine capillary pressure to enhance fluid transport along a single wicking fiber as opposed to a single capillary channel¹⁴. The cross-sectional geometry increases the shape factor of the wicking fiber so the surface area is 2.5-3.2 times a conventional circular cross-sectional fiber or macro channel of nominal diameter, resulting in significantly greater wicking capabilities^{18,19}.

The objective of these studies was to investigate the capabilities of wicking fibers to enhance the transport of not only fluid, but transport of biomolecules and progenitor cells. The first phase of this study assessed the transport efficacy of round and wicking

polylactide fibers of various bundled configuration. The second phase of this aim investigated the movement of fluorescently labeled biomolecules in a 3-dimensional (3D) collagen-agarose hydrogel 3-dimensional (3D) constructs containing round or wicking fibers. The final phase investigated the ability of wicking fibers to transport and distribute osteoprogenitor cells both along the fiber and through a 3D construct.

Fluid Transport of Fibers

Methods and Materials

Polymer Extrusion

Poly-L-lactide (Natureworks LLC, USA) wicking fibers were extruded with irregular cross-sectional dimensions of 0.72 mm by 0.55 mm and poly-L-lactide round fibers were extruded with cross-sectional diameter of 0.5 mm. Wicking and round fibers were sliced with razor blade into individual fibers of 2, 3, and 6 cm lengths. Both fiber types were cleaned in three changes of ethanol, for 1 hour each, and placed under ultraviolet light for 6 hours. Samples were then soaked in a phosphate-buffered saline (PBS, Invitrogen) solution for 2 hours and air-dried overnight in a sterile hood.

Fluid Transport Tests of Round and Wicking Fibers

The transport phenomena through fibers includes diffusion and wicking--the spontaneous flow of liquid driven by capillary action. The wicking behavior of the fibers can be assessed using a vertical wicking test, commonly performed in the textile industry to characterize transport phenomena in fabrics²⁰⁻²². The wicking tests were performed using two methods. The first method assessed wicking capabilities of the fibers by

recording the height of the fluid front moving vertically along the fiber at various time points, shown in image A of Figure 2.2. The second method assessed the wicking rate of the fibers by evaluating the change in mass of the fluid reservoir over regular time intervals presented in image B.

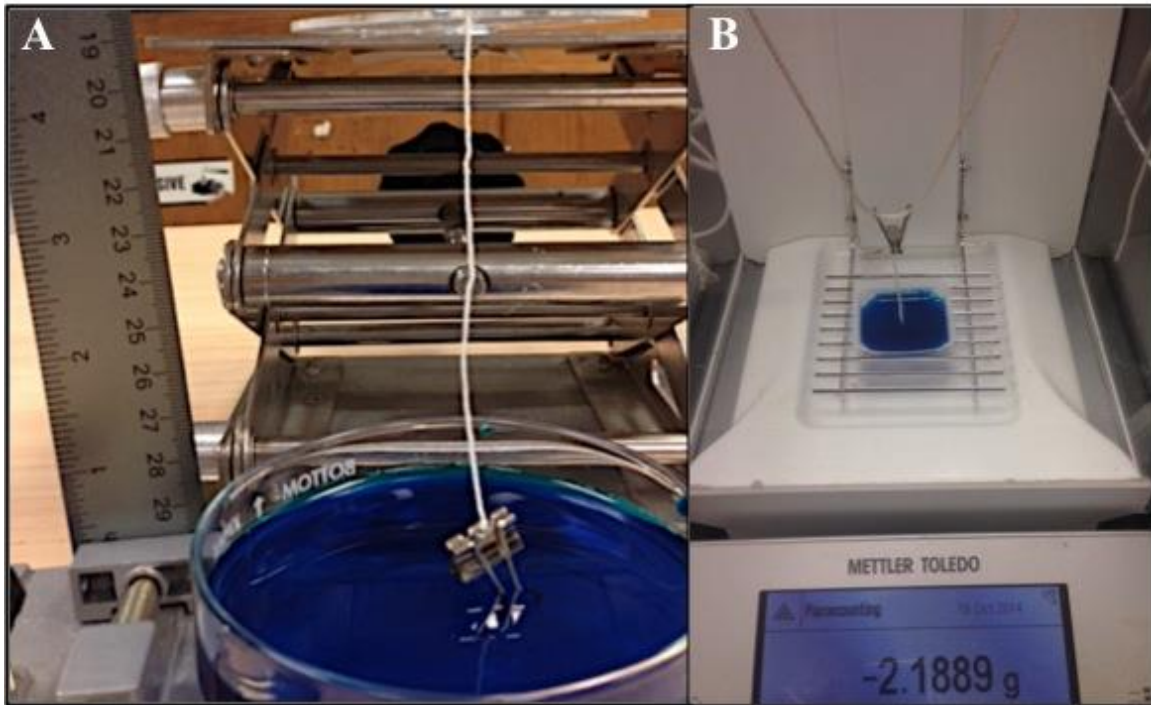


Figure 2.2: (A) Vertical test apparatus to evaluate the rate of the fluid front in various fiber configurations. (B) Vertical test set-up to assess the amount of fluid wicked through the fiber over a time interval

Both test methods were used to evaluate the wicking capabilities of round and the wicking properties were characterized in conformations of single fibers and of bundled fibers in a braided or twisted configuration (Table 2.1: Experimental groups of fiber configuration for vertical test investigating wicking height).

Table 2.1: Experimental groups of fiber configuration for vertical test investigating wicking height

Experimental Group	Fiber Type	Configuration	Number of fibers in bundle
1	Round	Single	1
2	Wicking	Single	1
3	Round	Twisted bundle	3
4	Wicking	Twisted bundle	3
5	Round	Braided bundle	3
6	Wicking	Braided bundle	3

One end of the 6 cm fiber configuration was attached to the clamp shown in the Figure 2.2A. The bottom end was weighed down by a clip and lowered into a reservoir of dye solution to create contact of only 10 mm of fiber. The dye solution was comprised of phosphate buffered saline (PBS, Invitrogen) and 10% blue assorted food coloring (McCormick). The vertical displacement of the fluid front was measured after 30, 60, 90, 120, 150, 300 seconds for each sample configuration, with each having a sample size of n=4. The fluid front rate was determined for each sample.

Vertical Test - Wicking Rate Assessment

To determine the mass of liquid removed by the fibers from the reservoir over time, the balance was set up to collect mass data measurements. The balance was connected to the computer using a USB to RS232 cable. PuTTY software was used to

transfer information from the balance to the computer. The balance was programmed to continuously measure the weight of the reservoir at a rate of two measurements per second. Fiber samples were then vertically dipped into the liquid reservoir using a clip and string to lower the samples through the top window of the balance. The fibers were suspended so only the tip was interfacing the fluid. Measurements were taken from the time of contact with the fiber to the fluid reservoir over 10 minutes. After ten minutes the continuous function was stopped and the recorded data was saved as a text file for further analysis in Excel. The wicking rate for each sample was calculated using a mass (mg) versus time (minutes) plot. The plots for each experimental group were normalized by an experimentally determined equation for the rate of evaporation of liquid from the reservoir, found in a similar method to sample evaluation.

Statistical Analysis

JMP software was used to conduct an unpaired two-sample t-test to compare the change in wicking rate of single wicking and round fibers using a significance level of $p < 0.05$. The average wicking rate of twisted wicking bundles was compared to the average wicking rate of twisted round bundles using an unpaired two-sample t-test. The final statistical assessment used an unpaired two-sample t-test to compare the mean wicking rate of braided wicking fibers and braided round fibers.

Results

Fluid Transport Tests

To characterize the round and wicking polylactide fibers the vertical test was used to evaluate the height of the fluid front over a 10 minute time interval. The qualitative results are shown in Figure 2.3. The blue dye-solution in the images corresponds to the height the fluid front traveled through the fiber.

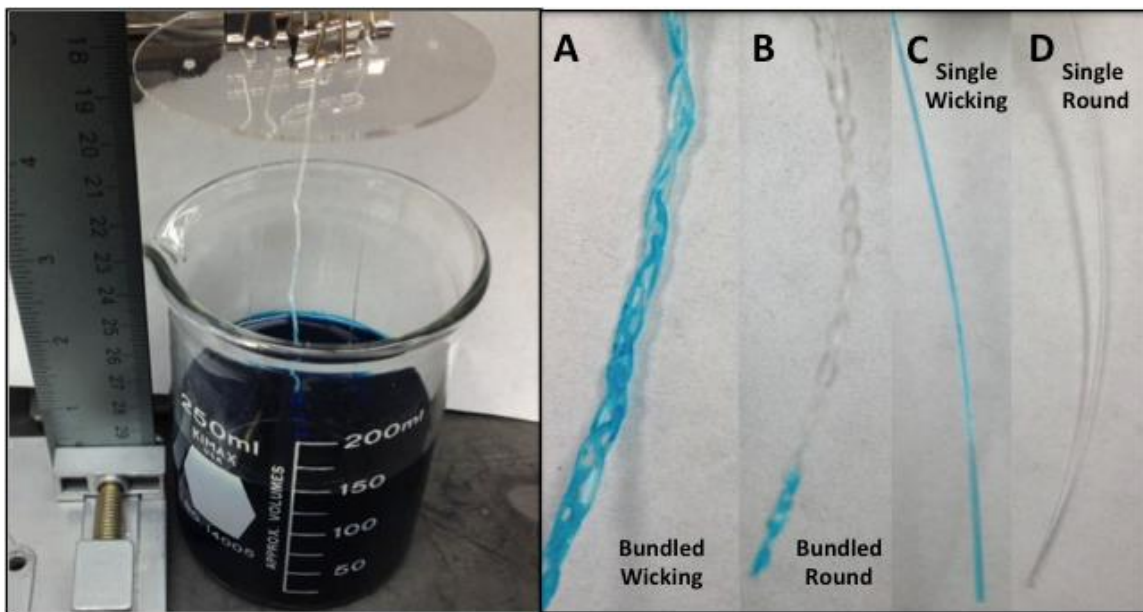


Figure 2.3: Results from vertical wicking test. Left image shows the vertical test apparatus. (A) Bundled and (C) single wicking fiber samples depict greater vertical movement of the dye-solution than (B) bundled and (D) single round fiber samples

The wicking rate was calculated for each experimental group by plotting the height of the fluid front by the time in seconds, as shown in image A of Figure 2.4. The wicking rate was determined by calculating the change in height of the liquid front over the time interval. The results (image B) show the single and bundled wicking fibers

wicking rate is significantly higher than samples of round fiber configurations. The height of the fluid front (image C) in both single and bundled wicking fiber samples is significantly greater than the round fiber samples. The twisted bundle round fibers depict greater vertical wicking height than the single round fibers. Additionally, the height and rate of the fluid front was assessed for wicking fibers of braided and twisted configurations. The twisted configurations showed higher wicking heights and increased wicking rate than braided wicking fiber configurations. The wicking rate was also assessed by measuring the change in mass continuously over a 10 minute time interval. The loss of water from the fluid reservoir on the balance correlates to the water gain from the fiber bundles. The results were normalized to the rate of evaporation from the fluid reservoir. The results show the wicking fiber samples have a significantly greater wicking rate than the twisted round fiber samples (Imaged D). Consequently, the wicking fibers also absorb greater amounts of water than round fiber samples.

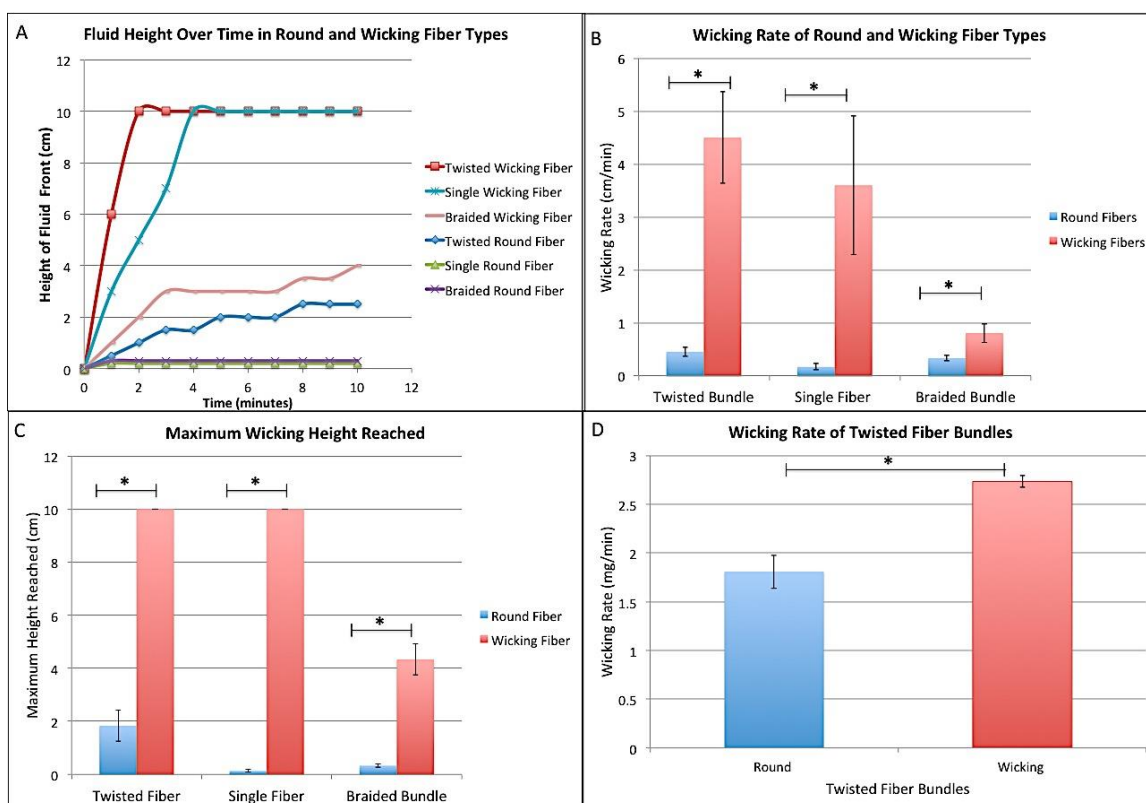


Figure 2.4: Wicking behavior of round and wicking fibers (A) Plot of wicking height vs time for round and wicking fibers (B) The wicking rate (cm/min) of single, bundle, and braided round and wicking fibers (C) The maximum height reached for each fiber type (D) Wicking rate (mg/min) of round and wicking twisted bundles (*) signifies significant difference between round and wicking fiber types, $p < 0.05$.

Effect of Wicking Fibers on Biomolecule Transport

Materials and Methods

Unimolecular Diffusion of FITC-Conjugated Bovine Serum Albumin in a Hydrogel

The effect of fibers on protein movement in a 3D system was evaluated by analyzing the unimolecular diffusion of FITC-conjugated bovine albumin (Sigma; St. Louis, MO, USA) in a 50:50 collagen-agarose composite hydrogel containing individual round or wicking fibers.

A 50:50 collagen-agarose hydrogel was formed creating a solution consisting 45% (by volume) of 2% (w/v) agarose (Sigma, St. Louis, MO, USA) in 1x phosphate-buffered saline (PBS, Invitrogen), 45% (by volume) of 3.2 mg/mL PurCol, Bovine Collagen Solution Type 1 (Advance Biomatrix; San Diego, CA, USA), and 10% (by volume) of collagen reconstitution buffer. The collagen reconstitution buffer was comprised of 4.8% HEPES buffer (Fisher Scientific; Waltham, MA USA), and 2.2% NaHCO₃ (Fisher Scientific) in deionized water. To make 2% agarose solution agarose powder was autoclaved at 124°C for 45 min and added to PBS solution. To dissolve the agarose the solution was stirred at low heat using a magnetic stirrer and hot plate. After agarose is completely dissolved the solution is cooled and stored at 4°C until further use. The agarose solidifies at room temperature and is melted in the microwave prior to use. The collagen gel is formed by change in pH using collagen reconstitution buffer and incubating at 37°C. The 50:50 collagen-agarose hydrogel was formed by first adding the collagen solution to the reconstitution buffer. After thorough mixing using the pipette, the melted 2% agarose solution was quickly added at the appropriate dilution. The agarose component was solidified by cooling the hydrogel at room temperature for 10 minutes followed by incubation at 4°C for 5 minutes. The samples were placed in a 37°C incubator overnight to allow the collagen to solidify.

The 50:50 collagen-agarose hydrogel was formed in half of an individual well on a 2-well chamber slide by turning the chamber slide on its side and loading it with 1 mL of collagen-agarose solution, as seen in image A of Figure 2.5. Three fibers with lengths of 2 cm were placed vertically, with forceps, in the center of the hydrogel while the

chamber slide was on its side and before the hydrogel was gelled as shown in figure below. Two samples with each fiber type were formed. After the hydrogel gelled, 1 mL of 100 $\mu\text{g}/\text{mL}$ solution of FITC-conjugated bovine albumin and serum free medium was pipetted into the section of the chamber well without the hydrogel, as shown in image B of Figure 2.5.

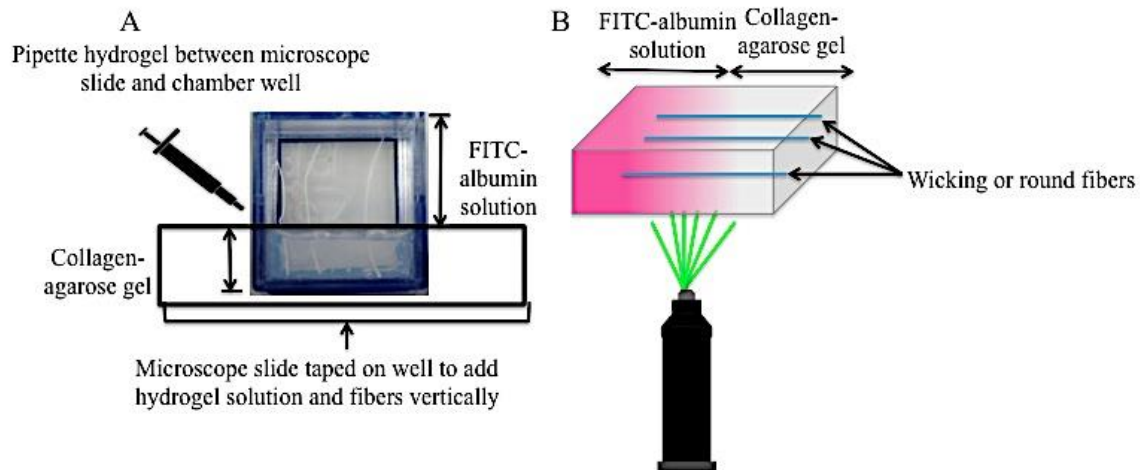


Figure 2.5: Schematics of experimental set-up of collagen-agarose gel containing fibers. (A) Digital image of the rotated chamber well to create a hydrogel in half the well and with inserted fibers. (B) The sample was then laid back on its side and tested and then imaged using fluorescent confocal imaging of the FITC albumin along the horizontal axis with laser confocal microscopy

The rate of FITC-albumin diffusing horizontally through the different fiber-hydrogel systems was evaluated using fluorescent laser confocal microscopy (Nikon Eclipse TI); NIS-Elements imaging software was used to obtain 3D time-lapse images. The intensity was measured in 7-second intervals for 15 minutes along the center image frame containing the fiber. The rate of FITC-albumin movement was determined in regions of interest (ROI) along the fibers at various distances from the interface of the

collagen-agarose gel and FITC-albumin solution. As shown in Figure 2.6, ROI at various distances from the interface were used to calculate the average rate of albumin movement.

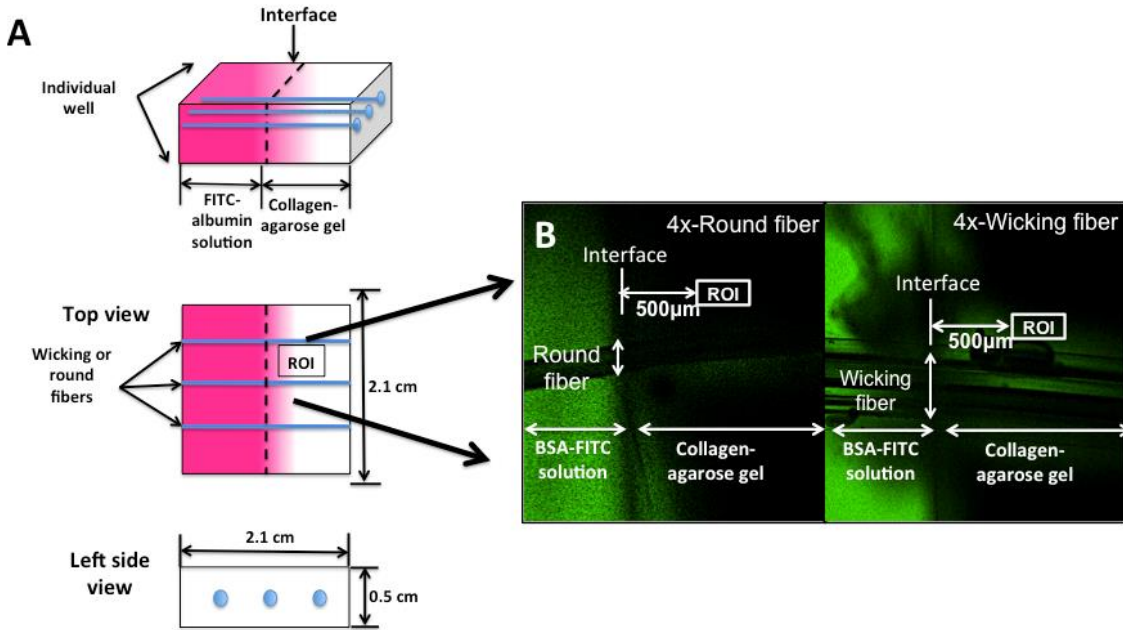


Figure 2.6: (A) Schematic of an individual well in a 2-well chamber slide filled partially containing with collagen-agarose gel containing either round or wicking fibers. The other portion of the well is filled with medium containing the BSA-FITC solution. (B) Image frame from confocal real-time video of the BSA-FITC diffusion diffusing into the collagen-agarose gel.

Statistical Analysis

JMP 10 statistical software was used to perform a repeated measures analysis with ($p < 0.05$) was performed to compare the rate of FITC-albumin movement in hydrogels containing wicking or round fibers for each distance from the interface.

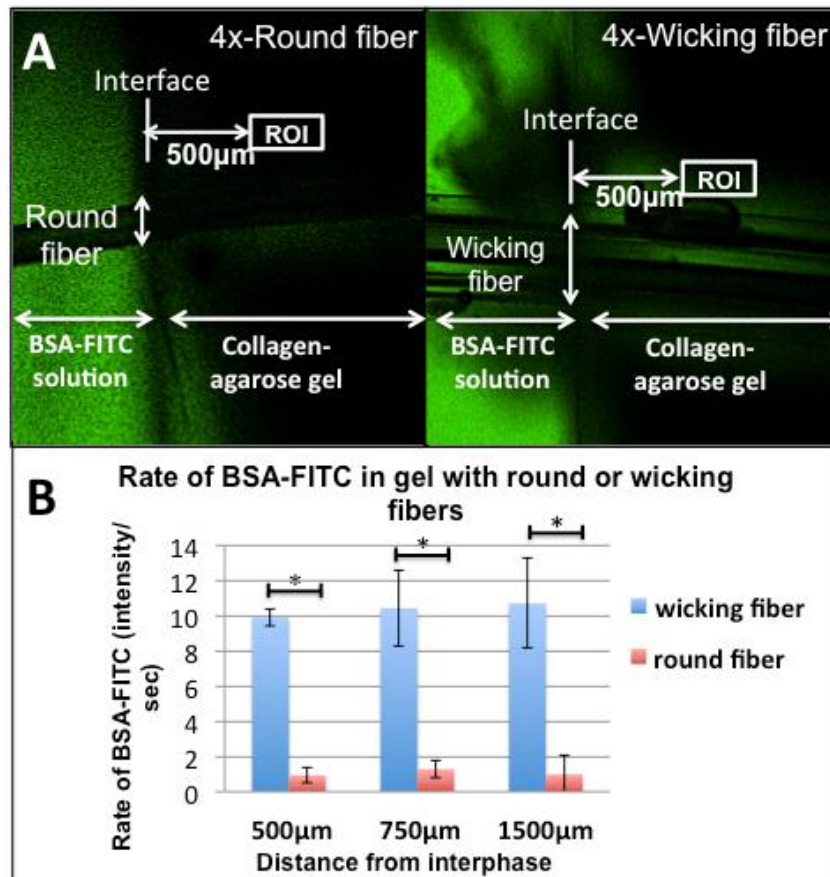


Figure 2.7: (A) Schematic indicates interface between hydrogel and FITC-albumin solution and the region of interest locations. (B) The rate of BSA-FITC in the collagen-agarose gel at various distances into the hydrogel. The hydrogel samples containing wicking fibers have a significantly greater rate than the samples with round fibers; $*p < 0.001$. The rate of BSA-FITC is consistent for various distances from the interface for both fiber types into the sample. (also published in Tabbaa et al. 2014 JTERM²³)

Results

The diffusion of FITC-albumin was analyzed in collagen-agarose hydrogels containing wicking or round fibers. The results showed the rate of the FITC-albumin movement in hydrogels with wicking fibers was significantly ($p < 0.001$) greater than in the gels containing round fibers for each ROI as presented in **Error! Reference source**

not found.. Statistical analysis also showed the distance from the interface did not significantly affect the rate of protein movement ($p=0.9342$), suggesting the wicking fibers increase the rate of movement homogeneously through the gel.

Enhanced Cell Transport Using Wicking Fibers

Materials and Methods

Progenitor Cell Transport through Wicking Fibers

The effect of fiber type on the transport of progenitor cells was evaluated using D1 mouse mesenchymal stromal cells (ATCC; Manassas, VA, USA). The cells were cultured in Dulbecco's Modified Eagle's medium (DMEM; Invitrogen; Grand Island, NY, USA) supplemented with 10% fetal bovine serum (FBS; Gibco; Grand Island, NY, USA), 10,000 U penicillin, and 10 mg streptomycin/mL (Sigma; St. Louis, MO, USA). D1 cells were labeled with CellTracker™ Green CMFDA probe (Invitrogen; Grand Island, NY, USA), following the manufacturer's protocol using a long term labeling concentration of 25 μ M, to evaluate the movement of cells along wicking and round fibers. Twelve poly-L-lactide wicking and twelve round fibers were cut into 3-cm length samples. The fibers were cleaned by extensive washes with 70% ethanol. After ethanol washes, the samples were soaked in 1x-phosphate buffered saline (PBS, Invitrogen; Grand Island, NY, USA) for 3 hours, washed three times with PBS, and air dried before use. Lids, with fitted holes and plastic tubes, were custom-made for the 12-well plate to securely hold the 3 cm wicking or round fibers vertical. After lids were prepared, 1 mL of D1 cell solution, containing 1 million cells in growth media, was pipetted into each well

of a low attachment 12-well, the fibers were individually and vertically placed into each well and secured by the custom-made lid.

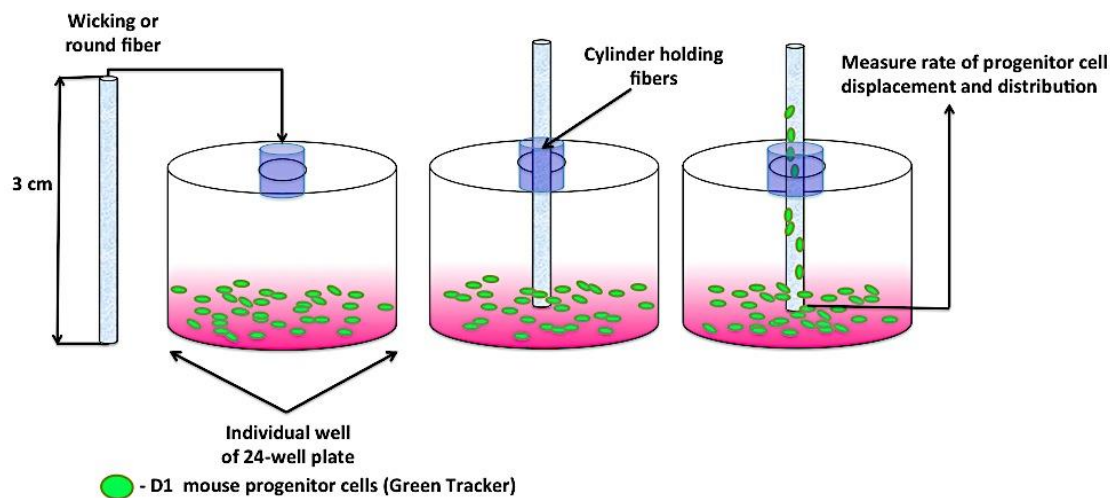


Figure 2.8: Schematic depicts experimental set-up to assess progenitor cells wicking in round or wicking fibers. The purple cylinders depict the holding mechanism of the fibers

The fluorescently tracked cells are carried in the media solution and wick with the media along the conduits of the fiber. The cells penetrating the fibers present the same spherical morphology as when the cells are suspended in solution. The vertical displacement of the cells along the fibers was determined at time points of 0.5, 6, and 24 hours with the initial time point being fiber placement into the cell solution. To assess the cell vertical displacement, the fibers were transferred to microscope slides and evaluated using fluorescent microscopy and imaging software.

Statistical Analysis

JMP 10 statistical software was used to perform statistical analysis for vertical cell movement. A block design of time was conducted to compare the vertical displacement of D1 cells on wicking fibers or round fibers with ($p < 0.05$).

Transport of Progenitor Cells through Fibers in Hydrogel

This study has adapted a 3-D *in vitro* system established by Takata et al. to evaluate the effects of progenitor cell movement in a collagen gel²⁴. This assay involves a simple system to assess cellular movement by preparing a double-layered collagen gel hemisphere with the first layer containing the cells and the second layer containing a growth factor molecule that has shown to be a chemotactic molecule that stimulates and encourages cell migration as shown in Figure 2.9. The distribution of progenitor cells within hemispheres containing round fibers, wicking fibers, or no fibers was assessed after 24 hours.

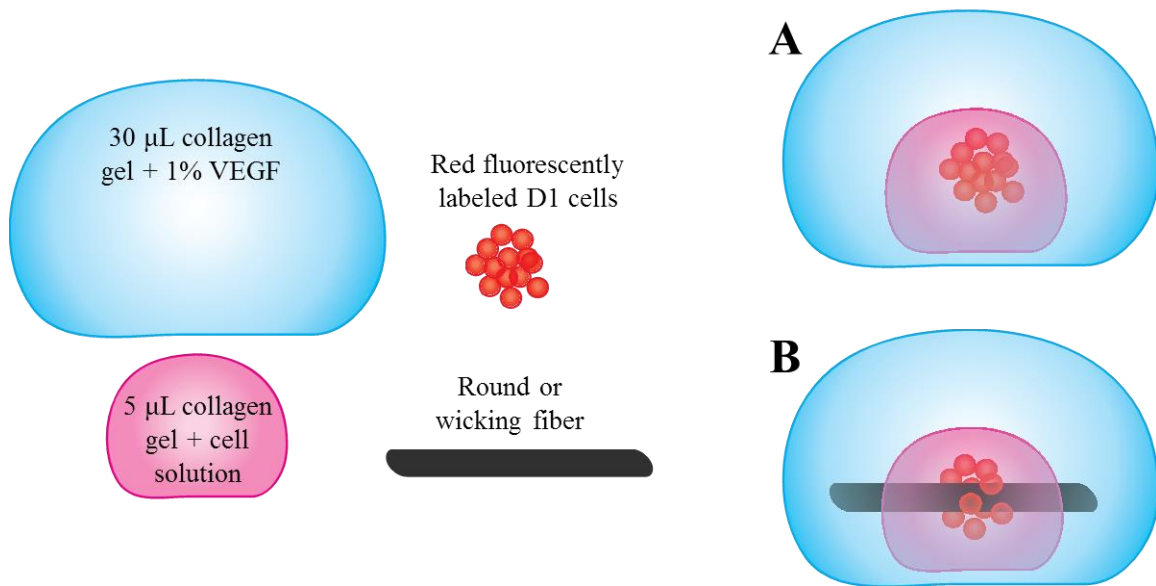


Figure 2.9: Schematic illustrates the arrangement for double-layered collagen hemispheres (A) without fibers and (B) with round or wicking fibers. The pink sphere corresponds to the first hemisphere layer containing fluorescently tracked D1 mouse progenitor cells. The blue sphere depicts the second larger collagen hemisphere containing a chemotactic growth factor encapsulating the first hemisphere with or without fibers.

Forming First and Second Layer of Collagen Gel Hemispheres

D1, mouse mesenchymal stromal (ATCC), cells were cultured in Dulbecco's Modified Eagle's medium (Invitrogen; Grand Island, NY, USA) supplemented with 10% fetal bovine serum (Gibco; Grand Island, NY, USA), 10,000 U penicillin, and 10 mg streptomycin/mL (Sigma; St. Louis, MO, USA). D1 cells were labeled with CellTracker™ Red CMTPX probe (Invitrogen; Grand Island, NY, USA), following the manufacturer's protocol using a long term labeling concentration of 25μM. The first layer of the 1.0mg/mL collagen gel hemisphere was formed by mixing 3.2mg/mL PurCol,

Bovine Collagen Solution Type 1 (Advance Biomatrix; San Diego, CA, USA), D1 mouse mesenchymal DMEM growth media, and 1 N NaOH. Immediately following mixing, D1 cells labeled with red tracker at a cell density of (2×10^6 cells/mL) were added to the collagen gel prior to gelation. The second layer was formed without cells using the same collagen gel composition and methods with the addition of 1% recombinant human vascular endothelial growth factor (rhVEGF, R&D Systems, Minneapolis, MN).

Fiber Preparation

To prepare the fibers, poly-L-lactide wicking and round fibers were cut into 5-mm length samples. The fibers were cleaned by extensive washes with 70% ethanol. After ethanol washes, the samples were soaked in phosphate buffered saline (Invitrogen; Grand Island, NY, USA) for 3 hours, washed three times with phosphate buffered saline, and air dried before use.

Forming Collagen Hemisphere Composite

Three different groups of collagen hemisphere composite samples were formed. The groups included hemispheres with round, wicking, or no fibers; each with a sample size of four and set up as shown in Figure 2.10.

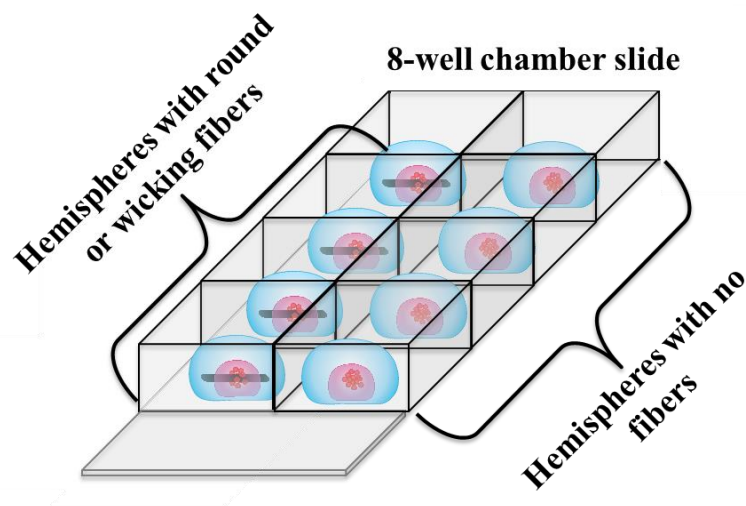


Figure 2.10: Two 8-well chamber slides were used to make two-layered collagen hemispheres samples ($n=4$) with and without fibers.

To form the first layer, 5 μL of 1 mg/mL collagen gel solution containing 2×10^4 D1 cells was dropped directly onto the glass bottom in each well of an 8-well glass chamber slide system (Fisher Scientific, Pittsburgh, PA). Single 5 mm round or wicking fibers were centered and placed directly on top of the first layer. Samples were incubated at 37°C and 5% CO_2 for 1 hour. After the first layer gelled, the second layer of 1mg/mL collagen gel containing 1% VEGF was directly dropped on the fiber encapsulating both fiber and first layer forming a double-layered collagen gel hemisphere. In samples without fibers the second layer was directly added to the first layer. After incubating the samples at 37°C and 5% CO_2 for 1 hour 250 μL of growth media was added to each sample incubated again for 24 hours. Following incubation the collagen hemispheres were imaged with an inverted fluorescence microscope and camera using 50x total

magnification. A tetramethyl rhodamine iso-thiocyanate (TRITC) filter was used to image the distribution of the red-labeled D1 cells. Image J software was used to quantitatively determine the extent of D1 cell expansion in the collagen hydrogel composite for each experimental group. To do this each image was converted to greyscale and split into each specific color channel: red, blue, or green. The cellular information from red-labeled D1 cells was solely on the red channel. Blue and green channel images were removed. Using the red channel the image was converted to a binary image. Figure 2.11 illustrates the conversion of a captured image through this imaging J processing method.

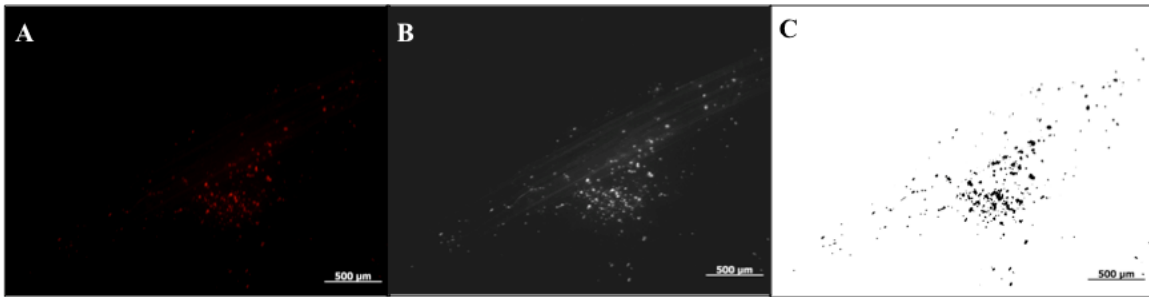


Figure 2.11: Depicts images after image J processing methods. (A) The initial fluorescent image captured, (B) the split red channel image, and (C) the converted binary image.

An elliptical region of interest was used to measure the distance of cell expansion from the center. The perimeter (in number of pixels) of cell expansion was calculated for each sample based on the elliptical region. The number of pixels was converted to micrometers using the length of the scale bar. The perimeter of expansion was determined for each experimental group using the same image processing method.

Statistical Analysis for Transport of Cells through a Fiber in a Hydrogel

Statistical analysis was assessed using JMP 10 software. The perimeter of expansion of cells was compared in double layer hemisphere samples with round and wicking fibers as well as samples without fibers.

Results

Progenitor Cell Transport through Wicking Fibers

The vertical displacement of fluorescently green-labeled D1 cells was assessed along wicking and round fibers. The results show a significantly ($p < 0.001$) greater vertical cell displacement along the wicking fiber than on the round fiber. Figure 2.12 illustrates a much higher density of cells along the wicking fiber compared to the round fibers suggesting the wicking fibers can significantly augment cell recruitment.

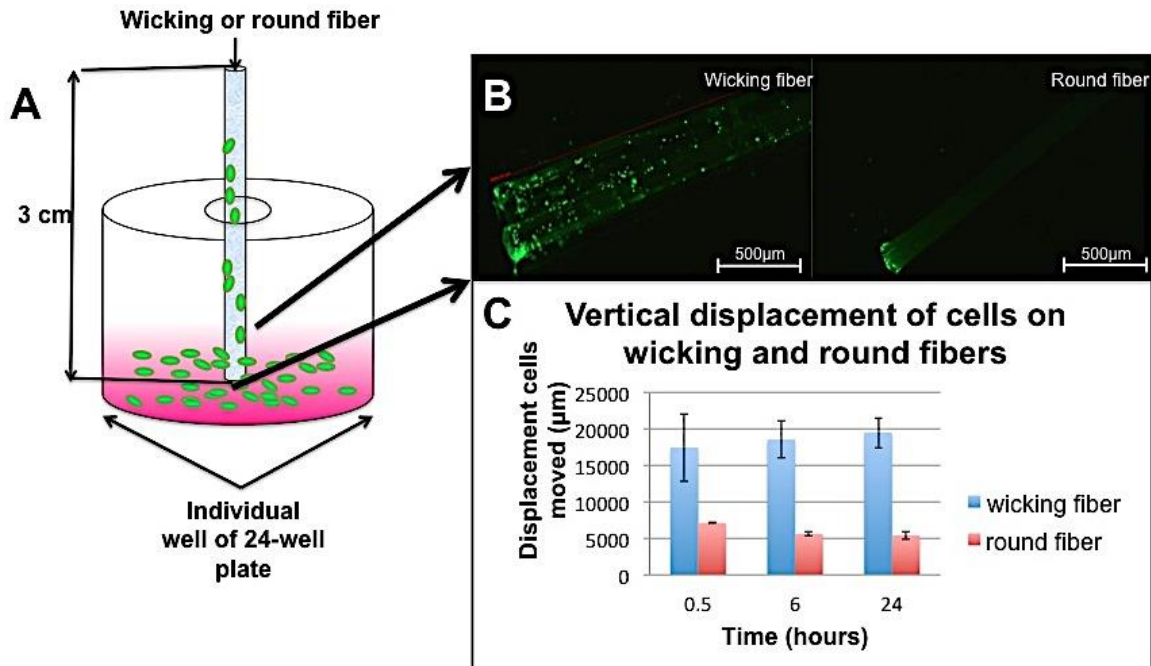


Figure 2.12: (A) Schematic illustrating the location of the captured fluorescent images shown in (B) along wicking or round fibers. Measurements of progenitor cell movement quantified through imaging software and shown in the chart (C). The vertical displacement and cell density along the wicking fibers is significantly greater than the round fibers; * $p < 0.001$.

Effect of Fibers on Transport of Progenitor Cell through a Hydrogel with and without Fibers

The expansion and distribution of progenitor cells was assessed in a double-layered collagen hydrogel in samples with and without round or wicking fibers after 24 hours of incubation. The fluorescent and binary images shown in Figure 2.13 depict greater progenitor cell expansion in collagen hemisphere hydrogels containing wicking fibers than hydrogel samples with round fibers or without fibers. The images further

illustrate greater progenitor cell expansion in collagen hemisphere samples with round fibers than hemispheres containing no fibers.

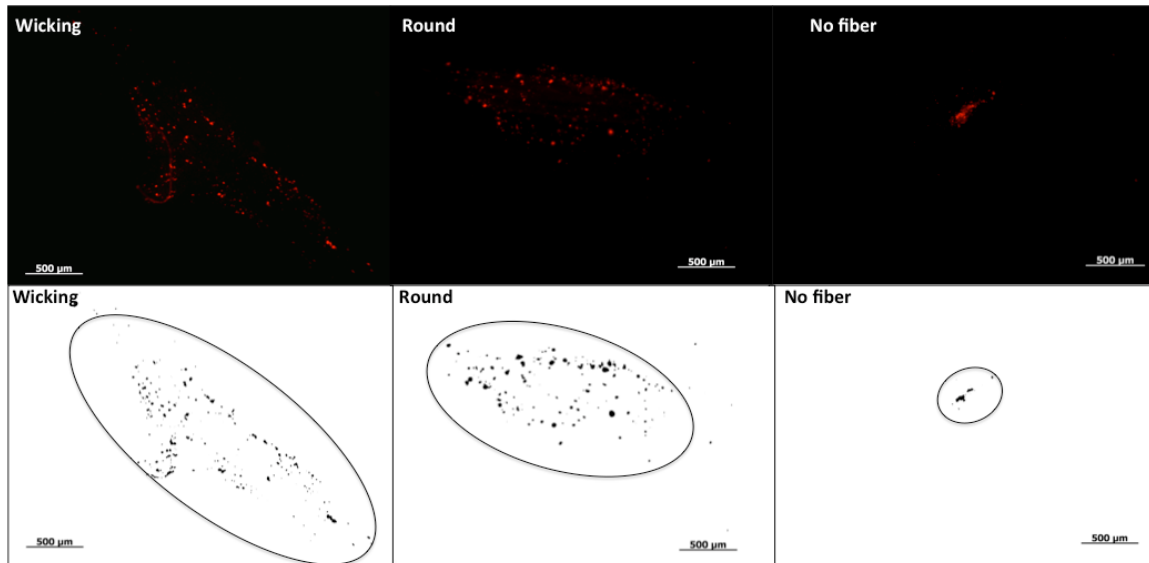


Figure 2.13: Qualitative fluorescent and binary images of collagen hydrogel hemisphere samples containing no fibers and samples with round or wicking fibers. Images show greatest cell expansion with wicking fibers compared to samples with round fibers or no fibers

The data was semi-quantitatively analyzed using image J processing. The perimeter of expansion of each hydrogel sample was determined in number of pixels and converted into units of micrometers using the scale bar. The chart below shows the results perimeter of cell expansion for each sample types. Expansion for hydrogel samples containing wicking fibers is significantly greater ($p < 0.05$) than all other treatment groups. Hydrogels with round fibers are also significantly greater than just the control group without fibers.

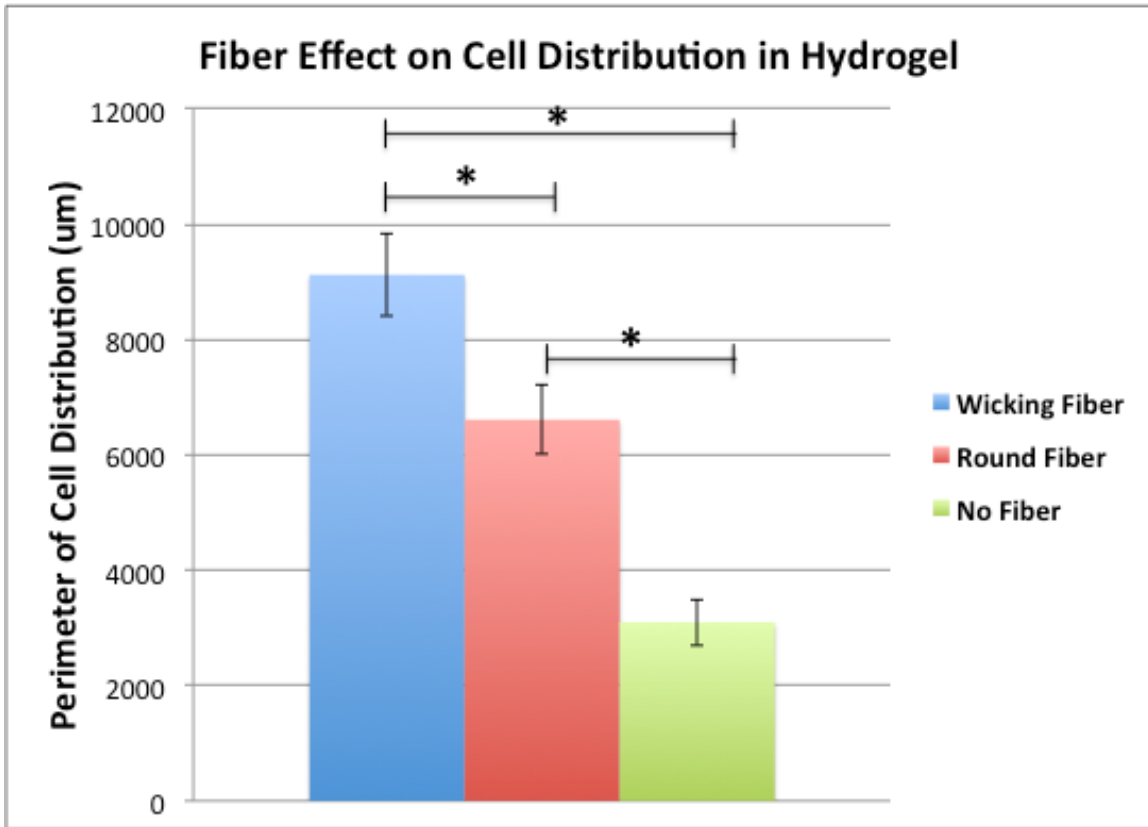


Figure 2.14: Results of progenitor cell expansion in double-layered collagen hydrogels. Samples with wicking fibers showed greatest cell distribution compared to all other experimental groups. (* represents significantly different groups with $p < 0.05$)

Discussion

It is well established that the proprietary wicking fiber shape provides highly efficient fluid transport in textile and chromatographic separation applications^{11-13,15,25}. The increased transport properties of the wicking fiber is achieved through geometrically optimized intra-fiber spaces or grooves that combine capillary pressure to enhance the fluid transport or wicking along a single wicking fiber^{11,14}. The unique architecture of a

single fiber greatly enhances the capillary action as opposed to a single channel. This is confirmed by the fluid transport studies conducted in this chapter.

Wicking occurs when fluid initially contacts the inter- or intra- fiber space and travels due to capillary pressure. The enhanced transport shown by the wicking fibers is a result of the shape factor^{19,20,26}.

Brojeswari Das and coworkers showed a linear relationship between shape factor and water uptake. As the shape factor of the fiber increases the water uptake and fluid transport increases linearly. The wicking fibers contain 2.5-3.2 times the surface area of conventional circular cross-sectional fibers with nominal diameter¹⁸. The increase in shape factor significantly increases the capillary pressure of the fiber, which improves the wicking properties of the fiber. This phenomena is described by Young-Dupre's equation shown below. Chung and coworkers showed that Polylactide wicking fibers have a much lower contact angle and superior wetting behavior than round PLA fibers²⁷. The capillary pressure is also directly related to the contact angle as described in Young-Dupre's equation. The low contact angle and high shape factor contribute to the superior capillary pressure and wicking behavior of the wicking fibers.^{19,20,27}

Equation 2.1: Young-Dupre's Equation

$$P_{\text{Capillary}} = \gamma_{LV} \cos \theta X$$

where,

θ = contact angle

X = Shape factor

$X_{\text{wicking fiber}} = 3$

$X_{\text{round fiber}} = 1$

$\theta_{\text{wicking fiber}} = 67^\circ$

$\theta_{\text{round fiber}} = 121^\circ$

$P_{\text{wicking fiber}} \gg P_{\text{round fiber}}$

The equation below shows the relationship between spontaneous wicking and contact angle and shape factor. Spontaneous wicking will occur with a wicking fiber due to the high shape factor and low contact angle. This relationship is not satisfied for round fibers.

Spontaneous wicking occurs if the following equation is satisfied:

$$(1 - X \cos \theta) < 0$$

where,

θ = contact angle

X = Shape factor

$(1 - X \cos \theta) < 0$ (Wicking fiber)

$(1 - X \cos \theta) > 0$ (Round fiber)

Fewer studies have assessed the effects of various bundling configurations on the diffusive and wicking properties of the fibers. Multiple groups have investigated the parallel packing of the wicking fibers for chromatography applications. Wicking occurs when fluid initially contacts the inter- or intra- fiber space and travels due to capillary pressure^{19,20,26}. By bundling the wicking fibers more intra- and inter- fiber spaces are

created. The increased spaces within the fiber bundles generates more capillary pressure and consequently leads to enhanced wicking rates. The studies assessing wicking properties of various bundled fibers showed a significant difference in wicking potential between braided and twisted fibers. The braided configuration creates discontinuities within the conduits of the bundle impeding the fluid flow. The braided configuration also shows larger pore sizes between fibers reducing the capillary pressure resulting in a lower maximum height of the fluid. Twisted fibers showed both higher fluid front heights and greater wicking rates. The twisted configuration shows less inter-fiber space with greater contact between individual fibers. The smaller inter-fiber spaces generate smaller pore sizes that will increase the capillary pressure of the bundle and result in higher maximum heights. The twisted bundles increase the continuity of the channels, which will improve the wicking rate of the sample.

The individual cross-sectional size of the wicking fibers comprising a fiber bundle and the number of individual fibers in a bundle will greatly influence the wicking properties. The tension of the twisted fiber bundles also plays a major role in the fluid properties. Fiber bundles of high tension may distort the grooves of the individual fibers blocking fluid flow. On the other hand, bundles with less tension lack the formation of inter-fiber spaces that create an increased number of capillary channels along the bundle. Future work will investigate the effect of various tensions and of cross-sectional sizes of the wicking fibers.

The wicking fibers were also able to significantly enhance the movement of biomolecules into a 3D collagen-agarose hydrogel. It has been well demonstrated that

wicking fibers can transport and separate compounds such as proteins, triglycerides, and inorganic and organic lead compounds for chromatographic separation by providing increased surface area and fluid transport^{12,28,29}. Similarly, the wicking fibers facilitate the transport of the FITC-albumin protein into the hydrogel. The parallel channels along the wicking fiber provide high surface area and increased capillary pressure that greatly increases the fluid transport and subsequently the rate of protein movement

These wicking fibers have previously been considered for tissue engineering constructs but investigation into the cellular movement was never evaluated^{12,29,30}. The final studies in this chapter investigated the potential of wicking fibers to transport progenitor cells to assess if these fibers can be used in tissue engineered constructs to improve progenitor cell recruitment. The results demonstrated the wicking fibers have capabilities to promote both cellular infiltration and distribution. The large surface area and superior capillary action and wettability properties promote cellular infiltration along the grooves of the wicking fibers. Cell transport was demonstrated by the vertical movement of green-labeled D1 cells along the wicking round fiber samples. Significantly more cells penetrated the wicking fibers and traveled higher than the round fibers. This influx of cells into the wicking fibers is enhanced by the increased surface area and wicking properties of the fibers. The intrinsic fluid properties of the fiber were shown to enhance the transport of cells, which can provide a unique approach to improving cellular seeding in scaffolds. Future work involves tailoring the fibers to recruit and transport specific cell types along the conduits.

In the last analysis collagen hemisphere hydrogels were used to investigate cell distribution and expansion in hydrogel samples containing round or wicking fibers. Prior to adapting and developing the collagen hemisphere hydrogel earlier systems using collagen-agarose hydrogels were used to optimize a system to assess cell movement in the gels with and without fibers. Optimization involved developing a system to observe cell mobility. Mobility of cells is dictated by matrix microarchitecture. Factors of the matrix that influence cell movement includes fiber density, pore size, stiffness, and bulk modulus.

Prior systems involved embedding round or wicking fibers in a collagen-agarose gel comprised of various ratios and assessing movement of fluorescently labeled cells into the hydrogel. The addition of agarose to the hydrogel greatly increases stiffness of the gel and reduces pore size. Cells show increased mobility in substrates with greater stiffness but lose mobility in substrates with reduced pore size. The addition of agarose increases stiffness, however, the reduction in pore size greatly inhibits cell movement. One mechanism to simulate cell movement is through gradients of stiffness. Cells interact with the matrix through mechanosensory molecules and will migrate to regions of higher stiffness. Mesenchymal progenitor cells move by binding to collagen fibers through their actin cytoskeleton. These cells move through contractility and relaxation of the matrix by their actin skeleton¹.

To stimulate progenitor cell movement, the hydrogels were formed to generate a gradient of stiffness. One mechanism for changing stiffness of the substrate is by adjusting the concentration of the hydrogel. In this case, varying amounts of agarose were

added to create a gradient of stiffness. This was reflected by the preliminary studies assessing cell movement in collagen-agarose hydrogels. To drive cell migration the hydrogels were formed with a gradient of stiffness. The hydrogels were comprised of various ratios of collagen-agarose (50:50, 65:35, and 80:20) to stimulate cell migration. The preliminary studies showed minimal cell migration in all ratios of collagen-agarose hydrogel illustrating the inhibitory effects of agarose on cell movement.

Building from the preliminary work, other systems were developed to assess the use of VEGF to drive cell migration in a collagen hydrogel. VEGF is a growth factor that can function as a mitogen and chemoattractant for mesenchymal stem cells. Preliminary systems showed both VEGF and changes in collagen concentration can be utilized in this to assess cell movement.

The collagen hemisphere hydrogel study described in this chapter used VEGF as the stimulant for the D1 cells to migrate into the second layer of the hemisphere. The results from this study showed the wicking fiber greatly increased the distribution and expansion of progenitor cells in the double-layered hemisphere compared to hemispheres without fibers and with round fibers. The increased surface area of the wicking fiber provided conduits within the collagen gel to augment the movement and dispersal of cells within the collagen hemisphere. The enhanced surface area and unique cross-section of the wicking fibers can be used to improve large tissue engineered scaffolds with limited transport capabilities. The fibers can be applied to these large scaffolds to provide conduits and capillary forces necessary to recruit and distribute cells.

Conclusion

The results indicate wicking fibers not only play a major role enhancing the movement of biomolecules into a 3-dimensional system, but also recruiting and transporting cells. This work suggests the intrinsic fluid properties of the wicking fibers have potential to greatly improve large bone tissue engineered constructs by providing conduits and enhanced capillary forces necessary for enhancing the transport of nutrients and movement of biomolecules and cells essential for bone formation.

References

1. Reichert J, Hutmacher D: Bone Tissue Engineering, Tissue Engineering: From Lab to Clinic. Edited by Pallua N, Suschek C. Berlin, Heidelberg, Springer, 2011, pp 431–56
2. Dimitriou R, Jones E, McGonagle D, Giannoudis P V: Bone regeneration: Current concepts and future directions. BMC Medicine 2011; 9:66
3. Lichte P, Pape HC, Pufe T, Kobbe P, Fischer H: Scaffolds for bone healing: concepts, materials and evidence. Injury 2011; 42:569–73
4. Hutmacher DW: Scaffolds in tissue engineering bone and cartilage. Biomaterials 2000; 21:2529–43
5. Amini AR, Adams DJ, Laurencin CT, Nukavarapu SP: Optimally porous and biomechanically compatible scaffolds for large-area bone regeneration. Tissue Engineering: Part A 2012; 18:1376–88
6. Muschler GF, Nakamoto C, Griffith LG: Engineering principles of clinical cell-based tissue engineering. The Journal of Bone and Joint Surgery 2004; 86-A:1541–58
7. Kneser U, Schaefer DJ, Munder B, Klemm C, Andree C, Stark GB: Tissue engineering of bone. Minimally Invasive Therapy & Allied Technologies 2002; 11:107–16
8. Kneser U, Schaefer D, Polykandriotis E, Horch R: Tissue engineering of bone: the reconstructive surgeon's point of view. Journal of Cellular and Molecular Medicine 2006; 10:7–19
9. Liu Y, Chan JKY, Teoh S: Review of vascularised bone tissue-engineering strategies with a focus on co-culture systems. Journal of Tissue Engineering and Regenerative Medicine 2012doi:10.1002/term
10. Tsigkou O, Pomerantseva I, Spencer J, Redondo P, Hart AR, O'Doherty E, Lin Y, Friedrich CC, Daheron L, Lin CP, Sundback C, Vacanti JP, Neville C: Engineered vascularized bone grafts. Proceedings of the National Academy of Sciences 2010; 107:3311–6
11. Phillips BM, Nelson JL, Bagrodia S: Bundles of fibers useful for moving liquids at high fluxes and acquisition/distribution structures that use the bundles, Patent Application 2001, EP1111100 A2 2001; 09897253

12. Brown P, Sinclair K, Fuller L, Webb K, Kenneth M: Capillary channeled polymer (c-cp) fiber based devices. *Polymer Prepr* 2006; 47:551–2
13. Nelson DM, Marcus RK: Potential for ultrafast protein separations with capillary-channeled polymer (C-CP) fiber columns. *Protein Pept Lett* 2006; 13:95–9
14. Phillips B, Bagrodia S: Fibers capable of spontaneously transporting fluids, US Patent 1999, 5,972,505 pp 1–90
15. Hirt DE, Zhu S: Improving the Wettability of Deep-Groove Polypropylene Fibers by Photografting. *Tex Res J* 2009; 79:534–47
16. Bagrodia S, Phillips B: Modified grooved polyester fibers and process for production thereof, US Patent 1990, 4,954,398 1990
17. Burg KJL, Brunson D: A novel use for capillary channel fibers: enhanced engineered tissue systems. *IEEE EMBS Annual International Conference* 2006:2358–61
18. Stanelle RD, Sander LC, Marcus RK: Hydrodynamic flow in capillary-channel fiber columns for liquid chromatography. *J Chromatogr A* 2005; 1100:68–75
19. Das B, Das A, Kothari VK, Fanguiero R, Araújo M de: Effect of fibre diameter and cross-sectional shape on moisture transmission through fabrics. *Fibers and Polymers* 2008; 9:225–31
20. Das B, Das A, Kothari VK, Fanguiero R: Development of mathematical model to predict vertical wicking behaviour. Part I: flow through yarn. *The Journal of the Textile Institute* 2011; 102:957–70
21. Fanguiero R, Filgueiras A, Soutinho F: Wicking behavior and drying capability of functional knitted fabrics. *Textile Research Journal* 2010; 80:1522–30
22. Temmerman E, Leys C: Surface modification of cotton yarn with a DC glow discharge in ambient air. *Surface and Coatings Technology* 2005; 200:686–9
23. Tabbaa SM, Burg KJ: The effect of wicking fibres in tissue-engineered bone scaffolds. *Journal of Tissue Engineering and Regenerative Medicine* 2014
24. Takata M, Maniwa Y, Doi T, Tanaka Y, Okada K, Nishio W, Ohbayashi C, Yoshimura M, Hayashi Y, Okita Y: Double-layered collagen gel hemisphere for cell invasion assay: successful visualization and quantification of cell invasion activity. *Cell Communication & Adhesion* 2007; 14:157–67

25. Park SB, Chung CK: Strategies of spinal fusion on osteoporotic spine. *Journal of Korean Neurosurgical Society* 2011; 49:317–22
26. Vaughn EA, Carman BG: Expanded surface area fibers: A means for medical product enhancement. *Journal of Industrial Textiles* 2001; 30:303–10
27. Chung S, Gamcsik MP, King MW: Novel scaffold design with multi-grooved PLA fibers. *Biomedical Materials* 2011; 6:1–12
28. Nelson DK, Marcus RK: A novel stationary phase: capillary-channeled polymer (C-CP) fibers for HPLC separations of proteins. *Journal of Chromatographic Science* 2003; 41:475–9
29. Sinclair KD, Webb K, Brown PJ: The effect of various denier capillary channel polymer fibers on the alignment of NHDF cells and type I collagen. *J Biomed Mater Res A* 2010; 95:1194–202
30. Lu Q, Simionescu A, Vyavahare N: Novel capillary channel fiber scaffolds for guided tissue engineering. *Acta Biomaterialia* 2005; 1:607–14

CHAPTER THREE

IMPROVING TRANSPORT LIMITATIONS OF LARGE SCAFFOLDS

Introduction

Spinal fusions are considered large volume bone defects and require large area bone grafts to augment repair similar to traumatic fractures. Like most implanted large tissue-engineered scaffolds, the surrounding environment and its interaction with the scaffold plays a critical role in the success of the graft. When the bone graft is first implanted in the fusion site the cellular component of the graft is supported by diffusion from the vascular sources of the surrounding site until new vessels are formed during the healing process. Therefore, understanding the vascular contribution of the bone graft and the surrounding tissue is essential for improving fusion rates¹.

Even with advancements in tissue engineering, the transport properties and vascularity of large bone scaffolds are very limited. In most cases, the furthest distance oxygen can reach from a capillary vessel via diffusion is roughly 100 μm through tissue. Most clinically available synthetic bone grafts exhibit structures that, while are not as densely packed as native tissue and may allow for better diffusion ability, are still ten times the maximum diffusive distance to the center of the bone graft² creating oxygen limitations. Typically, bone marrow aspirate (BMA) containing osteoprogenitor cells is seeded on the bone graft prior to implanting in the fusion site. Due to the increased diffusion distance in these scaffolds progenitor cells seeded on the grafts compete for oxygen and nutrients. The diffusion distance in large scaffolds limits the amount of viable cells that can be supported and proliferate. Muschler and coworkers describes a simple

engineering model that relates the size of the bone graft, the seeded cell density, oxygen levels, and cell viability². Necrosis within a bone graft can be theoretically modeled based on the oxygen levels at the surface, the cell density within the scaffold, the metabolic activity of the cells, and the diffusivity properties of the scaffold. The graph in the figure below illustrates the decreased ability of oxygen to reach the central region of the scaffold.

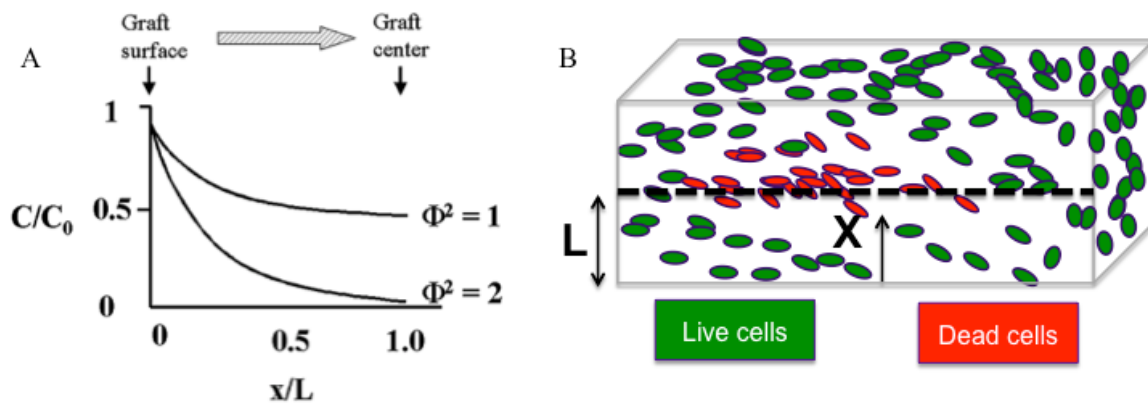


Figure 3.1: (A) The model developed by Muschler and coworkers shows the highest concentration of oxygen is at the surface of the graft and decreases towards the center of the graft². (B) The minimum oxygen concentration occurs at the center of the graft. Depending on the number of cells seeded and their metabolic activity necrosis can occur.

Equation 3.1: Muschler's Model Describing of Oxygen Consumption and Diffusion²

$$\frac{d\left(\frac{C}{C_o}\right)}{d\left(\frac{x}{L}\right)} = \phi^2 = \frac{[Cell]Q_{cell}L^2}{C_oD_{oxygen}} \rightarrow \frac{\text{Reaction rate}}{\text{Diffusion rate}} < 2$$

C = Concentration of oxygen in implant site

[Cell] = Cell density in the scaffold

x = Distance from surface into scaffold

Q_{cell} = Oxygen consumption rate per cell

L = Distance from the surface to the center of the scaffold

D_{oxygen} = Diffusion coefficient

The solution to the theoretical equations described by this model provides the oxygen concentration profile with the lowest oxygen concentration occurring at the center of the device. This is determined by the cellular consumption of oxygen and diffusion of oxygen. The parameter, Φ^2 , represents the relative ratio of consumption to diffusion. When the ratio of consumption to diffusion of this parameter is equal to two the oxygen concentration at the center is zero. This model can be useful to predict necrosis in large bone scaffolds and determine the optimal number of cells to seed the grafts to prevent necrosis. This model can also be used to predict the mass transport of small biomolecules such as glucose, fatty acids, amino acids, and other small biomolecules transport into and out of scaffolds². Larger molecules, such as growth factors are transported by convection caused from the surrounding vasculature. The convection generates pressure gradients to transport the larger biomolecules². The lack of transport of biomolecules will also contribute to necrosis or inadequate tissue formation in the central region.

In this chapter, the transport limitations of a commercially available bone graft, chronOS strip, and potential modifications to improve this were investigated. The chronOS strip is a commercially available synthetic bone graft manufactured by Synthes and FDA approved for use in posterolateral fusion shown in image A of Figure 3.2 below. This graft is a composite osteoconductive bone graft comprised from beta tricalcium phosphate granules and poly(lactide-co-ε-caprolactone) resorbable polymer.

Similar to most bone grafts used in large defects, the chronOS strip has a thickness of 6 mm as shown in Image B below. The oxygen diffusion distance to the center of the graft is 3mm, which is 30 times the normal diffusion distance resulting in inadequate sustainable oxygen levels or essential bone forming biomolecules². It is important to note, the main vascular supplies of the posterolateral fusion site are the transverse processes, positioned at the outer region of the fusion site, and surrounding tissue muscle shown in images C and D. Decortication of the transverse processes allows them to contribute as a source of vasculature to the fusion site. Image D depicts the 30 mm fusion site to which the transverse processes must provide vasculature. This gap places the central region of the bone graft 15 mm from the vasculature source; more than 100 times the normal diffusion distance. Other research groups have shown the surrounding muscle, depicted in image C, also plays a major role in contributing nutrients, biomolecules, and progenitor cells to the fusion site³. However, the extent of contribution from the muscle tissue as well as the mechanism and factors contributed from muscle are less established.

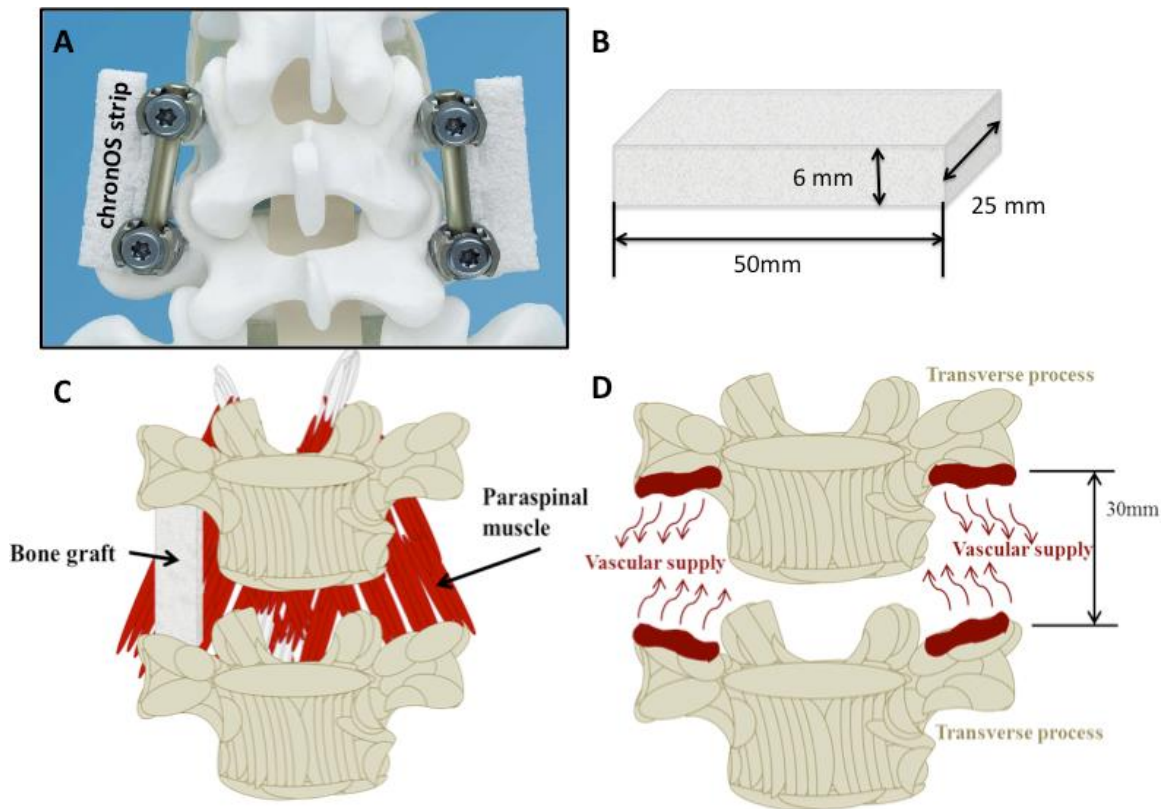


Figure 3.2: (A) Illustrates placement of chronOS strip during posterolateral fusion (B) Dimensions of chronOS strip (C) and (D) depict the two major sources of vasculature to the fusion site, transverse processes and paraspinal muscles, respectively. (Also published in Tabbaa et al. 2014⁴)

The limited transport to the central region of the fusion site is mirrored in the research conducted by multiple groups, most notably Boden and coworkers, who discovered a discrepancy between bone formation in the outer regions of the fusion site near the transverse processes and in the central region of posterolateral fusion using a New Zealand rabbit model. The outer regions experienced significantly faster cancellous bone formation compared to the central region, which experience a lag effect or delayed bone formation⁵⁻⁹. The delayed bone formation or fibrous formation in the central region

greatly increases the susceptibility of pseudarthrosis⁹⁻¹³. Cinotti et al. confirmed the vascular density in the outer regions is significantly higher than the central region indicating the transverse processes are the main source of vascular supply¹²⁻¹⁴. The delayed bone formation in the central zone is a result of both a lack of neovascularization within the region as well as a limited surrounding vascular supply.

Tissue engineering approaches for improving mass transport in large bone grafts involve modifying scaffold architecture. Scaffold porosity, shape, interconnectivity, permeability along with other parameters can affect mass transport properties. Optimal pore size has been extensively studied and defined typically between 150 μ m to 500 μ m to improve mass transport and promote bone in growth^{15,16}. Researchers have also extensively studied the ideal porosity for effective diffusion and cell penetration for bone regeneration. Typically, researchers have shown a higher porosity of around 90% and a greater surface area improves mass transport and overall bone regeneration¹⁷⁻¹⁹. However, other studies have shown porosity and permeability to have limited effects on cell penetration and proliferation, and found the macrostructure including pore shape, distribution, and alignment to have a greater influence on the success of the scaffold^{20,21}.

In this chapter wicking fiber bundles were incorporated into the chronOS scrip scaffolds to improve the transport properties by increasing porosity and providing conduits that enhance transport and diffusion. The goals of this study were to first test if the intrinsic transport properties and architecture of the wicking fibers will improve fluid transport. The porosity, as well as the fluid retention and distribution of the chronOS strip scaffolds were investigated with and without wicking fibers. The second goal of this

chapter was to analyze the effects of the fiber bundles on cell viability, distribution, and proliferation in the chronOS strip. The last goal was to investigate if the wicking fibers would improve bone formation by evaluating the differentiation of bone progenitor cells into an osteoblast phenotype within the chronOS strips.

Scaffold Characterization with Fibers

Materials and Methods

ChronOS Strip Preparation

Commercially-available chronOS strips (Synthes Inc.; West Chester, PA, USA) with length of 2.0 cm, width of 2.0 cm, and thickness of 0.60 cm; or length of 4.0 cm, width of 2.0 cm and thickness of 0.60 cm were modified with wicking fibers. Poly-L-lactide (Natureworks; LLC, USA) wicking fibers were extruded with non-circular cross-sectional dimensions of 0.12 mm x 0.05 mm. Three bundles containing ten wicking fibers, 2.0 cm in length, were securely fit through three separately drilled tunnels with diameter and length, 1.04 mm and 2.0 cm, respectively that parallel the long axis of chronOS strip. Two bundles of ten wicking fibers, 2.0 cm in length, were securely fit through two separately drilled holes in the chronOS strips with smaller dimensions.

Porosity Measurements

A liquid displacement method established by Ramay and coworkers was used to determine the porosity of the chronOS strip samples, 2.0 cm x 2.0 cm x 0.60 cm, with and without wicking fiber bundles²². To determine the porosity, the chronOS strip scaffold

with or without fibers was submerged in a graduated cylinder containing a known volume of 100% ethanol (V_0). The graduated cylinder containing the scaffold was placed under vacuum in a transparent desiccator as shown in image below (Nalgene™ Transparent Polycarbonate Classic Design Desiccator, Thermo Scientific, Waltham, MA, USA).



Figure 3.3: Experimental set-up to assess porosity in chronOS strip scaffolds with and without fibers

The vacuum allows the ethanol to penetrate the scaffold and displace the air from the scaffold. After no air bubbles were observed the volume of the ethanol was recorded (V_1). The graduated cylinder was removed from the desiccator and final volume (V_2) was determined by removing the scaffold from the ethanol and the measuring the remaining ethanol volume in the graduated cylinder. To determine the porosity, ϵ , the following equation was used.

*Equation 3.2: Porosity*²²

$$\varepsilon = \frac{(V_0 - V_1)}{(V_1 - V_2)}$$

Statistical Analysis

JMP software was used to conduct an unpaired two-sample t-test to compare the average porosity for chronOS strip samples with and without fibers using a significance level of $p < 0.05$.

Fluid Transport in Scaffolds

The vertical test method described in chapter 2 was used to assess absorption, wicking, and distribution of fluid in chronOS strip samples of dimensions, 2.0 cm x 4.0 cm x 0.60 cm. One end of the chronOS strip samples with or without fibers was vertically submerged in a reservoir of dye-solution that was comprised of phosphate buffered saline (PBS, Invitrogen) and 10% green assorted food coloring (McCormick). The vertical displacement of the fluid front was measured through video recording over a 30 minute interval with the initial time point starting at the time the scaffolds contact the dye solution, shown in image A of Figure 3.4 below. The rate of the capillary rise of the fluid front was determined for each sample.

A “horizontal test” was also conducted to investigate absorption and distribution of fluid in the chronOS strip samples with and without fibers of dimensions, 1.0 cm x 1.0 cm x 0.60 cm. To simulate direct cellular seeding, 50 μ L of a dye-solution containing PBS and 10% blue green food coloring was pipette directly to the top face of the chronOS strip scaffolds. The initial time point is shown in image B in Figure. After 24 hours, the

scaffolds were sectioned in half lengthwise and the digital images of the cross-section were imaged to analyze the distribution of the dye-solution.

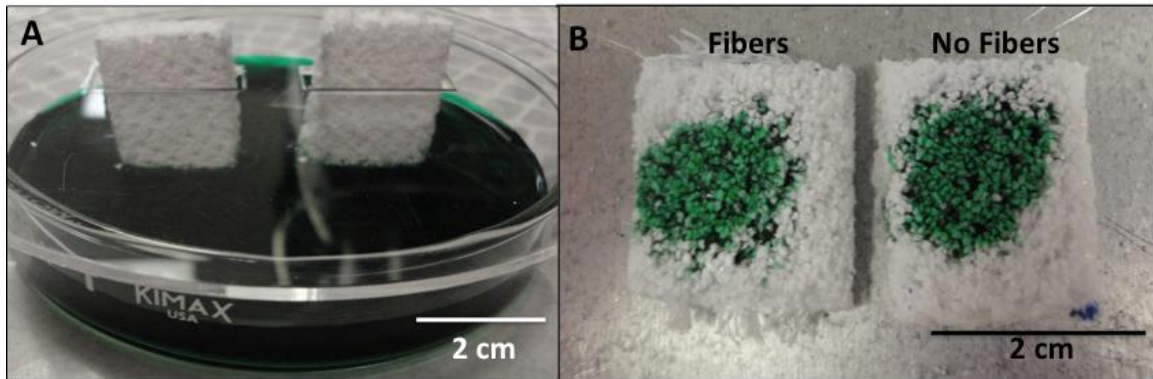


Figure 3.4: (A) Initial time point of chronOS strips scaffolds with (Right) and without fibers (Left) (B) Horizontal test initial time point

Results

Porosity Measurements

The average porosity for chronOS strip samples containing wicking fibers and without fibers was 74.5% and 65.6%, respectively. The porosity of chronOS strip samples with wicking fibers was significantly higher than the unmodified chronOS strip samples (Figure 3.5).

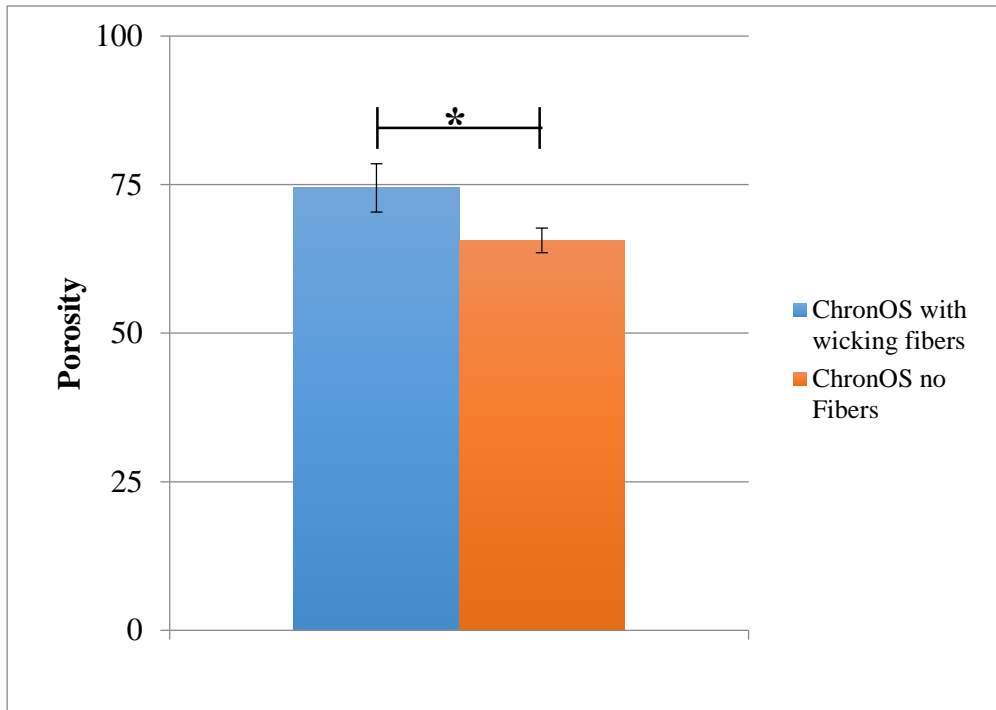


Figure 3.5: The wicking fibers increase the porosity of the chronOS strip samples by ~10%. The asterisk () represents statistically significant differences with $p < 0.05$*

Fluid Transport in Scaffolds

The vertical test of the dye-solution in scaffolds with and without fibers assessed the wicking rate and absorption of fluid. The digital images in Figure 3.6 illustrate the modified scaffolds enhanced the wicking rate and absorption of fluid over the 30 minute time interval.

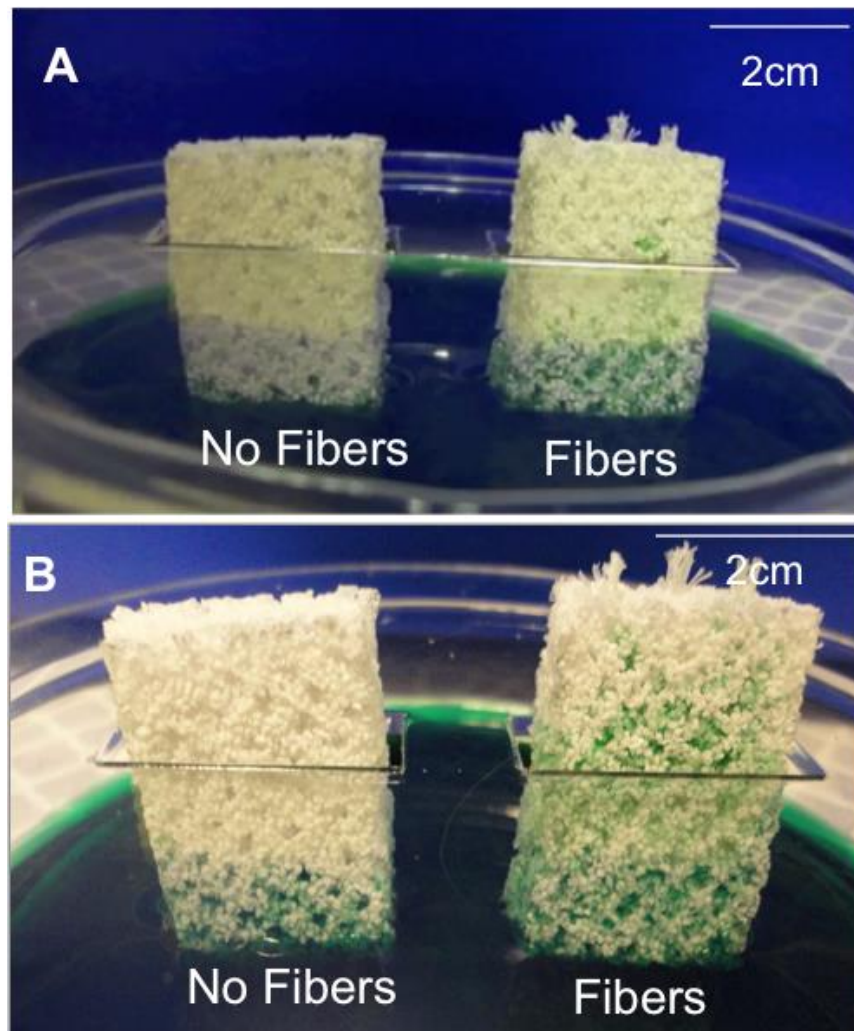


Figure 3.6: (A) Digital image of vertical test after 5 minutes (B) Digital image of vertical test after 30 minute. Images depict wicking fibers enhance fluid transport in scaffolds

The horizontal test evaluated fluid distribution in scaffolds with and without fibers after applying the fluid through direct seeding method by directly pipetting the solution to the front face of the scaffold. Image B of Figure 3.7 shows the spread of the dye-solution in the cross-sectional images of the samples after 24 hours. Samples

containing fibers showed more homogenous distribution of dye-solution along the interior cross-section.

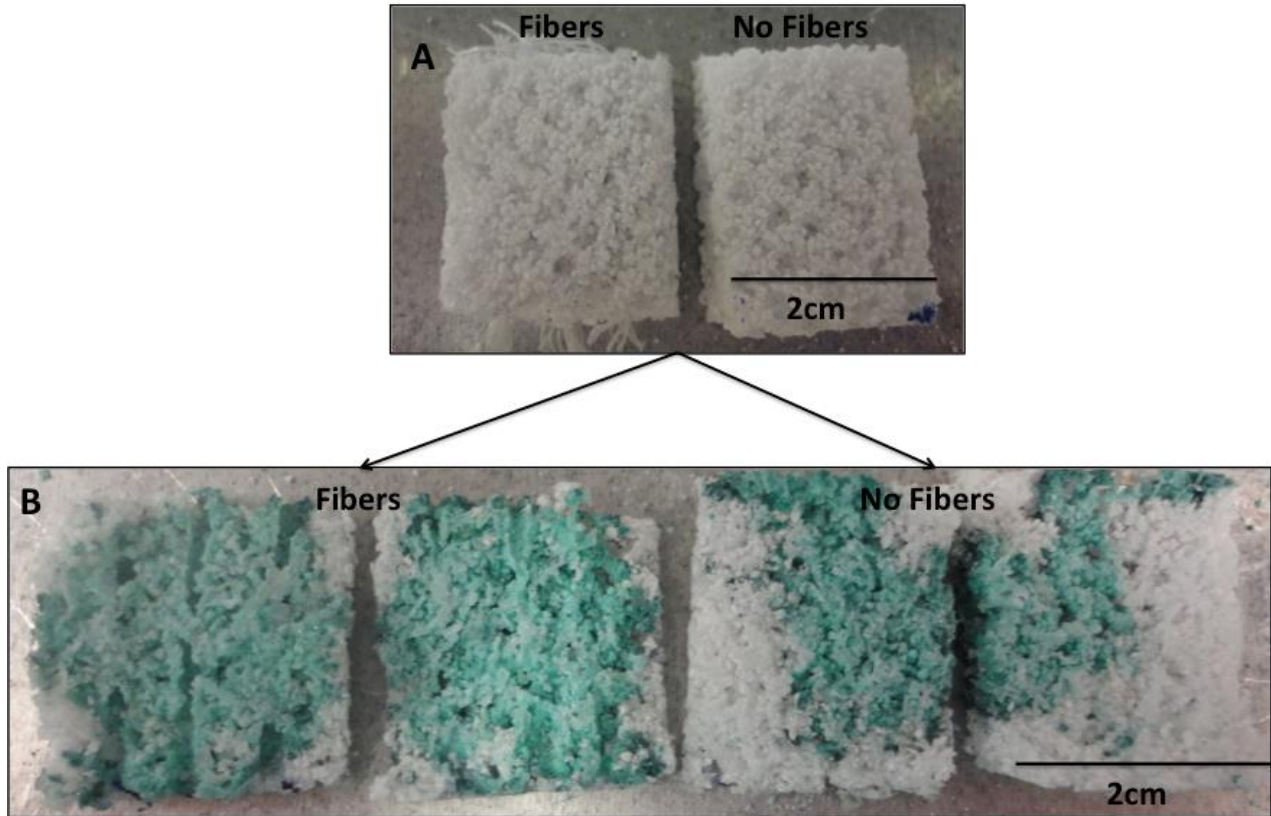


Figure 3.7: Results from horizontal test. (A) Scaffolds prior to directly seeding dye-solution to top face of scaffolds (B) Interior cross-sectional images of chronOS strips with and without fibers. Scaffolds with fibers show more homogenous distribution of dye-solution

Assessment of Progenitor Cell Recruitment into ChronOS strip

Materials and Methods

ChronOS strip Preparation

Commercially-available chronOS strips (Synthes Inc.; West Chester, PA, USA) were sectioned into samples with length of 2.0 cm, width of 1.3 cm, and thickness of 0.61 cm. Samples were prepared with and without wicking fiber bundles (N=3). Poly-L-lactide (Natureworks; LLC, USA) wicking fibers were extruded with non-circular cross-sectional dimensions of 0.12 mm x 0.05 mm. Three bundles containing ten wicking fibers, 2.0 cm in length, were securely fit through three separately drilled tunnels with diameter and length, 1.04 mm and 2.0 cm, respectively that parallel the long axis of chronOS strip. ChronOS strip samples, with and without wicking fibers, were cleaned by soaking in three changes of ethanol for 1 hour, and placed under ultraviolet light for 6 hours. After cleaning, the samples were soaked in three changes of phosphate-buffered saline solution for 2 hours (Invitrogen; Grand Island, NY, USA) and soaked in growth media consisting of Dulbecco's Modified Eagle's medium (Invitrogen; Grand Island, NY, USA) supplemented with 10% fetal bovine serum (Gibco; Grand Island, NY, USA), 10,000 U penicillin, and 10mg streptomycin/mL (Sigma; St. Louis, MO, USA) for 12 hours.

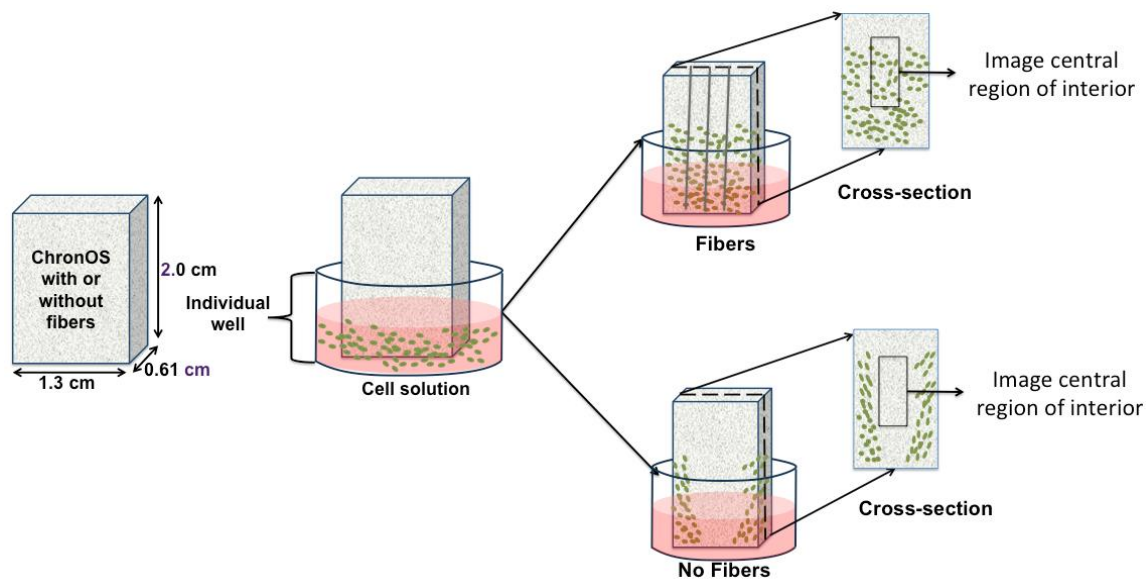


Figure 3.8: Experimental set-up assessing if wicking fibers improve cellular penetration and distribution in chronOS strip scaffolds

Progenitor Cell Distribution in chronOS Strip

Cellular recruitment and distribution was evaluated in modified and unmodified chronOS samples of dimensions 1.3 x 2.0 x 0.61 cm using a vertical wicking procedure illustrated in the figure below. The vertical wicking procedure involves submerging 10% of a vertically aligned scaffold into a well of a low-attachment 24-well plate containing 500 μ L of cellular solution with 1 million cells, and analyzing the vertical wicking of medium and cells into the scaffolds.

The wicking and distribution of D1 mouse mesenchymal stromal cells (ATCC; Manassas, VA, USA) in chronOS scaffolds, with and without fibers, was evaluated using the vertical test method. D1 cells were cultured in Dulbecco's Modified Eagle's medium (Invitrogen; Grand Island, NY, USA) supplemented with 10% fetal bovine serum (Gibco;

Grand Island, NY, USA), 10,000 U penicillin, and 10mg streptomycin/mL (Sigma; St. Louis, MO, USA). These progenitor cells were labeled with CellTracker™ Green CMFDA probe (Invitrogen; Grand Island, NY, USA), following manufacturer's protocol, using a long-term labeling concentration of 25µM. After samples were placed vertically in cell-tracker solution for 12 and 48 hours, the samples were halved along the longitudinal axis and the interior center region of the cross-section was imaged for each scaffold, as shown in the figure above.

The distribution of green-labeled D1 cells was also assessed after directly seeding the cell solution onto the top face of the scaffold, experimental set-up shown in Figure 3.9.

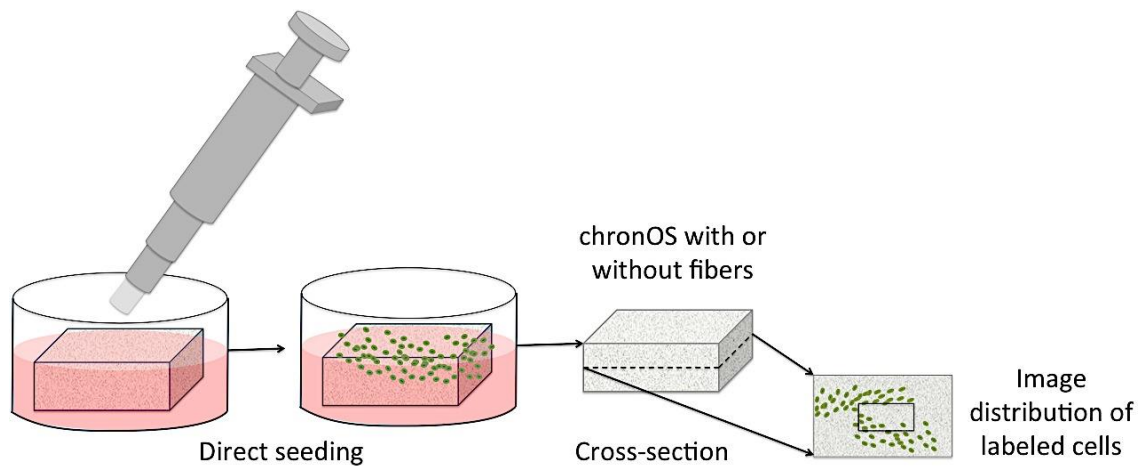


Figure 3.9: Schematic illustrating experimental set-up to assess the horizontal test of green labeled cells in scaffolds with and without fibers

One million D1 cells labeled with CellTrackerTMGreen were seeded on scaffolds with and without fibers by pipetting 50 μ L of cell solution directly on the top face of the samples. After 24 hours, the scaffolds were bi-sectioned lengthwise to assess the cell distribution of the samples in the central interior region. Fluorescent microscopy was used to image the cell distribution in the cross-sectional regions of the scaffolds. Cell penetration and attachment to wicking fiber bundles was also investigate.

Evaluation and Statistical Analysis of Cell Distribution

The images were semi-quantitatively analyzed using ImageJ cell counter software and plugin from the National Institutes of Health. The graph in Figure 3.10 depicts the percentage of cells in the center region of the cross-section images at the various time points for scaffolds with and without wicking fibers. Statistical analysis was conducted using an unpaired t-test through JMP statistical software to compare modified and unmodified chronOS scaffolds.

Results

Cross-section images of chronOS strips containing fibers revealed an increase in cell count and homogeneous distribution in the center region following the vertical test. The cross-section images of samples without wicking fibers depicted fewer cells, distributed mostly along the periphery of the scaffolds. The results showed a statistically significant difference ($p < 0.05$) of percentage of cells in the center when comparing scaffolds with fibers and scaffolds without fibers.

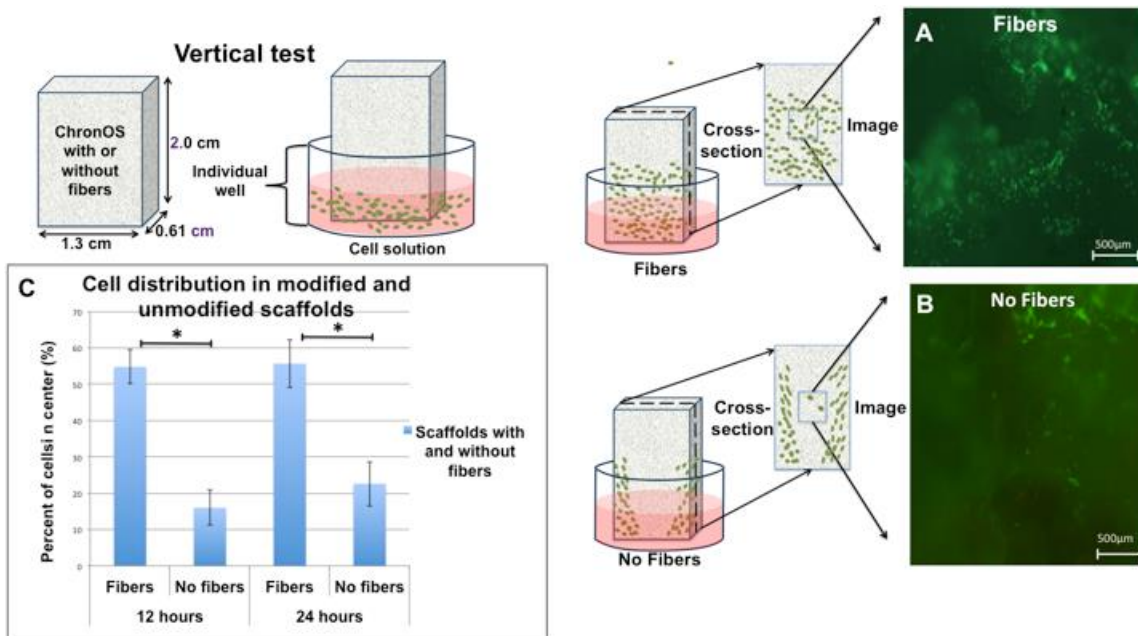


Figure 3.10: The schematic illustrates the vertical wicking of cells into scaffolds with and without fibers. (A) Fluorescent cross-section of densely populated green-tracked cells distributed homogeneously in the center region of the scaffold with fibers (B) Fluorescent cross-section of fewer green-tracked cells unevenly distributed in the center region of the scaffold without fibers (C) Data associated with the fluorescent images comparing the percentage of cells in the center region of the scaffolds with and without fibers using image J software

The results from the horizontal test, conducted by directly seeding cell solution on the top face of scaffolds with and without fibers, showed greater cell penetration and distribution in scaffolds containing fibers. The fluorescent images below (Figure 3.11) are of the central region of the cross-sectional regions of scaffolds with fibers (A) and without fibers (B).

The images depict enhanced penetration and distribution of the green-labeled bone progenitor cells in scaffolds with fibers. The wicking fiber bundles were directly imaged to assess if cells penetrate and attach to polylactide fibers. Images (C) and (D) below show significant cell penetration and attachment to wicking fiber bundles after 24 hours.

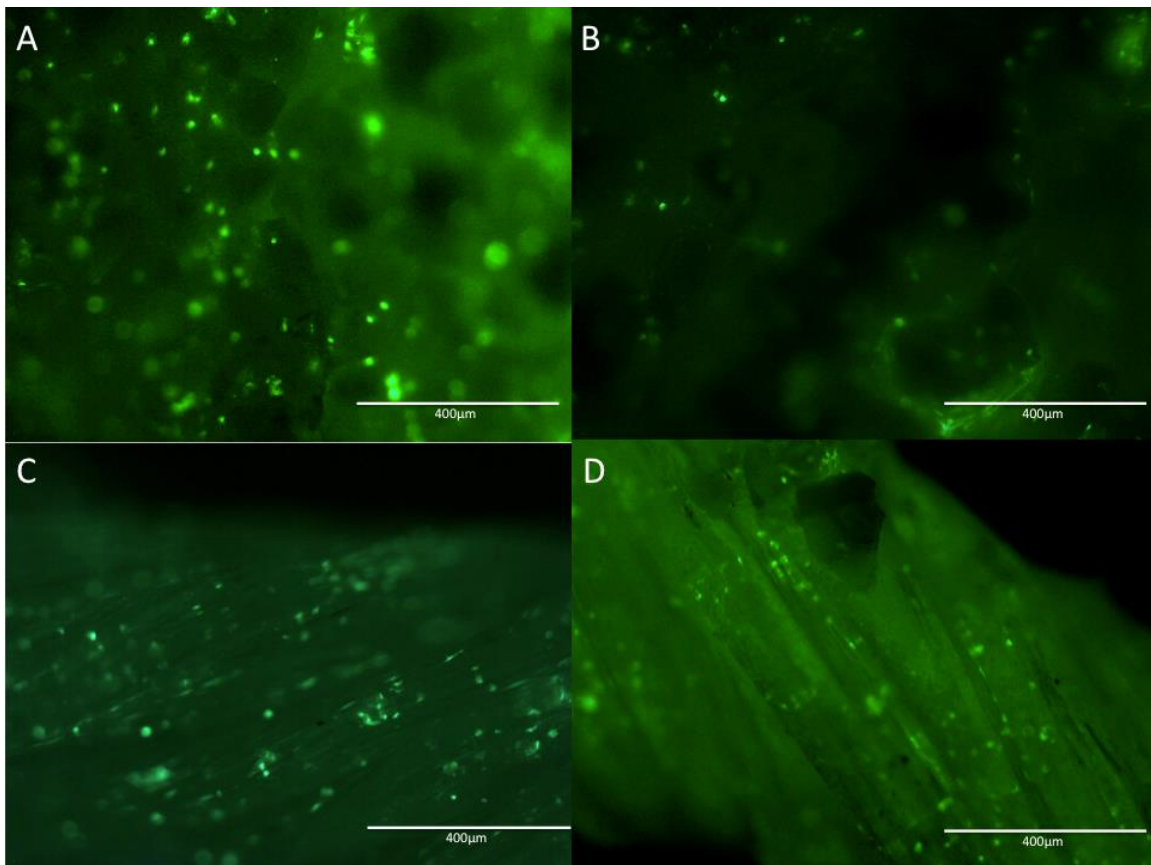


Figure 3.11: Fluorescent images of central region of cross-sectional regions of chronOS strips with and without fibers. (A) Scaffolds with fibers depict greater green-labeled cell penetration and distribution (B) Unmodified chronOS strip scaffolds shows fewer cells and less spread. (C) and (D) show significant cell penetration of the polylactide wicking fiber bundles

Cell Viability and Proliferation in ChronOS

Materials and Methods

ChronOS Strip Preparation

Commercially-available chronOS strips (Synthes Inc.; West Chester, PA, USA) with length of 1.0 cm, width of 1.0 cm and thickness of 0.61 cm were modified with wicking fiber bundles. Poly-L-lactide (Natureworks; LLC, USA) wicking fibers were extruded with non-circular cross-sectional dimensions of 0.12 mm x 0.05 mm. Three bundles containing ten wicking fibers, 1.0 cm in length, were securely fit through two separately drilled tunnels with diameter and length, 1.04 mm and 1.0 cm, respectively that parallel the long axis of chronOS strip. ChronOS strip samples with and without wicking fibers, were cleaned by soaking in three changes of ethanol for 1 hour, and placed under ultraviolet light for 6 hours. After cleaning the samples were soaked in three changes of phosphate-buffered saline solution for 2 hours (Invitrogen; Grand Island, NY, USA) and soaked in growth media consisting of Dulbecco's Modified Eagle's medium (Invitrogen; Grand Island, NY, USA) supplemented with 10% fetal bovine serum (Gibco; Grand Island, NY, USA), 10,000 U penicillin, and 10mg streptomycin/mL (Sigma; St. Louis, MO, USA) for 12 hours.

Cell Seeding and Experimental Set-up

D1 cells were seeded on scaffolds with and without fibers by pipetting 50 μ L of cell solution containing 1 million cells in growth media along the tunnels or on the 1.0 x 0.61 cm face of samples not containing fibers. The samples were placed in a low-attachment 24-well plate and placed in the incubator for 3 hours to allow the progenitor

cells to adhere. After 1 hour, 500 μ L of growth medium was added to the scaffolds and, after 3 hours, the samples were submerged in growth medium. Cell viability and proliferation were assessed by Live/Dead viability/cytotoxicity assay (Life Technologies; Grand Island, NY USA), ViaCount assay (Guava Technologies, Hayward, CA, USA) using flow cytometry, and PicoGreen assay (Invitrogen; Grand Island, NY USA). Live/Dead assay was used to qualitatively analyze the number of viable and dead cells after 12 and 48 hours. ViaCount assay quantified the number of viable cells in both experimental groups after days 1, 3, 7 and 10 were evaluated using flow cytometry (Guava Technologies; Hayward, CA, USA). Cell proliferation was determined by quantifying the total amount of double stranded DNA (dsDNA) on both sample types using PicoGreen assay after days 4 and 7. The table below summarizes the experimental set-up of the study including the time points and number of samples uses for each analysis. Medium was replaced every two days for each experimental group.

Table 3.1: Experimental setup

	Live/Dead (12 and 48 hours)	PicoGreen (Days 4 and 7)	ViaCount (Days 1,3,7,10)
chronOS strip (unmodified)	N=3	N=3	N=3
chronOS strip (with wicking fibers)	N=3	N=3	N=3

Initial Cell Viability on Interior of Scaffolds

Live/Dead viability/cytotoxicity assay (Invitrogen; Grand Island, NY, USA) was used to qualitatively assess the initial cell viability in the interior central region of the scaffolds after 12 and 48 hours of culturing cells. Two fluorescent probes, calcein AM and ethidium homodimer-1, were used according to manufacturer's protocol to determine live and dead cells in the samples. Samples were bisected lengthwise to assess the viability of the samples in the central interior region. The sections were washed with phosphate-buffered saline (PBS, Invitrogen, Grand Island, NY) and 500 μ L of 2 μ M calcein AM and 4 μ M of ethidium homodimer was added to each sample. After 45 minutes of incubation live and dead cells on the scaffolds were imaged using the fluorescein isothiocyanate (FITC) and tetramethyl rhodamine isothiocyanate (TRITC) filters, respectively, of the inverted fluorescent microscope (Zeiss Axiovert 135; Zeiss). The CCD camera (ProgRes C10plus; Jenoptik) was used to capture images. Image J processing was used to semi-quantitatively assess the number of live and dead cells in each sample and overlay the respective red and green channels of the images. The percentage of dead cells in the center interior region was determined for each scaffold type.

Long-term Cell Viability

Cells were removed from scaffolds by pipetting 1mL of trypsin-EDTA solution (Sigma; St. Louis, MO, USA) into each well and placing the plate on a flattop shaker (VWR maybe) set at 200 rpm in a 37°C incubator for 20 min. Following cell removal, the removed cells were resuspended in 1mL of growth medium and diluted with ViaCount

reagent in a 96-well plate (Guava Technologies, Hayward, CA, USA). The flow cytometer was calibrated using Guava Easy Check Kit (EMD Millipore, Billerica, MA, USA). The ViaCount assay was conducted following the manufacturer's instructions. The ViaCount assay determines the total number of viable and non-viable cells based on a fluorescent dye that stains nucleated cells. The number of viable cells and total cell count was determined after Days 1, 3, 7 and 10 of culturing cells on scaffolds.

Cell Proliferation on Scaffolds

After culturing samples for 4 and 7 days cell proliferation of chronOS strip samples with and without fibers was assessed using PicoGreen Assay (Quanti-iT PicoGreen dsDNA Kit; Invitrogen). Samples were washed with PBS and 1 mL of 1X Tris-EDTA buffer was added to each sample. The samples were lysed by ultrasonication (Sonic Dismembrator, Fisher Scientific) the samples for two 30-second cycles. The lysate was collected and stored in microcentrifuge tubes. The DNA concentration in each lysate from both experimental groups was determined using the PicoGreen assay by following the manufacturer's protocol. Acellular chronOS strip samples were used as controls. The number of cells for each scaffold was determined by using a calibration curve that was found by correlating the amount of DNA isolated to a known number of D1 cells counted using an automated hemocytometer (EMD Millipore, Billerica, MA,).

Statistical Analysis

Statistical analysis was conducted with JMP statistical software using a block model of time to compare the amount of viable cells in modified chronOS strips with wicking fibers and unmodified chronOS strips, with $p < 0.05$.

Results

Live/Dead assay investigated the number of viable and dead cells in the center region of chronOS strip scaffolds with and without fibers. The fluorescent images of the modified scaffolds illustrated significantly more viable cells (green) and less dead cells (red) in the center region of the scaffolds than scaffolds without fibers at both 12 hour and 24 hour time points as depicted in the figure. Image J software was used to quantify the percentage of dead cells in both scaffolds types. The semi-quantitative data shown in the chart shows significantly less dead cells in scaffolds with fibers than scaffolds without at 12 and 48 hours.

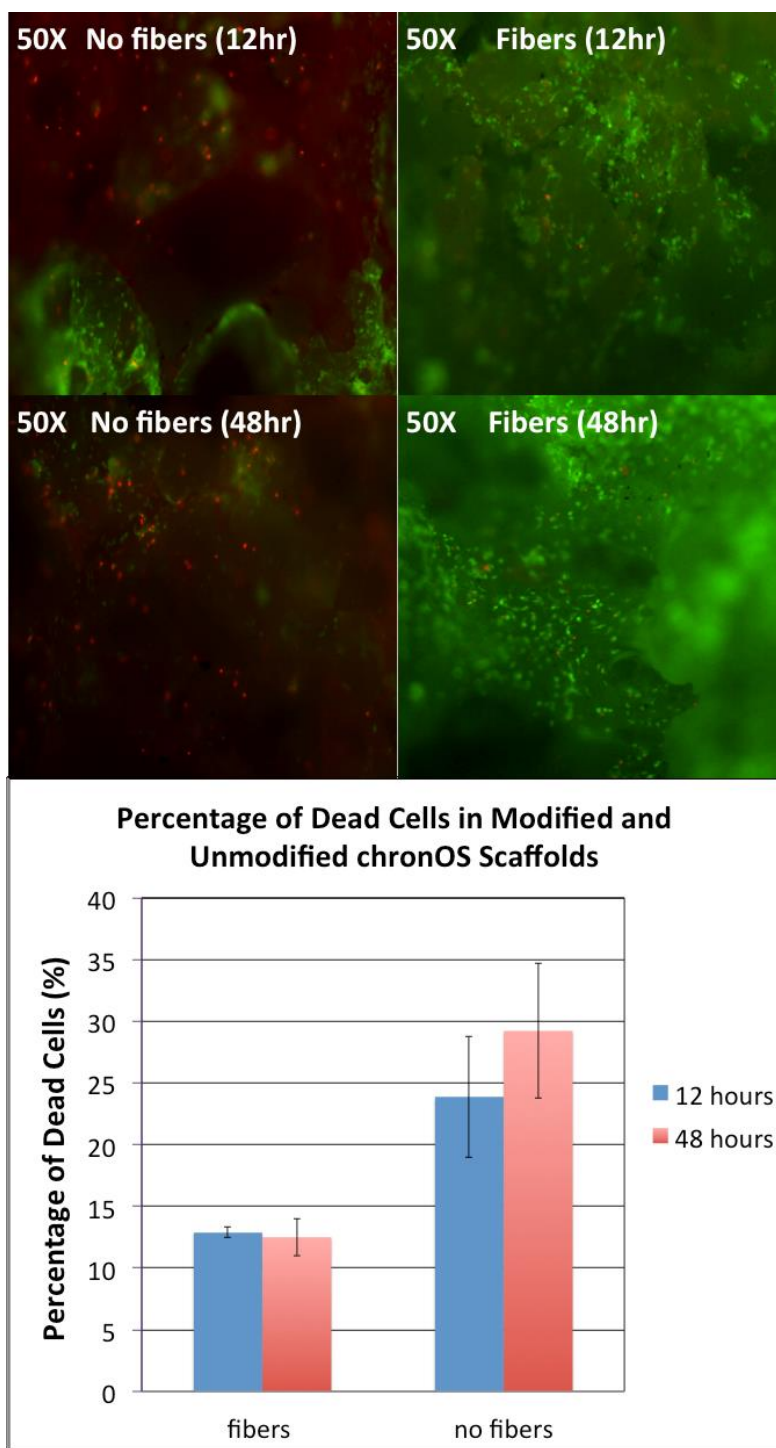


Figure 3.12: Top image shows an overlay of composite live/dead fluorescent images for chronOS strip samples with and without wicking fibers. Bottom chart illustrates percentage of dead cells in both scaffold types

Cell proliferation was determined by quantifying the amount of DNA in each scaffold type using PicoGreen assay. The amount of DNA was correlated to the number of D1 cells using the established calibration curve shown in graph below.

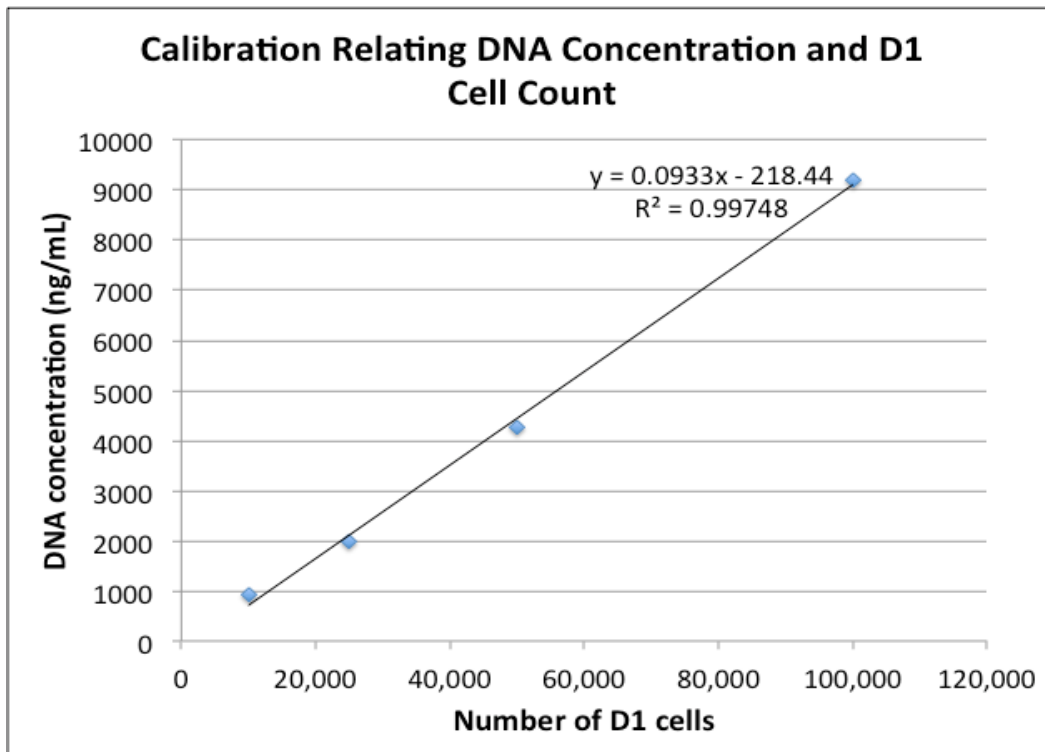


Figure 3.13: Calibration line that relates a known number of D1 cells to the DNA concentration found by using PicoGreen. Determined lysing a known number of cells placed in microvials.

The PicoGreen results show greater amounts of D1 cells in scaffolds with fibers than unmodified chronOS strip scaffolds after days 4 and 7. Both scaffold types show an increase in D1 cell count from Day 4 to Day 7, which indicates cells are proliferating on chronOS with and without fibers.

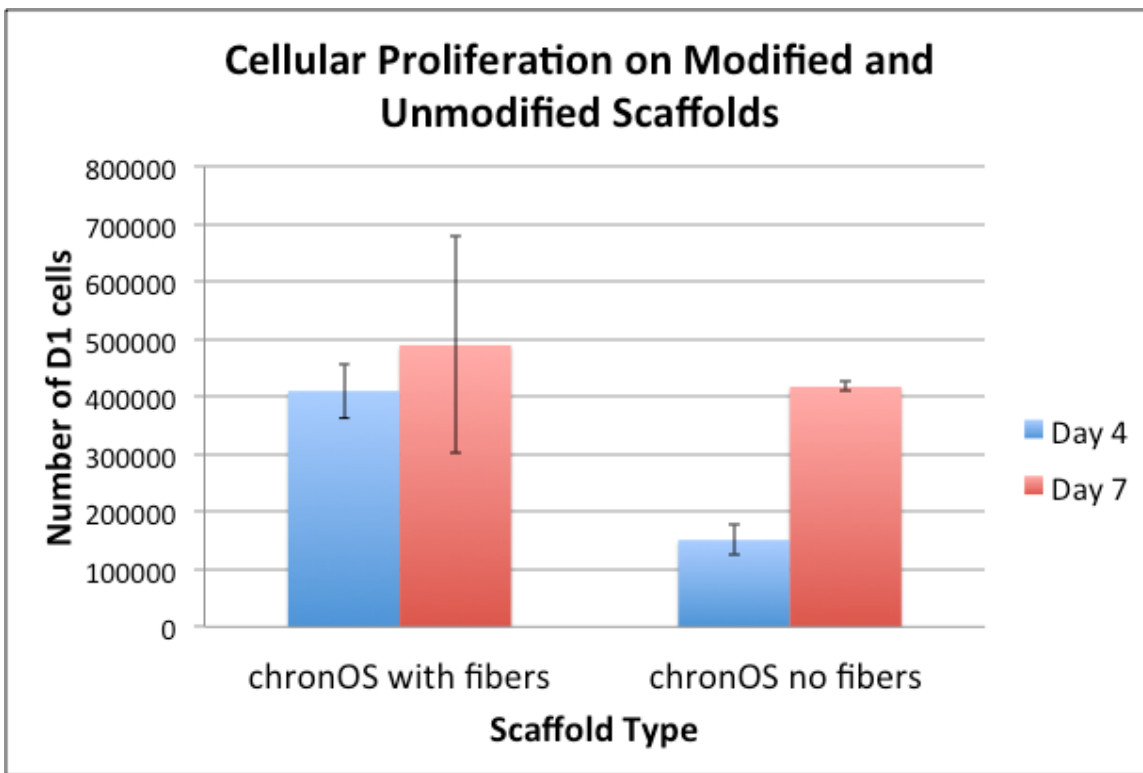


Figure 3.14: Results of the PicoGreen assay. ChronOS strips with fibers show more D1 cell proliferation on Days 4 and 7

Cell proliferation and viability was also quantified using flow cytometry.

ViaCount assay successfully stained the viable and non-viable cells for each scaffold type. The results of viable cells from Days 1, 3, 7, and 10 are shown in the graph below. The results show the chronOS scaffolds containing fibers have significantly more viable cells and a higher level of proliferation compared to scaffolds without fibers.

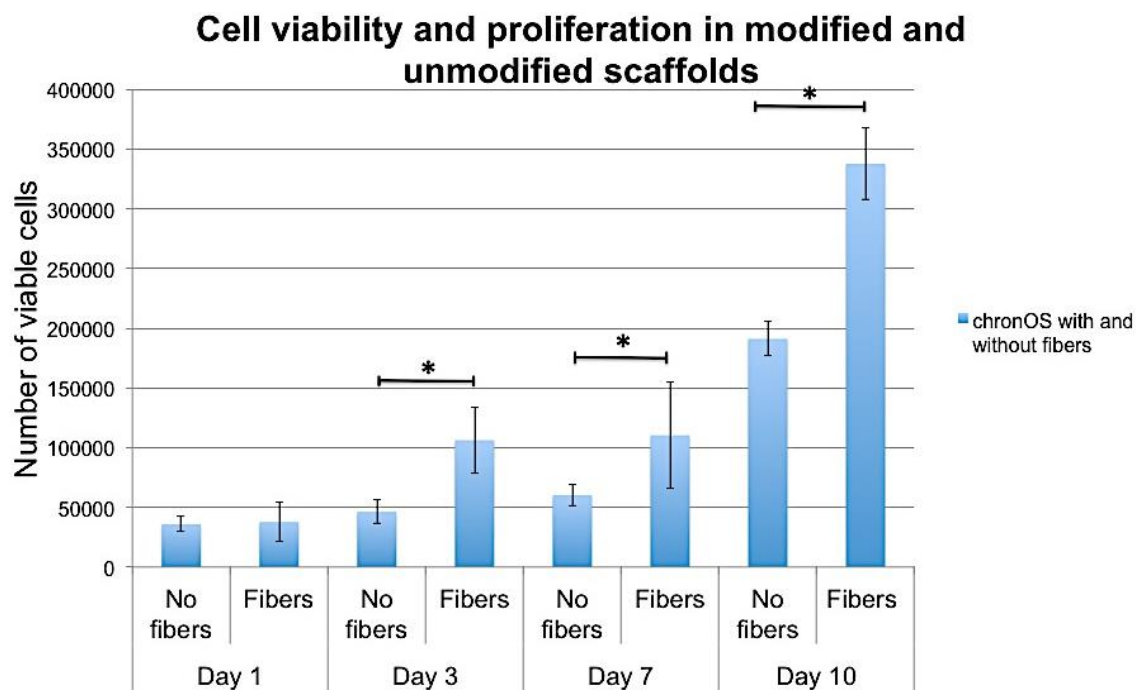


Figure 3.15: Flow cytometry analysis indicate significantly more viable cells after days 3, 7, and 10 in scaffolds containing wicking fibers; * $p < 0.05$.

Statistical analysis was conducted with JMP statistical software using a block model of time to compare the amount of viable cells in modified and unmodified scaffolds. The results showed the cell viability in scaffolds with fibers is significantly greater ($p < 0.01$) than scaffolds without fibers. Both scaffold type results indicate a significant difference of cell number between days ($p < 0.001$).

Effect of Wicking Fibers on Bone Formation

Methods and Materials

Scaffold Preparation

Commercially-available chronOS strips (Synthes Inc.; West Chester, PA, USA) with length of 1.0 cm, width of 1.0 cm and thickness of 0.61 cm were modified with wicking fibers. Poly-L-lactide (Natureworks; LLC, USA) wicking fibers were extruded with non-circular cross-sectional dimensions of 0.12 mm x 0.05 mm. Three bundles containing ten wicking fibers, 1.0 cm in length, were securely fit through two separately drilled tunnels with diameter and length, 1.04 mm and 1.0 cm, respectively that parallel the long axis of chronOS strip. ChronOS strip samples with and without wicking fibers, were sterilized with ethylene oxide for 12 hours in an AN74i cabinet sterilizer (Anprolene, Haw River, NC) with sterilizing gas ampule of 5cc (Anprolene, Anderson Products Inc., Haw River, NC). Samples were degassed in a chemical hood for 72 hours prior to use. Following the degassing period, scaffolds were transferred to three 24-well plates using autoclaved tweezers and were washed and soaked in PBS for two hours. The PBS was removed and 1.5 mL of growth media containing was added to each well containing scaffolds and placed in the incubator (37°C and 5% CO₂) overnight to allow protein attachment. The growth media was comprised of Minimal Essential Medium α without ascorbic acid (Gibco; Grand Island, NY, USA) supplemented with 10% fetal bovine serum (Gibco; Grand Island, NY, USA), 10,000 U penicillin, and 10mg streptomycin/mL (Sigma; St. Louis, MO, USA).

Cell Seeding and Experimental Set-up

MC3T3E1 Subclone 4 (ATCC) mouse preosteoblast cells, were cultured by growing cells until they reached confluence in a 75 cm² size area culture flask (Corning, Fisher Scientific) and splitting the smaller flask into four larger 150 cm² area cell culture flasks. The larger culture flasks were used to grow a large number of preosteoblast cells needed for the study. The study required 54 chronOS strip samples with and without fibers total with 1 million cells per sample. Cells were cultured with growth medium consisting of Minimal Essential Medium α without ascorbic acid (Gibco; Grand Island, NY, USA) supplemented with 10% fetal bovine serum (Gibco; Grand Island, NY, USA), 10,000 U penicillin, and 10mg streptomycin/mL (Sigma; St. Louis, MO, USA). Once the large culture flasks reach confluence the cells were split and one million MC3T3E1 cells were seeded on scaffolds with and without fibers by pipetting 50 μ L of cell solution along the tunnels or on the 1.0 x 0.61 cm face of samples not containing fibers. The samples were placed in low-attachment 24-well plates and placed in the incubator for 3 hours to allow the progenitor cells to adhere. After 1 hour, 500 μ L of growth medium was added to the scaffolds and, after 3 hours, the samples were submerged in growth medium. Three low-attachment 24-well plates, containing nine samples for each group (chronOS with or without fibers), were used for each endpoint of the study, which included Days 0, 7, and 14. Each endpoint assay contained three samples (n=3) of chronOS strip scaffolds with fibers or without fibers as well control samples (n=3). The control group was MC3T3E1 cells cultured directly on the 2-dimensional surface of the well plate. The endpoint analyses include: alkaline phosphatase (ALP) activity, PicoGreen assay,

Immunohistochemistry (IHC), Histological staining, and reverse transcription real-time polymerase chain reaction (qRT-PCR). The experimental set-up is depicted in the schematic below.

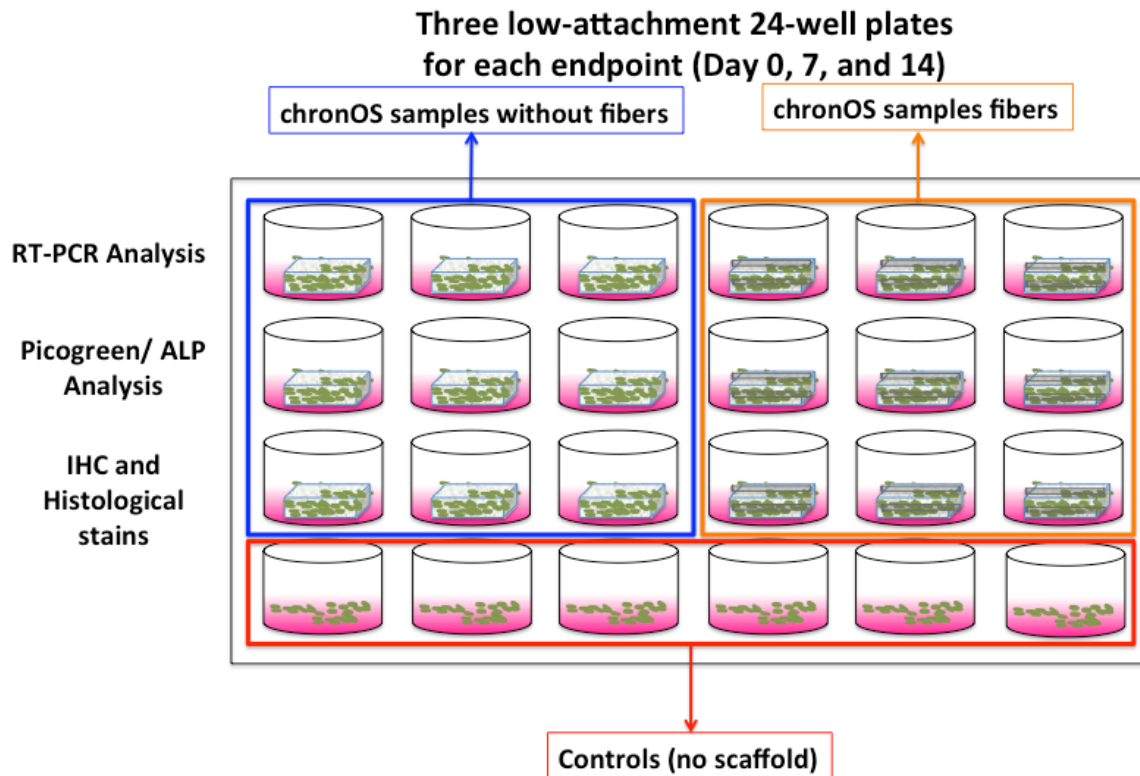


Figure 3.16: Experimental set-up for each endpoint (Days 0, 7, and 14). Each 24-well plate includes both experimental groups (chronOS with and without fibers) and a control group with no scaffold

Osteogenic Medium

Samples were cultured in growth medium to promote cellular attachment proliferation for 4 days on the scaffolds prior to adding osteogenic differentiation medium. After cell growth for 4 days the samples and controls were stimulated with osteogenic medium. Day 0 is considered the first day samples are cultured in the

osteogenic medium. The osteogenic medium consists of Minimal Essential Medium α without ascorbic acid (Gibco; Grand Island, NY) supplemented with 10% fetal bovine serum (Gibco; Grand Island, NY), 10,000 U penicillin, and 10mg streptomycin/mL (Sigma; St. Louis, MO), 10nM dexamethasone (Sigma; St. Louis, MO), 10mM β -glycerophosphate (Sigma; St. Louis, MO), and 50 μ g/mL ascorbic acid (Sigma; St. Louis, MO). The first 24-well plate initial time point samples (Day 0) were also collected accordingly, as described in subsequent sections, for each endpoint analyses.

RNA Isolation and RT-PCR

Related bone forming gene expression markers were assessed for chronOS strip samples. The related bone forming markers investigated in this assay, shown in table below includes: BMP-2, osteopontin, RUNX2, ALP, and osteocalcin. At days 0, 7, and 14 chronOS strip samples with and without fibers and controls were collected for RNA isolation using Trizol Reagent (Invitrogen; Grand Island, NY, USA). Prior to adding Trizol, scaffolds were snap frozen using liquid nitrogen and pulverizer (Tissue pulverizer, Cole-Parmer; IL, USA). One mL of Trizol reagent was added to samples containing samples and controls to lyse the cells. To isolate the RNA 0.2 mL of chloroform (Honeywell; Muskegon, MI, USA) was added to 1 mL Trizol reagent. The addition of the chloroform results in a phase separation with the RNA in the aqueous top phase. The aqueous phase was collected and isopropyl alcohol (VWR; Radnor, PA, USA) was added to precipitate the RNA. The samples were centrifuged, and the RNA was isolated from the samples by removing the supernatant. The samples were washed once with 1 mL of 75% ethanol (Sigma; St. Louis, MO), centrifuged, and the supernatant was carefully

removed. Prior to resuspending the participated RNA in 30 μ L of nuclease-free water (Life Technologies; Grand Island, NY, USA) the samples were air dried for 15 minutes. DNA was removed from the isolated RNA samples using a TURBO DNASE-Free kit (Life Technologies; Grand Island, NY, USA) and following manufacturer's instructions. The quality and quantity of the isolated RNA samples was determined using the Nanodrop 2000 spectrophotometer (Thermo Fisher Scientific Inc.; Waltham, MA, USA). Reverse transcriptase was performed using 1 μ g of RNA for each sample and the RETROscript kit (Ambion; Life Technologies; Grand Island, NY, USA) to synthesize the RNA to cDNA with a final concentration of 25ng/1 μ l according to manufacturer's instructions.

Table 3.2: Primer Sequences for RT-PCR

Primer	Sequence	T_m (°C)
ALP	F 5' - GCCTTCTCATCCAGTTCGTAT - 3'	54.2
	R 5' - CAAGGACATCGCATATCAGCTA - 3'	54.5
RUNX2	F 5' - CGTCCACTGTCACTTTAATAGCTC - 3'	55.3
	R 5' - GTAGCCAGGTTCAACGATCTG - 3'	55.5
Osteocalcin	F 5' - GCTTGGACATGAAGGCTTTG - 3'	54.5
	R 5' - ACCATCTTTCTGCTCACTCTG - 3'	54.5
BMP-2	F 5' - ACACTCTCCATCACAGTAGTTG - 3'	54.1
	R 5' - AGAAGCATGAGCTCTATGTGAG - 3'	54.2
GAPDH (Internal Standard)	F 5' - AATGGTGAAGGTCGGTGTG - 3'	54.3
	R 5' - GTGGAGTCATACTGGAACATGTAG - 3'	54.9

Real-time PCR was performed using the primers shown in the table below and the QuantiTech SYBR Green PCR kit (QIAGEN; Gaithersburg, MD, USA). The primers used were predesigned assays with optimized sequences (PrimeTime qPCR Primers; Integrated DNA Technologies; Coralville, Iowa, USA). However, prior to use the efficiency of the primers were tested using the QuantiTech SYBER Green PCR kit. The standard curve for each primer showed an efficiency greater than 99% for each primer tested. PCR was performed using StepOnePlus™ Real-Time PCR System (Life Technologies; Grand Island, NY, USA). The cycling parameters used were cycling for 40 cycles, denaturing at 94°C for 15 seconds, annealing at 54°C for 20 seconds, and extending at 72°C for 20 seconds. The Comparative C_T method or ΔΔCT method was used to calculate the relative gene expression ratios using GAPDH as the internal standard and comparing the target gene expression to the undifferentiated samples.

Equation 3.3: Comparative Ct Method

$$\Delta C_{t(Sample)} = C_{t(Target)} - C_{t(GAPDH)}$$

$$\Delta C_{t(Control)} = C_{t(Target)} - C_{t(GAPDH)}$$

$$\Delta C_t = C_{t(Sample)} - C_{t(Control)}$$

$$Relative\ Expression = 2^{-\Delta\Delta C_t}$$

Cell Proliferation Assay

Cell proliferation of the scaffold groups and the controls were assessed using PicoGreen Assay (Quanti-iT PicoGreen dsDNA Kit; Invitrogen) at days 0, 7, and 14. Samples were washed with PBS and 1 mL of 1X Tris-EDTA buffer is was added to each

sample. The samples were lysed by ultrasonication (Sonic Dismembrator, Fisher Scientific) the samples for two 30-second cycles. The lysate was collected and stored in microcentrifuge tubes. The DNA concentration in each lysate from both experimental groups was determined using the PicoGreen assay by following the manufacturer's protocol. The amount of DNA determined in this assay was used to normalize the determined ALP activity.

Alkaline Phosphatase (ALP) Activity

ALP activity of the scaffold groups and the controls were assessed using a standard colorimetric enzyme ALP Assay (Quanti-iT PicoGreen dsDNA Kit; Invitrogen) at days 0, 7, and 14. This assay measures the amount of produced yellow p-nitrophenol product by the cells due to the ALP-catalyzed hydrolysis reaction with p-nitrophenyl phosphate (pNPP). The same lysate samples that were collected and stored for PicoGreen assay were analyzed for ALP activity. A standard curve was prepared by diluting phosphate substrate (pNPP, Sigma; St. Louis, MO) to concentrations shown in Table 3.3.

Table 3.3: Phosphate substrate dilutions for standard curve

Standard Samples	Initial concentration pNPP solution (μM)	Initial volume of pNPP solution (μL)	Final Concentration of pNPP standard (μM)	Final Volume of standard solution (μL)
Sample 1	0	0	0	120
Sample 2	1000	1	8.33	120
Sample 3	1000	2	16.67	120
Sample 4	1000	4	33.33	120
Sample 5	1000	8	66.67	120
Sample 6	1000	16	133.33	120
Sample 7	1000	20	166.67	120
Sample 8	1000	40	333.33	120

The phosphatase substrate was made by dissolving pNPP in ALP buffer, comprised of 16.7 mL of 1.5M Alkaline buffer (Sigma; St. Louis, MO), deionized (DI) water, and 50mg MgCl₂ (Sigma; St. Louis, MO). Each 96-well plate contained two sets of the ALP standard. In the remaining wells, 80 μL of lysate sample and 50 μL of pNPP solution were added accordingly. Each sample was added in triplicate. One mg/mL ALP enzyme solution (Sigma; St. Louis, MO) was added to the standard wells. The plate was covered with foil and incubated for 1 hour at room temperature. Following incubation, 3M NaOH solution (Thermo Fisher Scientific Inc.; Waltham, MA, USA) was added to each well to stop the reaction. The absorbance of the samples was read at 410 nm using a Synergy MX Multi-Mode Reader (BioTek; Winooski, VT USA). A standard curve with a linear curve fit and equation was generated using the known ALP dilutions. The ALP activity was determined by the fit equation and the following ratio.

$$ALP \text{ Activity} = \frac{A/V}{T}$$

A = Amount (μmol) of phosphate substrate based on linear curve

V = Volume of sample (mL)

T = Reaction time (minutes)

Histology and Immunohistochemistry

At days 0, 7, and 14 samples for histological and immunohistochemistry (IHC) analysis were fixed in 10% formalin solution (Sigma; St. Louis, MO) and stored in PBS at 4°C. Prior to cryosectioning samples the scaffolds were decalcified for approximately four days using decalcifying solution (Sigma; St. Louis, MO). Routine chemical test for determining the end of decalcification was performed by preparing a working solution of

equal parts 5% ammonium hydroxide solution and 5% ammonium oxalate solution. Decalcification solution below samples was removed and mixed with the working solution. No precipitate was observed confirming the end of the decalcification process.

Following decalcification, optimal cutting temperature (OCT) tissue freeze medium (Tissue-Tek O.C.T. Compound; VWR, Radnor, PA) was used to infiltrate the scaffolds. OCT medium was used to completely submerge the samples in a disposable mold prior to sectioning with the cryostat. To enhance infiltration of freeze medium samples were covered with parafilm and placed in the vacuum overnight. After 12 hours under vacuum samples were removed and placed on cryostat chuck in the cryostat to freeze at -26°C . Samples were sectioned with $6\mu\text{m}$ thickness and mounted on a positively charged microscope slides (Superfrost Plus Microscope Slides; Fisher Scientific; Waltham, MA, USA). Sections were taken from the top, middle, and bottom regions of the sample. Frozen sectioned samples were immersed in acetone for 24 hours prior to histological stains and IHC to improve the adherence of the section to the slide. Sections were stained hematoxylin and eosin (H&E) following the protocol outline below in the table.

Table 3.4: H & E procedures for frozen sections

H & E Staining Procedure for Frozen Sections		Masson's Trichrome Staining Procedure for Frozen Sections	
Solution	Duration	Solution	Duration
Tap water	Until "sheeting" occurs	Tap water	1 minute
Hematoxylin	1 minute	Mordant in Bouin's fixative	1 hour at 56°C
Tap water	Until clear	Running tap water	Rinse Until clear
Bluing Reagent	2-3 dips	Weigert's Iron Hematoxylin Working Solution	10 minutes
Tap water	10 dips	Running tap water	10 minutes
95% ethanol	20 seconds	Distilled water	10 dips
Eosin	25 seconds	Biebrich Scarlet- Acid Fuchsin	2 minutes
95% ethanol	10 dips	Distilled water	10 dips
95% ethanol	10 dips	Phosphotungstic - Phosphomolybdic Acid	15 minutes
100% ethanol	10 dips	Aniline Blue Solution	5 minutes
100% ethanol	10 dips	Distilled water	10 dips
100% ethanol	10 dips	Acetic acid 3%	3 minutes
Xylene	10 dips	95% ethanol	10 dips
Xylene	10 dips	95% ethanol	10 dips
		100% ethanol	10 dips
		100% ethanol	10 dips
		Xylene	10 dips
		Xylene	10 dips

Prior to performing IHC, frozen sections were immersed in acetone for 24 hours to improve the sample adherence to the slide. Samples were rinsed extensively in PBS and blocked at room temperature for 1 hour in a blocking solution containing 2% BSA, 5% goat serum, and 0.1% triton X. Following the blocking step, the samples were incubated overnight at 4°C with primary antibodies BMP-2 (mouse anti-human, Abcam; Cambridge, MA, USA) and osteopontin (rabbit-anti-mouse, Abcam; Cambridge, MA, USA) using a 1:500 dilution for both antibodies. After the overnight incubation the primary was removed and stored for later use and the samples were gently washed with PBS and incubated in the diluted secondary antibody solution at room temperature for 2 hours. The secondary antibodies used include Alexa Fluor 488 goat anti-mouse antibody (Life Technologies Molecular Probes; Grand Island, NY, USA) and Alexa Fluor 568 goat anti-rabbit antibody (Molecular Probes; Grand Island, NY, USA). The antibodies used for

immunofluorescence staining and the dilutions are summarized in the table below.

Following the 2 hour incubation with the secondary antibody the sections were washed three times with PBS and coverslips were mounted using 40 μ L of ProLong Gold Antifade Mountant with DAPI (Molecular Probes; Grand Island, NY, USA). Samples were stored at 4°C away from light until the samples were imaged with the fluorescent microscope.

Table 3.5: Antibodies used for IHC staining

Primary Antibody	Dilution
Anti-BMP2 (mouse)	1:500 dilution (1 μ g/mL)
Anti-Osteopontin (rabbit)	1:500 dilution
Secondary Antibody	Dilution
Alexa Fluor 488 goat anti mouse	1:1000 dilution
Alexa Fluor 568 goat anti rabbit	1:1000 dilution

Statistical Analysis

For each target gene the average relative gene expression and standard deviation were determined. JMP 11 was used to perform a student's t-test to determine significant differences in average gene expression between fibers and no fibers for each time point. A student's t-test was also used to compare the average ALP activity at each time point for chronOS strips with or without fibers.

Results

Alkaline Phosphatase Activity

The outcomes from the ALP activity assay depicted in Figure 3.17 showed the modified chronOS strip samples had significantly higher ALP activity after Days 0 and 7. The unmodified chronOS strip samples demonstrated significantly higher ALP activity after Day 14. The modified samples showed a decrease in ALP activity at Day 14.

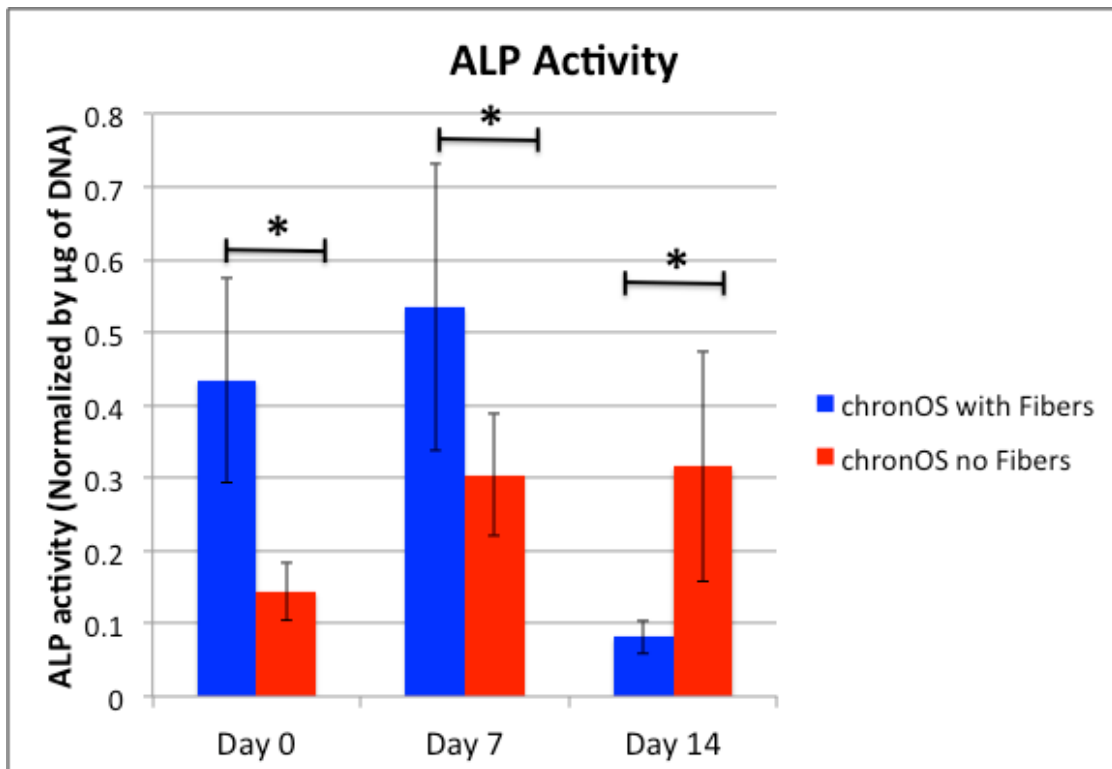


*Figure 3.17: ALP activity of chronOS strips with and without fibers normalized by amount of DNA. Day 0 and Day 7 show chronOS samples with fibers had significantly higher ALP activity than chronOS without fibers. Day 14 showed significantly higher ALP activity for chronOS samples without fibers; * $p < 0.05$.*

Real Time-PCR

The osteogenic differentiation of MC3T3E1 cells was analyzed by monitoring gene expression of ALP, Runx2, osteocalcin, and BMP-2. Relative expression of osteocalcin showed no significant difference between modified and unmodified chronOS strip samples. The modified chronOS strip samples showed higher Runx2 expression after Days 0 and 14. Similarly, the modified samples showed higher levels of ALP after Days 7 and 14. BMP-2 is a late osteogenic marker and was only observed for both samples at the Day 14 time point and showed no significant difference.

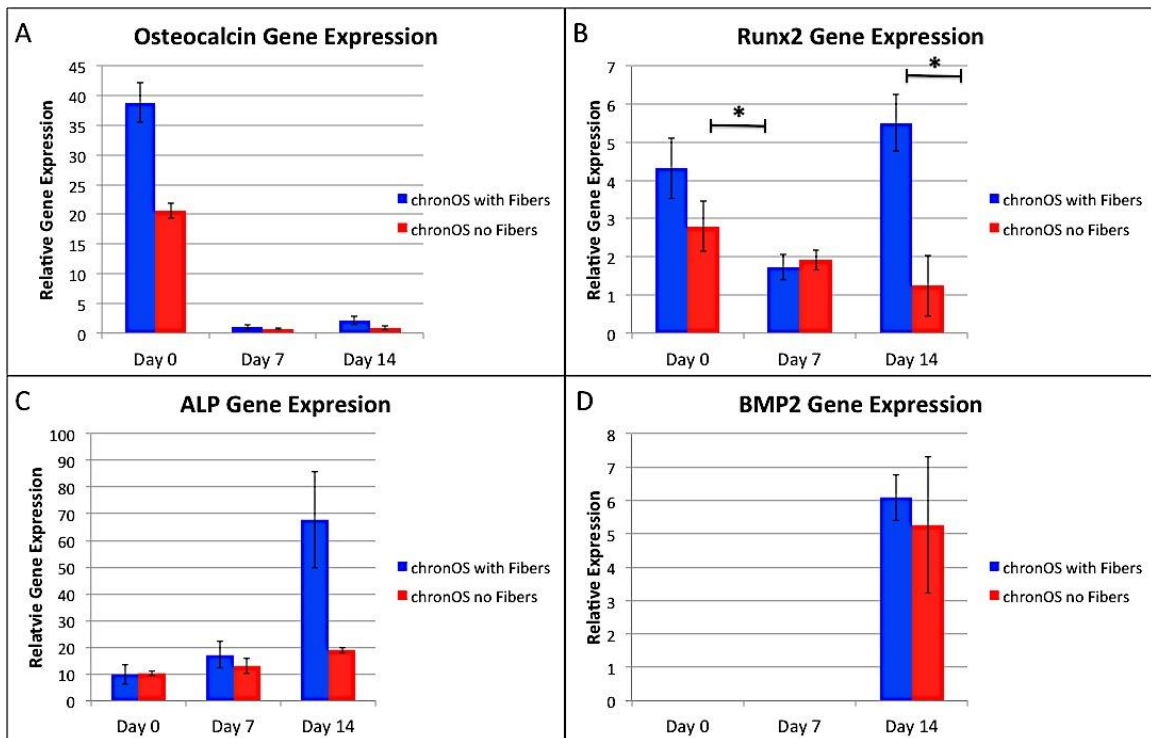


Figure 3.18: qRT-PCR results for osteoblastic differentiation markers: osteocalcin (A), Runx2 (B), ALP (C), and BMP2 (D). Modified chronOS showed significantly higher Runx2 expression than unmodified chronOS, * $p < 0.05$.

Histology

The H&E staining for chronOS strips samples are illustrated in Figure 3.19. Sections were obtained from the interior regions of the scaffolds. For both groups the staining showed greater cell densities after Days 7 and 14. Modified chronOS scaffolds show more cellular content and collagen than scaffolds without fibers. Image E shows the fibers have oriented the cellular and collagen content.

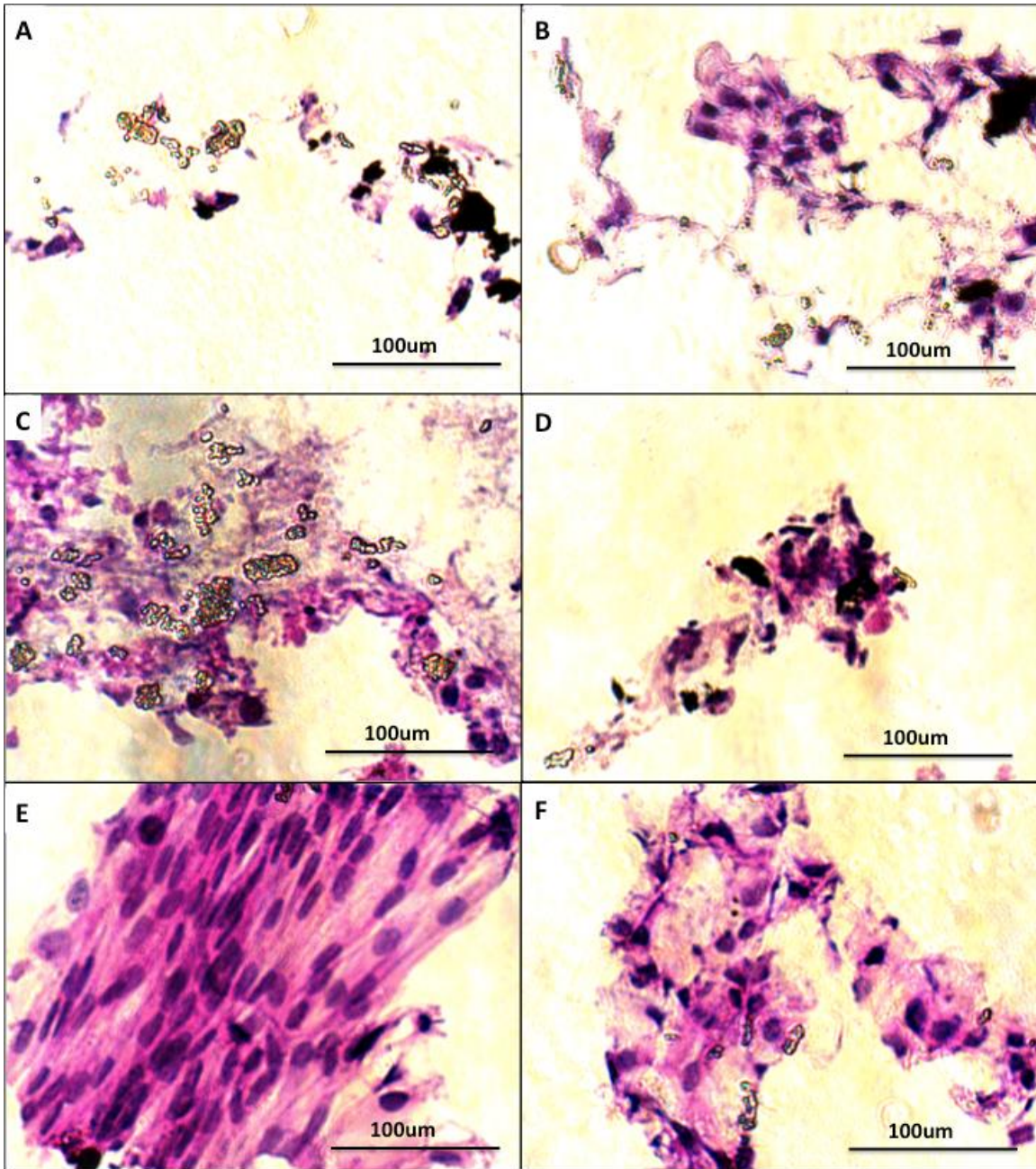


Figure 3.19: H&E staining for chronOS strip samples with fibers after Day 0 (A), Day 7 (C), and Day 14 (E), as well as chronOS strip samples without fibers after Day 0 (B), Day 7 (D) and Day 14 (F). Images show more cells in samples containing fibers. Day 14 samples with fibers show the aligned cells and formation of collagen.

Immunohistochemistry (IHC)

IHC was used to analyze the amount of osteoblast related proteins. The protein expression of BMP-2 and osteopontin was analyzed in sections from the interior of modified and unmodified chronOS scaffolds. Fluorescent images after Day 0, Figure 3.20, showed higher expression of BMP-2 in modified scaffolds. Both scaffolds types show low expression of osteopontin.

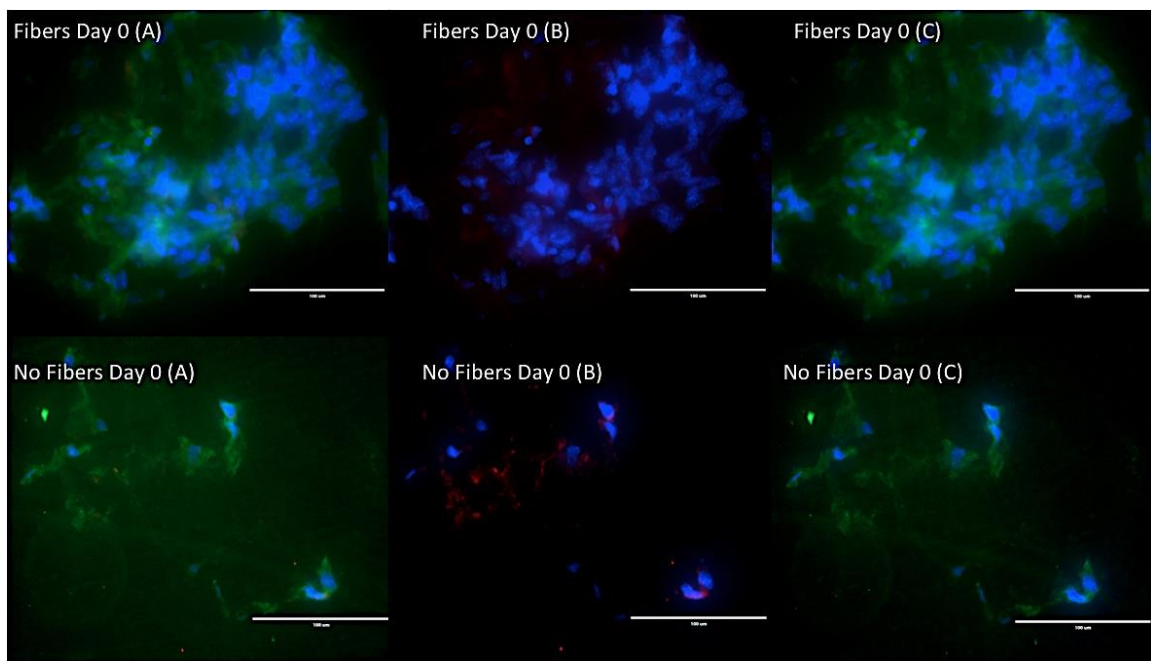


Figure 3.20: IHC staining for BMP-2 (green), osteopontin (red), and nuclei (blue) for Day 0 time point. Top row and bottom row depict chronOS with fibers and without, respectively. (A) Overlaid images of BMP-2, osteopontin, and nuclei. (B) Osteopontin expression and nuclei staining (C) BMP-2 and nuclei staining. ChronOS containing fibers shows greater expression of BMP-2. Both scaffold types show low expression of osteopontin.

After Day 7 both scaffold types showed an increase in BMP-2 and osteopontin expression. However, the modified chronOS strip samples showed significantly more

BMP-2 and osteopontin expression after Day 7 as indicated by the fluorescent images in Figure 3.21.

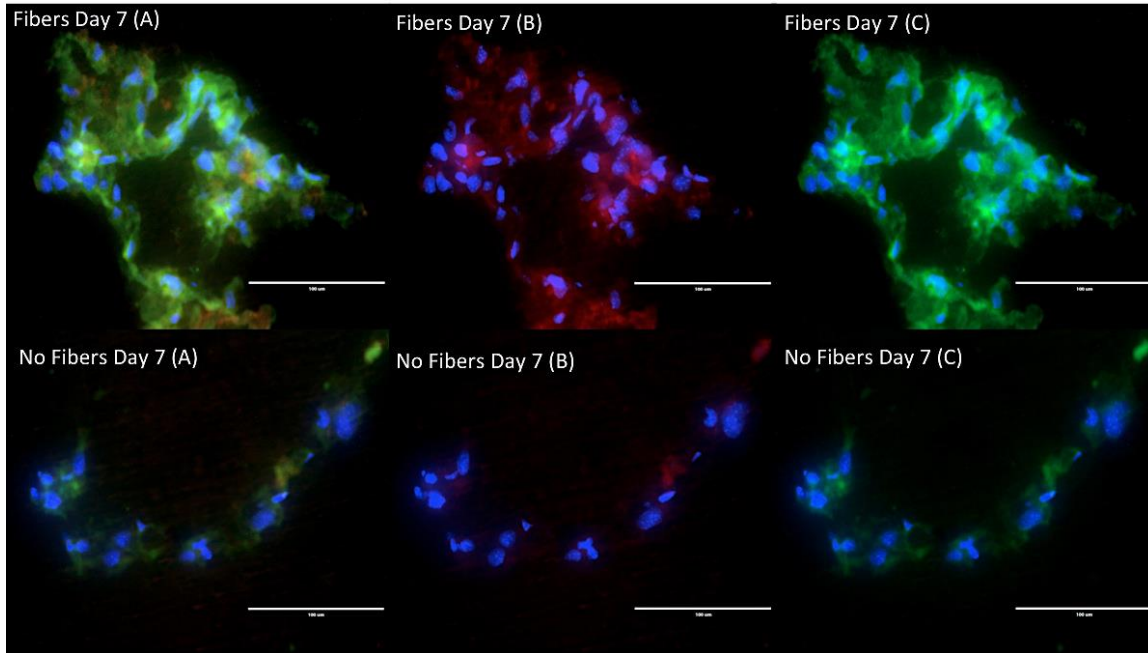


Figure 3.21 IHC staining for BMP-2 (green), osteopontin (red), and nuclei (blue) for Day 7 time point. Top row and bottom row depict modified and unmodified chronOS, respectively. The modified chronOS scaffolds show significantly more (B) osteopontin expression and (C) BMP-2 expression compared to the unmodified scaffolds.

Day 14 shows the greatest expression of BMP-2 and osteopontin for chronOS with and without fibers. The chronOS strip samples with fibers show greater expression of BMP-2 and osteopontin, depicted in Figure 3.22. The modified scaffold showed a significant increase in osteopontin expression, fluorescently labeled red in image B.

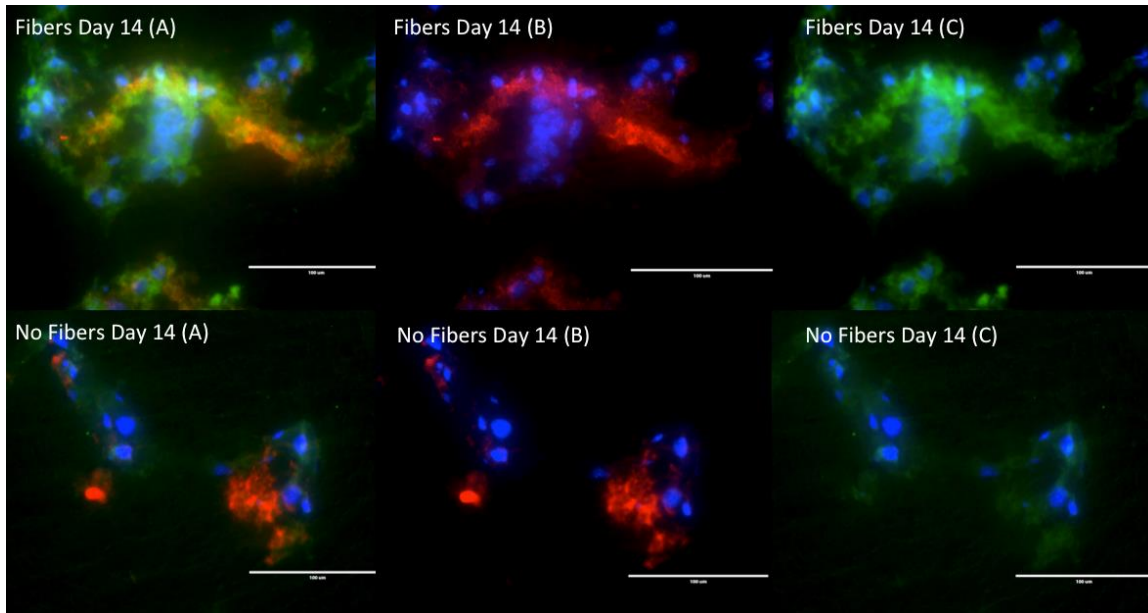


Figure 3.22: IHC staining for BMP-2 (green), osteopontin (red), and nuclei (blue) for Day 14 time point. Top row and bottom row depict modified and unmodified chronOS, respectively. The modified chronOS scaffolds show significantly more (B) osteopontin expression and (C) BMP-2 expression compared to the unmodified scaffolds.

Discussion

The goal was to investigate the effects of wicking fibers on a commercially available bone graft with limited diffusion to the central region due to the thickness of the scaffold. The fluid transport, cell viability, distribution, proliferation, and osteogenic differentiation were assessed in both the available scaffold and the wicking fiber altered scaffold. Changes in porosity by the incorporation of the wicking fibers into the chronOS strip samples were also investigated.

Fluid and cellular infiltration and distribution were investigated using horizontal and wicking tests of the chronOS strip scaffolds. The scaffolds were bi-sectioned

longitudinally for both tests to investigate the ability of the fibers to improve both transport of cells and fluid to the central region of the scaffold, where transport via diffusion is most limited. The outcomes depict the wicking fibers enhance both fluid and cell infiltration especially to the central region of the scaffold. Fluid and cell transport assessment showed the wicking fibers also significantly improved the distribution of cells and fluid in both the central and peripheral regions of the scaffold. Adequate cell infiltration to the central region is essential to promote cell growth on the surface and the interior regions simultaneously reducing the potential for heterogeneous bone formation in the central and peripheral regions. The outcomes from these studies suggest the architecture and transport capabilities of the wicking fibers promote cell penetration and distribution. The bundled wicking fibers provide increased micro-conduits as well as nano-sized and macro-sized channels that greatly enhance the fluid and cellular transport. The twisted configuration of the wicking fibers creates inter- and intra- fiber spaces of micro-sized channels of limited tortuosity. Micro-size pores have been shown to promote cell migration and movement. The bundling effects of the fibers increases the number of micro-channels, which will increase the initial fluid and cell transport through enhanced capillary action. Furthermore, the fiber bundles greatly increase the surface area to volume ratio as well as the porosity and interconnected pores. The results from the porosity tests showed the wicking fibers increases the porosity of the chronOS strip scaffolds by approximately 10%. It is well documented that higher porosity will improve cell infiltration and diffusion. The increased scaffold porosity by the wicking fiber

bundles, limited tortuosity, and interconnectivity by the channels provides more efficient mass transport and channels to facilitate cell movement and attachment.

Fluorescent images of the D1 green-labeled cells on the wicking fibers after 24 hours of direct cell seeding show increased amount of cell penetration and attachment along the wicking fiber bundles. As mentioned in chapter 2, the contact angle of polylactide fibers with the wicking fiber 8-grooved cross-sectional shape is significantly lower than round cross-sectional fibers resulting in a more hydrophilic fiber compared to a similar round cross-sectioned polylactide fiber. The enhanced wettability and grooved surface promote cell infiltration and cell adhesion, which is mirrored by the fluorescent images of the wicking fiber bundles. Interestingly, the wicking fiber architecture of the polylactide improves cell adhesion of progenitor cells. Typically polylactide surfaces are modified structurally through microtexture, adsorption of adhesive proteins, or chemical modifications, to enhance cell adhesion²³⁻²⁵. The results suggest the 8-grooved architecture of the wicking fibers promote the adhesion of cells. This outcome may be a result of the hydrophilic and transport properties of the polylactide wicking fibers and their ability to enhance the accumulation of extracellular matrix proteins providing a favorable environment for the progenitor cells to adhere²⁶.

The outcomes assessing cell viability and proliferation suggest the wicking fibers improve both cell viability and proliferation of chronOS strip scaffolds. The Live/Dead results showed the wicking fibers significantly improved the amount of viable cells in the scaffold as well as a significant reduction in the percentage of dead cells in the interior central region of the scaffolds. These results suggest the wicking fiber bundles increase

mass transport and cells to the central region of the scaffold due to the increased porosity, micro-sized conduits, and increased surface area architecture. The ViaCount assay quantified the number of viable and dead cells after days 1, 3, 7 and 10 and PicoGreen assay assessed proliferation after days 4 and 7. The outcomes showed a significant increase in viable cells initially after a week of culture and increase in cell proliferation after Day 4. This suggests the wicking fiber may provide enhanced mass transfer both initially and long-term.

The effect of wicking fibers on osteogenic differentiation of pre-osteoblast cells was investigated in this chapter. The RT-PCR results showed significantly higher expression of the early bone differentiation marker, RUNX2. No significant difference was observed for ALP, BMP-2, or osteocalcin. The ALP assay showed significantly higher activity for chronOS with fibers at the earlier time points. These outcomes suggest the scaffolds with fibers showed earlier differentiation than scaffolds without fibers. Furthermore, the immunohistochemistry results revealed high levels of expression of BMP-2 and osteopontin for chronOS scaffolds containing fibers after days 7 and 14. These results also indicate that differentiation may occur faster in scaffolds containing fibers and may improve the amount of bone formation. The limitation of this study was the scaffold size used. The chronOS strip samples used for this study were 1cm x 1cm x 0.6 cm (length x width x thickness) and completely submerged in media. Due to the small geometry used there may not be a significant mass transport deficiency to the central regions of the scaffold. Future work will investigate bone formation in larger scaffolds in a more physiologically relevant environment.

References

1. Johnson EO, Troupis T, Soucacos PN: Tissue-engineered vascularized bone grafts: Basic science and clinical relevance to trauma and reconstructive microsurgery. *Microsurgery* 2011; 31:176–82
2. Muschler GF, Nakamoto C, Griffith LG: Engineering principles of clinical cell-based tissue engineering. *The Journal of Bone and Joint Surgery* 2004; 86-A:1541–58
3. Bawa M, Schimizzi AL, Leek B, Bono CM, Massie JB, Macias B, Chung CB, Hargens AR, Garfin SR, Kim CW: Paraspinal muscle vasculature contributes to posterolateral spinal fusion. *Spine* 2006; 31:891–6
4. Tabbaa SM, Horton CO, Jeray K, Burg K: Role of vascularity in successful bone formation and repair. *Critical Reviews in Biomedical Engineering* 2014; 42:1–29
5. Kolk A, Handschel J, Drescher W, Rothamel D, Kloss F, Blessmann M, Heiland M, Wolff K-D, Smeets R: Current trends and future perspectives of bone substitute materials - From space holders to innovative biomaterials. *Journal of Cranio-Maxillo-Facial Surgery* 2012; 40:1–13
6. Neidlinger-Wilke C, Wilke H-J: *The Biology of Intervertebral Disc Degeneration, Surgery for Low Back Pain*. Edited by Szpalski M, Gunzburg R, Rydevik BL, Huec J-C Le, Mayer HM. Berlin, Heidelberg, Springer, 2010, pp 3–10doi:10.1007/978-3-642-04547-9
7. Brown CR, Boden SD: Fracture repair and bone grafting, *Principles of Orthopaedics: Orthopaedic Knowledge Update 9*. American Academy of Orthopaedic Surgeons, 2011, pp 13–22
8. Boden SD: Biology of lumbar spine fusion and use of bone graft substitutes: Present, future, and next generation. *Tissue Engineering* 2000; 6:383–99
9. Boden SD: Overview of the biology of lumbar spine fusion and principles for selecting a bone graft substitute. *Spine* 2002; 27:26–31
10. Morone M, Boden SD: Experimental posterolateral lumbar spinal fusion with a demineralized bone matrix gel. *Spine* 1998; 23:159–67
11. Louis-Ugbo J, Boden SD: *Biology of Spinal Fusion*, *Spine*. Edited by Bono C, Garfin S. Philadelphia, Lippincott Williams and Wilkins, 2004, pp 297–306
12. Toribatake Y, Hutton WC, Tomita K, Boden SD: Vascularization of the fusion mass in a posterolateral intertransverse process fusion. *Spine* 1998; 23:1149–54

13. Giannicola G, Ferrari E, Citro G, Sacchetti B, Corsi A, Riminucci M, Cinotti G, Bianco P: Graft vascularization is a critical rate-limiting step in skeletal stem cell-mediated posterolateral spinal fusion. *Journal of Tissue Engineering and Regenerative Medicine* 2010; 4:273–83
14. Cinotti G, Corsi A, Sacchetti B, Riminucci M, Bianco P, Giannicola G: Bone ingrowth and vascular supply in experimental spinal fusion with platelet-rich plasma. *Spine* 2013; 38:385–91
15. Reichert J, Hutmacher D: Bone Tissue Engineering, *Tissue Engineering: From Lab to Clinic*. Edited by Pallua N, Suschek C. Berlin, Heidelberg, Springer, 2011, pp 431–56
16. Hutmacher DW: Scaffolds in tissue engineering bone and cartilage. *Biomaterials* 2000; 21:2529–43
17. Karande TS, Ong JL, Agarwal CM: Diffusion in Musculoskeletal Tissue Engineering Scaffolds: Design Issues Related to Porosity, Permeability, Architecture, and Nutrient Mixing. *Annals of Biomedical Engineering* 2004; 32:1728–43
18. Lee M, Wu BM, Dunn JCY: Effect of scaffold architecture and pore size on smooth muscle cell growth. *Journal of biomedical materials research. Part A* 2008; 87:1010–6
19. Mitsak AG, Kemppainen JM, Harris MT, Hollister SJ: Effect of polycaprolactone scaffold permeability on bone regeneration in vivo. *Tissue Engineering: Part A* 2011; 17:1831–9
20. Innocentini MDM, Faleiros RK, Pisani R, Thijs I, Luyten J, Mullens S: Permeability of porous gelcast scaffolds for bone tissue engineering. *Journal of Porous Materials* 2009; 17:615–27
21. Dias MR, Fernandes PR, Guedes JM, Hollister SJ: Permeability analysis of scaffolds for bone tissue engineering. *Journal of Biomechanics* 2012; 45:938–44
22. Ramay HR, Zhang M: Preparation of porous hydroxyapatite scaffolds by combination of the gel-casting and polymer sponge methods. *Biomaterials* 2003; 24:3293–302
23. Ho M-H, Hou L-T, Tu C-Y, Hsieh H-J, Lai J-Y, Chen W-J, Wang D-M: Promotion of cell affinity of porous PLLA scaffolds by immobilization of RGD peptides via plasma treatment. *Macromolecular Bioscience* 2006; 6:90–8

24. Liu H-C, Lee I-C, Wang J-H, Yang S-H, Young T-H: Preparation of PLLA membranes with different morphologies for culture of MG-63 Cells. *Biomaterials* 2004; 25:4047–56
25. McGlohorn JB, Holder WD, Grimes LW, Thomas CB, Burg KJ: Evaluation of smooth muscle cell response using two types of porous polylactide scaffolds with differing pore topography. *Tissue Engineering* 2004; 10:505–14
26. Matsuzaka K, Walboomers XF, Ruijter JE De, Jansen JA: The effect of poly-L-lactic acid with parallel surface micro groove on osteoblast-like cells in vitro. *Biomaterials* 1999; 20:1293–301

CHAPTER FOUR

IMPROVING CELL SEEDING OF LARGE SCAFFOLDS

Introduction

Another limitation of bone scaffolds is effective cell seeding. This includes cell distribution as well as cell viability in all regions of the scaffold. Large scaffolds are limited by the ability of cells to fully penetrate scaffolds and retain cell viability. Researchers have well established these limitations with large scaffold and have shown viable cells to proliferate only on the periphery of the scaffold approximately 250 to 500 μm from the interface of fluid and the scaffold *in vitro* or the vascular source and implant *in vivo*¹. The architecture of bone scaffolds is designed to provide a network for cells to proliferate, migrate, and develop matrix. As cells proliferate and form matrix within the scaffold, nutrients are diminished in the interior of the scaffold and the developed matrix provides a barrier for diffusion. Cells remain along the peripheral regions where sufficient nutrients and biomolecules are diffusing. This leads to viable tissue along the peripheral regions of the scaffold and limited tissue formation in the interior. Karande and coworkers describe this process as an “M&M effect”². This analogy correlates the hard shell of the M&M candy with the peripheral tissue formation and the soft interior of the candy with the lack of formation of tissue in the center. Furthermore, researchers have correlated cells in different spatial regions of the scaffold alter the diffusion profile of nutrients, oxygen, and waste products leading to non-homogeneous tissue formation³. Adequate cellular distribution and viability in large scaffold is dictated by the scaffold architecture, vascularization, porosity, and other factors discussed in Chapter 2. However,

just as importantly, the sufficient uniform cellular seeding with high cellular infiltration plays a critical role in homogeneous bone formation.

Various cellular seeding methods have been explored by previous work conducted in our lab as well as by numerous researchers in the field^{1,4,5}. Typically, cell seeding approaches are described as static, perfusion, or dynamic techniques. Static techniques are the most commonly used and typically involve direct surface seeding and spinner flask seeding methods. Table 4.1 shows the outcomes of using various seeding methods.

Table 4.1: Limitations of various cell seeding strategies

Approaches to improve cell seeding	Outcomes	Reference
Oscillating Perfusion Bioreactors	Perfusion improves the cell distribution compared to static approaches	Wendt. et al. 2003 ³
Orbital shaker seeding	Homogeneous distribution on surface but distribution interior depends on scaffold	Thevenot et al. 2008 ⁵
Static seeding	Homogeneous distribution on surface with limited cell penetration	Thevenot et al. 2008 ⁵
Low pressure vacuum	Vacuum seeding showed less homogeneous	Buizer et al. 2014 ⁶

The effectiveness of seeding methods can vary based on scaffold type, which is defined by the architecture, porosity, overall size, and pore size⁷. The aim of this chapter is to modify the chronOS strip using a passive transport system to more effectively distribute high densities of cells homogeneously on the surface and interior of the

scaffold. The chronOS strip is frequently augmented with bone marrow aspirate prior to implantation in the defect site. Typically the scaffolds are seeded with cells by injecting the scaffold with bone marrow aspirate (BMA). Synthes has developed a perfusion pack system to more effectively distribute cells from the BMA within the scaffold. The perfusion pack, shown in image below, is a vacuum-sealed system that allows the surgeon to inject and cycle BMA using a syringe.

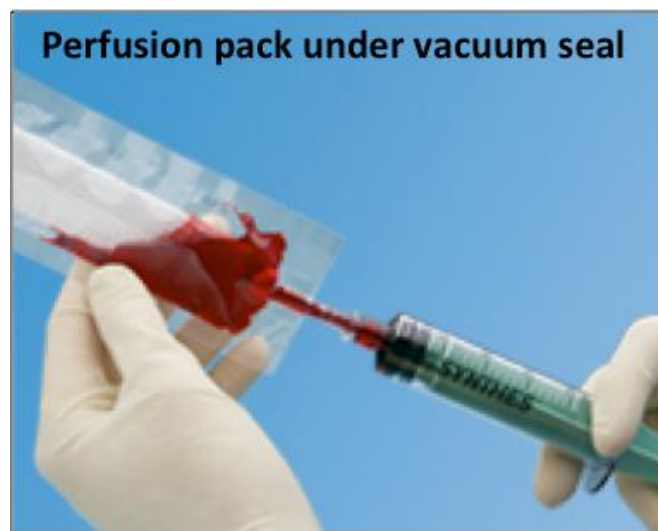


Figure 4.1: Synthes developed perfusion pack for chronOS strip (www.synthes.com)

Synthes Spine has conducted an *in vitro* study comparing the cell seeding of progenitor cells isolated from BMA by applying the cells with the perfusion pack seeding method or by the direct seeding method. The outcomes of this study showed no significant difference in cell viability between the two seeding methods, but around a 40% increase in cell count using the perfusion pack method. The distribution of cells was also analyzed in this study. Synthes showed the perfusion pack allowed more cells to

infiltrate the central region and bottom face of the scaffold compared to the direct seeding method. Although the perfusion method is better than direct application, the amount of cells on the top surface is still significantly greater than the amount of cells in the center and bottom surface of the scaffold as shown from the fluorescent images below captured in this study.

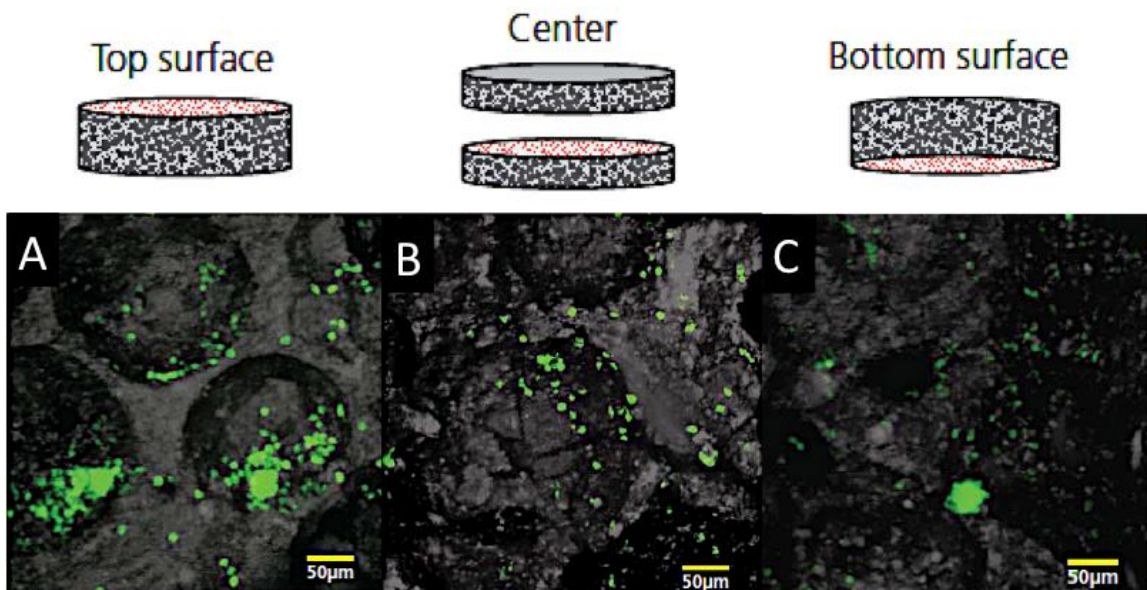


Figure 4.2: Results from Synthes in vitro assessment of the perfusion pack seeding. (A) Top surface of scaffold shows significantly more cells than the central region (B) and bottom surface of the scaffold (C)

The limitations of the current cell seeding systems have motivated the development of this system that has the potential to be incorporated into other large dense scaffolds with limited mass transport and cell infiltration. The objective of this study was to develop and evaluate if our proprietary passive transport system, comprised of bundled wicking fibers and an absorbent alginate cap (referred to as a “**modified wicking bundle**”) will improve

cell seeding efficiency of the chronOS strip samples. The wicking fiber and absorbent cap construction mimics a passive pump that creates an intrinsic cell seeding system within the scaffold. The absorbent cap component provides high absorption that enhances transport through the wicking fiber bundles and provides a sink to direct and collect progenitor cells. Each hydrogel cap encloses one end of the wicking fiber bundle. The cap increases the volume, rate, and duration of the transported liquids and cells. The first phase of this chapter characterized and assessed the fluid transport properties of the modified wicking bundle, as well as, the ability of this system to transport biomolecules and progenitor cells. The second phase of this chapter involved the development of a vacuum-sealed perfusion pack to assess the perfusion cell seeding efficiency in (1) chronOS strip samples containing the modified wicking bundle (referred to as a “**modified chronOS strip**”) and (2) unmodified chronOS strip scaffolds. To assess cell seeding, assays were performed investigating cell viability, proliferation, and count in varying locations of the scaffolds.

Characterizing the Modified Wicking Fiber Bundle

Fluid Transport Tests

Production of the Modified Wicking Bundle

Poly-L-lactide (Natureworks LLC, USA) wicking fibers were extruded with irregular cross-sectional dimensions of 0.72 mm by 0.55 mm and poly-L-lactide round fibers were extruded with cross-sectional diameter of 0.5 mm. Wicking fibers were sliced with razor blade into individual single wicking fibers of 10 cm lengths. The 10 cm wicking fibers were used to form wicking fiber bundles. Ten individual fibers were twisted, using

an apparatus, at 11 rotations per centimeter twist. The bundle was sliced into 10 cm, 2 cm, and 3 cm long sections. Single and bundled wicking fibers were cleaned by soaking in three changes of ethanol for 1 hour each, and placed under ultraviolet light for 6 hours. Samples were then soaked in a phosphate-buffered saline (PBS, Invitrogen) solution for 2 hours and air-dried overnight in a sterile hood. The alginate cap was formed by dipping one end of the wicking fiber bundle in 100 μ L of 5M CaCl_2 solution (Fisher Scientific; Waltham, MA, USA) in a well of a 96-well plate and pipetting 100 μ L of 1.4% (w/v) alginate solution, comprised of alginic acid sodium salt from brown algae (Sigma; St. Louis, MO) in 155 mM NaCl (Sigma; St. Louis, MO), directly on the submerged fiber tip in the well. The alginate immediately adheres to the fiber end and solidifies forming the modified fiber construct shown below.

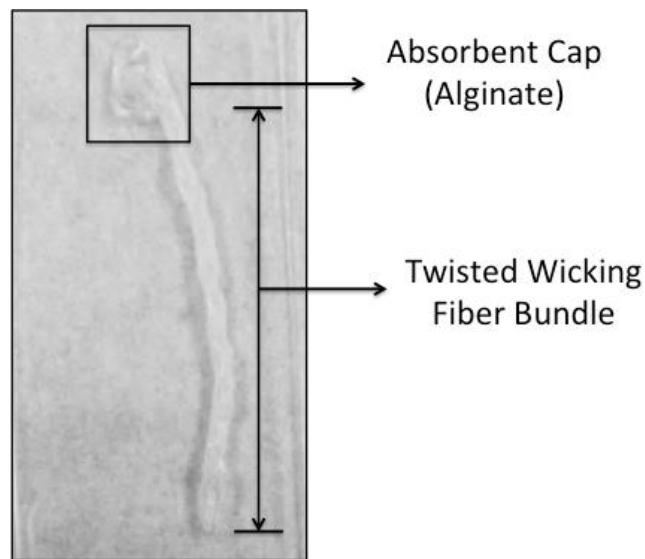


Figure 4.3: Modified wicking bundle comprised of 1.4% alginate hydrogel cap and a wicking fiber bundle

Wicking Tests of Modified Wicking Bundle

The wicking behavior of the modified wicking bundles were assessed using the vertical test methods introduced in Chapter 2. The first test assessed the wicking rate of modified and unmodified wicking fiber bundles by evaluating the change in mass of the fluid reservoir over regular time intervals depicted in image A of Figure 4.4. The second test (image B) investigated the amount of fluid absorbed in modified and unmodified wicking bundles after 12 and 24 hours by measuring the volume of fluid remaining in the well. The final test assessed the wicking capabilities of the modified wicking bundles, unmodified wicking bundles, and unmodified round bundles by recording the wicking height of the fluid front moving vertically upward along the fiber at various time points shown in image C.

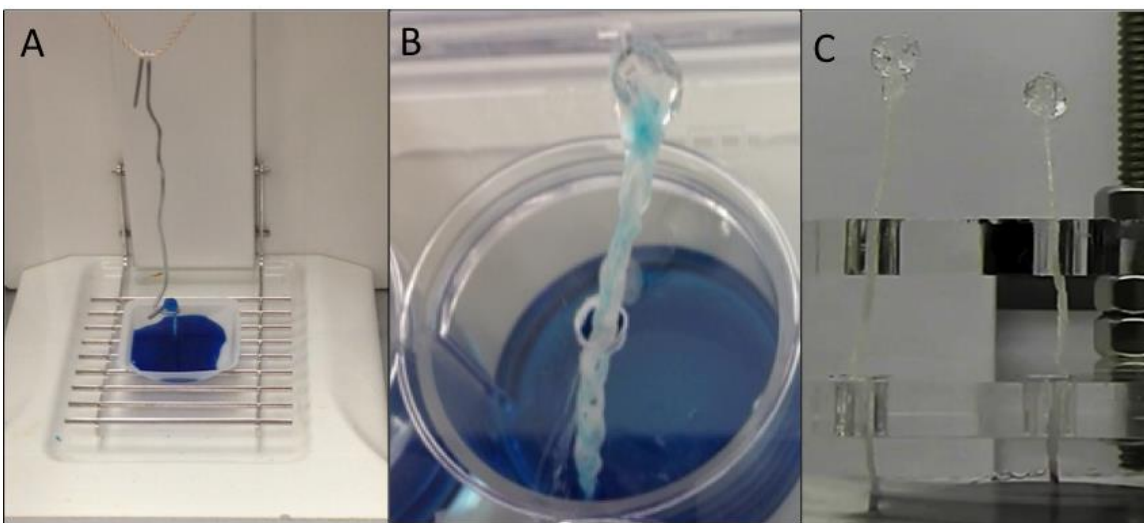


Figure 4.4: Wicking behavior tests. (A) Assessing the change in mass over various time intervals. (B) Measuring fluid absorbed after 12 and 24 hours in modified and unmodified fiber bundles (C) Measuring fluid height front every minute for a 10 minute interval.

Both tests methods were used to evaluate the wicking capabilities of round and wicking fibers. The experimental groups are described in table below.

Table 4.2: Experimental groups of twisted bundle configurations for round and wicking fibers

Experimental Groups	Fiber Type	Bundle Configuration	Number of Fibers in Bundle
1	Round	Twisted bundle	10
2	Modified Wicking	Twisted bundle	10
3	Unmodified Wicking	Twisted bundle	10

Vertical Test 1 – Fluid Height Assessment

One end of the various 10 cm long fiber bundles was placed in a dye-solution reservoir and held vertical using a custom-made apparatus shown in Figure 4.4 image C. The bundles were dipped in the reservoir to assess the wicking height of the dye-solution comprised of phosphate buffered saline (PBS, Invitrogen) and 10% blue assorted food coloring (McCormick). The fluid front vertical displacement of each sample was measured every minute for a 10 minute interval. The capillary rise rate of the fluid front was determined for each sample.

Vertical Test 2 – Volume of Fluid Absorbed

The amount of fluid absorbed in modified and unmodified wicking bundles was determined after 12 and 24 hours. Samples were vertically placed in individual wells of a 12-well plate with 1 mL of dye-solution, 10% blue assorted food coloring in PBS, using a

custom lid to hold the samples vertical. After 12 and 24 hour time points the bundles were removed and the amount of fluid remaining was measured.

Vertical Test 3 – Wicking Rate Assessment

To determine the change of mass in the liquid reservoir over time, the balance was connected to the computer using a USB to RS232 cable. PuTTY software was used to connect to the serial port and transfer information from the balance to the computer. The balance was programmed to continuously measure the weight of the reservoir at a rate of two measurements per second. After 10 minutes, the continuous function was stopped and the recorded data was saved as a text file and imported into Excel for further analysis. To measure the amount of fluid the bundles transported, the fibers were suspended so only the tip was interfacing the fluid. The wicking rate for each sample was calculated from the mass (mg) by time (minutes) plot. The average wicking rate was determined in one minute intervals (0-1 minutes, 1-2 minutes, and 2-3 minutes) to determine the average instantaneous wicking rate. The change in wicking rate was determined by plotting the instantaneous wicking rate at each time point.

Statistical Analysis

JMP 10 software was used to conduct an unpaired two-sample t-test to compare the average volume of liquid drawn out of the reservoir by modified and unmodified wicking bundles at 12 and 24 hours using a significance level of $p < 0.05$. The same analysis was used to compare the change in wicking rate of unmodified and modified wicking bundles using a significance level of $p < 0.05$.

Results

Vertical Test 1 – Fluid Height Assessment

Test 1 evaluated the fluid height change between experimental bundles over a 10 minute interval. The results presented in Figure 4.5 image A show the modified wicking bundles have a significantly greater wicking rate (change in height/time interval) compared to the unmodified wicking bundles and unmodified round bundles. The digital image (Image B) shows the enhanced fluid transport of the modified wicking bundle (left) compared to the unmodified (right).

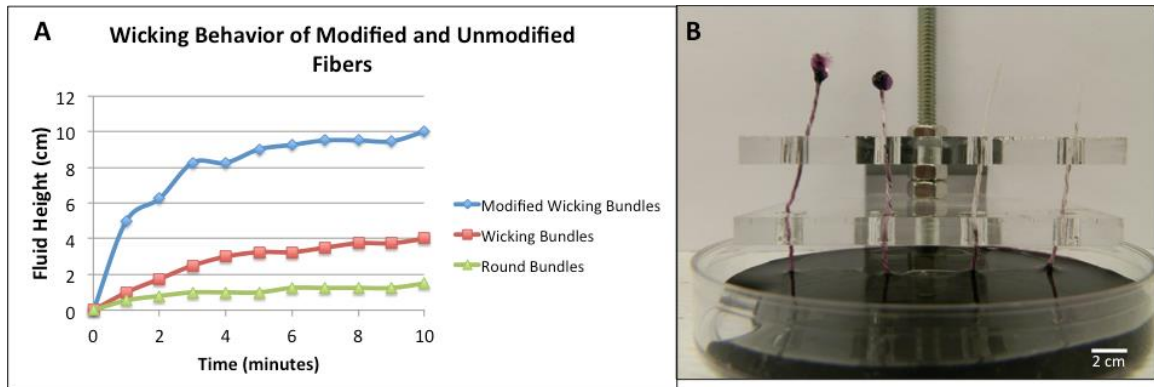


Figure 4.5: (A) The modified wicking bundle depicts the greatest change in fluid front height over a 10 minute interval (B) Modified wicking bundles on left depicts significantly greater fluid absorption and fluid height than unmodified wicking fiber bundles on the right

Vertical Test 2 – Volume of Fluid Absorbed

The second test evaluated the amount of fluid absorbed by the modified and unmodified wicking bundles. The modified wicking bundles absorbed significantly more fluid after 12 and 24 hours compared to the unmodified (Image A below). Digital images

after 5 minutes and 12 hours qualitatively show significantly more fluid transport in modified wicking bundles.

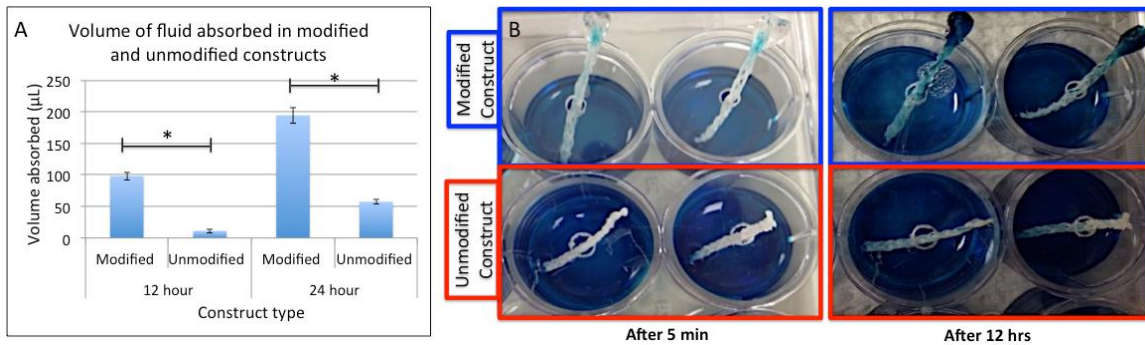


Figure 4.6: (A) Modified wicking bundles absorb significantly more fluid after 12 and 24 hours than unmodified () indicates significant difference of $p < 0.05$ (B) Qualitatively illustrates enhanced fluid absorption by modified wicking bundles after 5 minutes and 12 hours*

Vertical Test 3 – Wicking Rate Assessment

The final test investigated the change in wicking rate of modified and unmodified wicking bundles. The linear plot of the wicking rate versus time (Figure 4.7) shows the modified bundles have an acceleration of 0.2934 mg/min^2 with increasing wicking rate over time and the unmodified wicking fiber bundles show a deceleration of 0.4022 mg/min^2 .

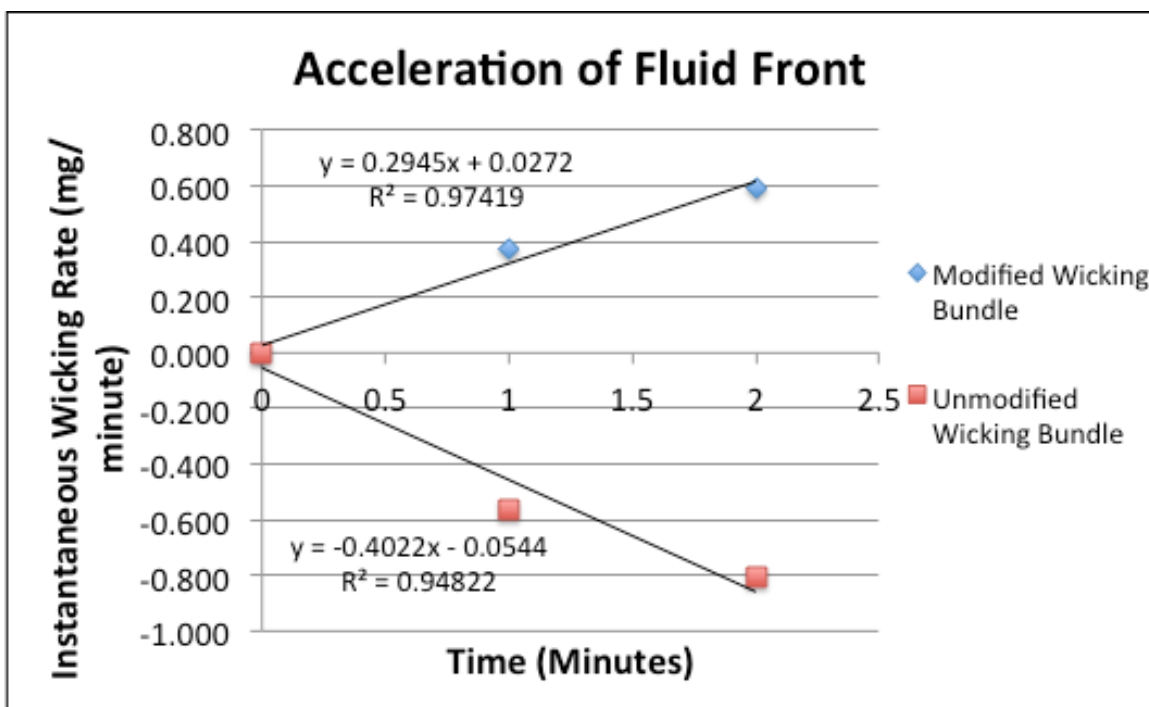


Figure 4.7: Plot of the change in wicking rate over a 3 minute time interval. Modified wicking bundles show an increasing wicking rate over time

Unimolecular Diffusion of FITC-Conjugated Bovine Serum Albumin in a Hydrogel

Protein movement in a 3D system was evaluated by analyzing the unimolecular diffusion of FITC-conjugated bovine serum albumin (Sigma; St. Louis, MO, USA) in a composite hydrogel containing modified wicking bundles, unmodified wicking bundles, or no fibers.

Using the methods described in chapter 2, a 50:50 collagen-agarose hydrogel was formed in half of an individual well on a 2-well chamber slide by turning the chamber slide on its side and loading it with 1 mL of collagen-agarose solution. Three modified wicking bundles (2 cm in length), unmodified wicking bundles (2 cm in length), or no

fibers were placed vertically in the center of the hydrogel while the chamber slide was on its side and before the hydrogel solidified, as shown in image A of (Figure 4.8).

Following hydrogel solidification, 1 mL of 100 μ g/mL solution of FITC-conjugated bovine albumin and serum free medium was pipetted into the section of the chamber well without the hydrogel, as shown in Figure 4.8.

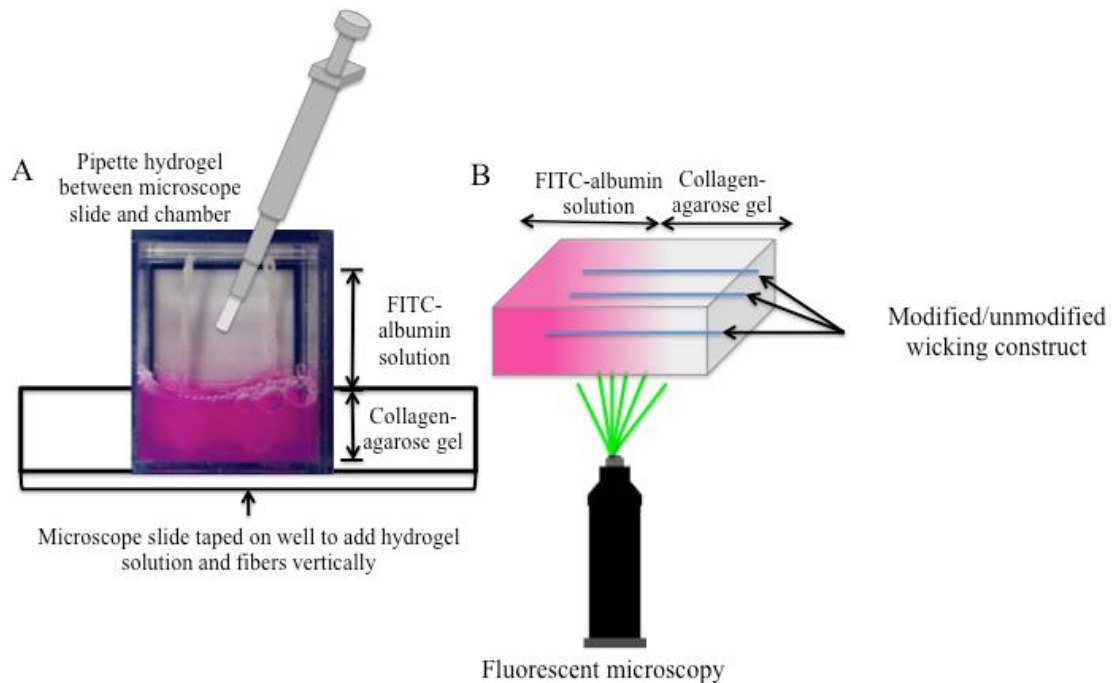


Figure 4.8: Schematic of experimental set-up of collagen-agarose hydrogel containing modified or unmodified wicking bundles. (A) Digital image of rotated chamber well to apply hydrogel to half the well (B) Fluorescent microscopy to image diffusion of FITC-albumin into hydrogel using time-lapse

The rate of FITC-albumin diffusing horizontally through the different experimental groups was evaluated using time-lapse fluorescent microscopy (EVOS; Fluid Cell Imaging Station, Life Technologies); Image J imaging software was used to combine the 3D time-lapse images into a z-stack stack and measure the average intensity

of a 350x350 pixel square region of interest (ROI) for each time frame. The intensity was measured in 1 minute intervals for 30 minutes along the center image frame containing the fiber. The rate of FITC-albumin movement was determined in a ROI adjacent the interface of the collagen-agarose gel and FITC-albumin solution shown in the schematic below.

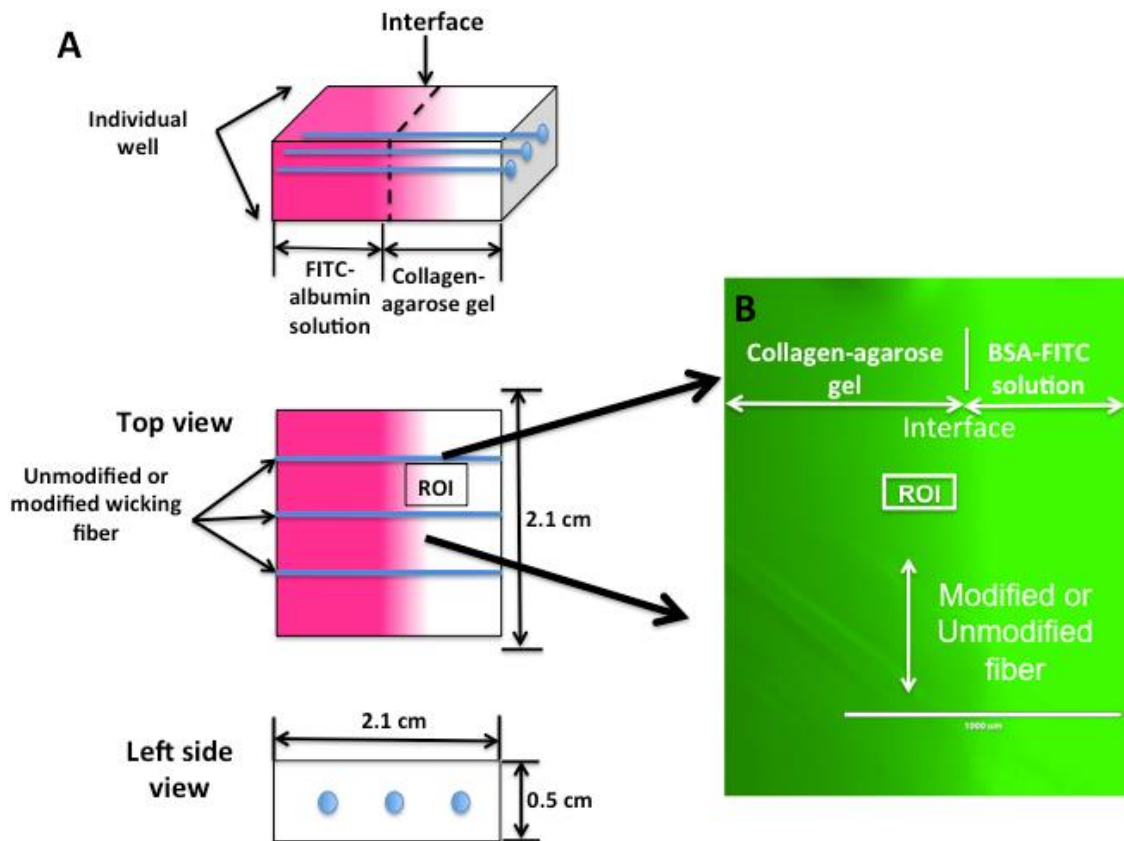


Figure 4.9: (A) Schematic of an individual well in a 2-well chamber slide filled partially containing with collagen-agarose gel containing either modified or unmodified wicking fiber bundles. The other portion of the well is filled with medium containing the BSA-FITC solution. (B) Image frame from time-lapse video of the BSA-FITC diffusion into the collagen-agarose gel. Average intensity was measured from labeled ROI adjacent to interface

Statistical Analysis

Statistical analysis was performed in JMP 10 using a Student's t-test to compare the average rate of protein movement between each treatment group using significance level of $p < 0.05$.

Progenitor Cell Transport through Modified Wicking Fiber Bundle

This study tested the ability of the modified wicking fiber bundles to transport progenitor cells by wicking phenomena. D1 mouse mesenchymal stromal cells (ATCC; Manassas, VA, USA) were cultured in Dulbecco's Modified Eagle's medium (DMEM, Invitrogen; Grand Island, NY, USA) supplemented with 10% fetal bovine serum (Gibco; Grand Island, NY, USA), 10,000 U penicillin, and 10 mg streptomycin/mL (Sigma; St. Louis, MO, USA). D1 cells were labeled with CellTracker™ Green CMFDA probe (Invitrogen; Grand Island, NY, USA), following the manufacturer's protocol using two different concentrations of 25 μ M and 0.5 μ M, to evaluate the movement of cells through modified and unmodified wicking bundles using fluorescent microscopy and flow cytometry (Guava EasyCyte™, Guava Technologies), respectively. The CellTracker Green label was optimized for flow cytometry use with D1 cells prior to performing this study (See appendix A for cell tracker optimization for flow cytometry study). Six poly-L-lactide modified (with alginate cap) and unmodified wicking fiber bundles were made using the wicking fiber of 3 cm lengths. Lids, with fitted holes and plastic tubes, were custom-made for the 12-well plate to securely hold the fiber bundles vertical. One million D1 cells tracked with 25 μ M were pipetted into 6 wells of a low attachment 12-well plate. The remaining 6 wells contained 1 million D1 cells of 0.5 μ M tracker concentration as

shown in the experimental set-up below Figure 4.10. Immediately following cell seeding the modified and unmodified wicking bundles were vertically placed into each well and secured by the custom-made lid.

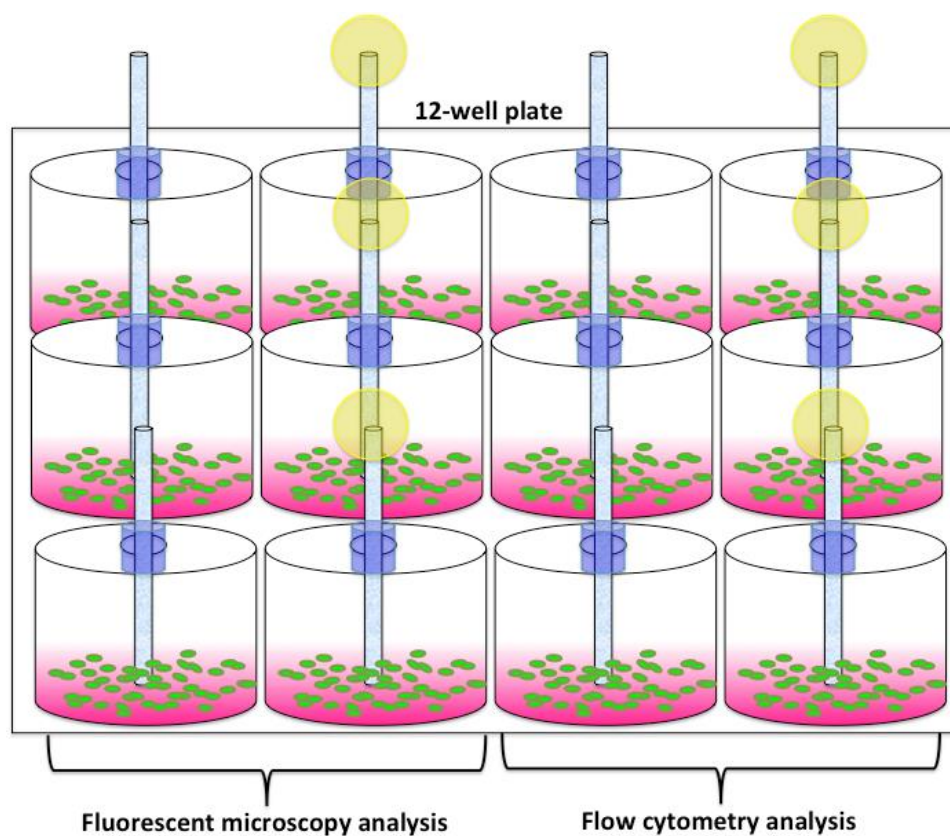


Figure 4.10: Schematic represents experimental set-up evaluating cell wicking in modified and unmodified wicking bundles

The vertical displacement of the cells along the unmodified and modified wicking bundles were determined after 1 hour with the initial time point being fiber placement into the cell solution. To assess the cell vertical displacement, the fibers were transferred to

microscope slides and were evaluated using fluorescent microscopy and imaging software. To quantify the cell recruitment into the fiber bundles, the cells were removed from the top and bottom regions of the samples. The bundles were sectioned with a blade and the top and bottom regions were placed into separate wells of a 24 well plate, Figure 4.11.

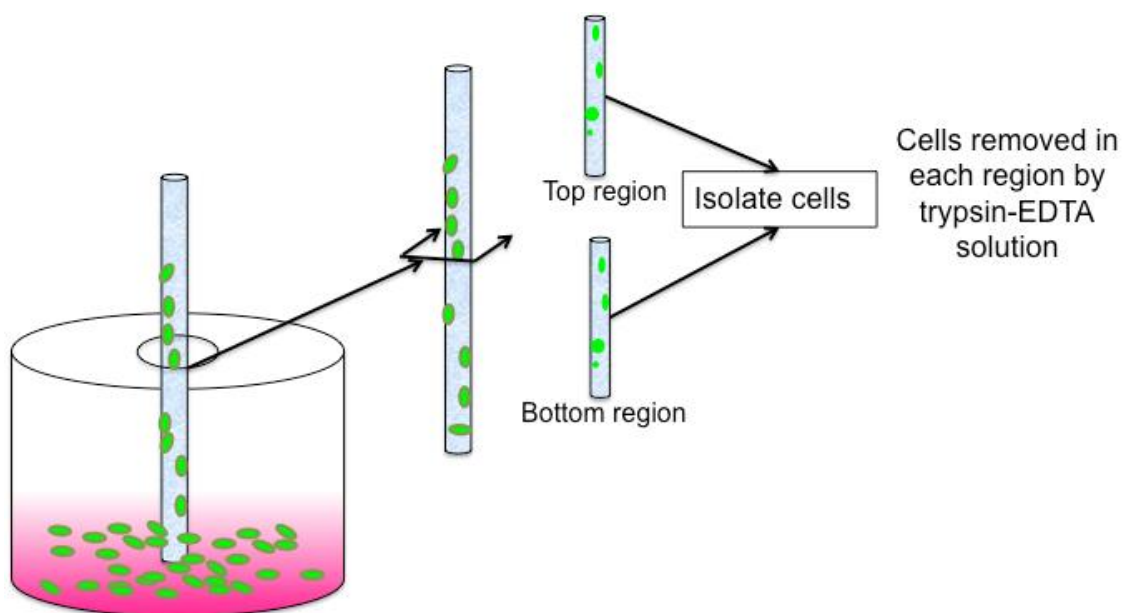


Figure 4.11: Schematic illustrating cell isolation from top and bottom regions of unmodified and modified wicking bundles

Samples were rinsed with PBS and untwisted. Cells were removed by adding 500 μL of trypsin-EDTA solution into the well with the fiber region and placing the plate on a flat-top (VWR) shaker at 200 rpm in a 37°C incubator. After 15 min the cells were diluted in 500 μL of growth media and the number of D1 cells in both regions of the constructs were evaluated using a Guava easyCyteTM flow cytometer (Guava

Technologies). The number of green-labeled D1 cells in each region was evaluated by following the manufacturer's instructions for InCyte software (Guava Technologies). D1 cells of known cell densities with and without green tracker, were used as positive and negative controls to calibrate the machine before measurements of the treatment groups were made.

Statistical Analysis

Statistical analysis was assessed using JMP 10 software. An unpaired two-sample t-test was conducted to compare the average cell count of D1 cells in the top and bottom regions of the unmodified and modified wicking fiber bundles using a significance level of $p < 0.05$.

Cell Recruitment in a Submerged System

This study investigated the ability of the modified wicking bundles to recruit fluorescently green-labeled D1 cells in a submerged system. D1 mouse mesenchymal stromal cells (ATCC; Manassas, VA, USA) were cultured in Dulbecco's Modified Eagle's medium (Invitrogen; Grand Island, NY, USA) supplemented with 10% fetal bovine serum (Gibco; Grand Island, NY, USA), 10,000 U penicillin, and 10 mg streptomycin/mL (Sigma; St. Louis, MO, USA). D1 cells were labeled with CellTracker™ Green CMFDA probe (Invitrogen; Grand Island, NY, USA), following the manufacturer's protocol using 25 μ M, to fluorescently image the movement of cells through the bundles.

Poly-L-lactide modified (with alginate cap) and unmodified wicking bundles (n=6) were made using 10 wicking fibers of 3 cm lengths. Samples were added to a well

of a low-attachment 6 well plate and submerged in 4 mL of growth media and incubated for 30 minutes at 5% CO₂ and 37°C on an orbital shaker. Following incubation 500µL of 500,000 fluorescently green-labeled D1 cells were pipette into each of the wells. After 12 hours of culture the samples were washed with PBS and fixed with 10% formalin.

Fluorescent microscopy was used to assess the cell infiltration and distribution in the top and bottom regions of the unmodified and modified constructs.

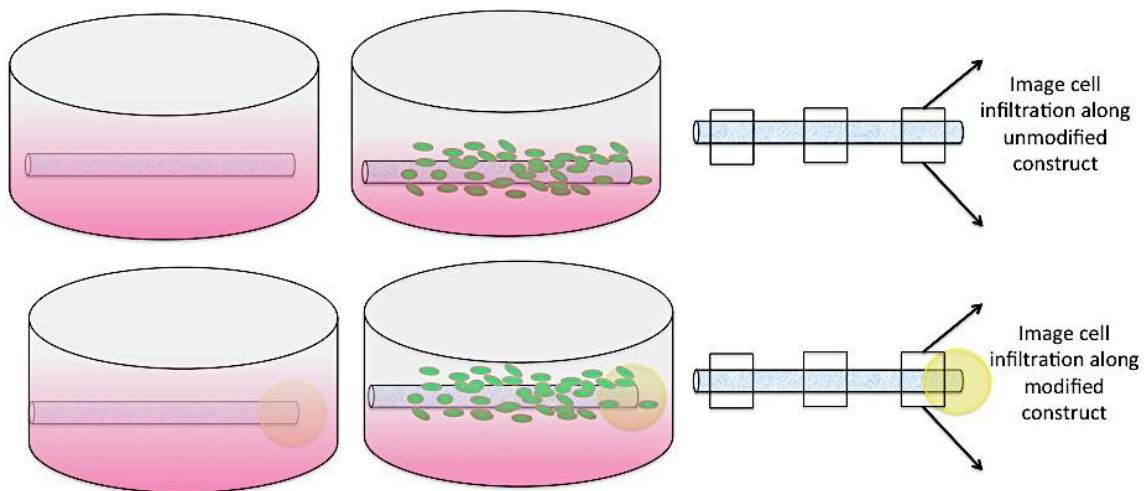


Figure 4.12: Experimental set-up to assess cellular infiltration in a submerged system. Modified and unmodified bundles were submerged in growth media in a 6-well culture plate. Cell solution was added to the wells after the samples were submerged. After 12 hours, the cellular recruitment was assessed by imaging various regions of the modified and unmodified bundles, depicted in schematic.

Results

Unimolecular FITC-albumin diffusion

The diffusion of FITC-albumin was analyzed in collagen-agarose hydrogels containing unmodified or modified wicking bundles, as well as control samples without

fibers. The plot depicted in Image A of Figure 4.13 shows the average intensity of modified wicking bundles was greatest compared to the other experimental groups over the 30 minute time-lapse interval. The results showed the rate of the FITC-albumin movement in hydrogels with modified wicking bundles was significantly ($p < 0.05$) greater than in the gels containing unmodified wicking bundles and hydrogels without fibers (Image B) **Error! Reference source not found..**

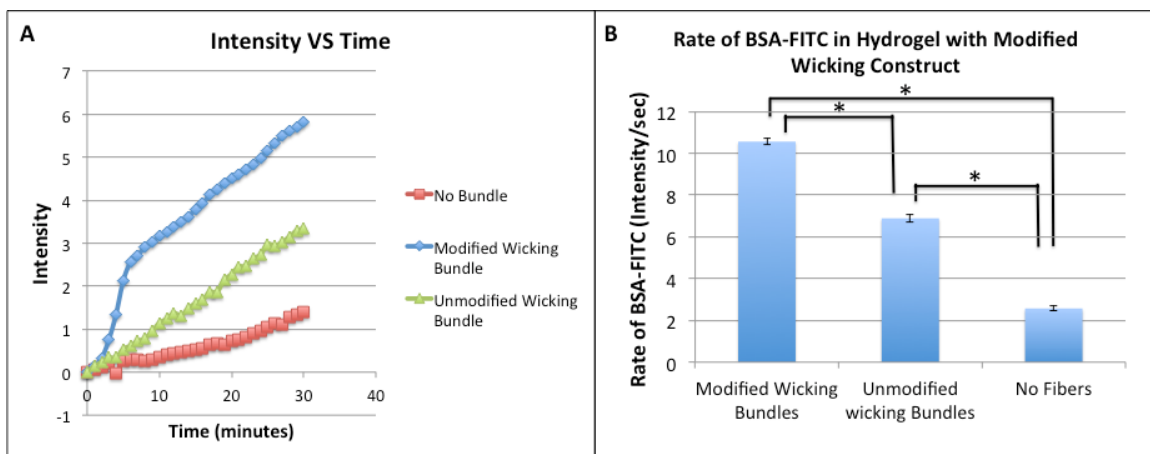
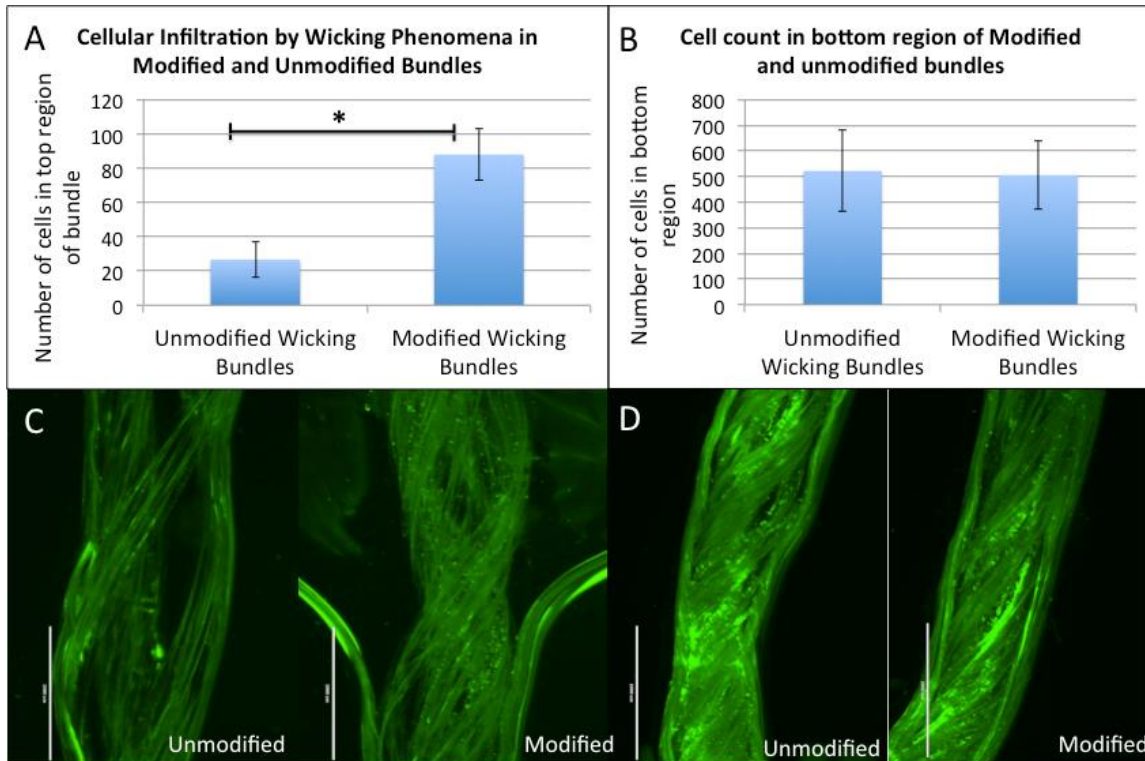


Figure 4.13: (A) Plot depicts the modified wicking fiber constructs show greatest increase in intensity over 30 minute time interval (B) Hydrogel containing modified wicking fiber constructs have significantly greater rate than samples with unmodified wicking fibers and samples without fibers; $*p < 0.05$.

Progenitor Cell Transport through Modified Wicking Bundle

Cell penetration by wicking phenomena was investigated in modified and unmodified wicking bundles. Both fluorescent microscopy and flow cytometry analysis (Image B and D) of bottom regions of samples showed similar cell densities in both construct types. The outcomes from cell isolation from the top regions showed

significantly more cell infiltration in the modified wicking bundles than in unmodified samples. The fluorescent images confirm the quantitative data and illustrate considerably more cell penetration in the top region of the modified wicking bundles.



*Figure 4.14: (A) Shows significantly more cells isolated from top regions of the modified wicking bundle than unmodified, $*p < 0.05$. (B) No significant cell count in bottom regions of bundles (C) Illustrates greater cell penetration in the top region of the modified wicking bundle (D) Qualitatively shows no significant difference in cell count in bottom regions*

Cell Recruitment in a Submerged System

Modified and unmodified wicking bundles were submerged in growth media to investigate if the modified wicking bundles would enhance cell infiltration in a fluid environment. The fluorescent images showed higher cell influx into the modified

wicking bundles than unmodified wicking bundles, shown in Figure 4.14. The modified wicking bundle depicted greater cell penetration in the fiber bundle region (image C) as well as in the absorbent component (image D).

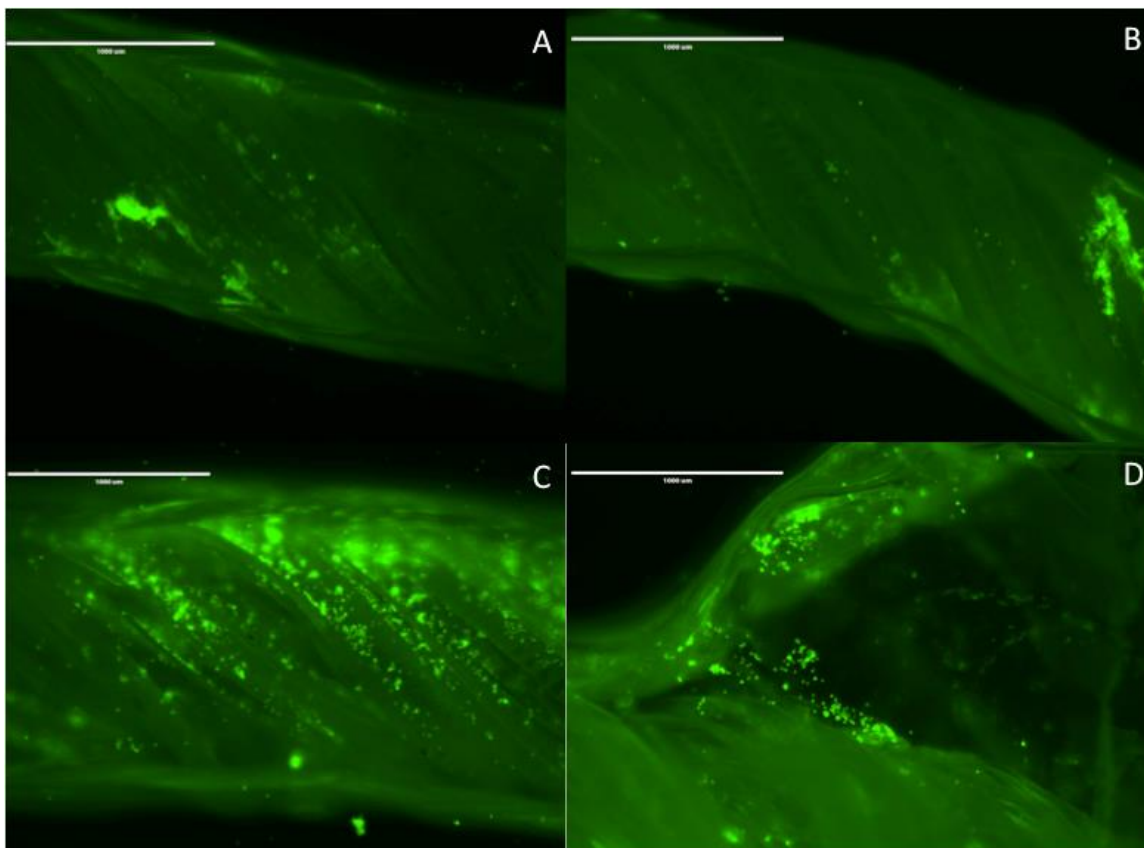


Figure 4.15: (A and B) Ends of unmodified wicking bundle show less cellular infiltration than (C) Modified wicking bundle end and (D) Alginate component

Cell Seeding Efficiency of Modified chronOS Strip

Development of Perfusion Pack

Six vacuum-sealed perfusion packs were custom-made using a Food Saver Vacuum Sealing System (V2244; Sunbeam Products; Boca Raton, FL). Heat seal pre-cut

bags (Food Saver; Sunbeam Products; Boca Raton, FL) were sliced into smaller 8 cm X 8 cm square plastic sheets. The ends of two square pieces were sealed along the edges of the perimeter leaving two sides open to add an injection valve on one side and add the sample through the other open edge. The injection valve was attached to the edge using a hot glue gun to completely seal the interface between the valve and the plastic sheets. The remaining edge containing the valve was heat sealed using the system. One edge was remained unsealed to add the chronOS strip samples and vacuum seal the pack using the system. Prior to use the perfusion packs were tested to confirm the sheets were sealed sufficiently and there were no air leaks.

chronOS strip samples (Synthes Inc.; West Chester, PA, USA) of length of 2.0 cm, width of 1.0 cm, and thickness of 0.60 cm were prepared by incorporating modified wicking bundles, (referred to as "**modified chronOS strips**"), N=30. To incorporate the modified wicking bundles, containing a wicking fiber bundle and alginate cap, two separate tunnels were drilled along the center region parallel to the long axis of the chronOS strip with diameter and length, 1.04 mm and 2.0 cm, respectively. Poly-L-lactide (Natureworks; LLC, USA) wicking fibers were extruded with non-circular cross-sectional dimensions of 0.12 mm x 0.05 mm. Two bundles containing ten wicking fibers, 3.0 cm in length, were securely fit through two separately drilled tunnels of the chronOS strip. The 1.4% alginate cap was formed on one end of both wicking fiber bundles. The wicking fiber bundle was dipped in 100 μ L of 5M CaCl₂ solution (Fisher Scientific; Waltham, MA, USA) in a well of a 96-well plate. Immediately following 100 μ L of 1.4% (w/v) (Sigma; St. Louis, MO) in 155 mM NaCl (Sigma; St. Louis, MO) was pipette

directly on the submerged fiber tip in the well. The alginate immediately adheres to the fiber end and solidifies forming the cap. ChronOS strip samples directly used out of packaging acted as the control (referred to as “**unmodified chronOS strip**”).

ChronOS strip samples, as well as the perfusion packs were cleaned by soaking in three changes of ethanol for 1 hour, and placed under ultraviolet light for 6 hours. After cleaning the samples were soaked in three changes of phosphate-buffered saline solution for 2 hours (Invitrogen; Grand Island, NY, USA) and allowed to air dry for 24 hours prior to vacuum sealing the samples in the perfusion packs. ChronOS strip samples were added through the unsealed edge of the perfusion pack and oriented in the central region of the pack below the inlet valve. Modified chronOS samples were positioned with the wicking fiber bundles facing the inlet and the alginate cap distal the valve. The perfusion packs were capped to prevent air from penetrating the packs and the unsealed edge was vacuum and heat-sealed using the food saver system. The vacuum-sealed samples in the perfusion packs are depicted below, Figure 4.16.

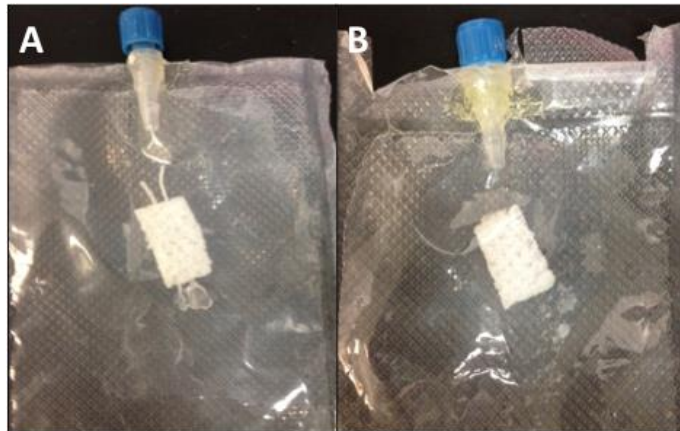


Figure 4.16: (A) Modified chronOS strip sample vacuum sealed with absorbent cap positioned distal the inlet valve (B) Unmodified chronOS strip vacuum sealed

ChronOS Cell Seeding and Experimental Set-up

MC3T3E1 Subclone 4, mouse preosteoblast cells, were cultured in a 150 cm² size area culture flask (Corning, Fisher Scientific) with growth media consisting of Minimal Essential Medium α without ascorbic acid (MEM α ; Gibco; Grand Island, NY, USA) supplemented with 10% fetal bovine serum (Gibco; Grand Island, NY, USA), 10,000 U penicillin, and 10mg streptomycin/mL (Sigma; St. Louis, MO, USA). Once the large culture flasks reached confluence the cells were split and resuspended in 30 mL of MEM α at a cell density of 500,000 cells per mL. A 10 mL Becton Dickinson (BD) disposable luer-lock syringe (Cole-Parmer; Vernon Hills, IL) was used to seed the scaffold in the perfusion packs. The syringe was filled with 5 mL of cell solution and inserted securely on the insertion valve immediately after removing the cap, Figure 4.17 (Image A). The cell solution was injected into the perfusion pack and the syringe was used to inject the cell suspension into the pack using 5 cycles of perfusion, following manufactures recommended instructions for infiltrating the chronOS strip scaffolds. Samples were incubated at room temperature for a clinically relevant waiting period of 60 minutes in the culture hood (Image B).

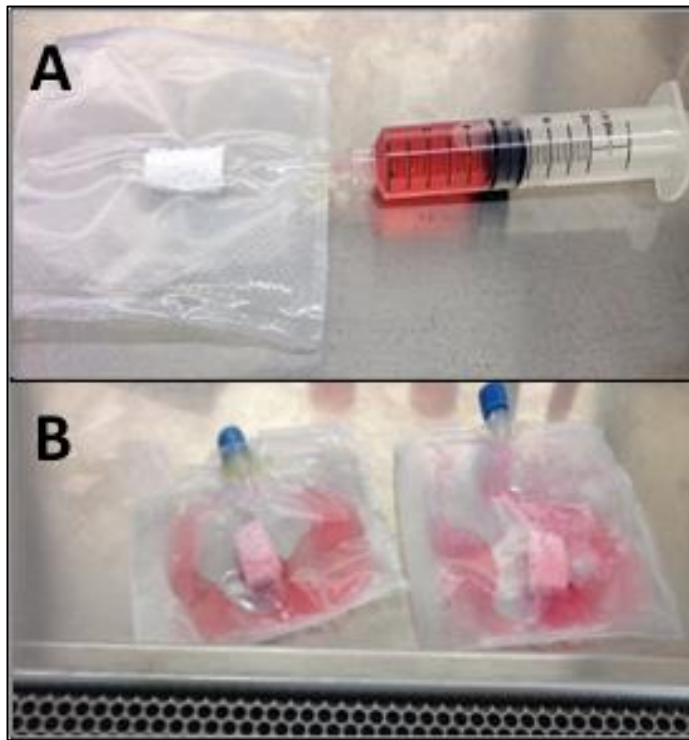


Figure 4.17: (A) Injected progenitor cell solution into vacuum-sealed perfusion pack through inlet valve (B) Incubated perfused samples with cell solution for 60 minutes at room temperature

After 60 minutes of incubation, cell infiltration, distribution, viability, and proliferation were assessed using the following assays shown in the Table 4.3

Table 4.3: Experimental set-up

	Live/Dead assay	ViaCount assay	PicoGreen assay	Cell Tracker Distribution	Cell Metabolic Activity	Dapi/Actin Distribution
Time Points	1 hour	1 hour	1 hour	1 hour	1, 24, 48, 72 hours	72 hours
Sample size	N=3	N=3	N=3	N=3	N=3	N=3

Cell Viability and Total Cell Count

Initial cell viability was qualitatively assessed using Live/Dead viability/cytotoxicity assay (Invitrogen; Grand Island, NY, USA) in the interior central and peripheral regions after 1 hour. Samples were bisected lengthwise to assess the viability of the samples in the central interior region. Two fluorescent probes, calcein AM and ethidium homodimer-1, were used according to manufacturer's protocol to determine live and dead cells in the samples, respectively. The sections were with washed with phosphate-buffered saline (PBS, Invitrogen, Grand Island, NY) and 500 μ L of 2 μ M calcein AM and 4 μ M of ethidium homodimer was added to each sample. After 45 minutes of incubation live and dead cells on the scaffolds were imaged using the fluorescein isothiocyanate (FITC) and tetramethyl rhodamine isothiocyanate (TRITC) filters, respectively, of the inverted fluorescent microscope (Zeiss Axiovert 135; Zeiss). The CCD camera (ProgRes C10plus; Jenoptik) was used to capture images. Image J processing was used to semi-quantitatively assess the number of live and dead cells in each sample and overlay the respective red and green channels of the images.

ViaCount assay using flow cytometry was used to quantify the number of dead and viable cells. Cells were removed from scaffolds by pipetting 1 mL of trypsin-EDTA solution (Sigma; St. Louis, MO, USA) into each well and placing the plate on a flat-top shaker set at 200 rpm in a 37°C incubator for 20 min. Following cell removal, the removed cells were resuspended in 1 mL of growth medium and diluted with ViaCount reagent in a 96-well plate (Guava Technologies, Hayward, CA, USA). The flow cytometer was calibrated using Guava Easy Check Kit (EMD Millipore, Billerica, MA,

USA). The ViaCount assay was conducted following the manufacturer's instructions. The ViaCount assay determines the total number of viable and non-viable cells based on a fluorescent dye that stains nucleated cells. The number of viable cells and total cell count was determined after the 1 hour time point.

PicoGreen Assay (Quanti-iT PicoGreen dsDNA Kit; Invitrogen) was used to determine the relative number of progenitor cells on each scaffold type by determining DNA concentration. After 1 hour chronOS strip samples were washed with PBS and 1 mL of 1X Tris-EDTA buffer was added to each sample. The samples were lysed by ultrasonication (Sonic Dismembrator, Fisher Scientific) for two 30-second cycles at 20 Hz. The lysate was collected and stored in microcentrifuge tubes. The double stranded DNA concentration in each lysate from both experimental groups was determined using the PicoGreen assay by following the manufacturer's protocol.

Cell Infiltration and Distribution

Cell distribution after 1 hour was evaluated by fluorescently labeling the MC3T3E1 preosteoblast cells with CellTracker Green CMFDA probe (Invitrogen; Grand Island, NY, USA), following manufacturer's protocol, using a long-term labeling concentration of 25 μ M, before seeding the chronOS strips with perfusion packs. After 1 hour of incubation the scaffolds were removed from the perfusion packs, washed with PBS, and fixed with 10% formalin for 20 minutes. Samples were sectioned in half along the longitudinal axis and the cell infiltration and distribution was evaluated in the central and peripheral regions of chronOS strips using fluorescent microscopy.

Cell distribution and proliferation was assessed after 72 hours by tagging the cells with nuclei and phalloidin molecular probes (Invitrogen). Following the 1 hour incubation period the samples were removed from the perfusion packs and placed in a 6-well plate. The samples were cultured for 72 hours at 37°C and 5% CO₂. After the 72 hour culture period the samples were washed with PBS and fixed with 10% formalin for 20 minutes. Formalin was removed and samples were further rinsed in PBS. To stain for actin and nuclei samples were blocked for 1 hour using blocking solution containing 2% BSA (Sigma; St. Louis, MO, USA), 5% goat serum (Sigma), and 0.1% triton X (ThermoScientific; Rockford, IL). Samples were washed with PBS and incubated in 500 µL of Alexa Fluor 488 phalloidin (Invitrogen; Grand Island, NY) solution using a 1:20 dilution for two hours at room temperature. Following the two hour incubation the phalloidin solution was removed and 1 mL of a 2mg/mL Hoechst 33342 solution (Thermo Scientific; Rockford, IL) of was added the samples at a 1:2000 dilution and incubated for 5 minutes at room temperature. Samples were rinsed with PBS and stored at 4°C. To analyze cell distribution and proliferation samples were transferred to a microscope slide and imaged using fluorescent microscopy (EVOS; Fluid Cell Imaging Station, Life Technologies); Image J imaging software was used to overlay images.

Cell Metabolic Activity

After 1 hour incubation, 1 mL of media from perfusion pack was removed from each sample to measure the amount of glucose consumption and lactic acid production using a YSI 2900 biochemistry analyzer (Yellow Springs Instruments; Yellow Springs, OH). Samples were removed from perfusion packs, transferred to a 6-well plate, and

cultured in growth medium for 72 hours. A volume of 1 mL was removed from the samples every 24 hours prior to a medium change for biochemical analysis. Samples without cells were also cultured in growth media and collected as negative controls for glucose and lactic acid concentrations. The YSI 2900 instrument was run according to manufacturer protocol and the glucose and lactic acid measurements from each time point were normalized to acellular controls.

Results

Cell Viability and Total Cell Count

The cell viability after 1 hour in modified and unmodified chronOS strip scaffolds was analyzed in the central plane of the scaffolds. Fluorescent images of viable (green) and dead cells (red) were obtained from the central and peripheral regions of the interior of the samples, shown in Figure 4.18. The Live/Dead fluorescent images of the peripheral regions of the modified chronOS scaffolds depicted more viable cells than unmodified chronOS strips, Figure 4.19. Similarly, the central regions also illustrated significantly more viable cells in the modified chronOS strip samples. The unmodified samples showed greater number of dead cells, especially in the central regions as shown in Figure 4.20.

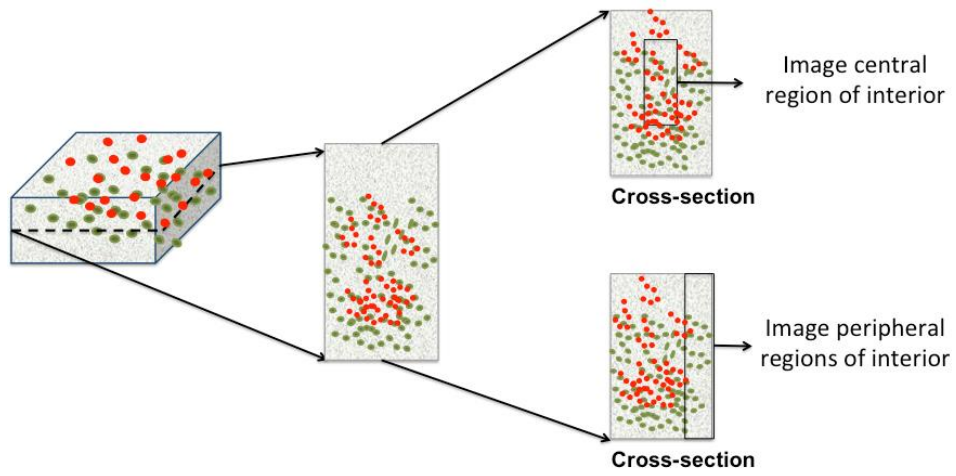


Figure 4.18: The interior cross-section of the modified and unmodified chronOS strip samples. Schematic illustrates central and peripheral regions along the cross-section

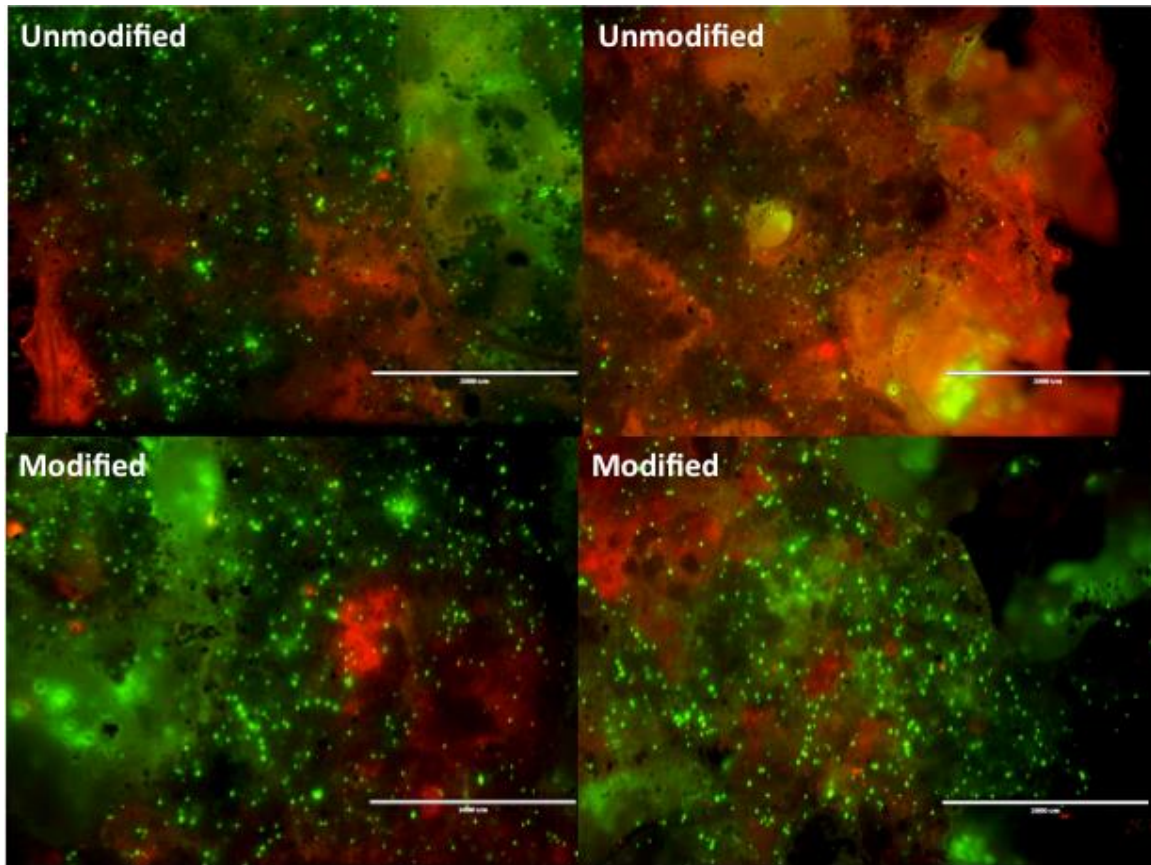


Figure 4.19: Composite images of viable (green) and dead (red) cells in modified and unmodified chronOS strip scaffolds. Illustrates more viable cells in modified chronOS strip samples

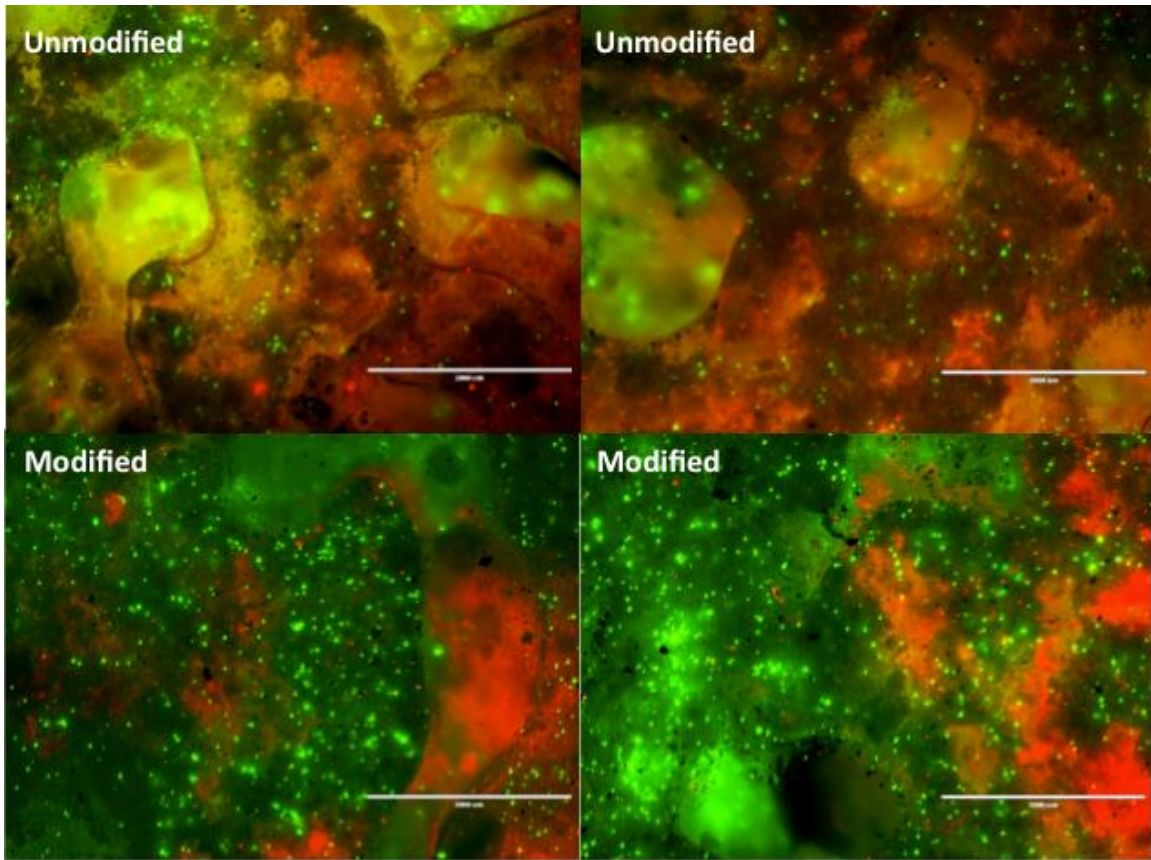


Figure 4.20: Unmodified chronOS scaffolds depict greater numbers of dead cells and fewer viable cells than modified chronOS strip samples

The incorporated modified wicking bundles (both the bundle and the alginate cap) were imaged to assess cell viability and recruitment of cells into the scaffolds. The fluorescent images, Figure 4.21, depict Live/Dead images. The schematic shows the regions where the fluorescent images were obtained along the bundle. The images illustrate high densities of viable cells along the wicking fiber bundle and in the alginate cap. The images suggest the modified wicking bundles significantly increase the amount of viable cells penetration the interior regions of the scaffold.

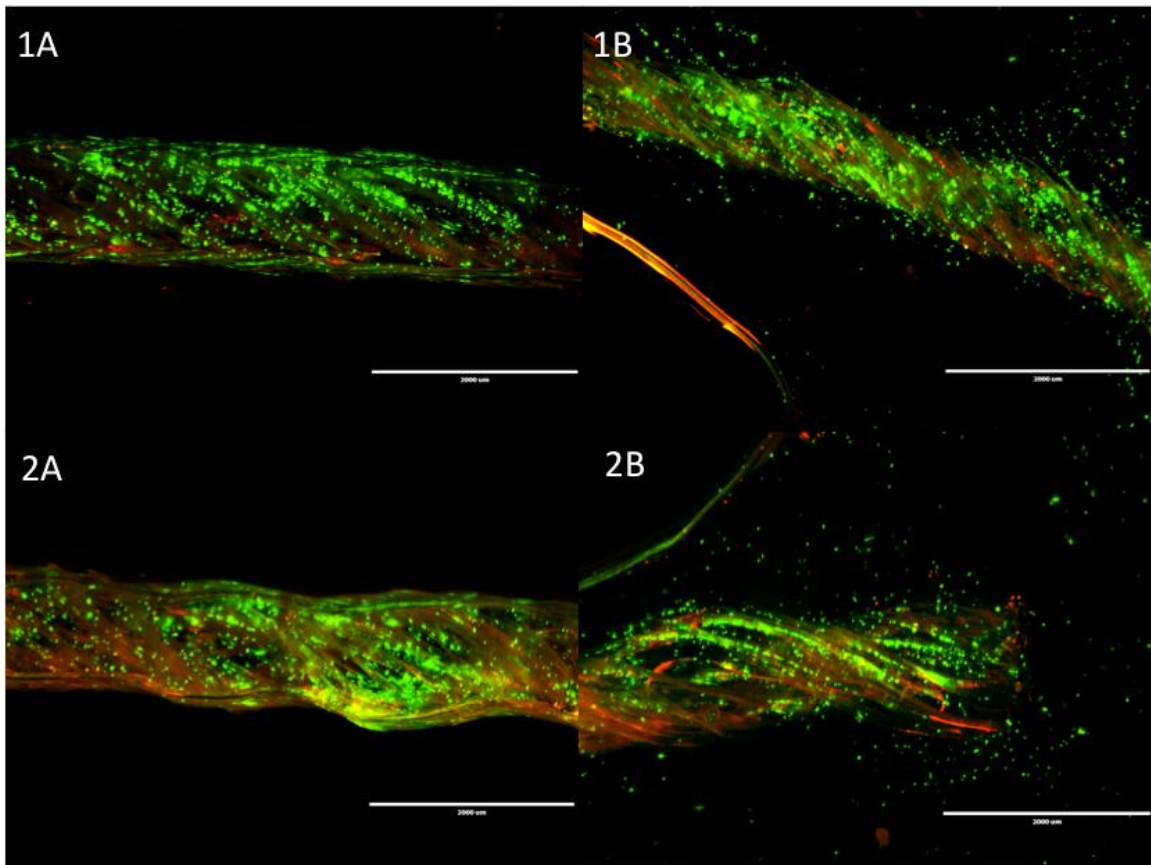
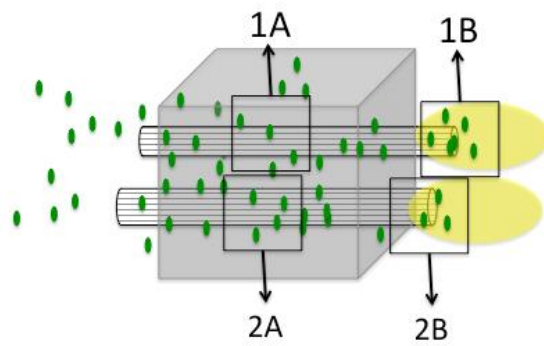


Figure 4.21: Schematic illustrations location of Live/Dead images along the modified wicking bundles in the chronOS strip scaffolds. The Live/Dead composite images illustrate significant cell penetration into the construct and high numbers of viable cells along the wicking fiber and alginate component.

Cell viability and total cell count was quantified using flow cytometry by removing cells from modified and unmodified chronOS samples. The outcomes showed the modified chronOS strip samples contained significantly more viable cells and total cells than the unmodified samples, Figure 4.22 (Image A).

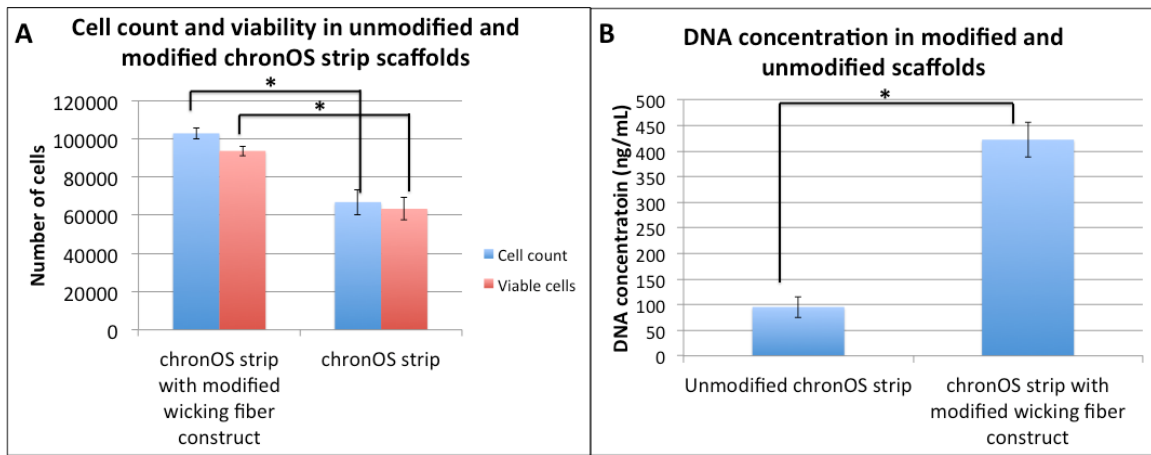


Figure 4.22: (A) Modified chronOS strip samples contained significantly more viable cells and total cell than unmodified samples, $*p < 0.05$. (B) Modified samples contained four times the amount of DNA isolated from unmodified samples, $*p < 0.05$

Cell Infiltration and Distribution

The modified and unmodified chronOS samples were perfused with fluorescently green-labeled progenitor cells. The cellular infiltration and distribution in both scaffold types was assessed with fluorescent microscopy. Cell densities and distribution were assessed in the central and peripheral regions of the cross-section. The central regions depicted in the fluorescent images below (Figure 4.23) show greater cell infiltration and more homogeneous distribution of progenitor cells in the modified chronOS samples than

the unmodified samples. The cell penetration and distribution in the peripheral regions of the modified scaffolds were similar to the unmodified scaffolds, Figure 4.24. Progenitor cell infiltration was also assessed in the modified wicking bundle that was incorporated into the modified chronOS strip scaffolds. Figure 4.25 depicts high progenitor cell recruitment into the modified wicking bundle.

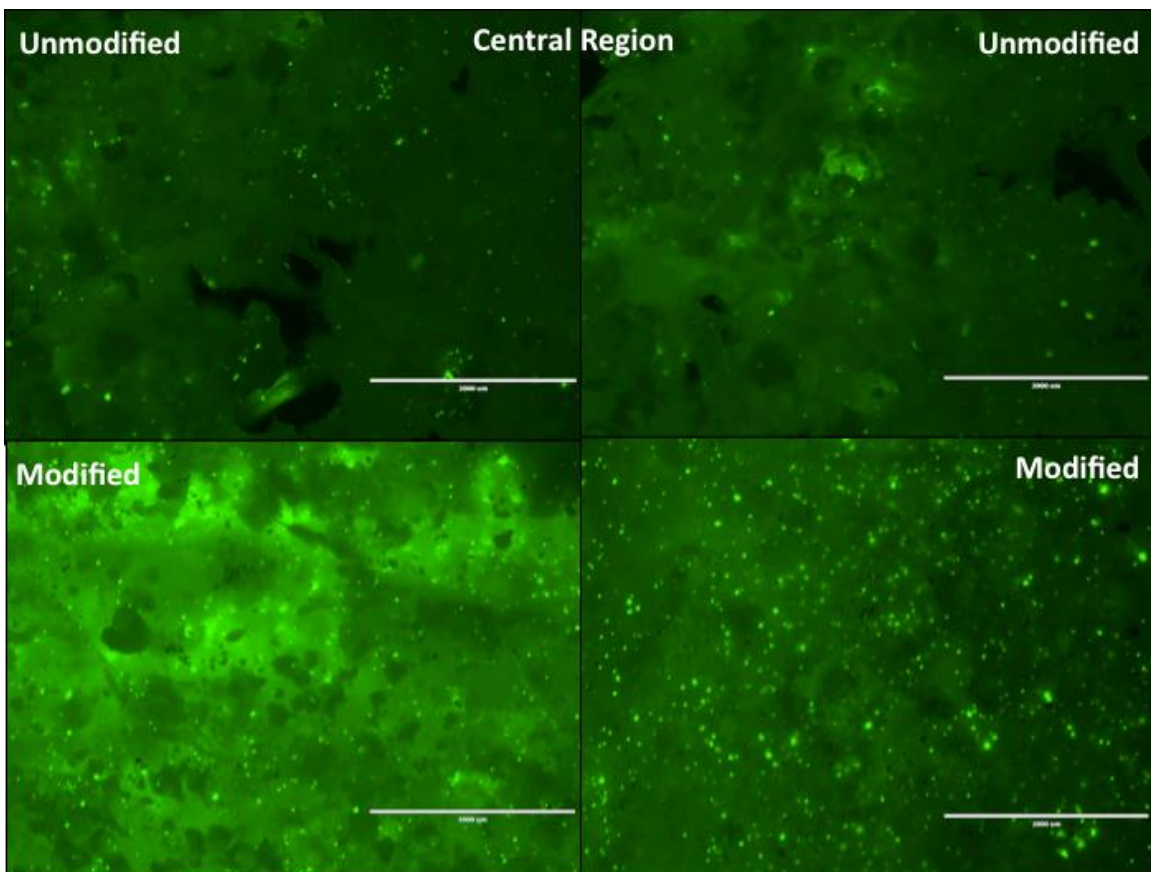


Figure 4.23: Central regions of the modified chronOS strip scaffolds depict greater cell penetration

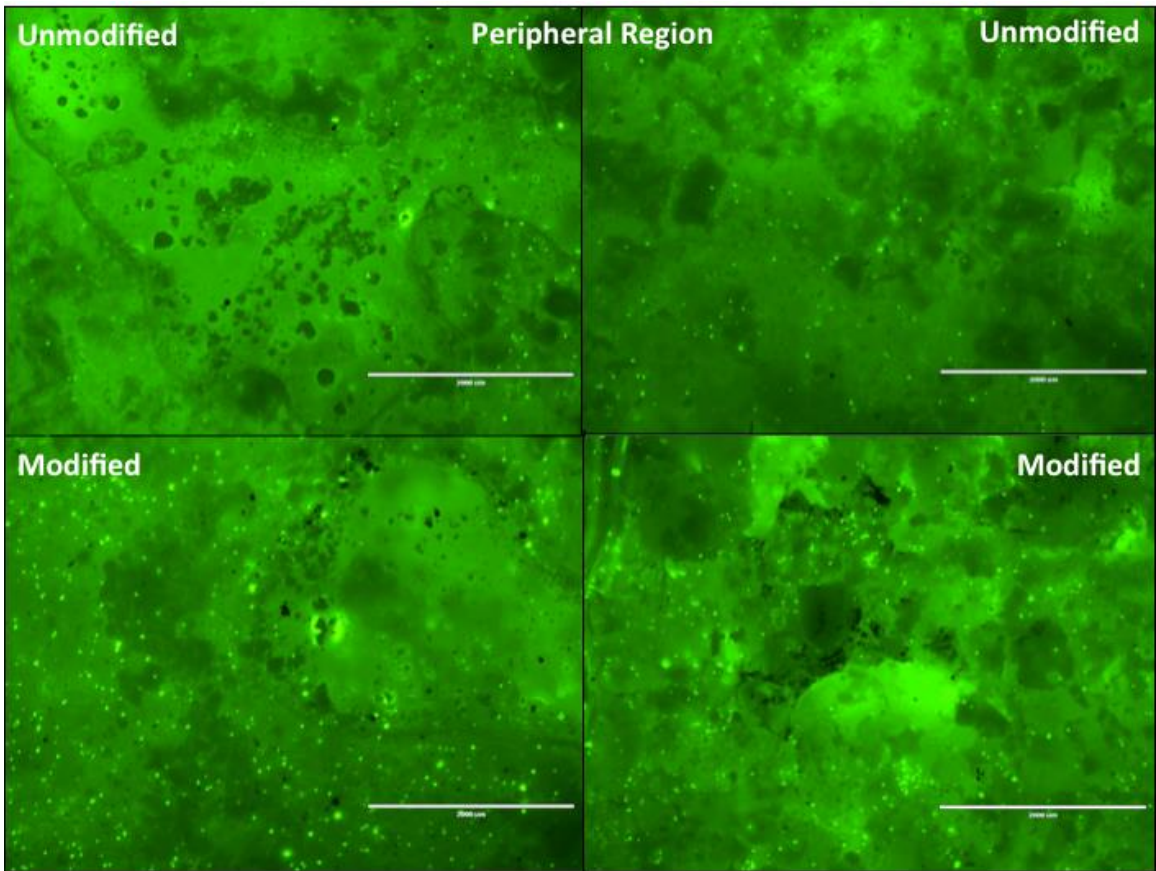


Figure 4.24: Peripheral regions of modified and unmodified chronOS strips show similar cell densities and distribution

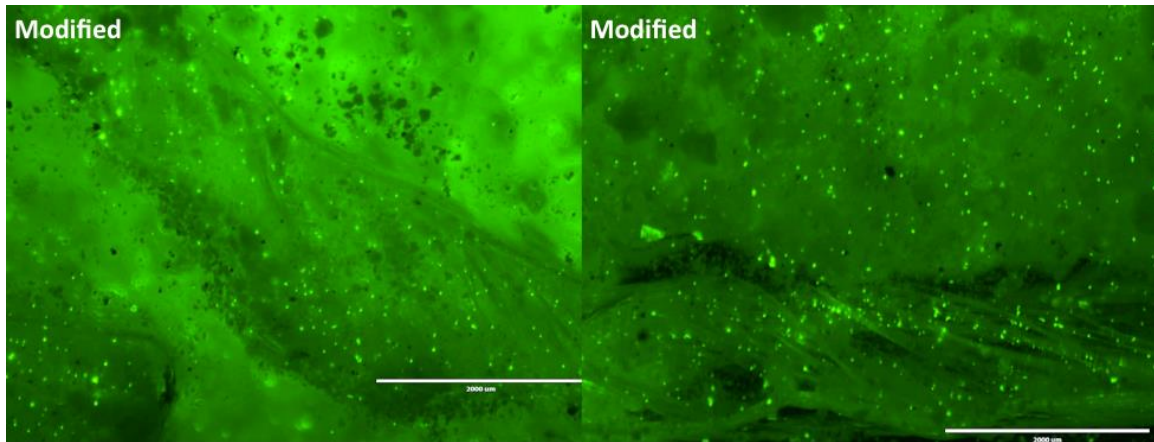


Figure 4.25: Depicts cell recruitment in modified wicking bundles of modified chronOS strips. Images depict cells along the twisted fiber bundle embedded in the chronOS scaffold.

The actin and nuclei fluorescent stains depicted cell distribution and proliferation after 72 hours. The images showed similar trends of cell distribution and penetration to the 2 hour time point. The peripheral images of both scaffold types showed high cell densities with increased proliferation and homogenous distribution (Figure 4.26).

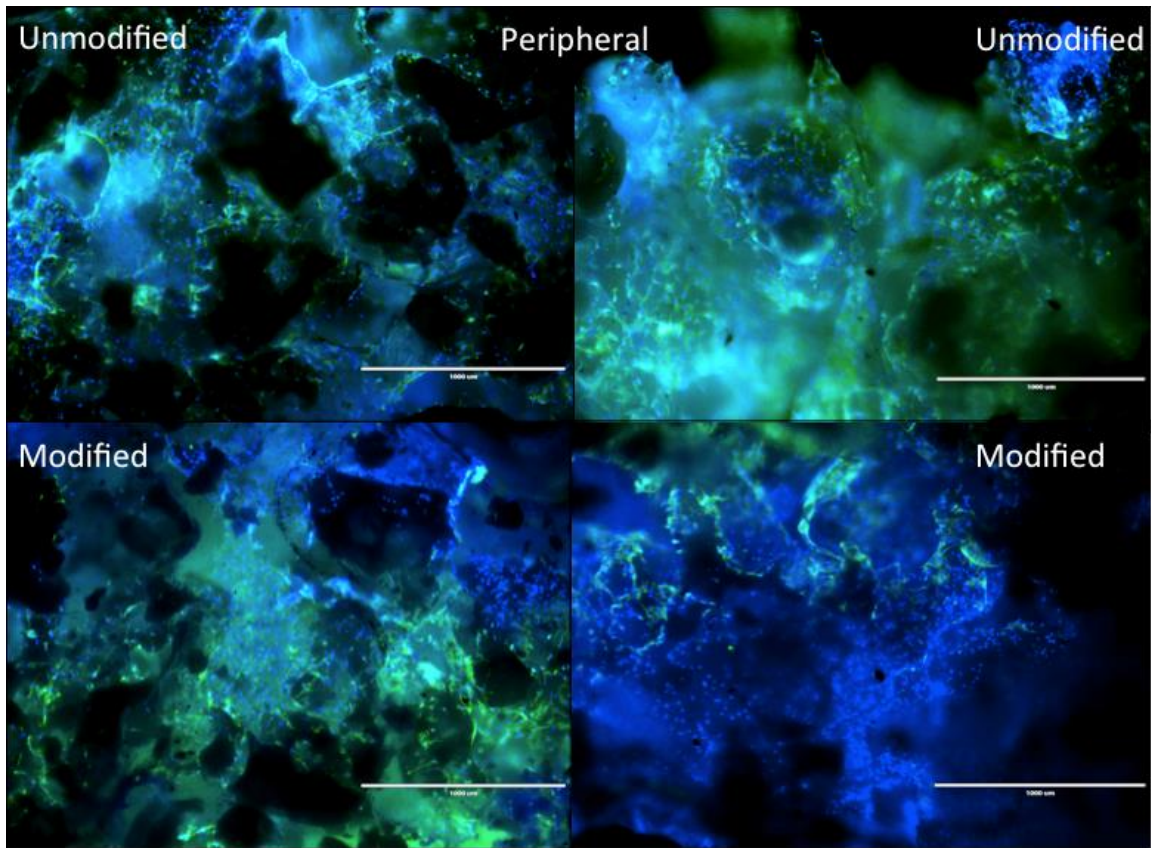


Figure 4.26: Actin and nuclei staining of progenitor cells shows high cell penetration and proliferation in the peripheral regions of both modified and unmodified chronOS strip scaffolds

The central region of the unmodified chronOS strip scaffolds illustrate significantly less cell infiltration and proliferation than the modified samples, as shown in unmodified labeled fluorescent images, Figure 4.27. The modified samples depict greater cell infiltration and proliferation in the central region of the scaffold than unmodified samples. The fluorescent images in Figure 4.28 show increased cell penetration and proliferation along the modified wicking bundle component.

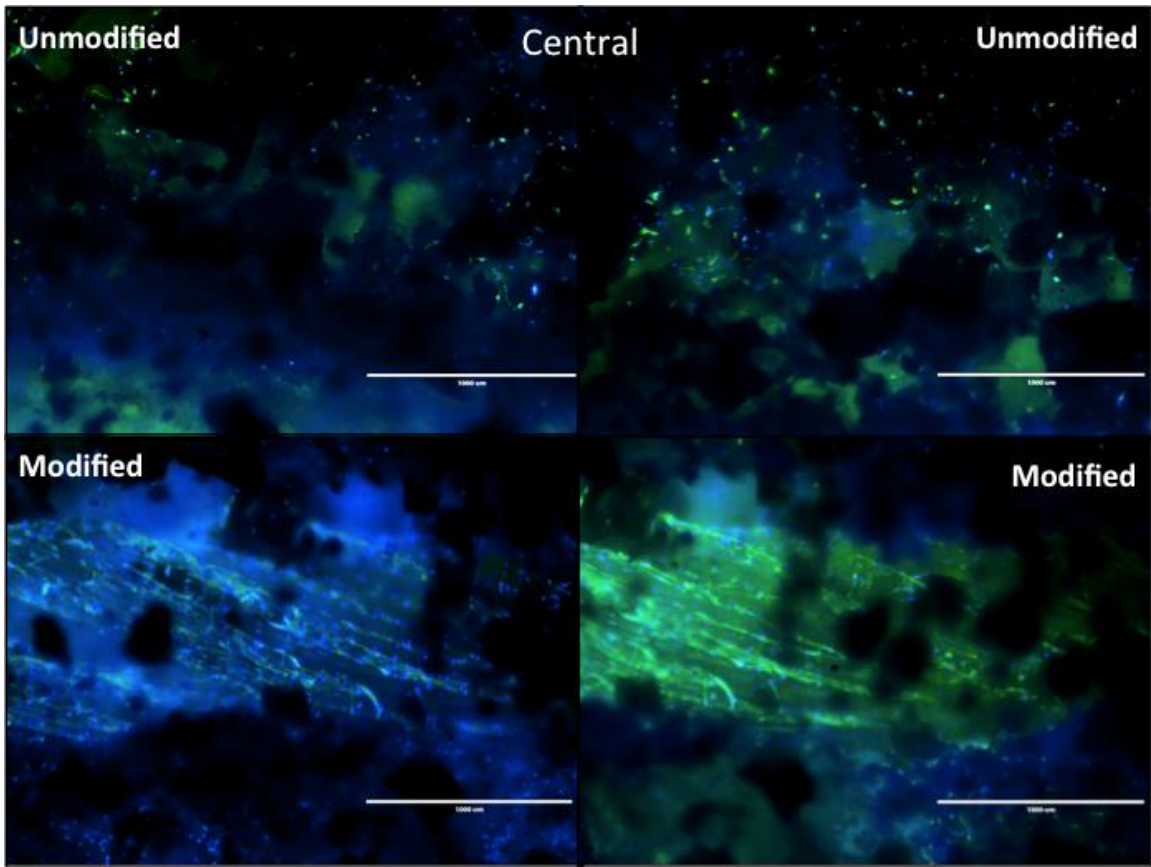


Figure 4.27: Cell distribution and proliferation in central regions of modified and unmodified chronOS strip scaffolds. Modified samples show significantly more cell penetration and proliferation, as well as cell infiltration along the modified wicking bundle component

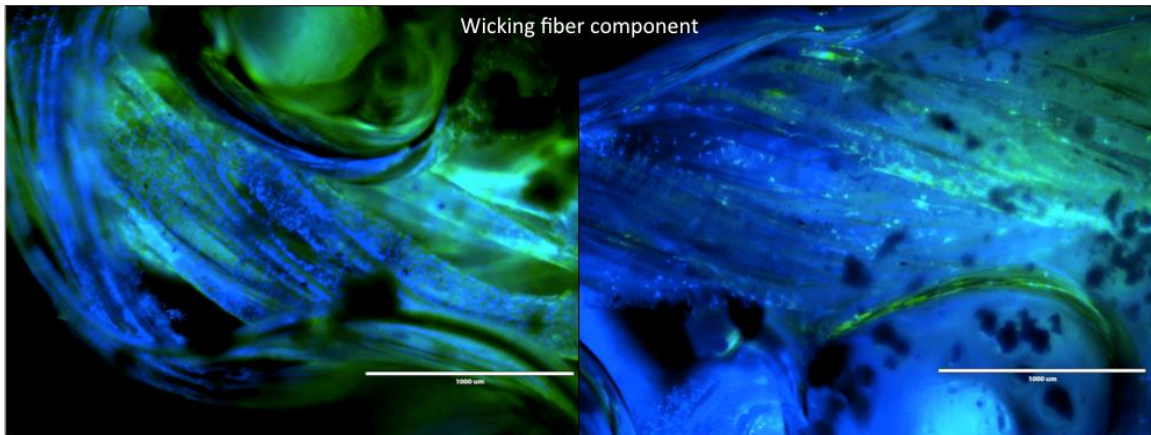


Figure 4.28: Images show significant cell infiltration along the wicking fiber - alginate construct. Images depict high cell densities along the wicking fiber bundle component

Cell Metabolism

Lactic acid production was higher in modified scaffolds than unmodified scaffolds for each time point, but only significantly higher at Day 2 with a significant value of $p < 0.05$. Both scaffold types also showed an increasing lactic acid production over the 72 hour time interval. The glucose consumption of modified and unmodified scaffolds were not significantly different. Both scaffolds showed increased glucose consumption after the 72 hour time point.

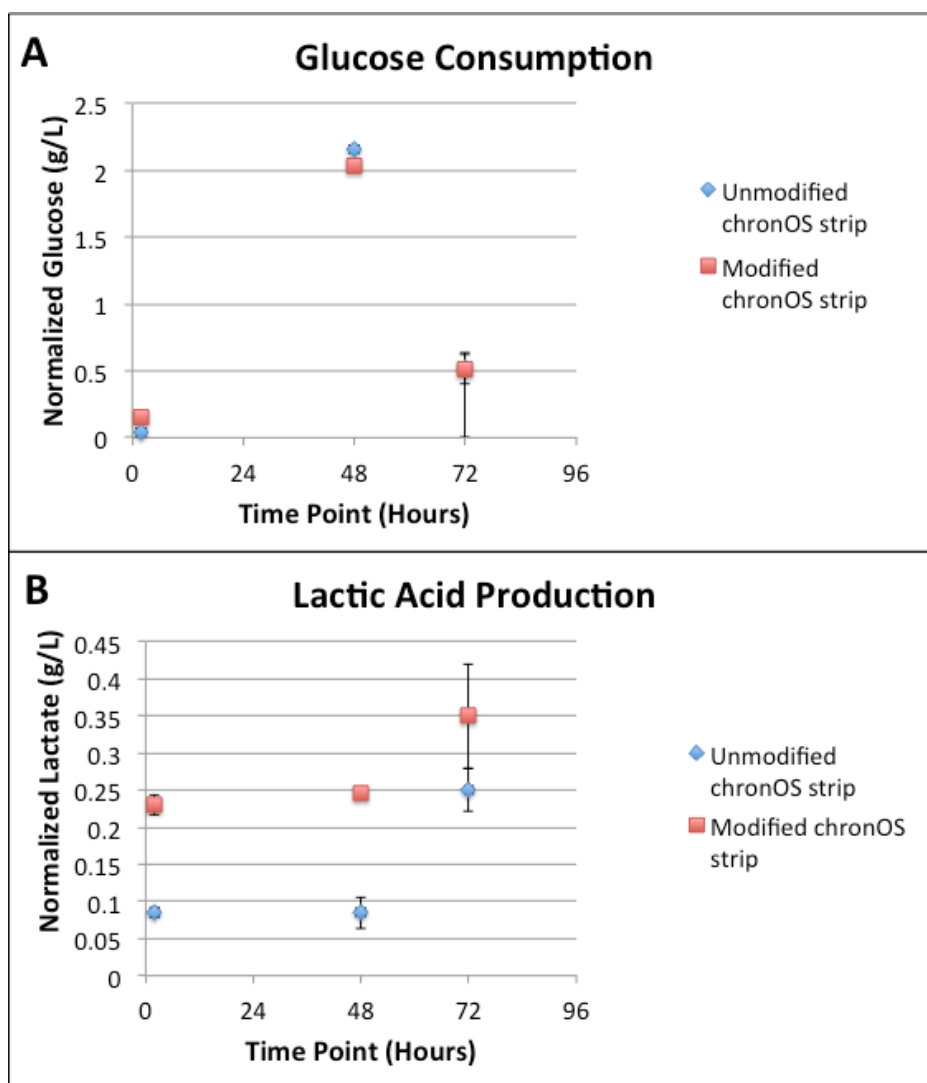


Figure 4.29: (A) Normalized glucose consumption after 2 hours, 48 hours, and 72 hours. No statistical significance was observed on any time point. (B) Normalized lactic acid production in modified and unmodified chronOS strip samples. Both scaffolds show increase in lactic acid production after 72 hours. The modified scaffolds show greater production than unmodified but are statistically significant after 1 hour.

Discussion

In this chapter we developed a passive fluid-driving pump based on wicking, or transport driven by capillary action. The outcomes of the fluid transport tests showed the absorbent alginate cap enhances the wicking behavior and fluid transport of wicking fiber bundles. The vertical test results demonstrated the absorbent cap significantly increases the change in the fluid front height over a ten-minute time interval as well as the amount of fluid absorbed after 12 and 24 hours. The final wicking test measuring the change in mass of the fluid transported over time revealed the wicking rate for the modified wicking bundle increases over time while the unmodified wicking bundle showed a decreasing wicking rate over time. The wicking rate plot for the unmodified wicking bundle will eventually plateau when the sample saturates. The saturation point of the fiber correlated to when the wicking rate reaches zero and the fluid reaches the maximum height. Interestingly, the wicking plot of the modified wicking bundle is parabolic with an increasing wicking rate. This suggests the absorbent cap provides an accelerating wicking rate. The acceleration is caused by the evaporation from the alginate cap. As the water evaporates from the cap the change in pressure of the system increases driving an increase in capillary pressure and consequently increasing the wicking rate. Root system in trees analogous phenomena, the fluid in the xylem conduits of trees is driven up by negative pressure or tension caused from the evaporation of water from the surface of leaves⁸⁻¹⁰. The modified wicking bundle follows the same mechanism of action. As water is evaporating from the alginate cap the water molecules from the conduits in the wicking fiber bundle are pulled into the more hydrophilic alginate component by adhesive forces.

The transport in the modified wicking bundle system can be described using tree hydraulics. The pressure that causes the upward fluid movement in the modified wicking bundle is due to the transpiration pressure from the absorbent material and the capillary pressure developed from the surface tension of the fiber surface (*Equation 4.1*)^{8,11}. The capillary pressure generated from the surface tension of the wicking fiber bundle is described using Laplace equation. The wicking rate is directly proportional to the change in pressure of the system. Hagen-Poiseuille law is used to describe liquid capillary rise (*Equation 4.2*). The modified wicking bundles contain the alginate cap that primes the system. The change in pressure of the modified and unmodified wicking bundles is illustrated in *Equation 4.3* and *Equation 4.4*. The transpiration pressure generated from the cap increases the change in pressure of the modified system, as reflected by the equation. The modified wicking bundles shows a greater pressure change compared to the unmodified bundles driving the enhanced wicking rate presented in the experimental data.

Equation 4.1: Laplace Equation

$$P_{Capillary} = \frac{\gamma_{LV} \cos\theta}{Rc}$$

$\theta = \text{contact angle}$

$Rc = \text{Radius of the capillary}$

$\gamma_{LV} = \text{Surface tension between liquid and air}$

Equation 4.2: Hagen-Poiseuille Law

$$\frac{dh}{dt} = \frac{r^2}{8\eta h} \Delta P = \frac{r^2}{8\eta h} \left(\frac{2\gamma \cos\theta}{r} - \rho gh \right)$$

$\theta = \text{Contact angle}$

$R_c = \text{Radius of the capillary}$

$\gamma = \text{Surface tension}$

$\rho = \text{Density of the liquid}$

$\eta = \text{Dynamic viscosity of the liquid}$

$h = \text{Height reached by liquid by time } t$

$\Delta P = \text{Pressure Difference}$

Equation 4.3: Pressure Change of Modified Bundles

$$\Delta P = P_T + P_C - P_H$$

$P_T = \text{Transpiration pressure}$

$$P_C = \text{capillary pressure} = \frac{\gamma_{LV} \cos\theta}{R_c}$$

$P_H = \text{Hydrostatic pressure} = \rho gh$

Equation 4.4: Pressure Change in Unmodified Bundles

$$\Delta P = P_C - P_H$$

$$P_C = \text{capillary pressure} = \frac{\gamma_{LV} \cos\theta}{R_c}$$

$P_H = \text{Hydrostatic pressure} = \rho gh$

The bundling effect of the fibers creates inter-fiber spaces that will also generate capillary pressure. This will increase the upward force moving the fluid. The additive effects of bundling the fibers and the absorbent cap transpiration pressure contribute the heightened wicking capabilities and fluid transport of this modified construct.

The improved fluid transport potential of the modified wicking bundle also increased the rate of biomolecule transport and progenitor cell recruitment. The outcomes revealed the modified wicking bundle increases the rate of FITC-albumin diffusion into a hydrogel compared to unmodified wicking bundles and the control group, a hydrogel without fibers. The intensity profiles over the first 5 minute time interval of the modified wicking bundle showed a significantly steeper slope than the unmodified bundle. Interestingly, we observed similar slopes after the first 5 minute interval. This profile indicates the modified wicking bundle was initially primed by the alginate causing an enhanced wicking rate. Once the alginate is saturated the wicking rates of the unmodified and modified bundles were comparable. This suggests the modified wicking bundle can initially improve the recruitment and distribution of biomolecules into a tissue engineered construct. Increased transport of bone-forming biomolecules to all regions of the scaffold will augment more homogeneous bone tissue formation. The results also depicted the modified wicking bundles can increase the initial cell penetration to the top regions of the fiber compared to the unmodified wicking bundles, implying the modified bundle may improve cell penetration into 3-dimensional scaffolds. Similar to the analysis of protein transport, the enhanced wicking is dependent on the saturation of the alginate. After the alginate is saturated the system will reach equilibrium. Pilot studies were conducted

investigating the equilibrium point of the alginate when submerged. Preliminary results demonstrated the alginate saturates after being submerged for 3 hours. Future will investigate the saturation point of the alginate and approaches to modify the absorbent material to sustain transport beyond the initial seeding phase.

The final study of this chapter tested the capabilities of the modified wicking bundle to recruit progenitor cells, provide homogeneous cell distribution, and improve cell viability and proliferation in a commercially available large bone graft. The outcomes showed we can effectively improve cell infiltration and distribution by incorporating modified wicking bundles in a diffusion-limited scaffold. Cross-sectional images of the central region of modified chronOS strip scaffolds demonstrated significantly more cell penetration and distribution than those of unmodified scaffolds. We also observed notable amounts of cell penetration along the wicking bundle and alginate cap. This verifies the modified wicking system will enhance transport of cells in a vacuum-sealed seeding technique. The high surface area of the wicking fiber bundles and increased capillary pressure from the alginate cap drives a sizeable force to transport not only fluid, but cell populations and biomolecules into a scaffold. In addition, the inter- and intra- fiber spaces generated by the fiber bundle are of varying micro- macro- and nano- conduit sizes. The micro sized conduits promote the capillary action of fluid and the nano- and macro- sized conduits have been shown to encourage cell adhesion and tissue ingrowth, respectively¹².

Modified chronOS strip scaffolds also revealed improved cell viability and cell seeding. Qualitative fluorescent images depicted significantly more viable cells in the

cross-sectional images of the modified scaffolds. The flow cytometry results validated the high number of viable cells on the modified chronOS strips. The total cell count determined by both DNA concentration and flow cytometry was significantly higher for modified scaffolds indicating the modified wicking bundles provide a mechanism to perfuse and distribute more cells in the scaffolds. The final assessment measuring lactic acid production and glucose consumption showed significantly more lactic acid production by the modified scaffolds than unmodified after the initial 1 hour waiting period. The modified scaffolds showed increased lactic acid production for all time points; however, no significant difference was observed after 48 and 72 hours. The outcomes further confirm the modified scaffolds initially have improved cell seeding. Future work will investigate proliferation after longer time points and bone differentiation and formation both *in vitro* and *in vivo* in an animal model.

Conclusion

Typically seeding progenitor cells on large-sized bone grafts for bone regeneration in critical defects have not been successful due to the diffusion limitations of the scaffold as well as the ability of the scaffold to effectively infiltrate cells and promote homogeneous bone formation. This work with the modified wicking bundle provides an intrinsic passive transport system, without the need for an external seeding system, to effectively infuse the scaffold with sufficient amounts of progenitor cells and successfully distribute the cells in the interior and surface regions.

References

1. Buckley CT, O'Kelly KU: Fabrication and characterization of a porous multidomain hydroxyapatite scaffold for bone tissue engineering investigations. *Journal of Biomedical Materials Research B: Applied Biomaterials* 2010; 93:459–67
2. Karande TS, Ong JL, Agarwal CM: Diffusion in Musculoskeletal Tissue Engineering Scaffolds: Design Issues Related to Porosity, Permeability, Architecture, and Nutrient Mixing. *Annals of Biomedical Engineering* 2004; 32:1728–43
3. Wendt D, Marsano A, Jakob M, Heberer M, Martin I: Oscillating perfusion of cell suspensions through three-dimensional scaffolds enhances cell seeding efficiency and uniformity. *Biotechnology and Bioengineering* 2003; 84:205–14
4. Burg KJL, Holder WD, Culberson CR, Beiler RJ, Greene KG, Loeb sack AB, Roland WD, Eiselt P, Mooney DJ, Halberstadt CR: Comparative study of seeding methods for three-dimensional polymeric scaffolds. *Journal of Biomedical Materials Research: Part A* 2000; 51:642–9
5. Thevenot P, Nair A, Dey J, Yang J, Tang L: Method to analyze three-dimensional cell distribution and infiltration in degradable scaffolds. *Tissue Engineering: Part C* 2008; 14:319–31
6. Buizer AT, Veldhuizen AG, Bulstra SK: Static versus vacuum cell seeding on high and low porosity ceramic scaffolds. *Journal of Biomaterials Applications* 2014; 29:3–13
7. Li Y, Ma T, Kniss DA, Lasky LC, Yang S: Effects of filtration seeding on cell density, spatial distribution, and proliferation in nonwoven fibrous matrices. *Biotechnology Progress* 2001; 17:935–44
8. Denny M: Tree hydraulics: how sap rises. *European Journal of Physics* 2012; 33:43–53
9. Tyree MT, Ewers FW: The hydraulic architecture of trees and other woody plants. *New Phytologist* 1991; 119:345–60
10. Sack L, Holbrook NM: Leaf hydraulics. *Annual Review of Plant Biology* 2006; 57:361–81
11. Das B, Das A, Kothari VK, Fanguiero R, de Araújo M: Effect of fibre diameter and cross-sectional shape on moisture transmission through fabrics. *Fibers and Polymers* 2008; 9:225–31

12. Hong M-H, Kim YH, Ganbat D, Kim D-G, Bae C-S, Oh DS: Capillary action: enrichment of retention and habitation of cells via micro-channeled scaffolds for massive bone defect regeneration. *Journal of Materials Science: Materials in Medicine* 2014; 25:1991–2001

CHAPTER FIVE

DEVELOPMENT OF AN ANTIBIOTIC RELEASE SYSTEM

Introduction

The incidence of infection is another major limitation of critical bone defects. Although the infection rate will vary based on type of fracture and patient indications, the addition of bone supplementation to the procedure increases the propensity to infection and can reach rates of 13%¹. These cases of infection become problematic as the treatment for infection is costly and risk for reinfection is very high¹⁻³. Conventional systemic antibiotic delivery limitations involve systemic toxicity and poor penetration into the postoperative tissue. As an alternative and more effective solution, local drug-eluting antibiotic is used preoperatively to help prevent the primary infection. The host matrix, the type of drug used, and the clearance rate dictate the efficiency of the current local release systems⁴. The major disadvantage of these delivery systems is the short-term burst release profile. Many systems release high effective concentrations of antibiotic up to 120 hours but subsequently drop out of the therapeutic window potentially resulting in resistant subpopulations of infective agents^{2,53}. Prolonged high antibiotic concentrations are needed to eradicate bacteria and prevent the formation of any resistant bacteria^{2,6}. Conversely, many of the current antibiotic eluting systems release drugs at concentrations significantly higher than the minimal inhibitory concentration (MIC) for preventing bacteria. High concentrations over the MIC can cause local toxicity and adversely affect bone formation⁷. The pharmacokinetics of the current systems is often not known and difficult to control and reproduce².

The goal of this chapter was to develop an antibiotic release system using the wicking fiber-alginate construct to effectively elute antibiotic long-term at optimal concentrations. The following studies tested the release profile of gentamicin for proof-of-concept. Gentamicin is frequently used as a locally administered antibiotic for orthopedic procedures. This antibiotic has the ability to eradicate staphylococcus aureus, the most common pathogen in orthopedic procedure related infections. The goal for antibiotic release of the system is to provide concentrations above the minimal inhibitory concentration and below the nephrotoxicity concentration⁸. Additionally, we aimed to maintain this range in effective concentration over a time span of 2 weeks to improve upon current clinical systems. Specifically, we investigated three different antibiotic loading mechanisms into the fiber bundles and tested the elution profile and effect on the properties of the polylactide. This work also investigated the antibiotic loading of the alginate cap and release profile over two weeks. The loading mechanisms were optimized to provide a long-term antibiotic release profile at sufficient inhibitory concentrations to reduce the rate of infection.

Gentamicin Release Profile from Fiber Bundles and Alginate Caps

Materials and Methods

Extrusion and Experimental Set-up of Fiber Bundles

Three different antibiotic loading mechanisms were tested with polylactide round and wicking cross-sectional fibers. The first mechanism involved loading the fibers after extrusion by wicking the antibiotic solution into the fiber bundles using the previously discussed vertical test procedure. The second and third loading mechanisms incorporated

the antibiotic during the polymer extrusion process. Briefly, the extrusion process, also depicted in the schematic below, involves feeding polymer beads into a funnel through a hopper that is connected to a barrel with a feed screw controlled by an electrical motor that transports the polymer through a heated conduit. The pellets are incrementally heated to a melting temperature, determined through differential scanning calorimetry (DSC), producing an amorphous polymer melt. The extruder contains a pump that provides pressure to push the polymer melt through the dye containing the cross-sectional mold. Changes in fiber diameter can partially be attributed to changes in the rotational speed of the pump motor. The extruded fiber is wrapped around sequential rollers and a spool, which can be manipulated to control the drawing rate also affecting fiber diameter. A water bath can be applied directly below the die to quench the polymer fibers immediately after extruding to reduce the effects of drawing on the fibers

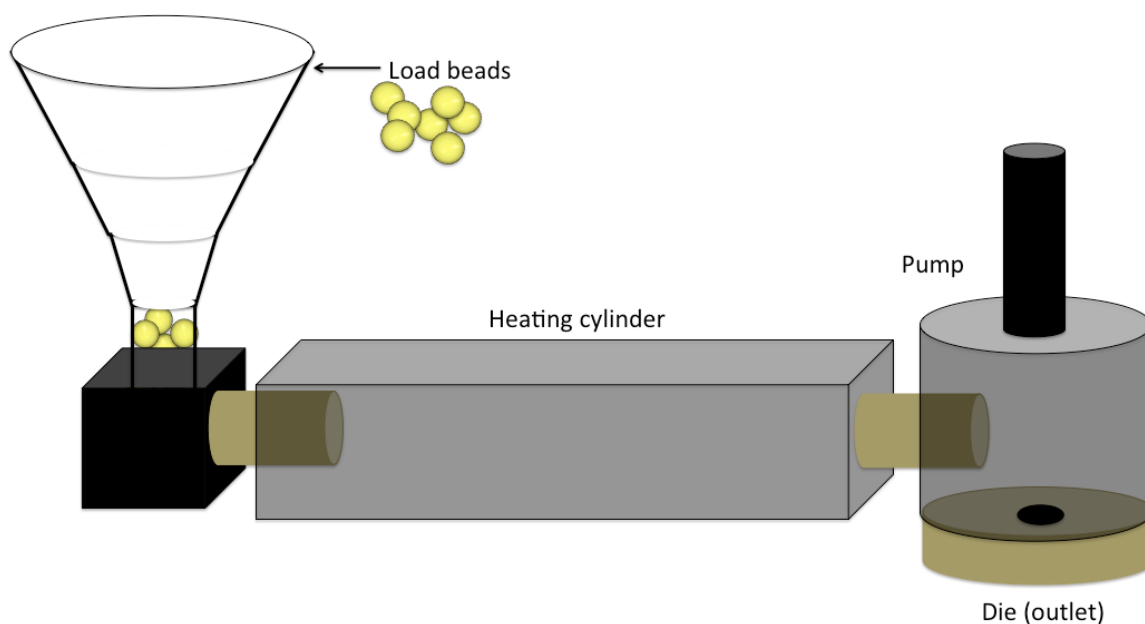


Figure 5.1: Schematic shows the extruding process of polymer fibers. Polylactide beads are inserted through a funnel into a hopper with a screw that transport the polymer through a heating cylinder. The pump pushes the melted polymer through a die to form the cross-section shape of the fiber

The second loading mechanism involves quenching the fibers immediately after the polymer is drawn from the die (outlet) into a water bath containing antibiotic solution. The final approach to incorporate antibiotic during the extrusion process involves mixing antibiotic powder with the polylactide beads prior to adding the beads to the funnel. The table below summarizes the antibiotic loading mechanisms and experimental groups tested in this study.

Table 5.1: Loading Mechanisms

	Loading Mechanism 1	Loading Mechanism 2	Loading Mechanism 3
Description	Wicking antibiotic solution into bundles	Incorporate antibiotic power with polymer pellets prior to extruding	Quench the extruded fiber in a water bath containing antibiotic solution
Round PLA fibers	N=5	N=5	
Wicking PLA fibers	N=5	N=5	N=5 (Small wicking Bundle) N=5 (Large wicking fiber)

Loading Mechanism 1

Round and wicking fiber bundles were extruded using a continuous melt-extruder and spinneret system (Alex James and Associates, Inc.; Greenville, SC) Polylactide (PLA) pellets (PL biopolymer ~228,000 Da; Natureworks LLC) were melt-spun into monofilament fibers. The extrusion melt temperature of the PLA pellets was based on the glass transition (T_g) and melt temperatures (T_m) previously determined using differential scanning calorimetry (DSC). The pellets were melt-spun at 167°C. The melted polymer was extruded through spinnerets containing either the wicking (eight-grooved) or round cross-sectional die. The wicking die used has an irregular cross-section with a long axis of 0.2045 inches and the short axis of 0.1494 inches as depicted in image A of the drawing below. The die used to extrude the round fibers had a diameter of 0.1500 inches. A slower pump speed of 5 RPMs was used to extrude both round and wicking fibers to produce monofilaments of smaller cross-sections. A water bath was used to quench the

fibers directly 12 inches below the die at the outlet of the system. The water bath system was modified with a rolling track to feed the polymer fiber through the quenching liquid and onto the successive rollers as demonstrated in the digital image below.

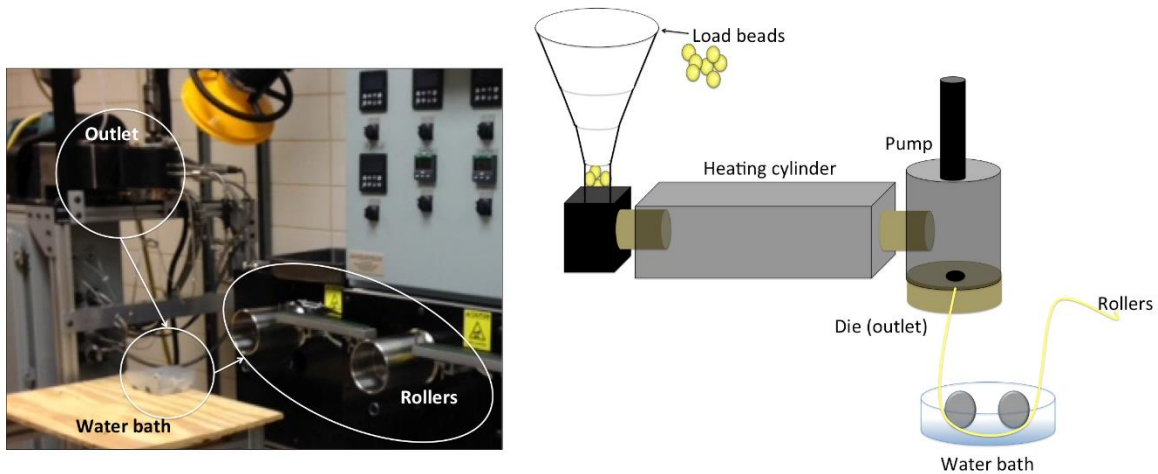


Figure 5.2: Depicts the feeding of the polymer monofilament from the outlet through the water bath and along the rollers

The extruding monofilament was wrapped around five successive rollers controlled by motors to effectively draw and collect the fiber onto a spool. The motor speed of the pump used in the extrusion process produced round extruded monofilaments with a cross-sectional diameter of 0.50 mm. The extruded wicking fibers had dimensions of 0.51 mm and short axis 0.33 mm, depicted in image B of figure 5.1.

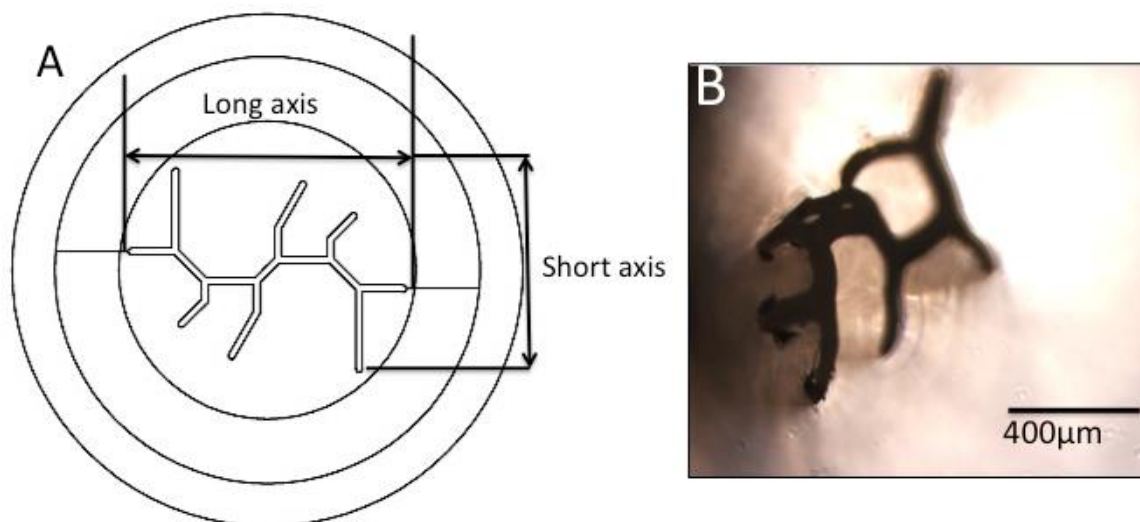


Figure 5.3: (A) Long and short axis dimension of the die used for extruding the wicking fibers. (B) Cross-sectional image of the PLA extruded wicking monofilament

Round and wicking bundles were sliced into individual fibers of 3 cm length from the spool. Ten of the individual fibers were twisted to form fiber bundles of round or wicking fibers. The fiber bundles were vertically placed in a 12-well plate with a custom-made lid to hold the fiber bundles vertically. Each well contained 1 mL of gentamicin sulfate salt powder (Sigma; St. Louis, MO) and phosphate-buffered saline (PBS, Invitrogen, Grand Island, NY) at a concentration of 150 µg/mL. The gentamicin solution was loaded into the fiber bundles by allowing the solution to wick into the bundles. After 1 hour of vertical wicking, the samples were removed and transferred to a 6-well plate containing 2 mL of PBS containing eluted gentamicin. This procedure was performed to determine the amount of gentamicin elution over 14 days. The initial time point was collected immediately following the placement of the wicking fiber bundles in the well

plates. The PBS was collected in 1.5 mL microcentrifuge tubes and stored at -20°C until the gentamicin analysis was performed. The wells were refilled with 2 mL of PBS and incubated at 37°C and 5% CO₂ until the next time point. Samples were collected initially for short time intervals after 15, 30, 45 minutes, and 12 hours. Samples were also collected for longer time intervals with daily collection after days 1-7. After the day 7 time point, samples were collected after day 10, 14, 21, and 28.

Loading Mechanism 2

The extrusion system and settings were used to extrude the round and wicking fiber bundles as in the first loading mechanism. However, instead of wicking the gentamicin solution, 250 mL of gentamicin solution (Sigma) was added directly to the water bath used to quench the fibers. The gentamicin solution again was at a concentration of 150 µg/mL in PBS. After the round and wicking fibers were extruded bundles were formed, and the elution profile was determined using the same procedure described in mechanism 1.

Loading Mechanism 3

The gentamicin solution was incorporated into the PLA by mixing a 1% w/w gentamicin sulfate salt powder (Sigma) with polylactide pellets (Natureworks) prior to loading the pellets into the extruder. Specifically, 500 mg of gentamicin sulfate was added to 50 g of PLA pellets. The inlet of the extruder is illustrated in figure 5.2. After mixing, the gentamicin coated polylactide beads were loaded into the inlet of the extruder. Wicking fibers were extruded with the melt-extruder and spinneret system with

the same extruding settings described in mechanism 1 with removal of the water bath. This approach drew the fibers directly onto the rollers without quenching the fibers with the water bath prior, shown in schematic below.

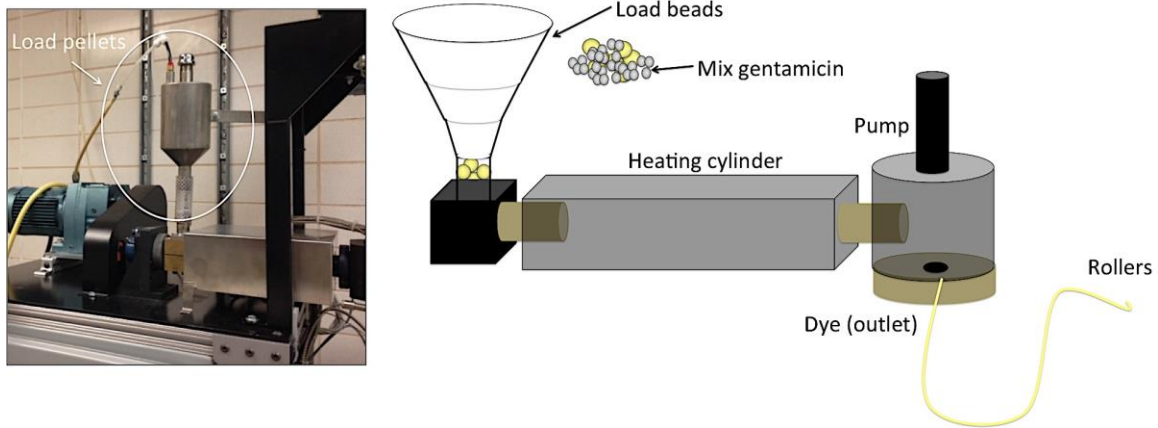


Figure 5.4: Depicts third approach for incorporating antibiotic into extruded polymer fibers by mixing the gentamicin powder and polylactide pellets prior to loading the extruder

The third mechanism investigated gentamicin elution from wicking fiber monofilaments extruded with two different cross-sectional sizes. The experimental groups of this loading approach involved two different sized wicking fiber filaments. The first experimental group (N=5) included a twisted fiber bundle of 10 individual small extruded filaments with cross-sectional dimensions of 0.51 mm x 0.33 mm and of 3 cm in length. The second experimental group (N=3) for this loading mechanism analyzed a single large wicking fiber that was extruded by removing all drawing functionality of the spooling process. The extruded large wicking fiber had dimensions of 1.4 mm and short

axis 0.83 mm. The large monofilaments were sliced into individual samples each 3 cm in length. Both experimental groups were placed in 2 mL of PBS and incubated at 37°C and 5% CO₂. Samples for this mechanism were collected after days 1, 2, 4, 10 and 14.

Experimental Set-up for Alginate Caps

The elution profile from the alginate caps was also investigated. The gentamicin loaded caps were formed by first creating an alginate-gentamicin solution of 1.4% (w/v) alginic acid sodium salt from brown algae (Sigma; St. Louis, MO) and 150 µg/mL of gentamicin sulfate salt (Sigma; St. Louis, MO) in 155 mM NaCl. The solidification agent, 5M CaCl₂ solution (Fisher Scientific; Waltham, MA, USA), was pipetted at 100 µL into a well of a 96-well plate. To form the cap, 100 µL of the alginate-gentamicin solution was directly added to the CaCl₂ solution in the well and immediately solidified. The alginate caps (N=5) were transferred to a 6-well plate containing 2 mL of PBS. To determine the elution profile of gentamicin from alginate the PBS was collected and replaced at the initial time point, immediately after submerging the caps in PBS, as well as after short term time points of 15 min, 30 min, 45 min, 1 hour, and 12 hours. Samples were also collected to investigate long term release after Days 1-3, 7, 14, 21, and 28.

Determining the Total Amount of Incorporated Gentamicin

This assay determined the total amount of gentamicin bound and incorporated into the round and wicking fibers from the various loading mechanisms. All sample types from each fiber loading mechanism (N=3) were dissolved in 1 mL chloroform (Honeywell; Muskegon, MI, USA) in glass microvials at room temperature for 10 minutes and mixed with a vortex mixer (VWR; Radnor, PA, USA) every 5 minutes. To isolate the gentamicin from chloroform 500 μ L of distilled water was added to the chloroform and mixed with the vortex. The samples were centrifuge resulting in a phase separation with water-soluble gentamicin in the aqueous phase. The aqueous phase was collected and analyzed using the following described gentamicin detection assay.

To assess the amount of gentamicin that was bound to the alginate, the hydrogel was dissolved in a dissolution buffer comprised of 100mM sodium citrate (Fisher Scientific; Waltham, MA USA), 10 mM HEPES buffer (Sigma; St. Louis, MO USA), and 27 mM NaCl (Sigma; St. Louis, MO USA) in 50 mL of distilled water. The alginate caps were transferred to a 1.5 mL Eppendorf microcentrifuge tubes (Sigma; St. Louis, MO USA) containing 1 mL of the stock dissolution buffer. The alginate caps were dissolved for 30 minutes at 37°C and mixed vigorously using the vortex every 5 minutes. Following complete dissolution of the alginate cap the amount of gentamicin left in the solution was analyzed following the detection assay.

Gentamicin Detection Assay

The amount of gentamicin over the 28 day time interval was determined using a spectrophotometric technique developed by Frutos and coworkers. To create a detectable

compound the gentamicin was derivatized by adding equal proportions of fluorescent agent o-phthaldialdehyde (OPA)⁹. Specifically, the OPA reagent reacts with the primary amine functional groups on the gentamicin forming a fluorescent detectable complex. Prior to analyzing the samples, a standard curve was generated and tested by creating the gentamicin in PBS concentrations seen in the table below. 100 μL of each standard concentration was added to a well of a black-bottom 96 well plated (Corning; Fisher Scientific, Waltham, MA USA). To detect the gentamicin, 100 μL of phthaldialdehyde reagent (Sigma; St. Louis, MO) was added and mixed with each well containing standard sample. The plate containing the standard was incubated at room temperature for 10 minutes and read with a Synergy MX Multi-Mode Reader (BioTek; Winooski, VT USA) at an excitation wavelength of 340 nm and an emission wavelength of 455 nm. The standard curve was generated using the fluorescent readings and a linear curve fit was performed to determine the equation.

Table 5.2: Standard curve concentrations for gentamicin detection assay

Standard curve concentrations	$0 \frac{\mu\text{g}}{\text{mL}}$	$1 \frac{\mu\text{g}}{\text{mL}}$	$2 \frac{\mu\text{g}}{\text{mL}}$	$5 \frac{\mu\text{g}}{\text{mL}}$	$10 \frac{\mu\text{g}}{\text{mL}}$	$20 \frac{\mu\text{g}}{\text{mL}}$	$100 \frac{\mu\text{g}}{\text{mL}}$	$150 \frac{\mu\text{g}}{\text{mL}}$
-------------------------------	-----------------------------------	-----------------------------------	-----------------------------------	-----------------------------------	------------------------------------	------------------------------------	-------------------------------------	-------------------------------------

To analyze the elution profile the samples stored at -20°C were thawed to room temperature and 100 μL of the sample were added to a black clear-bottom 96-well plate (Corning; Fisher Scientific, Waltham, MA USA). Subsequently, 100 μL of o-phthaldialdehyde reagent was added and mixed with each well containing sample. Due to the variability of readings between plates each 96-well plate containing samples

contained standard gentamicin samples in duplicate to generate a standard curve for each plate. The sample was incubated at room temperature for 10 minutes and the fluorescent spectrometry was performed using a Synergy MX Multi-Mode Reader (BioTek; Winooski, VT USA) at an excitation wavelength of 340 nm and an emission wavelength of 455 nm.

Differential Scanning Calorimetry

Differential scanning calorimetry (DSC) was used to investigate any effects of the loaded gentamicin on the melting point and glass transition temperature as well as the endothermic and exothermic processes during the physical transitions of the polylactide monofilaments. The experimental groups analyzed were (1) polylactide monofilaments without gentamicin (2) polylactide monofilaments with gentamicin from the loading approach using the water bath (Mechanism 2) and (3) polylactide monofilaments with gentamicin from incorporating antibiotic with pellets prior to extrusion (Mechanism 3). Fiber samples were sliced with a razor and added to the bottom of a standard aluminum pan. Approximately 2-3 g of sample were added to each pan bottom. A lid was used to cover the pan and tweezers were used to manually crimp the pan to seal the edges. The DSC was performed using a TA instruments Q1000 DSC (TA Instruments; New Castle, DE) using helium purge gas. The scans were performed from 10°C to 200°C with a heating rate of 10°C/minute. Universal Analysis 2000 software was used to integrate the peaks. The melting point and glass transition temperatures were compared for each experimental group. The DSC curves were also qualitatively analyzed to determine any alterations in percent crystallinity.

Statistics

JMP 10 software was used to conduct an unpaired two-sample t-test to compare the average gentamicin concentration release from round and wicking fibers for both loading mechanisms 1 and 2 for each time point. The average amount of antibiotic initially loaded in round fiber bundles by mechanism 2 was compared to the initial antibiotic loaded in wicking fiber bundles using an unpaired two-sample t-test.

Results

Elution Profile from Fiber Bundles (Mechanism 1 and 2)

Gentamicin was incorporated into extruded round or wicking fibers by wicking the antibiotic solution into the bundles (Mechanism 1) and by quenching the fibers in a water bath (Mechanism 2). The loading mechanisms were tested by analyzing the elution profile of gentamicin from both round and wicking fiber bundles at various time points. The short-term release of gentamicin by the fiber bundles was evaluated for the first 45 minutes. The outcomes depicted the highest release of gentamicin at the initial time point from the fiber bundles for all experimental groups, presented in image A of Figure 5.5. The wicking fiber bundles loaded through mechanism 1 showed significantly more release of antibiotic initially than any other group ($p < 0.05$). The gentamicin released from the wicking fibers modified with mechanism 2, showed significantly higher concentrations at the initial time point than round fiber bundles loaded with gentamicin from either mechanism. After 15 minutes the wicking fibers incorporated with antibiotic through mechanism 1, showed significantly more release of gentamicin than round fibers

loaded with antibiotic through the same mechanism. The later time points show no significant difference in gentamicin release from any of the experimental groups. The results demonstrate that the loading mechanism and fiber type will affect the initial release of antibiotic but neither factor plays a significant role after 15 minutes. The minimal inhibitor concentration (MIC) for various bacterial strands is considered around $1\mu\text{g/mL}$, indicated by the red dotted line. Ideally, the antibiotic delivery system should elute above the MIC value. The outcomes show only the wicking fiber groups reach this concentration after the initial time point, and none of the experimental groups reach the MIC concentration after time zero. The results illustrated in image B of Figure 5.5 shows the cumulative release of gentamicin from the fiber bundles after 45 minutes. This can be used to determine how much antibiotic is left in the fiber bundles.

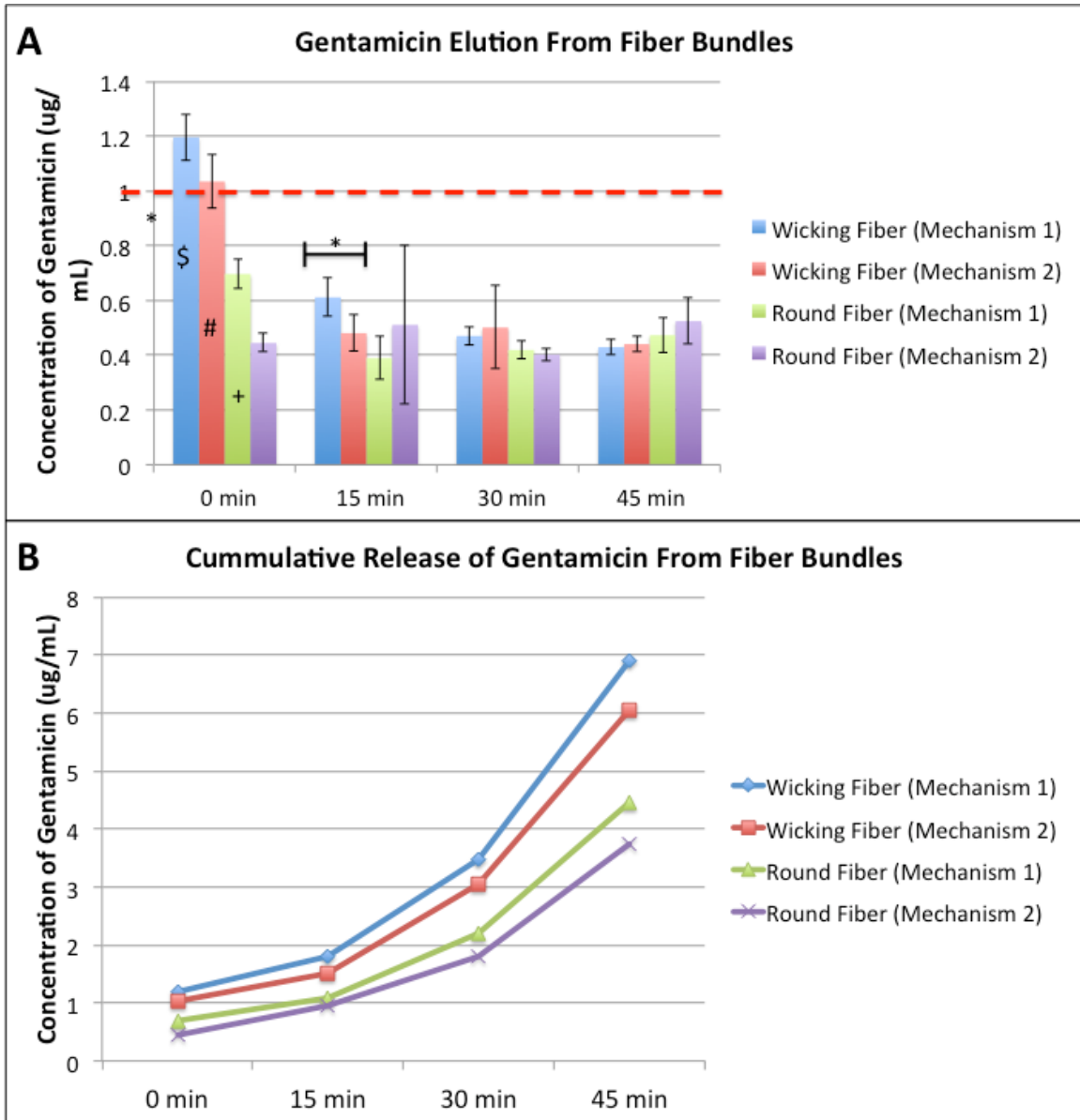


Figure 5.5: (A) Gentamicin release from round or wicking fiber bundles loaded with gentamicin from mechanism 1 or 2. At the initial time point all the experimental groups show a significantly different concentration of gentamicin (#,\$,*,+) signify each group is significantly different within the initial time point ($p < 0.05$). After 15 minutes the wicking fiber group loaded by mechanism 1 is significantly greater than the round fiber group loaded by the same mechanism, (*) signifies statistical differences between these groups with $p < 0.05$. The red dotted line indicates the target elution concentration. (B) Depicts the cumulative release of gentamicin from each experimental group

The release profile of gentamicin was also analyzed over longer time intervals. The results shown in Figure 5.6 below show similar eluted concentrations of gentamicin from each experimental group for each time point. From 12 hours to 2 days all experimental groups depicted negligible concentrations of gentamicin except the wicking fiber group loaded by mechanism 2. However, after days 7 and 14 gentamicin was released and detectable. After days 7 and 14 there is no significant difference in eluted concentrations between fiber bundle groups. Image B depicts the cumulative release profile of gentamicin from each experimental group. The wicking fiber bundle group loaded with gentamicin through mechanism 2 shows the greatest cumulative concentrations over time compared to the other experimental groups.

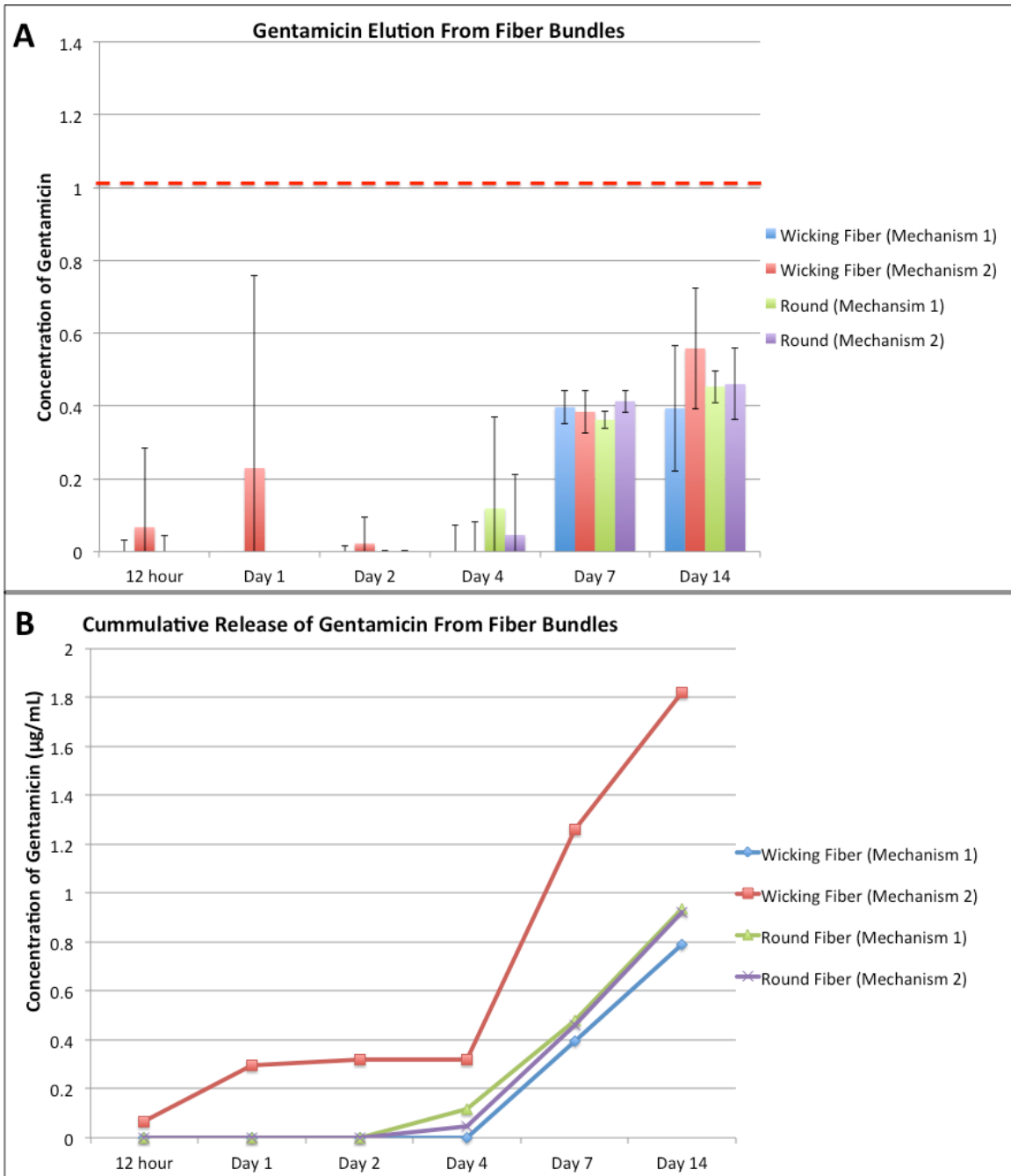


Figure 5.6: (A) Release of gentamicin from wicking fiber bundles after longer time intervals. Gentamicin was undetectable in early time points for all experimental groups. No significant difference in gentamicin elution was found at any of the time points (B) Cumulative release profile of the gentamicin elution from each experimental group shows the wicking fiber loaded by mechanism 2 has the greatest cumulative elution over this time interval.

Gentamicin Elution from Mechanism 3

This study investigated the elution profile of gentamicin in a bundle of small wicking fibers and a single large fiber to explore the effect of cross-sectional size on elution of gentamicin. This mechanism incorporated the antibiotic by mixing the PLA pellets and gentamicin prior to extruding. The release profile, shown in image A of Figure 5.7, shows both wicking fiber types eluted above the MIC concentration for the duration of the study. Both fiber types showed an initial burst release of gentamicin. The burst release from the large wicking fiber was much greater than the release from the small fiber bundle. The cumulative release for each time point from the large single fibers, Image B, of gentamicin was greater than the release from the small fiber bundles.

Amount of Antibiotic Loaded for Mechanism 2 and 3

The amount of antibiotic loaded into each of the fiber types by mechanism 2 or mechanism 3 was determined by dissolving the PLA fibers and isolating the gentamicin in the aqueous phase. The amount of antibiotic loaded by mechanism 3 was significantly greater than the second loading mechanism, Figure 5.8. The wicking fiber loaded by mechanism 2 contained ten times the amount of gentamicin loaded by the same mechanism. This confirms the high surface area of the wicking fiber can incorporate more gentamicin. The large single fiber loaded by mechanism 3 has less total gentamicin loaded than the single fiber bundles.

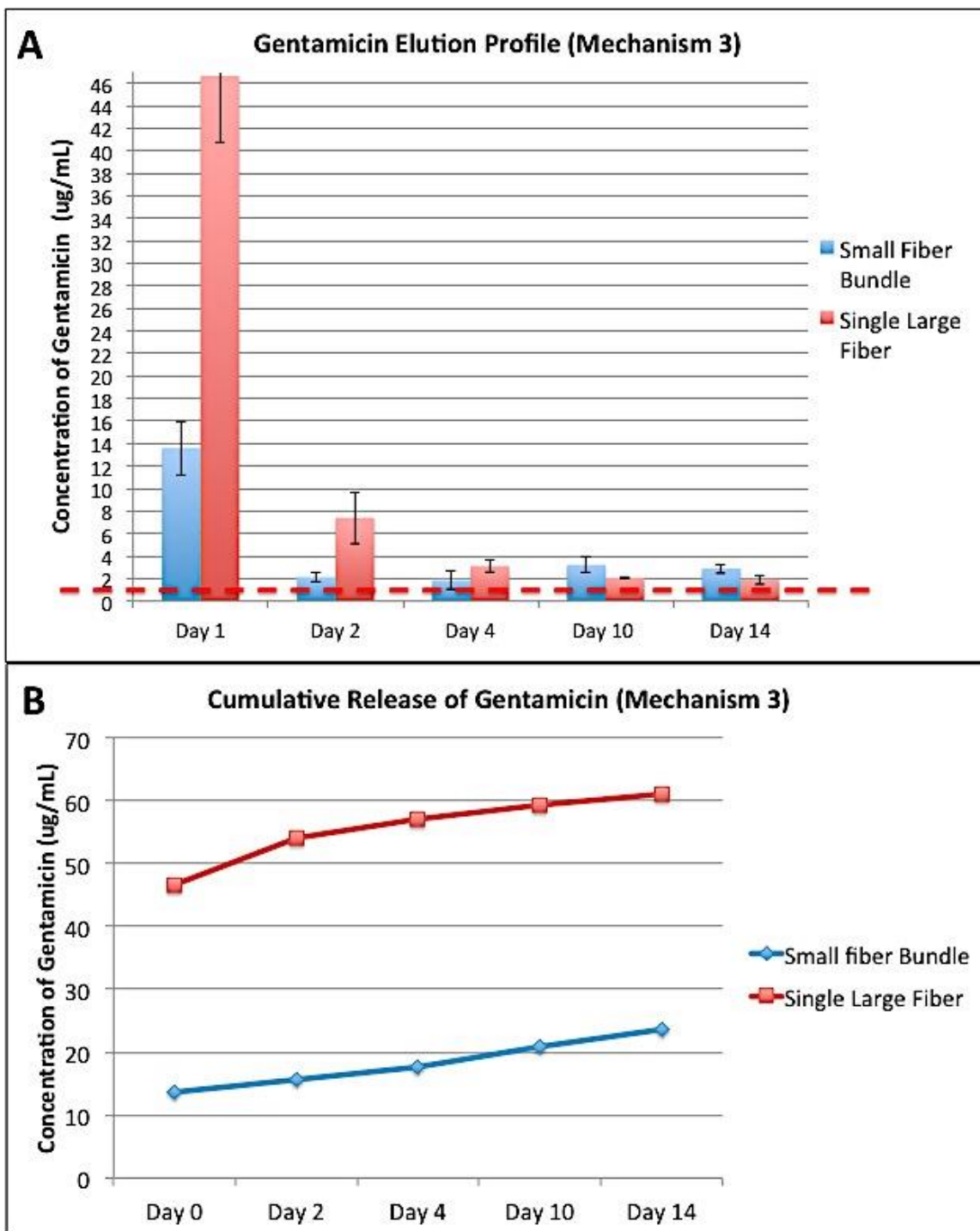


Figure 5.7: Release profile of gentamicin loaded by mechanism 3. (A) Elution profile of small bundled wicking fiber and a single large wicking fiber (B) Cumulative release of both wicking fiber types over a 14 day time period.

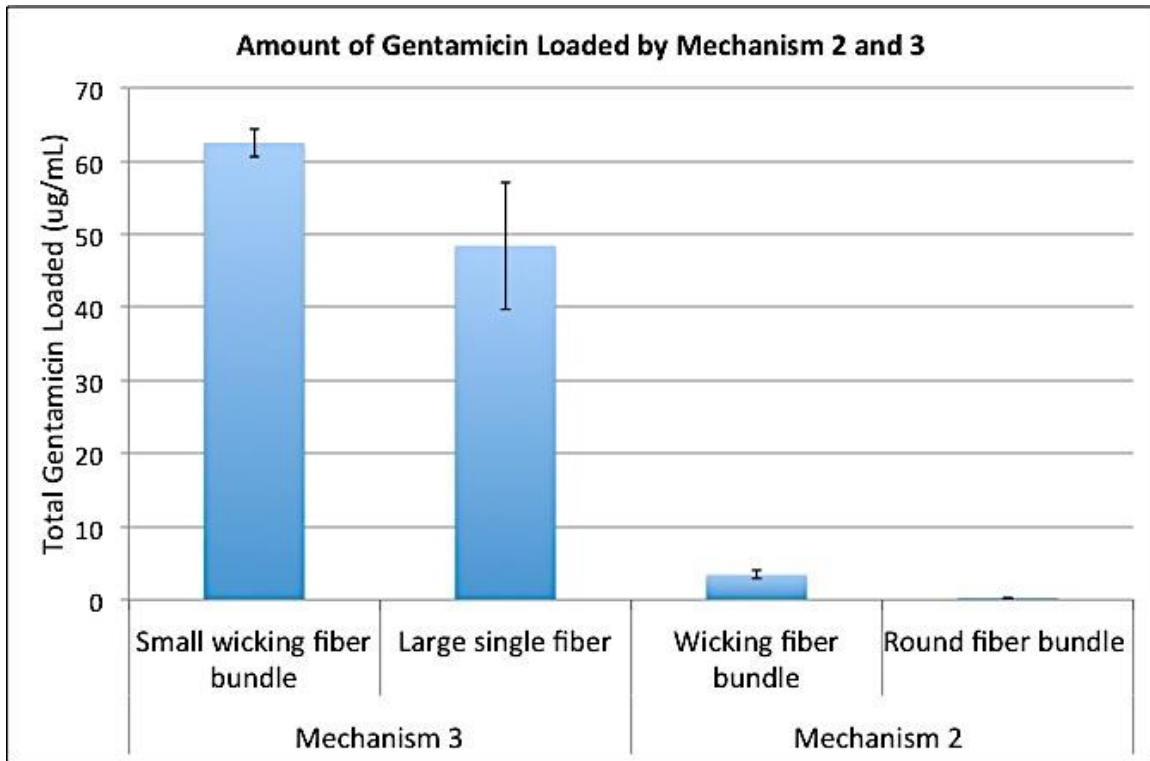


Figure 5.8: The amount of gentamicin incorporated into the PLA fibers from loading mechanisms 2 and 3

Elution Profile from Alginate Caps

The gentamicin release profile from the alginate caps is depicted in Figure 5.9. The results demonstrate a burst of antibiotic from the initial time point and slower steady release of antibiotic after 15 minutes. The total amount of gentamicin loaded in the caps was determined by dissolving the alginate, indicated by the “dissolved” group in Figure 5.9. Image B depicts the cumulative release of gentamicin from the alginate caps. The profile illustrates by 15 minutes almost half of the total concentration of antibiotic has been eluted and by day 14, the entire loaded antibiotic was released. Image A also depicts

the red dotted line that correlates to the target elution concentration. The outcomes reveal the alginate reaches this target concentration until Day 7.

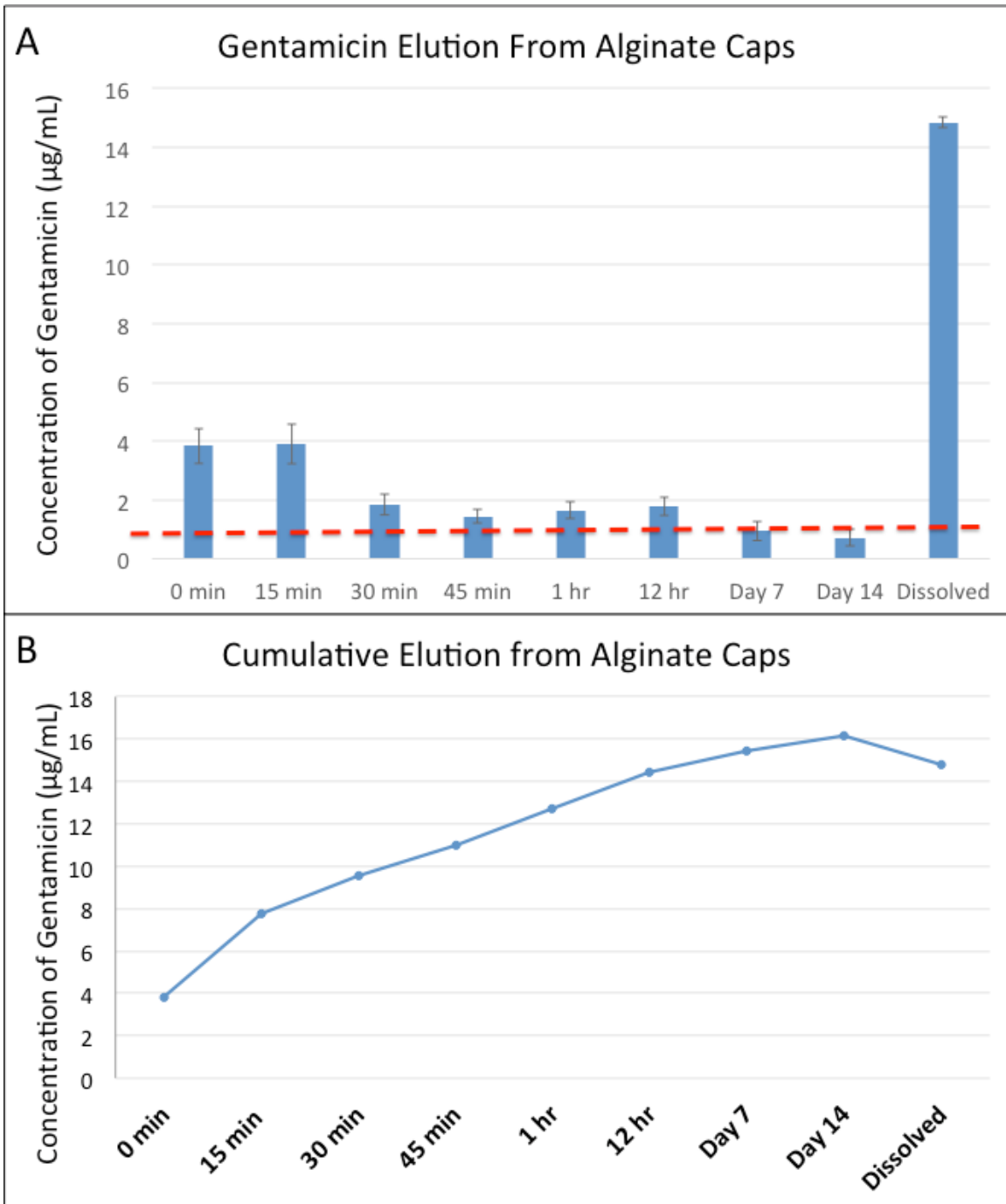


Figure 5.9: (A) Elution from alginate caps shows an initial burst and steady release of gentamicin. The total amount of gentamicin loaded in the alginate is depicted in both graphs. The red dotted line indicates MIC. The release from the alginate cap reaches the target concentration until Day 7. (B) The cumulative release profile shows that all of the gentamicin loaded was completely eluted by day 14.

Differential Scanning Calorimetry

The DSC plots of the control polylactide wicking fiber group and the experimental groups containing gentamicin through loading mechanisms 2 and 3 are shown in Figure 5.10. Plot A shows the DSC curve after the first heat cycle. Mechanism 2 (red) and the control group (green) show similar glass transition temperatures (T_g) and melting temperatures (T_m). Mechanism 3 (blue) depicts similar T_g value with different heat flow values compared to Mechanism 2 and the control group. Mechanism 3 also shows two different melting temperatures, as indicated by the double blue peaks (Image A). Mechanism 3 also demonstrates a different crystallinity profile than both the control group and mechanism 2. Image B shows the DSC plots after the second heating cycle. The T_g values and heat flows are similar for all groups. The melting curves show similar melting temperatures for each group but different heat flow values. The table reported below summarizes the T_g and T_m values for the control and experimental groups. The plot also shows varying crystallinity curves for each group. The DSC preliminary results suggest the gentamicin may alter the crystallinity and raw properties of the monofilaments, which may affect the mechanical performance and degradation rate.

Table 5.3: Results from DSC showing T_g and T_m for each polylactide wicking fiber experimental group

	T_m (Cycle 1)	T_g (Cycle 1)	T_m (Cycle 2)	T_g (Cycle 2)
No Gentamicin	149.6	59.42	151.68	57.87
Mechanism 2	150.98	60.55	150.98	59.41
Mechanism 3	147.61	62.00	150.87	59.07
	154.47			

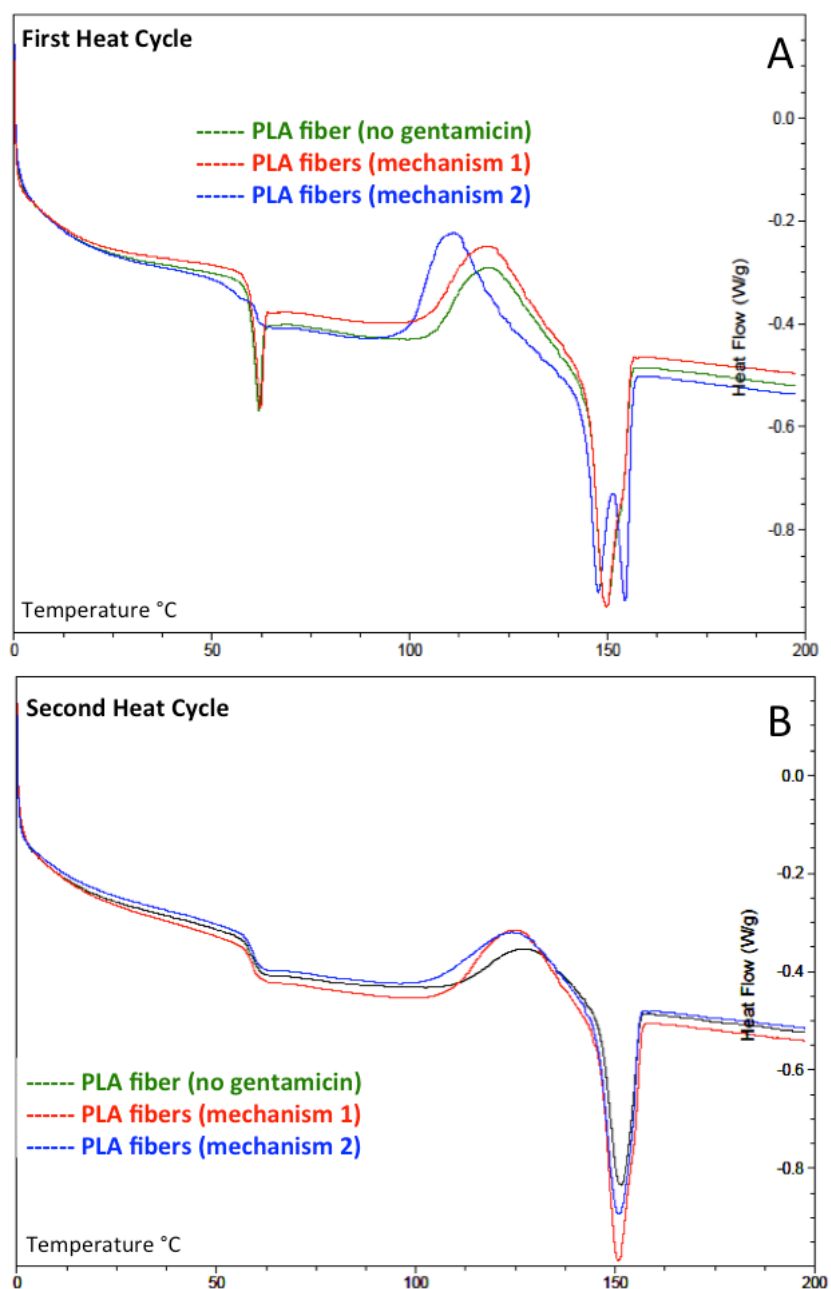


Figure 5.10: (A) DSC plot after first heating cycle of the experimental and control group. The control group and Mechanism 2 show different heat flow curves at the T_g value. Control group and Mechanism 2 show the same T_m values. Mechanism 3 depicts a different T_m value with two melting temperatures. All the groups show a varying crystallinity curve (B) DSC curve after second heat cycle shows similar T_g and T_m values but different crystallinity curves than the control polylactide group

Discussion

The outcomes demonstrate the fiber type, round or wicking, will affect the elution of gentamicin. Mechanism 1 successfully incorporated the gentamicin by wicking the antibiotic solution through round or wicking fiber bundles. Mechanism 2 loaded the fiber bundles by quenching the monofilaments in a water bath containing the gentamicin solution. The wicking fiber bundles loaded by mechanism 1 showed greater gentamicin release initially. By wicking solution into the bundles the gentamicin remains on the surface of the bundles trapped between the inter fiber spaces and grooves. Since gentamicin is water-soluble we expect to see high releases of the antibiotic from the surface initially for samples loaded by mechanism 1. The wicking fiber bundles showed significantly greater release of gentamicin at the initial time point than round fibers. This suggests the wicking fibers incorporate more gentamicin through wicking than the round fibers. The later time points show the wicking fiber bundles loaded by mechanism 2 has the greatest cumulative release from day 1 to day 14. By incorporating the antibiotic during the quenching process the gentamicin will bind more strongly to the surface, since the polymer has not quite solidified. The results show the antibiotic is released more slowly from mechanism 2 compare to mechanism 1. The wicking fibers loaded by mechanism 1 and 2 reached the minimal inhibitory concentration (MIC) of $1\mu\text{g/mL}$ at the initial time point and remained below the MIC for the remaining time points. This implies the loading concentration of the water bath should be increased or the amount of fibers used should be increased to produce higher elution concentrations. The results demonstrate the wicking fibers initially elute significantly higher concentrations of

antibiotic compared to the round fibers suggesting the increased surface area and geometry of the fibers plays a role in the gentamicin elution profile. This was also confirmed by the dissolution of the PLA fibers to determine the total concentration of antibiotic loaded. The wicking fiber loaded by mechanism 2 showed a ten-fold increase in gentamicin loaded than the round fibers loaded by the same mechanism.

Mechanism 3, however, showed a rapid burst release of the antibiotic after 24 hours and a steady release of the antibiotic above the minimal inhibitory concentration for 14 days. This high release can be attributed to incorporating the gentamicin into the raw material. Mechanism 1 and mechanism 2 incorporate gentamicin primarily on the surface leading to quick release of the antibiotic. The large single fiber showed a much higher burst release and cumulative release of the gentamicin. Interestingly, the amount of gentamicin loaded in the large single fibers was less than the gentamicin incorporated into the small wicking bundles. This implies the bundle has a slower release profile than the single large wicking fiber. The large fiber bundle has significantly greater surface area in contact with the buffer solution compared to the small fiber bundle. The reduced surface area in contact with the buffer and the tortuosity of the small fibers may contribute to the slower release from the bundle. After Day 14 most of the gentamicin has eluted from the large fiber bundle. The small fiber bundle, however, has eluted approximately 30% of the total antibiotic incorporated. We would expect consistent release from the bundles for 4 more weeks. Future work will investigate the long-term release from mechanism 3.

The antibiotic loading mechanisms 2 and 3 incorporate the antibiotic into the polylactide fiber. This was confirmed by the change in crystallinity of the DSC plots. Further work will investigate if the gentamicin will alter the degradation of the polymer.

Other research has been conducted investigating the release of gentamicin from polylactide beads or films for bone regeneration applications. Methods to incorporate gentamicin into polylactide involve creating a polymer solvent with gentamicin and casting the solution to form a film^{7,10}. Other methods have created polylactide beads loaded with gentamicin by sintering the polymer and antibiotic into a mold to form the bead¹⁰. Wang et al. has correlated the degradation of polylactide and antibiotic release. This research showed significant degradation and weight loss of the polymer at the surface with fractures and holes forming in the interior of the material over time. After 1 week, the surface degradation showed large holes on the surface and small holes initiating in the center. The increased concentration of gentamicin at days 7 and 14 in our study can correlate to the degradation rate of the polylactide. This suggest the fiber bundles may provide a long-term sustained release critical to preventing infections over months. Future work needs to investigate the release over longer periods of time. The water bath mechanism may not have bound gentamicin to the interior bulk of the polymer fibers.

The combined elution profiles of the alginate and wicking fiber construct has the potential to elute high concentrations of antibiotic initially when there is high infection risk for the patient by the alginate and also sustain release long-term with polylactide fibers.

References

1. Hickok NJ, Shapiro IM: Immobilized antibiotics to prevent orthopaedic implant infections. *Advanced Drug Delivery Reviews* 2012; 64:1165–76
2. Gimeno M, Pinczowski P, Vázquez FJ, Pérez M, Santamaría J, Arruebo M, Luján L: Porous orthopedic steel implant as an antibiotic eluting device: prevention of post-surgical infection on an ovine model. *International Journal of Pharmaceutics* 2013; 452:166–72
3. Musib M, Jones J, Chakote K, Hayes W, Saha S: Microhardness of bi-antibiotic-eluting bone cement scaffolds. *Progress in Biomaterials* 2012; 1:1–7
4. Zilberman M, Elsner JJ: Antibiotic-eluting medical devices for various applications. *Journal of Controlled Release* 2008; 130:202–15
5. Bormann N, Schwabe P, Smith MD, Wildemann B: Analysis of parameters influencing the release of antibiotics mixed with bone grafting material using a reliable mixing procedure. *Bone* 2013; 59:162–72
6. Anagnostakos K, Schröder K: Antibiotic-impregnated bone grafts in orthopaedic and trauma surgery: a systematic review of the literature. *International Journal of Biomaterials* 2012; 2012:1–9
7. Aviv M, Berdicevsky I, Zilberman M: Gentamicin-loaded bioresorbable films for prevention of bacterial infections associated with orthopedic implants. *Journal of Biomedical Materials Research: Part A* 2007; 83A:10–9
8. Triffo T: Master's Thesis: In Vivo Efficacy of Antibiotic-Eluting Phospholipid Coated Implants 2011:pp 1–97
9. Frutos P, Torrado S, Perez-Lorenzo ME, Frutos G: A validated quantitative colorimetric assay for gentamicin. *Journal of Pharmaceutical and Biomedical Analysis* 2000; 21:1149–59
10. Wang G, Liu S-J, Ueng SW-N, Chan E-C: The release of cefazolin and gentamicin from biodegradable PLA/PGA beads. *International Journal of Pharmaceutics* 2004; 273:203–12

CHAPTER SIX

DEVELOPMENT AND TESTING OF THE MODIFIED WICKING BUNDLE FOR CELL SEPARATION AND ISOLATION

Introduction

The National Cancer Institute estimates ten million Americans have or have had some form of cancer. The annual economic cost of cancer is \$126 billion¹. The high incidence rate of cancer drives the need for reliable and accurate testing. While testing ability has increased, the incidence of diagnostic error, including failure to diagnosis the existing cancer and delayed diagnosis can occur as frequently as 1 in 5 cancer cases². A major contributing factor for this error is the extensive oncologic pathology testing process. From the time the test for a patient is ordered to the time the test result is obtained the oncology pathology testing consists of 200-300 individual steps. This extensive process provides frequent opportunities to switch or contaminate samples, as well as chances to inadequately prepare, analyze, or interpret specimen properly³. The process can take up to ten days and often requires multiple pathologists and oncology specialists to confirm and analyze results. This system is time-consuming, expensive, and the testing frequently delivers subjective results.

The in vitro diagnostic (IVD) tests including histological analysis use biomarkers as an essential component for detection. The world market for IVD testing is expected to reach \$7 billion this year⁴. This technology is a relatively established market for biopsy analysis. However, the biomarker market is emerging for technologies that analyze liquid biological samples such as blood, serum, and urine⁵. Although the use of biomarkers has

improved prognosis of patients and developing therapeutics it considerably contributes to the incidence of oncology diagnostic error. A major limitation in using biomarkers to identify cancer is that there is no universal tumorigenic marker. The complexity and heterogeneity of the cancer cells within a tumor create a challenge for researchers to characterize the tumor based on phenotypic and genotypic biomarkers. Tumors are reported to have different subpopulations of cancer cells with varying phenotypes and degrees of tumor initiating capabilities⁶. Cancer stem cells are primarily considered to be a tumor propagating subpopulation that have the ability to self-renew and differentiate to form a hierarchy of cancer cells with varying metastatic potential and tumorigenic capabilities⁷⁻¹². The transient phenotypes of these cells create complexities for current detection methods and treatments¹³. For instance, cancer stem cells have the potential to be dormant or aggressive¹⁴. This ability to phenotypically change may cause resistance to treatment and recurrence¹⁵. The origin of these cancer stem cells remains elusive; however, researchers are finding cancer stem cells to have similar functions and protein expressions as progenitor cells¹⁶. The conventional methods for identifying progenitor or cancer cells involve detecting biomarkers and analyzing gene expression⁷. The use of phenotypic and genotypic biomarkers to identify progenitor lacks specificity, and provides limited information regarding the stem cell potential. Similarly, the use of biomarkers to detect cancer is very limited due to the heterogeneity of the cancer cells and plasticity of the expressed biomarkers.

Diagnostic techniques are shifting from invasive tissue samples towards liquid biopsy analysis, such as blood biopsy. A non-invasive blood biopsy sample can be used

for detecting circulating tumor cells (CTCs) to diagnose the cancer stage, monitor treatments, and provide insight into the metastatic process^{4,17}. However, major limitations for detecting CTCs are the exceedingly low concentrations of CTCs in blood samples and the heterogeneous phenotypes within the CTC population^{18,19}. As a result, the current CTC detection and isolation systems have low capture efficiencies and low specificity. Technologies for CTC detection and separation include macro-scale systems and microfluidics that use physical characteristics of the cells as well as surface labels. Most macro-scale systems use antibody-dependent techniques that detect epithelial markers to target CTCs. These approaches assume all CTCs are expressing epithelial markers, which therefore limit these approaches to a specific subpopulation of CTCs. Aggressive CTC populations may have mesenchymal phenotype that lack epithelial markers in the bloodstream are missed by these conventional technologies^{13,20–23}. Other CTC detection methods include microfluidic devices and chips that use both antigen-dependent and – independent techniques to detect and separate cancer cells. These approaches have better specificity and isolation efficiency but are restricted to small volumes of sample and low yield of isolated CTCs^{19,24}.

We have investigated the use of wicking fibers to separate cancerous from normal cell types, as well as, progenitor cell types from more differentiated cells. One aspect of this chapter was to evaluate the capability of wicking fibers to identify and isolate cancer cells from benign cells and metastatic cells from non-metastatic cells in heterogeneous cellular solutions. The other aspect was to assess the cell separation and isolation of progenitor cells and differentiated cell lines.

We first tested the ability of the single and bundled wicking fibers to (1) separate a mixture of normal mouse mammary epithelial cells (MMTV-neu) from mouse epithelial breast cancer cells (NMuMG), (2) separate and isolate malignant human breast epithelial cells (MCF-7) and benign human breast epithelial cells (MCF-10A), and (3) separate a mixture of mouse mesenchymal progenitor cells (D1) from mouse pre-osteoblast cells (MC3T3E1).

In the subsequent analysis, the ability of the modified wicking bundle (previously described in Chapter 4) to increase the rate and number of cells recruited and separated was investigated and tested. The cell separation and isolation of various cell types in the modified wicking bundle was investigated using (1) Human cancerous breast epithelial cells (MCF-7) and benign breast epithelial cells (MCF-10A), (2) Metastatic human breast cancer epithelial cells (MDA-MB-231) and benign breast epithelial cells MCF-10A, (3) Non-metastatic cancer cells (MCF-7) and metastatic cancer cells (MDA-MB-231), (4) a tri-culture mixture of benign (MCF-10A), non-metastatic (MCF-7), and metastatic (MDA-MB-231), and (5) Mouse mesenchymal progenitor cells (D1) and mouse pre-osteoblast cells (MC3T3E1). In this work we analyzed the wicking behavior, displacement, and isolation of various cell lines. We believe cellular characteristics including cell size, deformability, shape, cell surface charge, and cell surface adhesion molecules play a role in the cellular wicking of various cell lines. This chapter investigated if various cancer cell types can be distinguished based on their wicking behavior. Furthermore, the wicking behavior of progenitor cells and more differentiated cell lines was analyzed to compare similarities of progenitor and cancer cells. A summary

of the cell lines used and the wicking fiber tests performed in this chapter are presented in Table 6.1.

Table 6.1: Summarizes the cell lines used in this chapter

CELL LINE	DESCRIPTION
MMTV-NEU	Normal mouse mammary epithelial cells
NMUMG	Mouse epithelial breast cancer cells
MCF-7	Human cancerous breast epithelial cells
MCF-10A	Human benign breast epithelial cells
MDA-MB-231	Human metastatic breast epithelial cells
D1	Mouse mesenchymal stem cells
MC3T3E1	Mouse pre-osteoblast cells
RAW	Mouse macrophage cells

To investigate the cell wicking behavior the cell lines were labeled with a fluorescent tracker or transfected with fluorescent protein. Fluorescent microscopy and imaging software were used to semi-quantitatively analyze cell displacement. Cells were isolated from various regions of the construct and quantified using flow cytometry.

Table 6.2 summarizes the wicking fiber configuration used, the cell types investigated, and the analysis used to determine the wicking behavior.

Table 6.2: Summarizes the type of wicking fiber construct used to cell wicking, the cell types analyzed, and the type of analysis

Wicking fiber configurations used	Cell types used	Analysis
Single wicking fiber	Mouse cancer (NMuMG) and normal (MMTV-neu) cells	Fluorescent microscopy and imaging software
Single wicking fiber	Human cancer (MCF-7) and benign (MCF10-A) cells	Fluorescent microscopy and imaging software
Bundled wicking fiber	Human cancer (MCF-7) and benign MCF-10A cells	Fluorescent microscopy and flow cytometry
Modified wicking bundle	Human cancer (MCF-7) and benign (MCF-10A) cells	Fluorescent microscopy and flow cytometry
Modified wicking bundle	Human metastatic (MDA-MB-231) and benign (MCF-10A) cells	Fluorescent microscopy and flow cytometry
Modified wicking bundle	Human metastatic (MDA-MB-231) and non-metastatic cancer (MCF-7) cells	Fluorescent microscopy and flow cytometry
Modified wicking bundle	Human metastatic (MDA-MB-231), cancer (MCF-7), and benign cells (MCF-10A)	Fluorescent microscopy
Modified wicking bundle	Progenitor (D1) and differentiated pre-osteoblast (MC3T3E1) cells	Fluorescent microscopy and flow cytometry

Cell Separation along Single and Wicking Fiber Bundles

Materials and Methods

Mouse Cancer Cell Separation Using Single Wicking Fibers

Cell Culture

Cells from a normal mouse mammary epithelial cell line, NMuMG (ATCC), were stably transfected with Green Fluorescent Protein (NMuMG-GFP). Cells from a cancer mouse epithelial cell line (cells isolated from a mammary tumor that spontaneously arose in a MMTV-neu transgenic female mouse) were stably transfected with Red Fluorescent

Protein (MMTV-neu-RFP). NMuMG-GFP cells were cultured in Dulbecco's Modified Eagle's Medium (DMEM, Invitrogen) supplemented with 10% fetal bovine serum (FBS, Gibco), and Mammary Epithelial Cell Growth Medium (MEGM) single quotes (Lonza) while MMTV-neu-RFP cells were cultured in DMEM (Invitrogen) supplemented with 10% FBS (Gibco), 10,000 U penicillin, and 10 mg streptomycin/mL (Sigma-Aldrich). Cells were cultured in a T150 flask (Corning) and maintained in a humidified incubator at 37°C and 5% CO₂. Once cells were confluent, NMuMG-GFP and MMTV-neu-RFP were detached using trypsin-EDTA solution (Sigma) and resuspended in growth media to prepare for the vertical test.

Fiber Preparation

Poly-L-lactide (Natureworks) wicking fiber was extruded to non-circular cross-sectional dimensions of 0.72 mm x 0.55 mm. Wicking fibers were sliced into individual single wicking fibers of 3.5 cm. The fibers were cleaned by soaking in three changes of ethanol for 1 hour each, and placed under ultraviolet light for 6 hours. Samples were then soaked in a phosphate-buffered saline (PBS, Invitrogen) solution for 2 hours and air-dried overnight in a sterile hood.

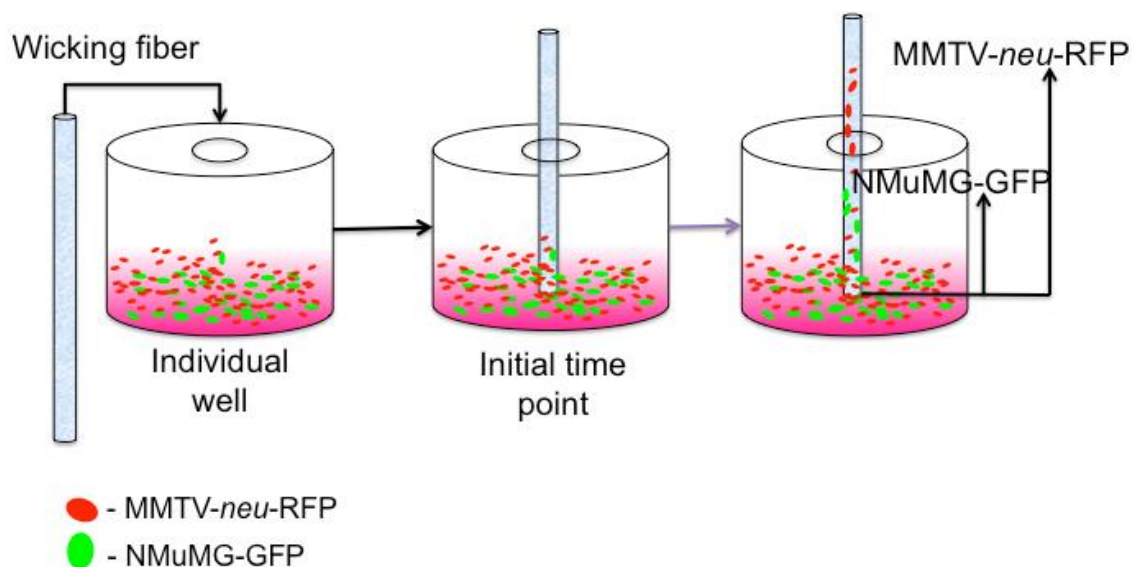


Figure 6.1: Schematic shows cell vertical wicking test set-up. The wells contain 1 mL of media consisting of equal densities of normal and cancer cells. The fiber is vertically placed into the cell solution so only 3 mm of the fiber is submerged. The cell movement is analyzed at various time points

Cellular Vertical Wicking Test

The vertical wicking test of cells, shown in Figure 6.1, involved a custom-made culture lid for a low-attachment 12-well plate (Corning). The lid provided holes with columns to securely hold the 3.5 cm wicking fibers and wicking fiber bundles in a vertical position. Both NMuMG-GFP and MMTV-neu cell lines were seeded in each well of a low attachment 12-well plate at a density of one million cells per well, along with 1 mL of growth media. Single wicking fibers were vertically inserted through the columns so only the bottom 3 mm of the fiber was contacting the cell solution. The custom 12-well plate set up was placed on a flattop shaker (VWR) at 100 rpm in a humidified incubator at 37°C and 5% CO₂. The vertical displacement of the mouse cancer and

normal mammary cells along the wicking were determined at time points of 0.5 and 24 hours, with an initial time point at the time of fiber placement into the cell solution.

To assess the cell displacement of both cell types the fibers were transferred to each well of 6-well plate, rinsed twice with phosphate buffered saline (PBS; Invitrogen), and fixed for 15 min with 4% paraformaldehyde. After the cells on the wicking fiber constructs were fixed, the fibers were transferred to microscope slides and the entire length of the fiber was imaged, using fluorescent microscopy, beginning with the seeded end of the wicking fiber construct using 25x total magnification. A FITC filter was used to view the vertical movement of normal cells transfected with Green Fluorescent Protein, and a TRITC filter was used to view the vertical movement of cancer cells transfected with Red Fluorescent Protein. Imaging software was used to determine the vertical displacement (μm) of the cells in each image taken along the fiber. Images were aligned to qualitatively show the total displacement of both normal and cancer cells, with total vertical displacement quantified by the summation of the individual images.

Statistical Analysis

Matched pairs analysis was conducting using JMP statistical software to compare ($p < 0.05$) the vertical displacement of MMTV-neu-RFP (cancer cells) and MMuMG-GFP (normal cells) at each of 0.5 and 24 hours.

Human Cancer Cell and Isolation Using Wicking Fiber Bundles

Cell Culture

Cells from a mammary epithelial cell line from benign breast tissue, MCF-10A (ATCC), were stably transfected with Green Fluorescent Protein (MCF-10A-GFP).

Cells from a human breast cancer cell line, MCF-7, (ATCC) were stably transfected with Red Fluorescent Protein (MCF-7-RFP). MCF-10A-GFP cells were cultured in DMEM (Invitrogen) supplemented with 10% FBS (Gibco), 1% Fungizone, and MEGM single quotes (Lonza). MCF-7-RFP cells were cultured in DMEM (Invitrogen) supplemented with 0.01 mg/mL human recombinant insulin (Gibco), 10% FBS, 1% Fungizone (Gibco), 10,000 U penicillin, and 10 mg streptomycin/mL (Sigma-Aldrich). Cells were cultured in a T-150 flask (Corning) and maintained in a humidified incubator at 37°C and 5% CO₂. Once confluent both cell types were removed with trypsin-EDTA solution (Sigma-Aldrich) and resuspended in culture medium to prepare for vertical testing.

Fiber Preparation

For this assessment, bundled fibers were used to increase the amount of cells along the fiber to quantify using the flow cytometer. Poly-L-lactide (Natureworks) wicking fiber was extruded to non-circular cross-sectional dimensions of 0.72 mm x 0.55 mm. Wicking fibers were sliced into individual single wicking fibers of 10 cm in length. Three of these fibers were twisted, using an apparatus, at 11 rotations per centimeter twist to create the wicking fiber bundle. The bundle was sliced into 3.5 cm long sections. Similar to the single fibers the bundles were cleaned by soaking in three changes of ethanol for 1 hour each, and placed under ultraviolet light for 6 hours. Samples were then soaked in PBS solution for 2 hours and air-dried overnight in a sterile hood.

Cellular Vertical Wicking Test

The vertical wicking test of cells as described above was performed using the wicking fiber bundles to analyze the wicking behavior of the cancerous cells, MCF-7-RFP, and the benign cells, MCF-10A-GFP. The vertical displacement of these cell lines along the fibers were determined at time points of 0.25 hours, 2 hours, 12 hours and 24 hours, with the initial time point being fiber placement into the cell solution. The fluorescently red-labeled cancer and green-labeled normal cells were imaged along the fiber bundles with fluorescent microscopy using 25x total magnification and following the same procedure described above.

Isolation of Cancer and Normal Cells from the Fibers

After 24 hours the vertical wicking fiber bundles were removed from the custom 12-well plate and the fibers were sectioned with a blade into top and bottom fiber regions (Fig 2). The top and bottom regions were placed in separate wells of a 24-well plate. The samples were rinsed with PBS twice and untwisted using forceps. The cells were removed by adding 500 μ L of trypsin-EDTA solution into the well with the fiber region and placing the plate on a flat-top (VWR) shaker at 200 rpm in a 37°C incubator. After 2 hours the cells were resuspended in 500 μ L of growth media and the number of MCF-10A and MCF-7 in both regions of the fiber were evaluated using a Guava easyCyte flow cytometer (Guava Technologies). We evaluated the number of MCF-10A-GFP and MCF-7-RFP in each region by following the manufacturer's instructions for InCyte software (Guava Technologies). Positive and negative controls with known cell densities were used to calibrate the machine before measurements of the treatment groups were made.

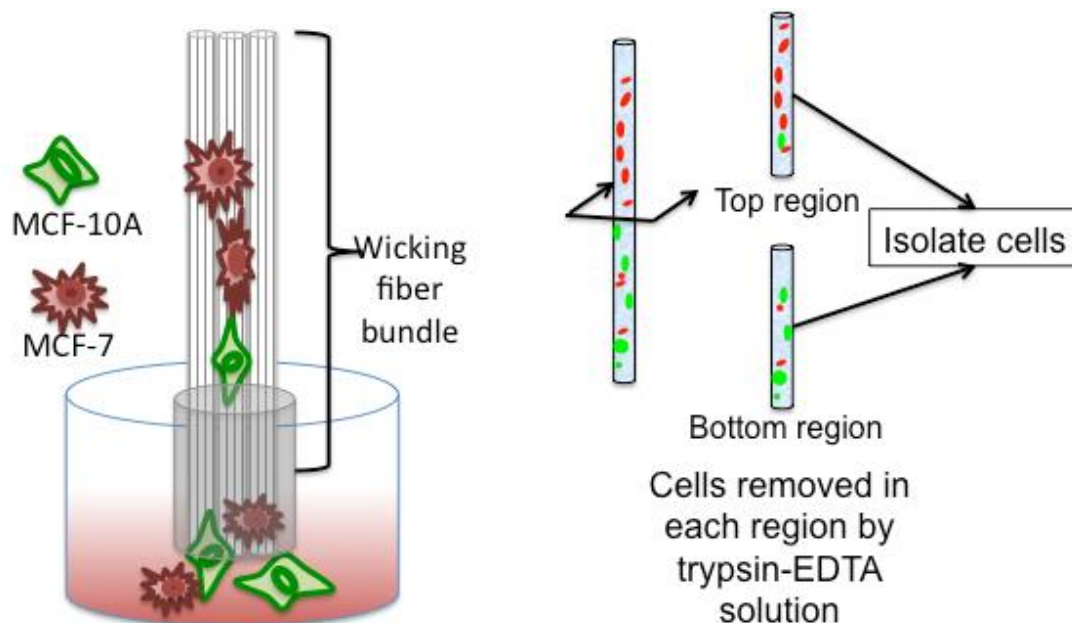


Figure 6.2: Left schematic shows the vertical test set-up of human cancer and benign cells. The right schematic shows the isolation of cells from the top and bottom regions of the wicking fiber bundle for analysis.

Statistical Analysis

A matched pairs analysis was conducted in JMP 10 to compare ($p < 0.05$) the fraction of MCF-7-RFP cells in top and bottom regions of the fiber bundle.

Separation of Mouse Progenitor and Monocyte Cells

Cell Culture

Mouse mesenchymal stromal cells, D1 (ATCC), and mouse monocytes, RAW 264.7 (ATCC), were both cultured in growth media consisting of Dulbecco's Modified Eagle's Medium (DMEM, Invitrogen) supplemented with 10% fetal bovine serum (FBS, Gibco), 10,000 U penicillin, and 10 mg streptomycin/mL (Sigma-Aldrich). Cells were cultured in a T150 flask (Corning) and maintained in a humidified incubator at 37°C and

5% CO₂. Once cells were confluent, D1 and RAW cells were detached using trypsin-EDTA solution (Sigma) and resuspended in growth media to prepare for the vertical test. RAW and D1 cells were fluorescently labeled with CellTracker Green CMFDA probe and CellTracker™ Red CMTPX probe (Invitrogen; Grand Island, NY, USA), respectively, following the manufacturer's protocol and using a long-term labeling concentration of 25µM.

Fiber Preparation

Poly-L-lactide (Natureworks) wicking fiber was extruded to non-circular cross-sectional dimensions of 0.72 mm x 0.55 mm. Wicking fibers were sliced into individual single wicking fibers of 3.5 cm. The fibers were cleaned by soaking in three changes of ethanol for 1 hour each, and placed under ultraviolet light for 6 hours. Samples were then soaked in a phosphate-buffered saline (PBS, Invitrogen) solution for 2 hours and air-dried overnight in a sterile hood.

Vertical Test Set-Up and Analysis

The vertical wicking test of D1 and RAW cells was performed using single wicking fibers. Both cell types were seeded in each of the wells of a low attachment 12-well plate with a cell density of 1 million cells per mL. The fibers were vertically inserted into the custom-made lids designed to keep the fiber vertical and only 3 mm of the tip submerged. The displacement of the D1 and RAW cells was determined at time points of 1 and 24 hours using fluorescent microscopy and imaging software. Imaging software was used to determine the vertical displacement (µm) of the cells in each image taken

along the fiber. Images were aligned to qualitatively show the total displacement of both normal and cancer cells, with total vertical displacement quantified by the summation of the individual images.

Results

Mouse Cancer Cell Separation Using Single Wicking Fibers

We developed a vertical test method to assess the vertical movement of different cell mixtures along the fiber. The vertical displacements of mouse mammary normal cells expressing green fluorescent protein (NMuMG-GFP) and mouse mammary cancer cells expressing red fluorescent protein (MMTV-neu-RFP) were determined at time points of 0.5 and 24 hours using fluorescence microscopy. Figure 6.3 is a composite of fluorescent images, showing the cancer and normal cells along the length of the fiber, aligned to qualitatively show the total displacement of both cell types after 24 hours of contacting cell solution. Image A demonstrates that MMTV-neu-RFP cells have vertically displaced 16.2 mm along the wicking fiber after 24 hours. Image B shows NMuMG-GFP cells vertically moved 3.0 mm, significantly less than the MMTV-neu-RFP cells, on the same wicking fiber. Images also depict higher cell densities of MMTV-neu-RFP cells along the fiber. Images qualitatively show a vertical separation of MMTV-neu-RFP and NMuMG-GFP cells, indicating the wicking fibers move different cell types various distances. Imaging software was used to quantify the vertical displacement (μm) of the cells. The total vertical displacement was found from assessing each individual image. The vertical displacement of the cancer cells, MMTV-neu-RFP, along the wicking fiber was significantly ($p < 0.05$) greater than that of the normal cells (NMuMG-GFP) at the 24-hour

time point (Image C). No significant difference was shown after 0.5-hour time point. Results suggest wicking fibers can separate and allow the rapid identification of cancer cells from a liquid with heterogeneous mix of cells.

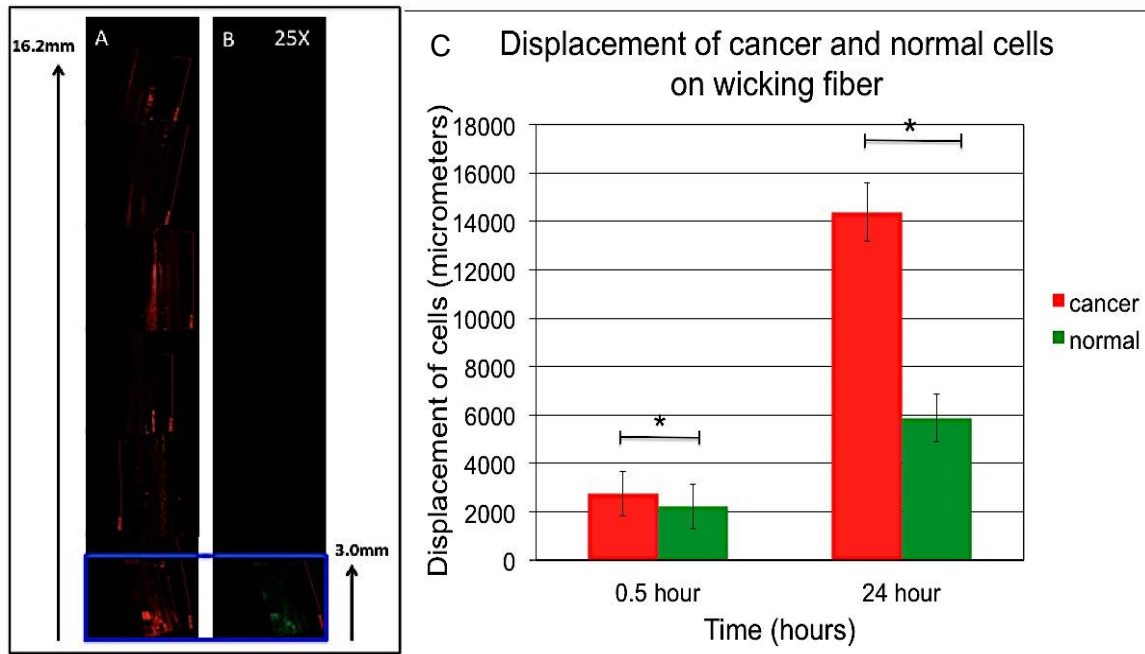


Figure 6.3: (A) Depicts compiled fluorescent images of the vertical displacement of MMTV-neu-RFP, cancer cells, along the length of the fiber. (B) Shows NMuMG-GFP, normal cells, progressed significantly less than the cancer cells. (C) Graph shows quantitative analysis of the vertical displacement of cancer cells (2759 ± 928.9 (SD), $n=4$) and mouse normal cells (2219 ± 940.6 (SD), $n=4$) after various time points. After 24 hours there was significantly greater vertical displacement of MMTV-neu-RFP (14380 ± 1192 (SD), $n=4$) than displacement of NMuMG-RFP (6220 ± 994.2 (SD), $n=4$) ($p < 0.05$), indicated by (*) in graph.

Human Cancer Cell Separation and Isolation Using Wicking Fiber Bundles

To observe and quantify the effects of wicking fibers on human cancer cell separation and isolation, we developed a wicking fiber bundle that enhances the rate of separation and increases cell capacity. The bundles demonstrated enhanced wicking

properties, i.e. the overall wicking rate and volume of liquid transported were enhanced. The wicking fiber bundle was used to separate and isolate malignant human breast epithelial cells expressing red fluorescent protein (MCF-7-RFP) from benign human breast epithelial cells expressing green fluorescent protein (MCF-10A-GFP). Fluorescent images of the bundles were used to evaluate the vertical displacement and separation of MCF-7-RFP and MCF-10A-GFP after 0.25, 2, 12, and 24 hours. Images show that, after 15 minutes and 2 hours, MCF-7-RFP cells have progressed along the entire fiber but in low numbers. After 12 hour and 24-hour time points, much higher numbers of MCF-7-RFP have traveled to the top region of the fiber. Fluorescent images indicate after 2 hours and the later time points, few benign epithelial cells progressed to the top region of the fiber bundles, Figure 6.4.

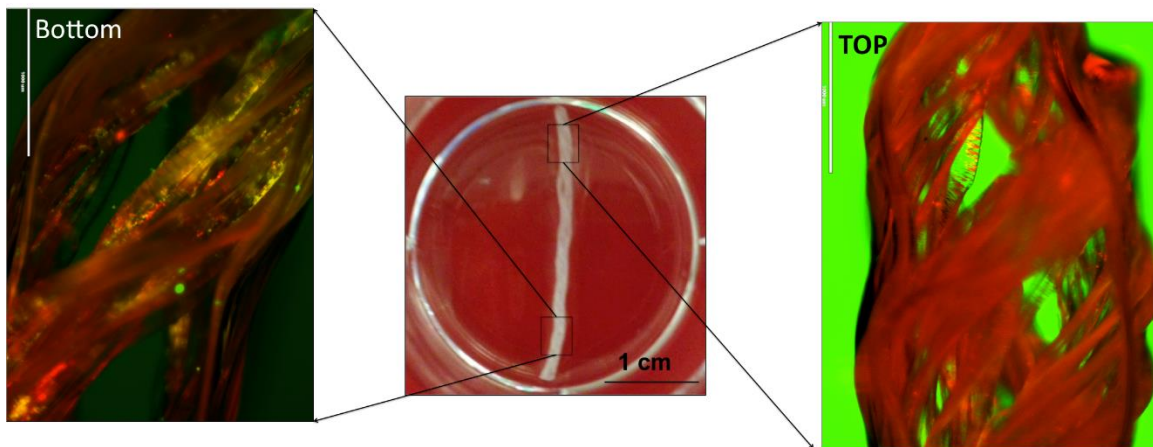


Figure 6.4: (Left) Approximately equal densities of red and green fluorescently labeled cancer and normal cells depicted in bottom region of the fiber. (Right) Mostly fluorescently labeled red cells in top region indicating cancer cells displace the entire wicking fiber bundle

To quantify the number of cancerous and benign cells along the fiber bundles, cells were removed from top and bottom regions of the bundles Figure 6.5. The number of MCF-7-RFP and MCF-10A-GFP was determined using flow cytometry (Guava Technologies) with InCyte software (Guava Technologies). The chart illustrates the percentage of each cell type in top and bottom regions; there is a significant difference ($p < 0.05$) between the percentage of MCF-7-RFP and the percentage of MCF-10A-GFP in the top region of the fiber bundles. These results strongly suggest that the wicking fiber bundles can separate and isolate cancerous cells, with high accuracy, from a mixture; as the graph indicates, 82% of cells isolated from the top fiber bundle regions are cancerous.

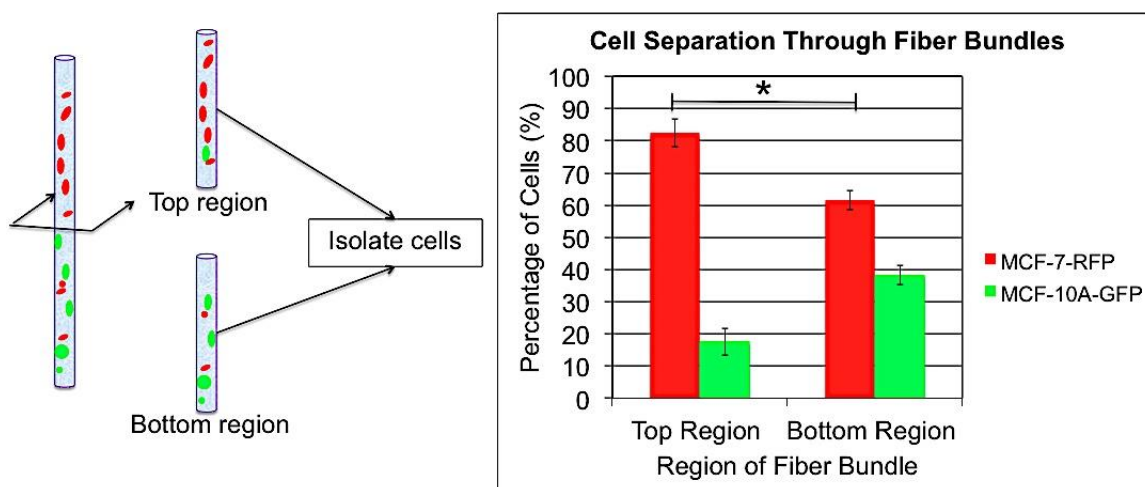


Figure 6.5: Schematic of the fiber regions and data depicting percentage of each cell type in fiber regions. Left image illustrates axial slicing of fiber bundle to extract cells from top and bottom regions. Graph exhibits quantitative analysis of top and bottom region of the fiber bundle, demonstrating significantly higher concentration of MCF-7-RFP cells in the top region of the fiber bundle (82.4 ± 4.3 (SD), $n=3$) than the bottom region of the fiber bundle (61.6 ± 3.04 (SD), $n=3$) The graph indicates a significantly lower concentration of MCF-10A-GFP cells in top region (17.6 ± 4.3 (SD), $n=3$) than bottom region (38.4 ± 3.04 (SD), $n=3$), (*) indicates significant difference, $p < 0.05$

Mesenchymal Stem Cell and Monocyte Separation Using Single Wicking Fibers

The outcomes of the vertical wicking of D1 and RAW cells along a single wicking fiber showed greater displacement of D1 cells after 1 hour and 24 hours than RAW cells, Figure 6.6. The composite fluorescent image of RAW and D1 cells after 1 hour shows higher cell density of D1 cells, labeled red, penetrating the bottom region of the fiber. Image J software was used to measure the total displacement of each cell line along the fiber. The total vertical displacement of D1 cells along the fiber was greater than RAW cells after 1 hour and 24 hours (Image B). The outcomes suggest the displacement of different cell types along the wicking fiber may provide a method to identify progenitor cells and more a differentiated cell line, monocytes.

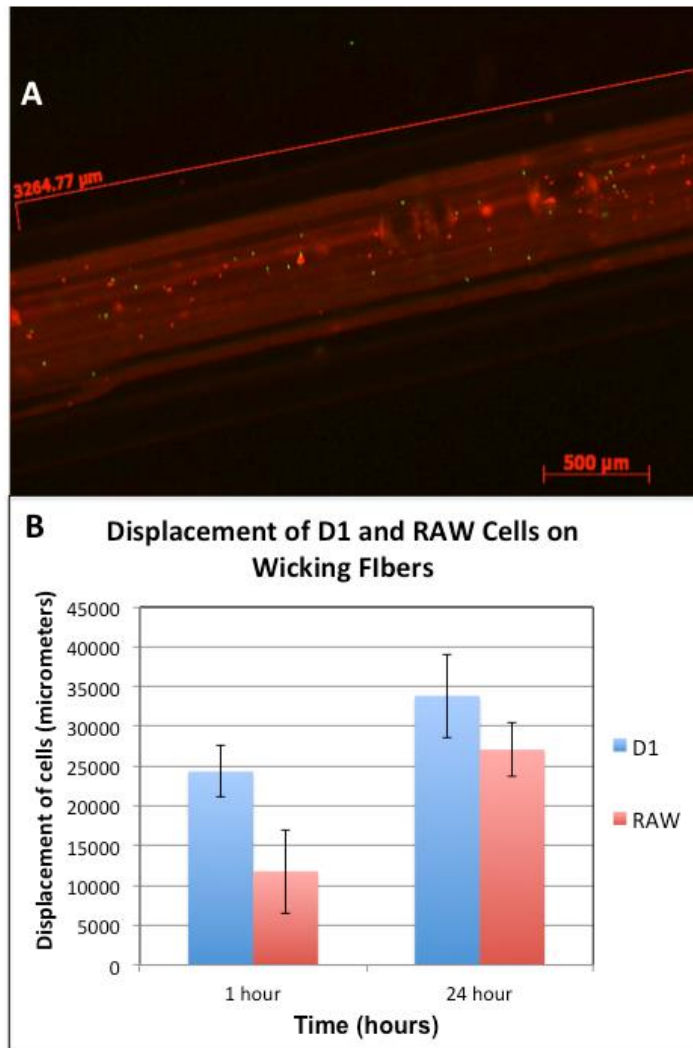


Figure 6.6: (A) Fluorescent image shows vertical displacement of RAW and D1 cells along the bottom region of the wicking fiber bundle. Image shows higher densities of red fluorescently labeled D1 cells. (B) D1 cells show increased vertical displacement after 1 hour and 24 hours

Cell Separation and Isolation along Modified Wicking Bundle

Materials and Methods

The modified wicking bundle, comprised of wicking fibers and an absorbent cap, was developed and tested to separate and isolate different cancer cell types. As shown from chapter 4 the absorbent cap enhances the fluid flow and infiltration of cells. The modified bundle was used in the following tests to more rapidly separate and isolate different cell types and isolate large numbers of cells to quantitatively analyze with flow cytometry.

Human Breast Cancer and Normal Cell Separation and Isolation along Modified Wicking Bundle

Cell Culture

Cells from a mammary epithelial cell line from benign breast tissue, MCF-10A (ATCC), and human breast cancer cell line, MCF-7, (ATCC) were cultured in DMEM (Invitrogen) supplemented with 10% FBS (Gibco), 1% Fungizone, and MEGM single quotes (Lonza) and DMEM (Invitrogen) supplemented with 0.01 mg/mL human recombinant insulin (Gibco), 10% FBS, 1% Fungizone (Gibco), 10,000 U penicillin, and 10 mg streptomycin/mL (Sigma-Aldrich), respectively. Cells were cultured in a T-150 flask (Corning) and maintained in a humidified incubator at 37°C and 5% CO₂. Once confluent both cell types were removed with trypsin-EDTA solution (Sigma-Aldrich) and resuspended in culture medium to prepare for vertical testing. MCF-10A and MCF-7 cells were fluorescently labeled with CellTracker™ Green CMFDA probe and CellTracker™ Red CMTPX probe (Invitrogen; Grand Island, NY, USA), respectively following manufacturer's protocol. Samples were prepared for both imaging and flow

cytometry analysis. To fluorescently image cells along the fibers, a long-term labeling concentration of 25 μM for both red and green cell tracker was used to label the cells. The red and green cell tracker was optimized for each cell line to detect using the flow cytometry (Appendix). To detect isolated cells from the wicking fiber-alginate constructs with flow cytometer, MCF-7 cells were labeled with 5.0 μM cell tracker red and MCF-10A cells were labeled with the optimized cell tracker green concentration of 0.05 μM .

Modified Wicking Bundle Preparation

Poly-L-lactide (Natureworks LLC, USA) wicking fibers were extruded with irregular cross-sectional dimensions of 0.72 mm by 0.55 mm. Wicking fibers were sliced with a razor blade into individual single wicking fibers of 10 cm lengths. The 10 cm wicking fibers were used to form the wicking fiber bundles comprised of ten individual and three individual fibers. The fiber bundles were twisted, using an apparatus, at approximately 11 and 5 rotations per centimeter twist for the large and small fiber bundles, respectively. The bundle was sliced into 3 cm long sections. Bundled wicking fibers were cleaned by soaking in three changes of ethanol for 1 hour each, and placed under ultraviolet light for 6 hours. Samples were then soaked in a phosphate-buffered saline (PBS, Invitrogen) solution for 2 hours and air-dried overnight in a sterile hood. The alginate cap was formed by dipping one end of the wicking fiber bundle in 100 μL of 5M CaCl_2 solution (Fisher Scientific; Waltham, MA, USA) in a well of a 96-well plate and pipetting 100 μL of 1.4% (w/v) alginate solution comprised of alginic acid sodium salt from brown algae (Sigma; St. Louis, MO) in 155 mM NaCl (Sigma; St. Louis, MO)

directly on the submerged fiber tip in the well. The alginate immediately adheres to the fiber end and solidifies forming the modified wicking bundle.

Experimental Set-up

The vertical wicking test of MCF-7 and MCF-10A cells was performed using the modified wicking bundle. Both cell types were seeded in each of the wells of a low attachment 12-well plate with a cell density of 500,000 cells per mL. MCF-7 and MCF-10A cells labeled with 25 μM cell tracker were seeded into six wells for fluorescent microscopy analysis. The remaining six wells were seeded with MCF-7 labeled with 5.0 μM red tracker and MCF-10A cells labeled with 0.05 μM of green tracker for flow cytometry analysis. Modified wicking bundles containing only 3 individual fibers were vertically inserted into the wells containing cells for fluorescent imaging, and bundles containing 10 fibers were vertically placed in wells containing cells for flow cytometry analysis. The bundles containing three fibers were used for imaging to improve the contrast and image deeper into the bundle. The bundles for flow cytometry contained 10 fibers to isolate enough detectable cells for the instrument to analyze. The experimental set-up is shown below in a 12-well plate. Immediately following the vertical placement of the modified fiber bundles in the appropriate wells the 12-well plate was placed on a flattop shaker (VWR) at 100 rpm in a humidified incubator at 37°C and 5% CO₂. The vertical displacement of the human cancer and benign breast epithelial cells along the wicking were determined after 2 hours of incubation, with the initial time point being fiber placement into the cell solution.

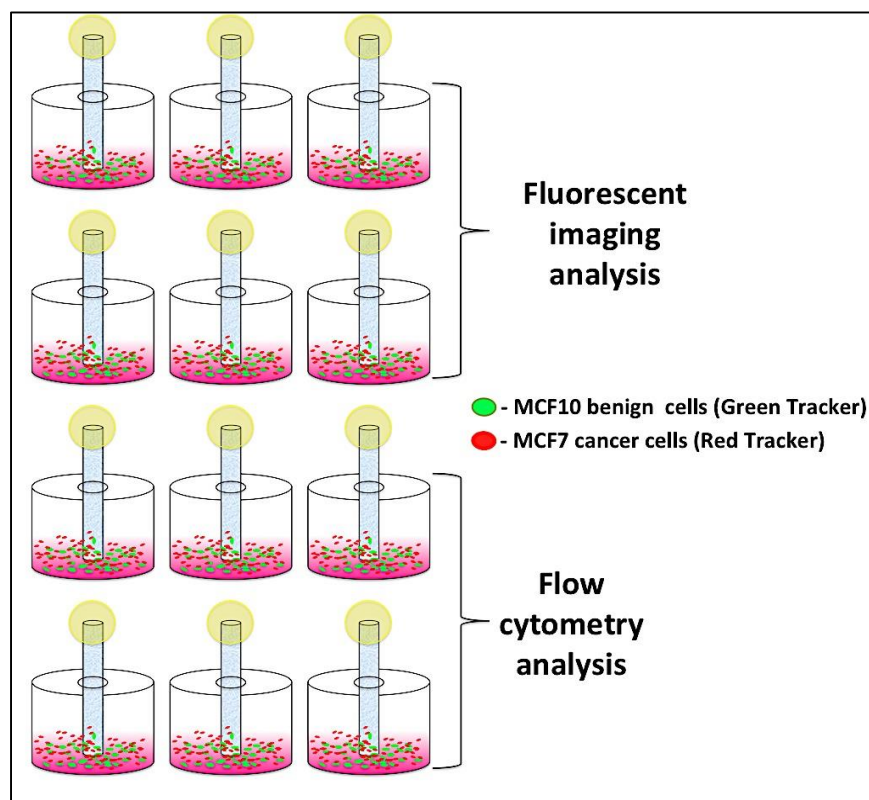


Figure 6.7: Set-up to analyze cell separation and isolation

Analysis of Cell Separation and Isolation

To qualitatively assess the cell separation along the modified wicking bundle the samples were transferred to a well of 6-well plate, rinsed twice with phosphate-buffered saline solution, and fixed for 15 min with 4% paraformaldehyde. After the cells on the modified wicking bundle were fixed, the fibers were transferred to microscope slides and the vertical displacement was evaluated using fluorescent microscopy and imaging software was used to overlay the images. Various regions of the construct were imaged using fluorescent microscopy, shown in the schematic below.

The bottom, middle, top, alginate-bundle interface, and alginate cap regions of the modified wicking bundle were imaged with a 20x or 40x total magnification. A FITC filter was used to view the vertical movement of normal cells labeled green, and a TRITC filter was used to view the vertical movement of cancer cells labeled red.

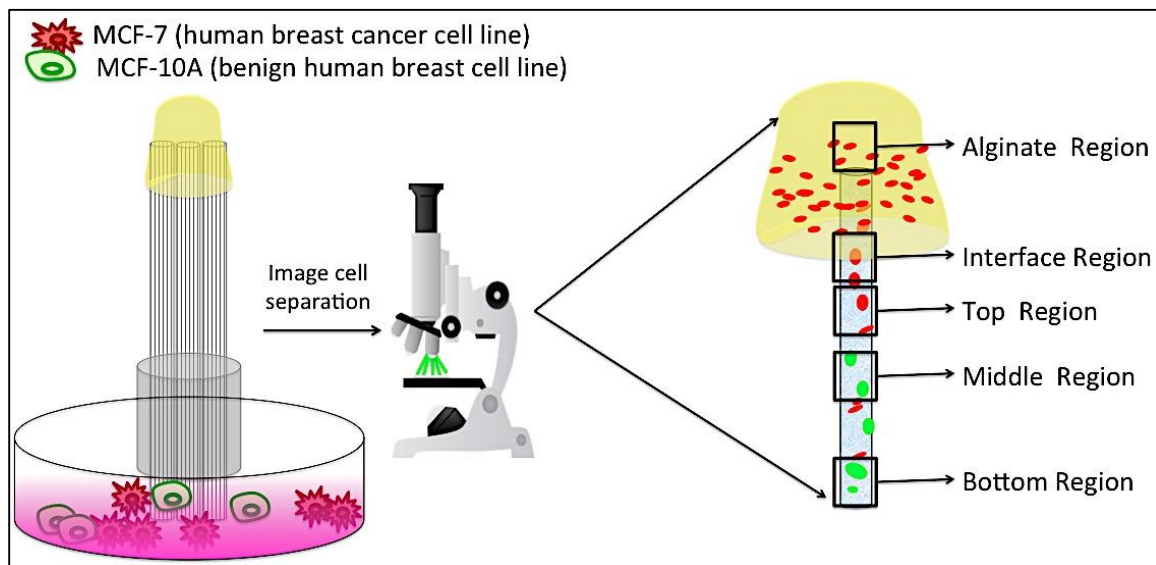


Figure 6.8: Schematic depicts fluorescent microscopy analysis and regions of interest images

To quantify the cancer normal cell separation the construct was sectioned into top, bottom and alginate regions and the cells were removed from each region, illustrated in schematic. The alginate caps were first removed from the fiber bundles and transferred to a 1.5 mL Eppendorf microcentrifuge tubes (Sigma; St. Louis, MO USA) containing 1 mL of the stock dissolution buffer. The buffer was comprised of 100mM sodium citrate (Fisher Scientific; Waltham, MA USA), 10 mM HEPES buffer (Sigma; St. Louis, MO

USA), and 27 mM NaCl (Sigma; St. Louis, MO USA) in 50 mL of distilled water. The alginate caps were dissolved for 30 minutes at 37°C and mixed vigorously using the vortex every 5 minutes. The wicking fiber bundle region was sectioned with a blade into top and bottom regions were placed into separate wells of a 24 well plate, Samples were rinsed with PBS and untwisted. Cells were removed by adding 500 µL of trypsin-EDTA solution into the well with the fiber region and placing the plate on a flat-top (VWR) shaker at 200 rpm in a 37°C incubator. After 15 min the cells were resuspended in 500 µL of growth media and the number of red labeled MCF-7 and green labeled MCF-10A cells were determined from the alginate caps and top and bottom regions of the fiber bundles using a Guava easyCyte flow cytometer (Guava Technologies). The number of cancer and normal cells in each region was evaluated by following the manufacturer's instructions for InCyte software (Guava Technologies). MCF-7 and MCF-10A cells of known cell densities with and without red and green tracker, were used as positive and negative controls to calibrate the machine before measurements of the treatment groups were made.

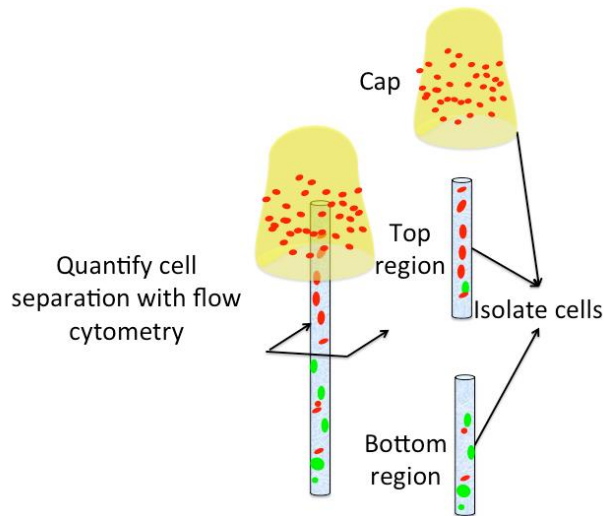


Figure 6.9: Schematic shows regions cancer and normal cells were isolated from along the modified wicking bundle

Statistical Analysis

A matched pairs analysis was conducted in JMP 10 to compare ($p < 0.05$) the fraction of red-labeled MCF-7 cells in top and bottom regions of the fiber bundle and the alginate cap.

Investigating Cell Separation and Isolation of Metastatic Cancer Cells and Benign Breast Epithelial Cells along Modified Wicking Bundle

Cell Culture

Cells from a mammary epithelial cell line from benign breast tissue, MCF-10A (ATCC), and metastatic breast epithelial cells, MDA-MB-231, (ATCC) were cultured in DMEM (Invitrogen) supplemented with 10% FBS (Gibco), 1% Fungizone, and MEGM single quotes (Lonza) and DMEM (Invitrogen) supplemented with 10% FBS, 1% Fungizone (Gibco), 10,000 U penicillin, and 10 mg streptomycin/mL (Sigma-Aldrich),

respectively. Cells were cultured in a T-150 flask (Corning) and maintained in a humidified incubator at 37°C and 5% CO₂. Once confluent both cell types were removed with trypsin-EDTA solution (Sigma-Aldrich) and resuspended in culture medium to prepare for vertical testing. MCF-10A and MDA-MB-231 cells were fluorescently labeled with CellTracker Green CMFDA probe and CellTracker Red CMTPX probe (Invitrogen; Grand Island, NY, USA), respectively following manufacturer's protocol. Samples were prepared for both imaging and flow cytometry analysis. To fluorescently image cells along the fibers, a long-term labeling concentration of 25 µM for both red and green cell tracker was used to label the cells. The red and green cell tracker was optimized for each cell line to detect using the flow cytometry (Appendix). To detect isolated cells from the wicking fiber-alginate constructs with flow cytometer, MDA-MB-231 cells were labeled with 5.0 µM cell tracker red and MCF-10A cells were labeled with the optimized cell tracker green concentration of 0.50 µM.

Experimental Set-up and Analysis

The cell separation and isolation of metastatic cancer cells, MDA-MB-231, and benign epithelial cells, MCF-10A, were investigated using the modified wicking bundle. The modified wicking bundles were formed using the same procedure above. Those containing three wicking fibers were used for imaging analysis and those containing ten wicking fibers were used for flow cytometry analysis. Following the vertical wicking procedure previously described, 500 µL of cell solution containing a cell density of 500,000 cells per mL was pipette in each of the wells of a low attachment 12-well plate with a custom-made lid to secure the modified fibers vertically in the well. Six samples

were prepared for fluorescent microscopy and six samples were prepared for flow cytometry analysis. The experimental set-up is shown below in Image A of Figure 6.10. Following the procedures above, the plate was placed on a flattop shaker at 100 rpm in a humidified incubator at 37°C and 5% CO₂. The separation of the human metastatic cancer and benign breast epithelial cells along the constructs were determined after 2 hours of incubation, with the initial time point being fiber placement into the cell solution. The samples were fluorescently imaged (Image B) and analyzed using flow cytometry (Image C) following the procedures from the preceding section.

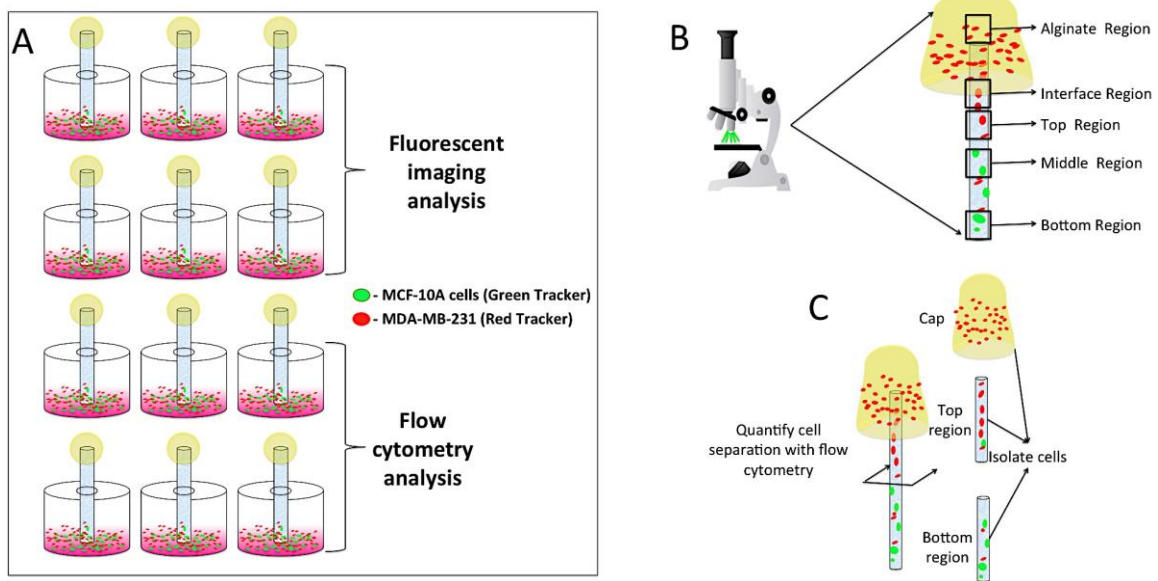


Figure 6.10: (A) Experimental set-up investigating vertical displacement of metastatic cancer cells and benign epithelial cells (B) Qualitative analysis using fluorescent microscopy (C) Flow cytometry analysis

Statistical Analysis

A matched pairs analysis was conducted in JMP 10 to compare ($p < 0.05$) the fraction of metastatic cancer cells (MDA-MB-231) in top and bottom regions of the fiber bundle and the alginate cap.

Investigating Cell Separation and Isolation of Metastatic Cancer Cells and Non-Metastatic Cancerous Breast Epithelial Cells along Modified Wicking Bundle

Cell Culture

Non-metastatic cancerous breast epithelial cells, MCF-7 (ATCC), and metastatic breast epithelial cells, MDA-MB-231, (ATCC) were cultured in DMEM (Invitrogen) supplemented with 10% FBS (Gibco), 1% Fungizone, and 0.01 mg/mL human recombinant insulin (Gibco) and DMEM (Invitrogen) supplemented with 10% FBS, 1% Fungizone (Gibco), 10,000 U penicillin, and 10 mg streptomycin/mL (Sigma-Aldrich), respectively. Cells were cultured in a T-150 flask (Corning) and maintained in a humidified incubator at 37°C and 5% CO₂. Once confluent both cell types were removed with trypsin-EDTA solution (Sigma-Aldrich) and resuspended in culture medium to prepare for vertical testing. MDA-MB-231 and MCF-7 cells were fluorescently labeled with CellTracker™ Green CMFDA probe and CellTracker™ Red CMTPX probe (Invitrogen; Grand Island, NY, USA), respectively following manufacturer's protocol. Samples were prepared for both imaging and flow cytometry analysis. To fluorescently image cells along the fibers, a long-term labeling concentration of 25 μM for both red and green cell tracker was used to label the cells. The red and green cell tracker was optimized for each cell line to detect using the flow cytometry (Appendix). To detect isolated cells from the wicking fiber-alginate constructs with flow cytometer, MCF-7

cells were labeled with 5.0 μM cell tracker red and MDA-MB-231 cells were labeled with the optimized cell tracker green concentration of 0.50 μM .

Experimental Set-up and Analysis

The cell separation and isolation of non-metastatic cancer cells (MCF-7) and further metastatic cancer cells (MDA-MB-231) were investigated using the modified wicking fiber bundle construct. The wicking fiber-alginate cap constructs containing three wicking fibers for imaging analysis or ten wicking fibers for flow cytometry analysis were formed using the same procedure above. Following the vertical wicking procedure previously described, 500 μL of cell solution containing a cell density of 500,000 cells per mL from each cell type was pipette directly in each of the wells of a low attachment 12-well plate with a custom-made lid to secure the modified fibers vertically in the well. Six samples were prepared for fluorescent microscopy and six samples were prepared for flow cytometry analysis. After performing the vertical test the samples were fluorescently imaged and analyzed using flow cytometry following the procedures from the preceding section.

Statistical Analysis

A matched pairs analysis was conducted in JMP 10 to compare ($p < 0.05$) the fraction of metastatic cancer cells (MDA-MB-231) in top and bottom regions of the fiber bundle and the alginate cap.

Investigating Cell Separation of Metastatic Cancer Cells, Non-Metastatic Cancerous Breast Epithelial Cells, and Benign Breast Epithelial Cells along Modified Wicking Bundle

Cell Culture

Benign breast epithelial cells (MCF-10A), Non-metastatic cancerous breast epithelial cells, MCF-7, and metastatic breast epithelial cells, MDA-MB-231, were cultured in DMEM (Invitrogen) supplemented with 10% FBS (Gibco), 1% Fungizone, and MEGM single quotes (Lonza), DMEM (Invitrogen) supplemented with 10% FBS (Gibco), 1% Fungizone, and 0.01 mg/mL human recombinant insulin (Gibco), and DMEM (Invitrogen) supplemented with 10% FBS, 1% Fungizone (Gibco), 10,000 U penicillin, and 10 mg streptomycin/mL (Sigma-Aldrich), respectively. Cells were cultured in a T-150 flask (Corning) and maintained in a humidified incubator at 37°C and 5% CO₂. Once confluent both cell types were removed with trypsin-EDTA solution (Sigma-Aldrich) and resuspended in culture medium to prepare for vertical testing. MCF-10A and MCF-7 cells were fluorescently labeled with CellTracker™ Green CMFDA probe and CellTracker™ Red CMTPX probe (Invitrogen; Grand Island, NY, USA), respectively following manufacturer's protocol using the recommended long-term labeling concentration of 25 µM. MDA-MB-231 cells were fluorescently labeled blue using a 1:500 dilution of a 2mg/mL Hoechst solution (Sigma; St. Louis, MO USA).

Experimental Set-up and Analysis

This study assessed the cell separation from a tri-culture of human cancer cells of varying metastatic potential. The vertical displacement and separation of metastatic cancer cells, MDA-MB-231, non-metastatic cancerous breast epithelial cells, MCF-7, and

benign breast epithelial cells was investigated using the modified wicking bundle. Modified wicking bundles were formed using the same procedure above. Those containing three wicking fibers were used for imaging analysis. Following the vertical wicking procedure previously described, 500 μ L of cell solution from each fluorescently labeled cancer cell line containing a cell density of 500,000 cells per mL was pipette in each of the wells of a low attachment 12-well plate with a custom-made lid to secure the modified fibers vertically in the well. Following two hours of incubation, the samples were removed, fixed with paraformaldehyde, and imaged using fluorescent microscopy.

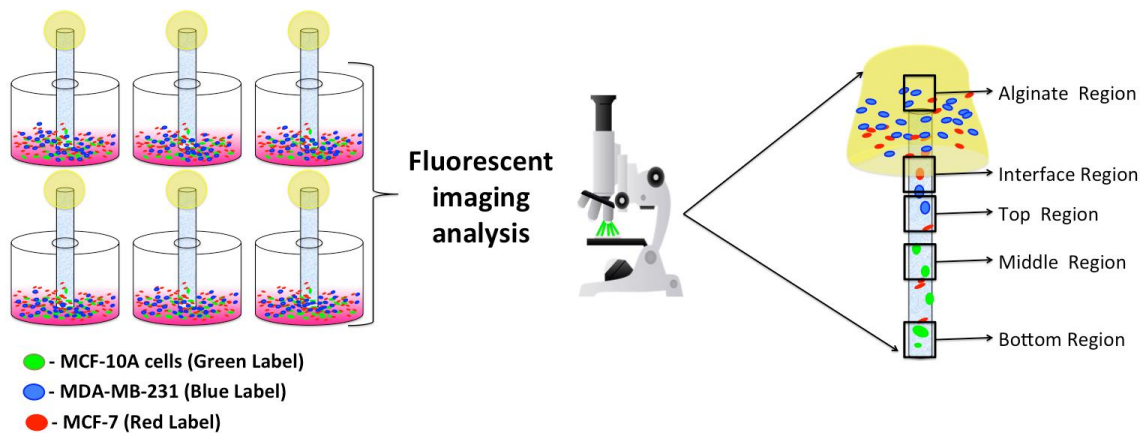


Figure 6.11: Schematic depicting experimental set-up to analyze a tri-culture of benign and of cancer cells of varying metastatic potential

Cell Separation and Isolation of Mesenchymal Stem Cells and Pre-Osteoblast Cells

Cell Culture

Mouse mesenchymal stem cells, D1 (ATCC), and mouse pre-osteoblast cells, MC3T3E1 (ATCC), were cultured in growth media consisting of Dulbecco's Modified

Eagle's Medium (DMEM, Invitrogen) supplemented with 10% fetal bovine serum (FBS, Gibco), 10,000 U penicillin, and 10 mg streptomycin/mL (Sigma-Aldrich), and Minimal Essential Medium Alpha without ascorbic acid (MEM α , Gibco) supplemented with 10% fetal bovine serum (Gibco), 10,000 U penicillin, and 10mg streptomycin/mL (Sigma), respectively. Cells were cultured in a T150 flask (Corning) and maintained in a humidified incubator at 37°C and 5% CO₂. Once cells were confluent, D1 and MC3T3E1 cells were detached using trypsin-EDTA solution (Sigma) and resuspended in growth media to prepare for the vertical test. D1 and MC3T3E1 cells were fluorescently labeled with CellTracker™ Green CMFDA probe and CellTracker™ Red CMTPX probe (Invitrogen; Grand Island, NY, USA), following manufacturer's protocol, respectively. Samples were prepared for both imaging and flow cytometry analysis. To fluorescently image cells along the fibers, a long-term labeling concentration of 25 μ M for both red and green cell tracker was used to label the cells. The red and green cell tracker was optimized for each cell line to detect using the flow cytometry (Appendix). To detect isolated cells with flow cytometer, MC3T3E1 cells were labeled with 5.0 μ M cell tracker red and D1 cells were labeled with the optimized cell tracker green concentration of 0.50 μ M.

Statistical Analysis

A matched pairs analysis was conducted in JMP 10 to compare ($p < 0.05$) the fraction of mouse mesenchymal stem cells (D1) in top and bottom regions of the fiber bundle and alginate cap.

Experimental Set-up and Analysis

The cell separation and isolation of bone progenitor cells, D1, and further differentiated pre-osteoblast cells, MC3T3E1, were investigated using the modified wicking bundle. The modified wicking bundles containing three wicking fibers for imaging analysis or ten wicking fibers for flow cytometry analysis were formed using the same procedure above. Following the vertical wicking procedure previously described, 500 μ L of cell solution containing a cell density of 500,000 cells per mL from each cell type was pipette directly in each of the wells of a low attachment 12-well plate with a custom-made lid to secure the modified fibers vertically in the well. Six samples were prepared for fluorescent microscopy and six samples were prepared for flow cytometry analysis. After performing the vertical test the samples were fluorescently imaged and analyzed using flow cytometry following the procedures from the preceding section.

Results

Human Breast Cancer and Normal Cell Separation and Isolation along Modified Wicking Bundle

The fluorescent images, Figure 6.12, of regions along the modified wicking bundle depict a clear separation of benign epithelial cells (MCF-10A) labeled green and cancerous epithelial cells (MCF-7) labeled red.

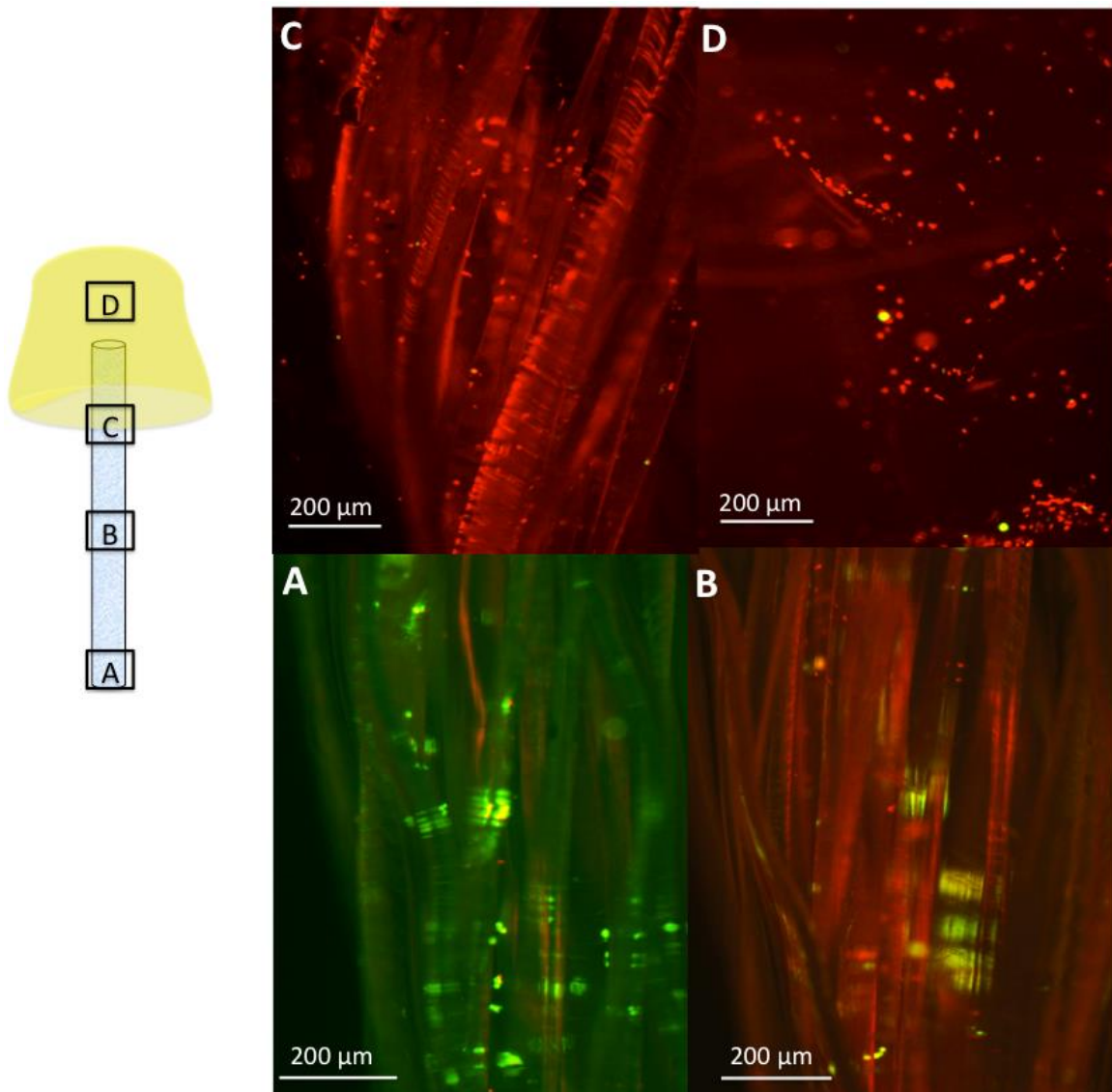


Figure 6.12: Fluorescent images of the cancerous MCF-7 (red) and benign MCF-10A (green) epithelial cell displacement along the modified wicking bundles. (A) Depicts more MCF-10A cells in the bottom region of the fiber bundle where the cell solution contacts the fiber bundle. (B) Similar cell densities of MCF-7 and MCF-10A cells in the middle region of the fiber bundle. (C) Depicts primarily MCF-7 cells along the top region of the fiber in the alginate cap. (D) Reveals significantly more cancer cells in the alginate cap

The flow cytometer was used to quantify the amount of green and red fluorescently labeled cells in each region of the construct. The flow cytometer scatter plots and fluorescent intensity plots indicate the cancer cell lines contain cells of different sizes and shapes. The MCF-7 cells depict a wider range of cell sizes and the MCF-10A cells illustrate a range of complexities (Figure 6.13). The results in Figure 6.14 report the percentages of benign and cancerous cells from each region. Image A shows more than 80% of the cells isolated from the alginate cap are cancerous cells. Similarly, the outcomes presented in image B demonstrate approximately 80% of the cells isolated from top region of the fiber bundle are the cancerous MCF-7 cells. The bottom region shows comparable amounts of benign and cancer cells. Although there were larger percentages of cancer cells in the top region of the bundle and the alginate cap, there were significantly less total cells in these regions as indicated by the scatter and fluorescent intensity in the decreased amount of cells in the top bundle regions and the alginate cap is likely due to the processing methods. The dissolution of the alginate cap may cause debris, as well as cell debris and clumping that will limit the number of cells detected. Furthermore, cells are tightly bound within the grooves of the fiber bundles, and the removal procedures used to isolate cells from the fibers may not reach the cells tightly bound in the inter-fiber and groove conduits. However, the amount of cancerous cells isolated from the regions is significantly higher than the benign cells and verifies the fluorescent images. The outcomes of both analyses show the modified wicking bundles can separate cancer cells from benign cells by isolating the cancer cells in the top fiber region and alginate cap. The modified wicking bundles enhanced the amount of cells that

penetrated the fiber compared to the unmodified wicking bundle and single wicking fiber samples. The alginate provided a collection sink for cancer cells as demonstrated by the images and by the flow cytometry analysis.

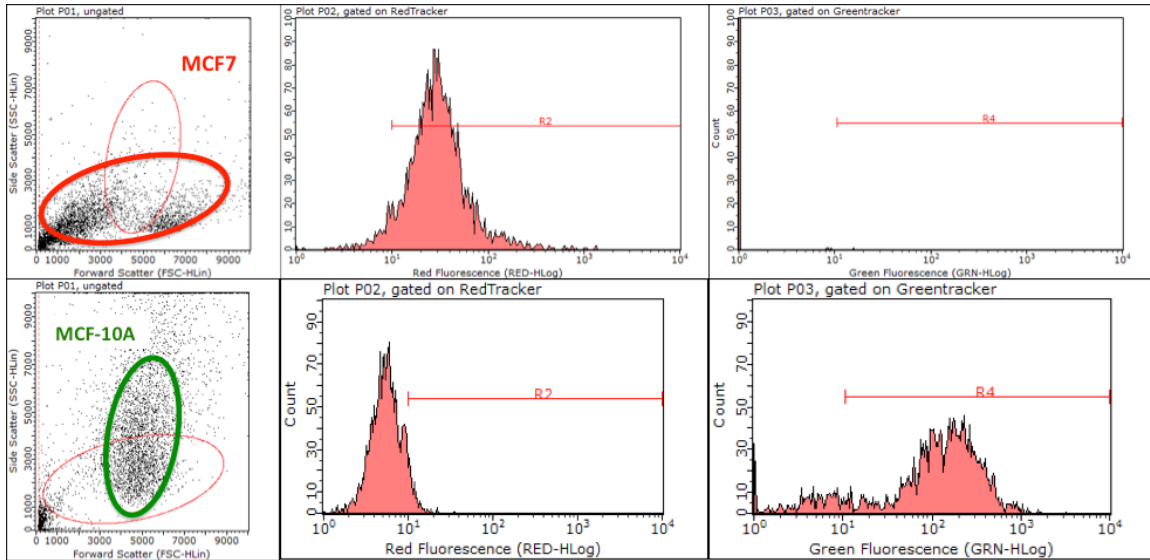


Figure 6.13: Scatter plots of control groups from flow cytometry analysis. Depicts the forward and side-scattering plots of MCF-7 (Top Row) and MCF-10A (Bottom Row). The red and green fluorescent intensity plots show the MCF-7 cells are labeled with red fluorescence and the MCF-10A cells are labeled with green fluorescence.

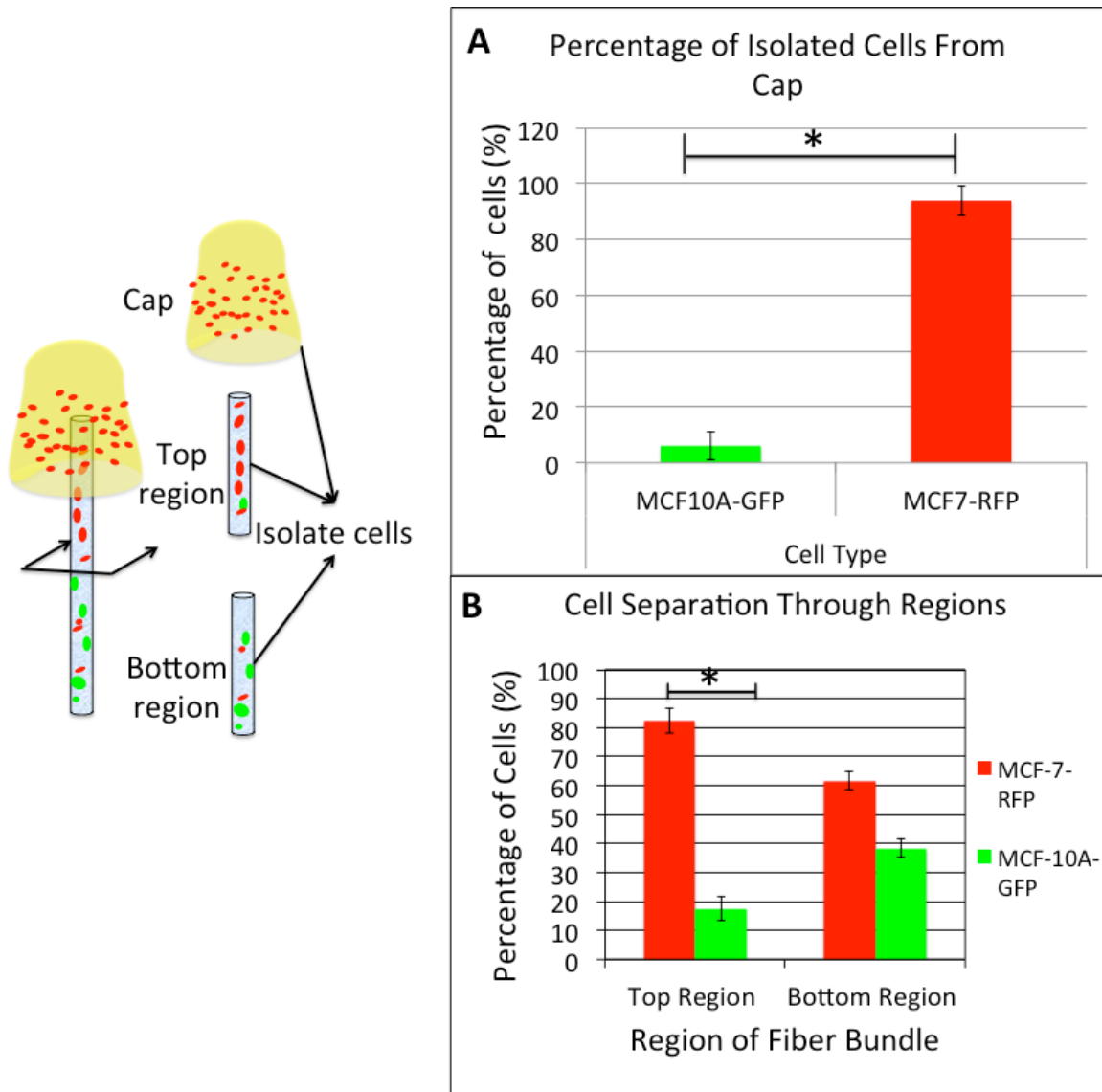


Figure 6.14: Flow cytometry results investigating the number of cancer and benign cells in each region. Chart illustrates significantly higher percentage of MCF-7 in alginate cap (A) and in top region of wicking fiber bundle (*) indicates significant difference of $p < 0.05$ (B). No comparable difference in percentage of MCF-7 and MCF-10A cells in bottom region of the wicking fiber bundle

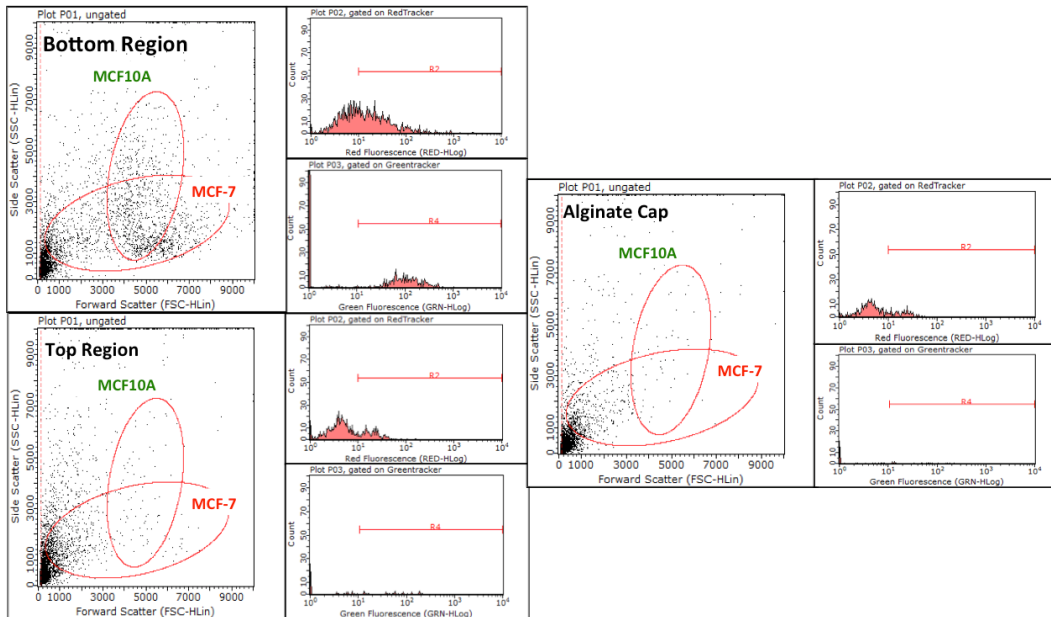


Figure 6.15: Forward scatter plots and fluorescence intensity of MCF-10A and MCF-7 cells in each region. The forward scatter plot shows greater numbers of both cell types in the bottom region compared to the top fiber region and the alginate cap. The bottom region depicts similar red and green fluorescent intensities. The top fiber region and alginate cap show high red fluorescent intensity counts correlating to mainly cancer cells in these regions

Investigating Cell Separation and Isolation of Metastatic Cancer Cells and Benign Breast Epithelial Cells along Modified Wicking Bundle

This test investigated the separation of cancer cell line with greater metastatic potential than the MCF-7 cells. The fluorescent images (Figure 6.16) show greater vertical displacement of the metastatic cancer cells (MDA-MB-231) labeled red into the middle and top regions of the fiber bundle. The bottom region (Image A) of the wicking fiber bundle depicts comparable cell densities of the MDA-MB-231 cells and benign breast epithelial cells (MCF-10A) labeled green. Higher cell densities of the metastatic cancer cells are collected in the top region (image C) of the fiber and alginate cap (image D).

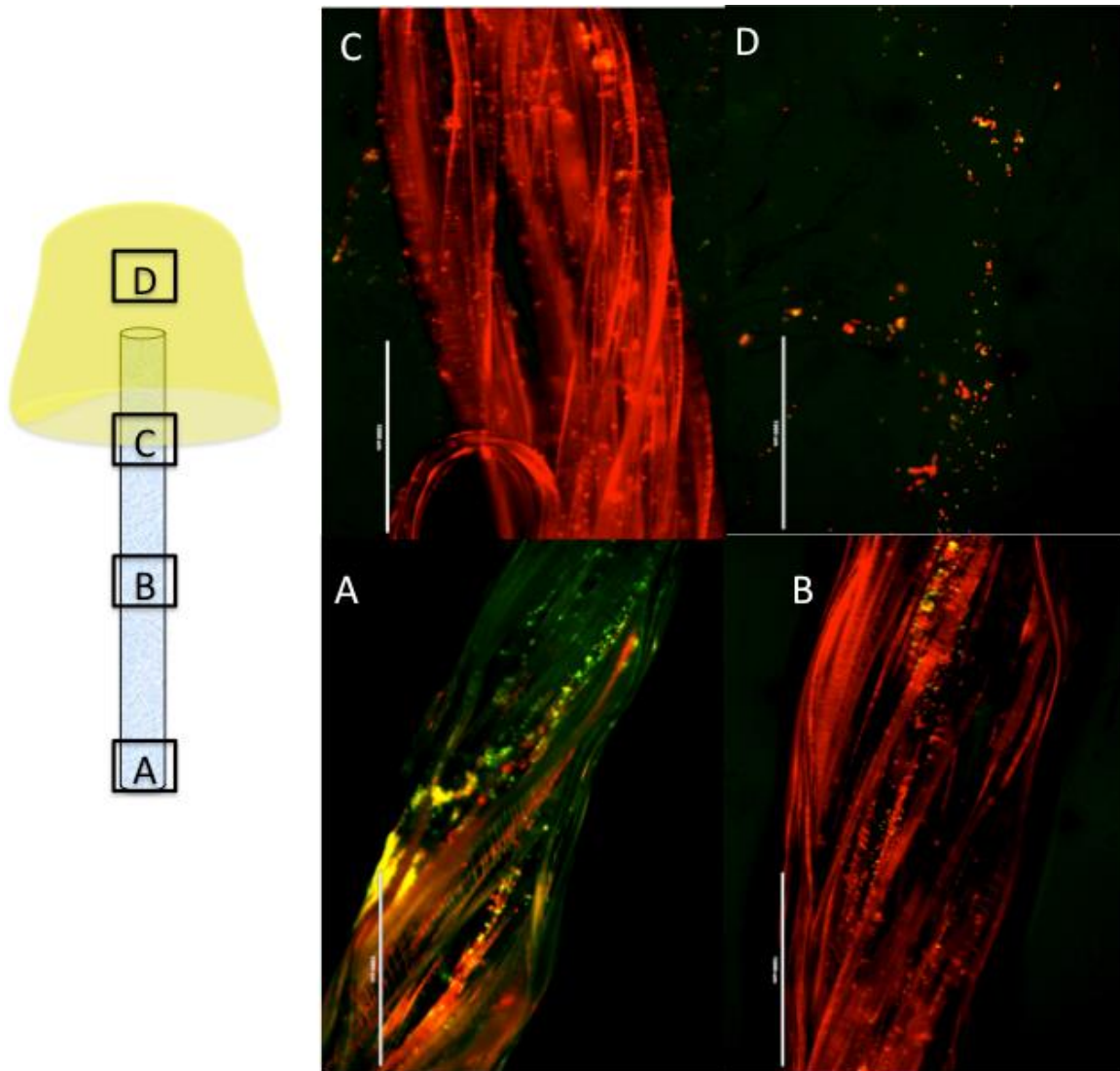


Figure 6.16: Fluorescent images analyzing the vertical displacement of metastatic breast cancer cells (red) and benign breast epithelial cells (green). Comparable cell densities are depicted in the bottom or seeded region of the fiber (A). Greater numbers of metastatic cancer cells (red) wick to the middle (B) and top (C) regions of the fiber. (D) The alginate cap consists of greater numbers of the metastatic cancer cells.

The flow cytometry outcomes illustrated analogous results to the previous study assessing separation of MCF-7 and MCF-10A cells. Both regions of the wicking fiber bundle and the alginate cap contained significantly more red-labeled metastatic cancer cells, MDA-MB-231 than the benign epithelial cells, as presented in Image C of Figure 6.19. The outcomes show modified wicking bundle provides a method to separate the metastatic cancer cells and benign cells along the fiber bundles.

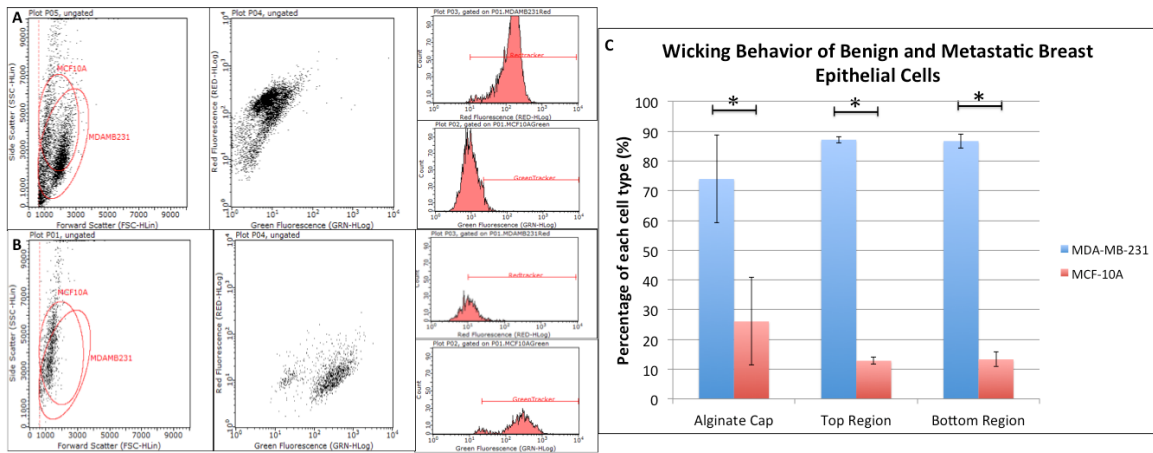


Figure 6.17: (A) Scatter and fluorescent intensity plots confirming the red-label of the MDA-MB-231 metastatic cancer cells. (B) Scatter and fluorescent intensity plots of green-labeled benign cells. (C) Depicts separation of the metastatic cells, MDA-MB-231 from MCF10A cells in each region of the fiber bundle and alginate cap.

Investigating Cell Separation and Isolation of Metastatic Cancer Cells and Non-metastatic Cancerous Breast Epithelial Cells along Modified Wicking Bundle

The fluorescent images in Figure 6.18 show more metastatic cancer cells (labeled green) in the top region (Image C) of the wicking fiber bundle and the alginate cap (Image D). Non-metastatic cancer cells (red) were still observed in the alginate cap but show in fewer numbers. The bottom and middle regions of the wicking fiber bundle

(Image A and B) show greater metastatic cancer cell infiltration. To enhance separation of the metastatic and non-metastatic cancer cells further work will increase the specificity of the construct by altering the cross-sectional sizes of the wicking fiber bundle and modifying the absorbent material.

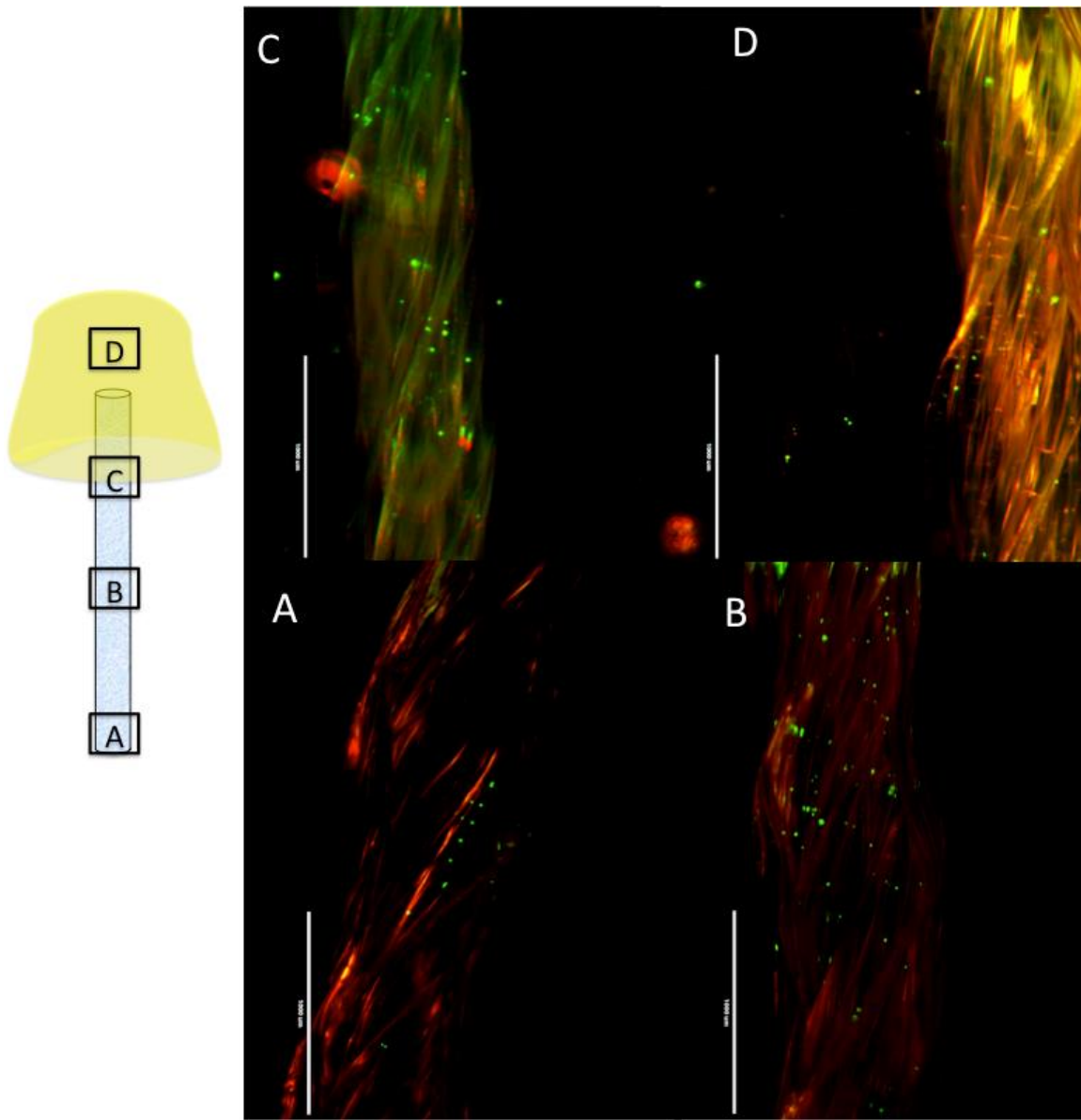


Figure 6.18: (A) and (B) depict similar cell densities of metastatic cancer cells (MDA-MB-231) labeled green and non-metastatic cancer cells (MCF-7) labeled red. (C) Top region of the wicking fiber bundle shows more metastatic cancer cells and (D) alginate cap depicts both metastatic and non-metastatic cancer cells.

The outcomes from flow cytometry depicted similar trends. The controls confirmed the metastatic cancer cells and non-metastatic cancer cells were successfully labeled with green and red cell tracker (Image A and B). The percentage of non-metastatic and metastatic cancer cells was measured from the cells removed from each region. The alginate and bottom region of the wicking fiber bundle contained similar amounts of non-metastatic and metastatic cells. The top region contained significantly more metastatic cancer cells (MDA-MB-231) than non-metastatic (MCF-7), using a significance value of $p < 0.05$.

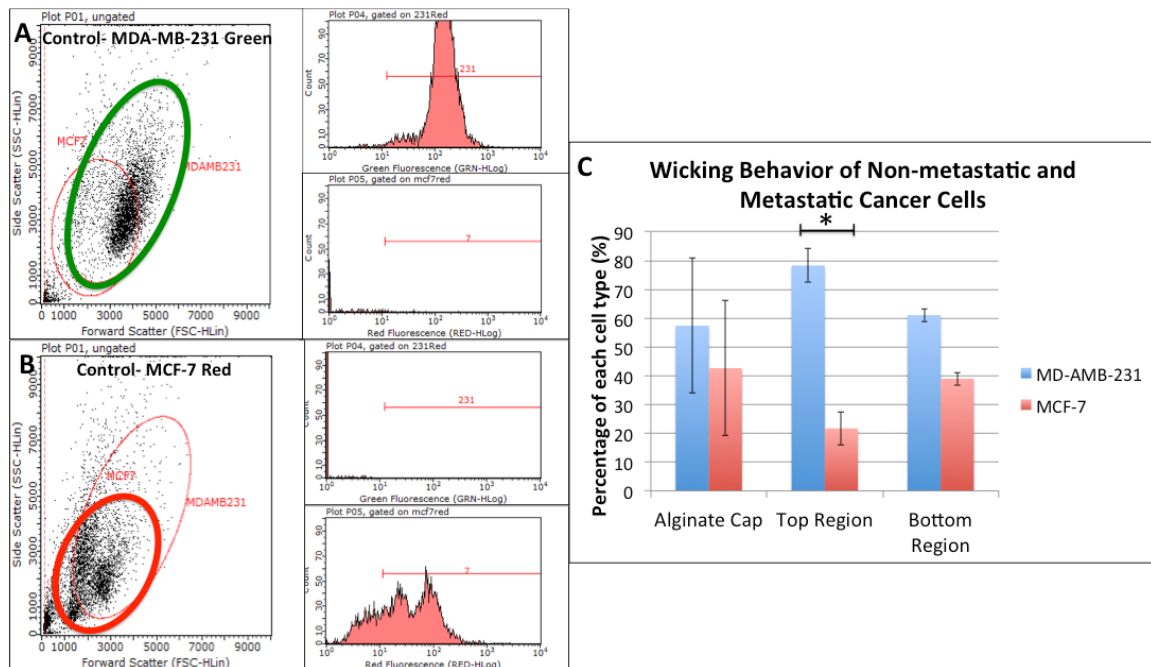


Figure 6.19: (A) Scatter plot of MDA-MB-231 metastatic cells. Red and green fluorescence intensity plots shows high green intensity and low red intensity confirming labeling procedure. (B) Scatter plot of MCF-7 non-metastatic cancer cells shows variation in size and shape of cells within cell line. The fluorescence intensity plots show high red intensity confirming the cells are fluorescently tagged red. (C) Comparable amounts of metastatic and non-metastatic cells in bottom region of the fiber bundle and the alginate cap. The top region depicts significantly more MDA-MB-231 cells than MCF-7 cells, (*) indicates significant difference, $p < 0.05$

The flow cytometry scatter plots showed significantly less total cells from the top region of the fiber bundle and the alginate cap. The low cell count detected by the flow cytometry in the alginate and wicking fiber bundle is due to the cell removal processing technique. More work is needed to improve the cell removal methods to increase the amount of cells removed without altering the cells and to obtain a more representative number of cells.

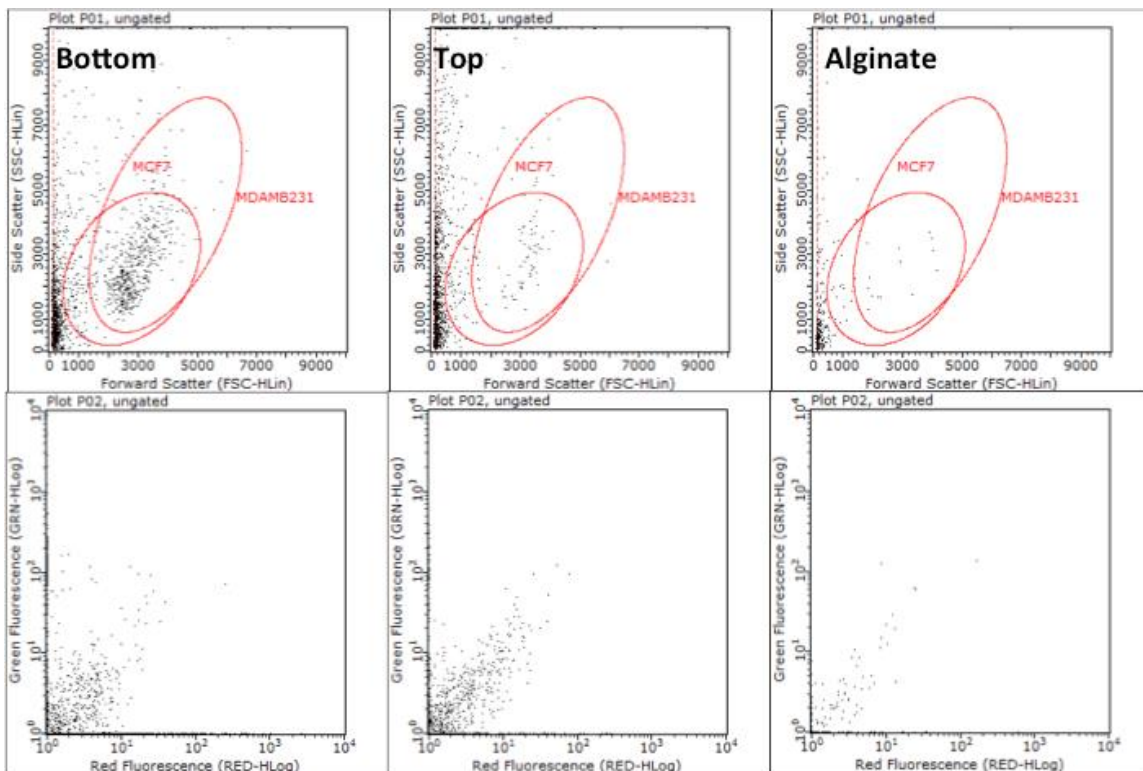


Figure 6.20: Scatter and fluorescent intensity plots depict low amounts of cell removal from the top fiber region and the alginate cap

Investigating Cell Separation of Metastatic Cancer Cells, Non-metastatic Cancerous Breast Epithelial Cells, and Benign Breast Epithelial Cells along Modified Wicking Bundle

The vertical displacement of a tri-culture was investigated along the modified wicking bundle using fluorescent microscopy, Figure 6.21. The bottom (Image A) and middle region (Image B) of the wicking fiber bundle depict all cell types consisting of MCF-10A cells labeled green, MCF-7 cells labeled red, and MDA-MB-231 cells labeled blue. The top region of the wicking fiber bundle (Image C) and the alginate cap (Image D) depict significantly more metastatic cancer cells, MDA-MB-231 cells than benign or cancerous cells. Interestingly, the MDA-MB-231 cells spread out in the alginate more than the other cell types.

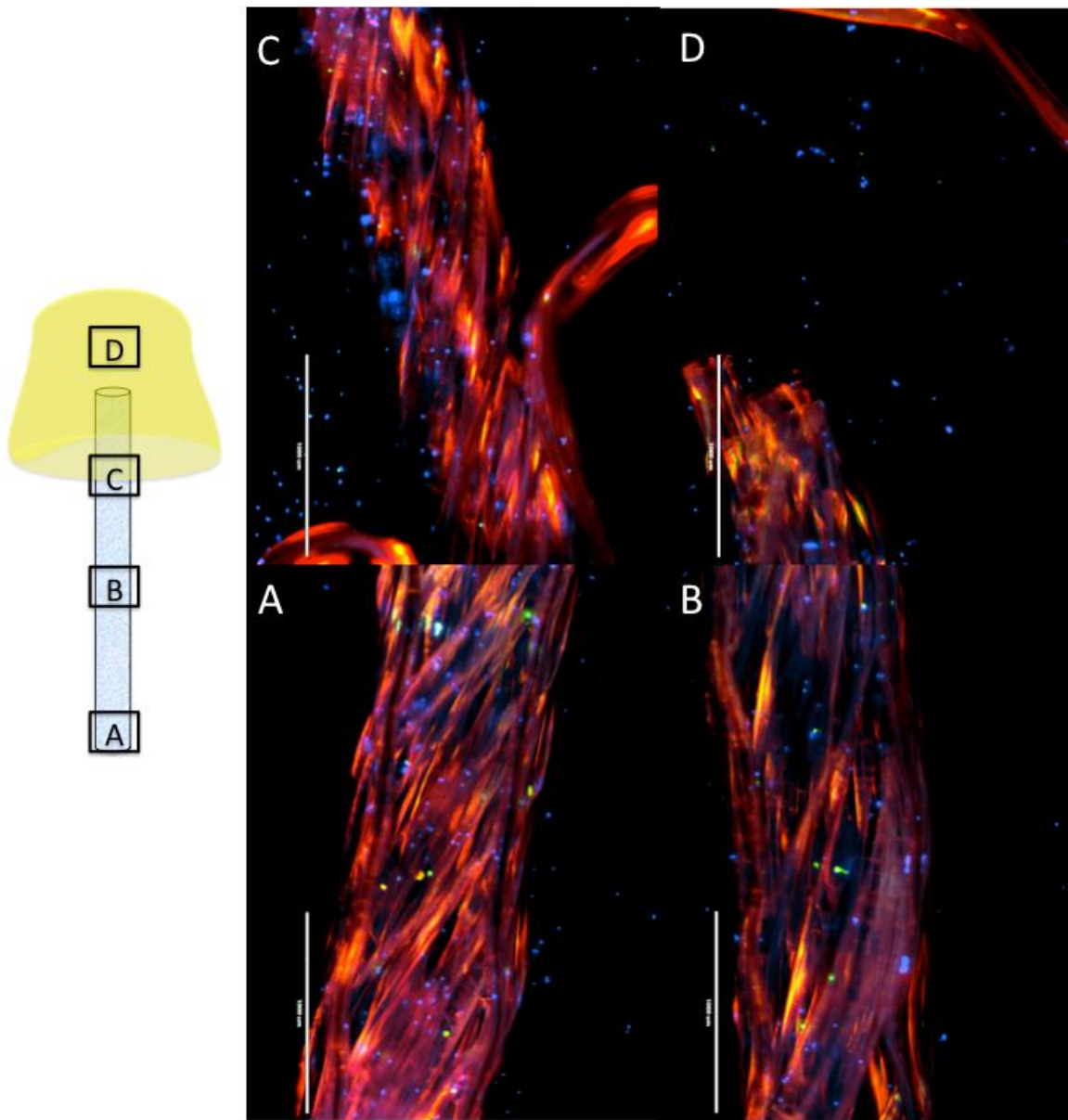


Figure 6.21: Cell displacement of metastatic cancer cells, MDA-MB-231 (blue), non-metastatic cancer cells, MCF-7 (red), and benign breast epithelial cells (green). The bottom (A) and middle (B) region of the fiber bundle depict all cancer cell types along the fiber. High densities of MDA-MB-231 are depicted in the top region of the fiber bundle (C) and the alginate cap (D).

Cell Separation and Isolation of Mesenchymal Stem Cells and Pre-Osteoblast Cells

The final assessment evaluated the potential of the modified wicking bundle to separate D1 mouse mesenchymal stem cells from MC3T3E1 pre-osteoblast cells, a further differentiated mouse cell type. The fluorescent images depicted cell separation of D1 progenitor cells labeled green and from MC3T3E1 pre-osteoblast cells labeled red. The bottom region (Image A) and the middle region (Image B) of the wicking fiber bundle illustrate a mixture of both cell types. The top and alginate cap (Images C and D) depict high cell counts of green-labeled progenitor cells. The outcomes of this assessment suggest similarities between the wicking behavior of progenitor and cancer cells.

The amount of progenitor and pre-osteoblast cells was quantified in each region of the wicking fiber bundle and the alginate cap presented in Figure 6.23. The forward scatter and fluorescent intensity plots (Images A and B) show the D1 cells and MC3T3E1 cells were successfully labeled with green and red fluorescent cell tracker. The top and bottom regions of the wicking fiber bundle, as well as the alginate cap (Image C) consisted of significantly more D1 progenitor cells, labeled with green tracker than MC3T3E1 cells, $p < 0.05$. The outcomes suggest the modified wicking bundle has potential to sort the progenitor cells and pre-osteoblasts. This also implies the progenitor cells may have similar behaviors to cancer cell types along the construct. It is also important to note, similar to the previous assessments, the alginate and top regions of the construct show less cell numbers than the bottom region of the wicking fiber bundle. Again, this is due to the inconsistencies and limitations of the cell removal process.

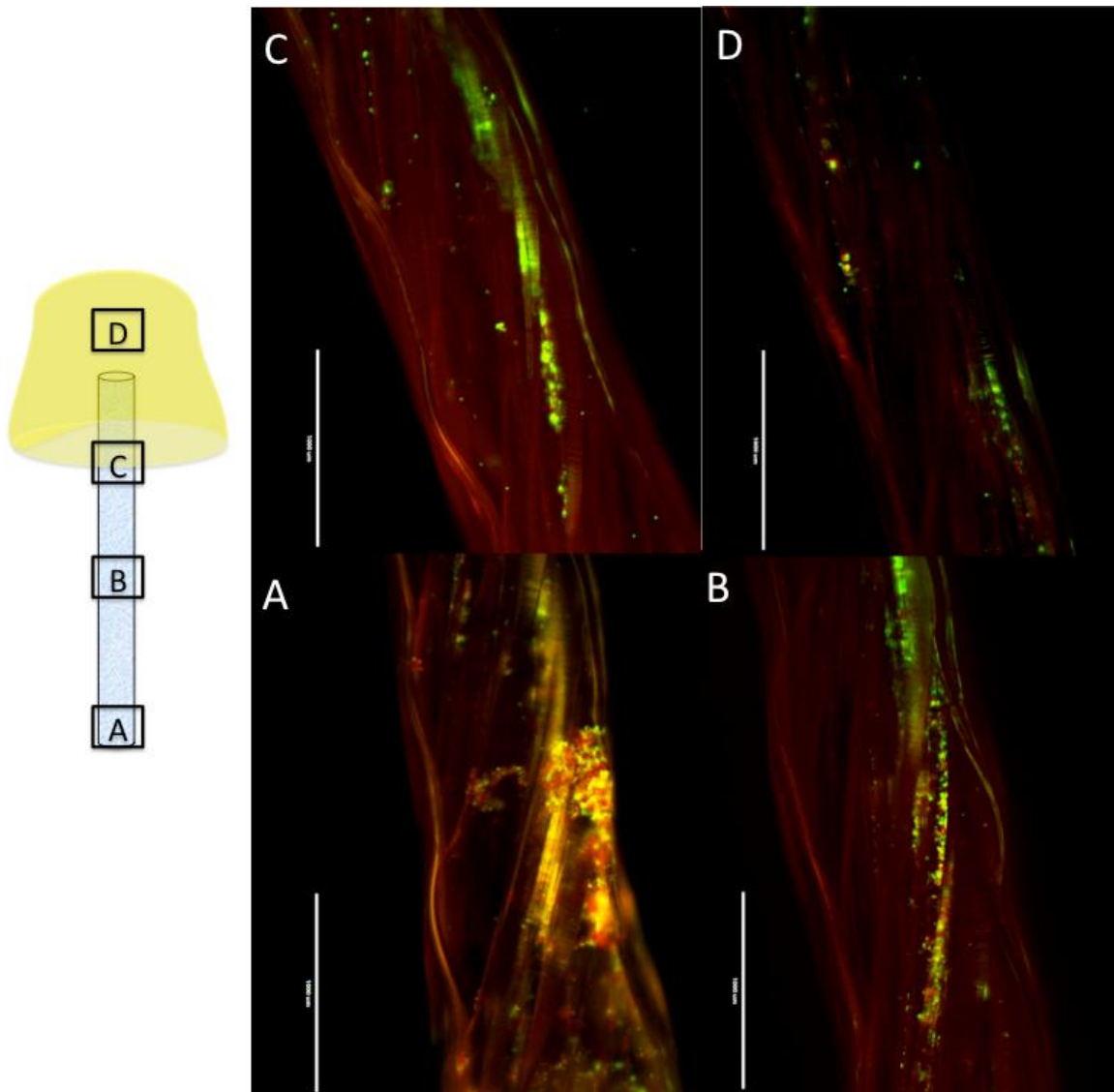


Figure 6.22: (A) and (B) Bottom and middle regions of the wicking fiber bundle show similar cell densities of D1 cells (green) and MC3T3E1 cells (red). (C) and (D) depict more D1 progenitor cells in top region and alginate cap.

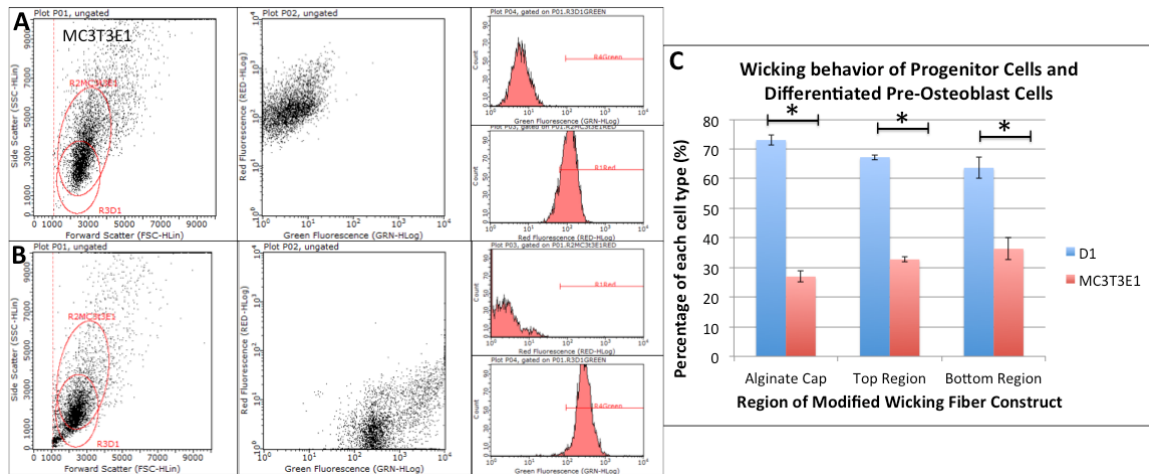


Figure 6.23: (A) Scatter and fluorescent intensity plots for MC3T3-E1 cells show cells were labeled with red tracker. (B) Scatter and fluorescent intensity plot for green fluorescently labeled D1 cells. (C) Quantifies the wicking displacement of D1 cells and MC3T3E1 cells. Depicts significantly more D1 cells ($p < 0.05$) in the alginate cap and fiber bundle regions than MC3T3E1 cells.

Discussion

The first part of this chapter explored the use of unmodified single and wicking fiber bundles to sort cancer and normal cells by their wicking behavior along the fibers. The outcomes from the single and bundled fibers assessments showed mouse and human cancer cell separation from normal or benign cells in the top region of the fiber. In both studies the cancer cells have greater vertical displacement and are presented in the top region of the fiber. The single wicking fiber was used to evaluate the vertical displacement of mouse mesenchymal stem cells and differentiated mouse monocytes. The semi-quantitative data showed progenitor cells displace to the top region of the fiber. The outcomes suggest the progenitor cells may share similar physical properties to the cancer cells.

We previously showed in Chapter 4 the wicking fiber bundles with an alginate cap (modified wicking bundles) greatly enhance the fluid transport and amount of cells collected within the construct after performing a vertical test assessment. The remainder of the chapter explored the use of the modified wicking bundle to separate various cancer cell types as well as progenitor cells from further differentiated cells. The wicking tests also investigated the use of the alginate cap as a collection source to isolate a cell type from a mixture of different cell types. The outcomes revealed the modified wicking bundle can be used to separate cancerous cells from benign cells. The isolation from various regions showed a significant increase in either metastatic or non-metastatic cancer cells along the fibers and in the alginate cap when tested with benign epithelial cells. Flow cytometry results investigating the movement of metastatic and non-metastatic cancer cells demonstrated a decreased ability to separate as compared to separation from benign cells. To increase specificity to isolate metastatic cancer cells in the alginate cap various approaches can be used to alter the system. The inter-fiber and intra-fiber spaces of the wicking fiber bundle can be altered, as well as, the polymer of choice used and the stiffness of the hydrogel.

Limitations of using the modified wicking bundle approach include inconsistencies between the fabricated samples, as well as, the processing technique to remove cells from the construct. The fabrication process of the modified wicking bundle involves the extrusion and twisting of fibers, as well as, the formation of the alginate cap. Inconsistencies between samples develop from the variation in cross-section sizing of the extruded fibers as well as the bundling process. To improve specificity the processing

technique of the constructs should be improved. The cell removal technique also presents a limitation. The cells are wicked through the conduits of the fibers as well as the compact intra-fiber spaces. The high tortuosity of the fiber component presents difficulties of using trypsin as a cell removal agent. The dissolution of the alginate cap takes approximately 30 minutes to dissolve the hydrogel. Small pieces of dissolved hydrogel may interfere with removal of cells as well as with detection during flow cytometry. Other cell removal techniques may need to be employed to ensure all cell information is obtained to provide precise results.

The mechanism for separation between different cell types is due to the physical and functional properties of the cells, wicking characteristics of the fiber bundle, and the cell-fiber interaction. Physical properties that may play a role include cell size, deformability, surface friction or charge, and expression of cell adhesion molecules. The size and shape of the cells may play a role in the ability for cells to penetrate the smaller channels created from the bundling of the fibers. Fiber bundle architecture will affect the wicking rate and vertical displacement of different cell types. The size of the individual fibers, the tension of the bundle, the hydrophobicity, and the inter-fiber space will play a role in the wicking of liquid and cell-interaction. These factors can be altered to increase the specificity of the system and increase the amount of cells reaching the top region of the fiber bundle and the alginate cap.

Other cellular properties influencing vertical movement include membrane impedance, expression of adhesion molecules, and cells stiffness. Membrane impedance, cell dielectric properties, or cell electric properties vary between cell types^{25,26}. Electrical

properties of the cell will influence the cell-interaction with the fiber based on the inherent charge of the fibers and the resultant vertical movement. Cells with greater impedance or surface charge may have more interactions with the fiber, thus hindering the vertical cell movement. Abdolahab and coworkers evaluated the cellular impedance for cancer cells of varying aggressiveness and demonstrated that a more aggressive cancer cell type (MDA-MD-231) has a significant reduction in impedance than a less aggressive cancer cell (MCF-7). Additionally they found a correlation between metastatic progression and membrane impedance reduction²⁷. Cell-fiber interaction and overall cell displacement will be affected by different membrane impedances and overall surface charge. The specificity and amount of cells wicked into the construct may be improved altering the hydrophobicity of the polymer wicking fibers.

Expression of cell adhesion molecules, such as EpCAM, can play a role in the cell-fiber interaction and ability of a cell to move through a confined space. Metastatic cells, as shown by the MDA-MB-231, are known to lose endothelial adhesion molecules and transition into a more motile mesenchymal phenotype²². Cancerous cells with fewer adhesion molecules may have less surface friction and altered shape that have less interaction with the fiber, allowing the cells to wick greater distances. The MDA-MB-231 cells are characterized with a mesenchymal phenotype and are classified as EpCAM-negative, CD24-negative, and CD44 positive with spindle-like shape^{28,29}. The high penetration of the MDA-MB-231 cells into the alginate cap as shown from the tri-culture separation assessment is due the ability of these cells to individually migrate and penetrate tissues, whereas MCF-7's require cell-cell interactions to maintain and

function. Future work can modify or layer the alginate to distinguish non-metastatic and metastatic cancer cells based on their dispersal through the hydrogel.

Cell deformability is another factor that will influence the ability for cells to deform, penetrate, and wick vertically through the twisted channels. In general, research shows cancer cells have a significantly lower Young's modulus compared to normal cells³⁰⁻³². Researchers have found that cancer cells of increased metastatic potential have higher deformability^{33,34}. This point suggests that MCF-7 cells are much softer and deform more easily than normal cells, allowing the cancer cells to migrate more readily. Microfluidic devices have been employed to distinguish cancer and normal cells, based on cellular deformability, by analyzing the ability of cells to squeeze and pass through confined constrictions^{31,35,36}. Indeed, Li and coworkers found the apparent Young's modulus of MCF-10A, non-malignant breast epithelial cells, to be significantly higher than MCF-7³⁷. The softer cytoskeleton and deformability of the MCF-7 cells may play a role in their ability to squeeze through channels and wick upward through the confined space.

Undifferentiated and differentiated stem cell separation shown in these tests are also affected by the same physical factors. Subpopulations of progenitor cells of varying differentiation potential are shown to have different electrical and mechanical properties, which can be used to identify the cell differentiation potential. Flanagan and coworkers used dielectrophoresis (DEP), a technique that detects the inherent charge characteristic of the cells, and established electrical signatures for progenitor cells of varying differentiation potential³⁸. Darling and coworkers characterized progenitor cells based on

their elastic and viscoelastic properties. The outcomes showed subpopulations of progenitor cells can be distinguished based on their mechanical markers^{39,40}. Progenitor cells of high differentiation potential are shown to have weaker cell membrane-cytoskeleton interaction as compared to mature cells. Similar to the cell separation of cancer cell types the alginate-modified wicking fiber construct was shown to identify progenitor cells from a more differentiated pre-osteoblast cell type. The physical properties of the cells such as size, shape, electrical charge, cell stiffness, and expression of adhesion molecules will also impact the movement of mesenchymal stem cells and differentiated cell types.

Conclusion

The outcomes of this chapter showed the prototype design of the modified wicking bundle separated various cell types based the cancer type and differentiated state of the cell. This work also showed similarities in wicking behavior of cancer cells and progenitor cell types. Further work needs to investigate the mechanisms affecting cell movement along the wicking fiber construct separation to optimize the design to improve specificity. The work in Chapter 7 will analyze some of the factors affecting the cell wicking behavior of different cell lines to improve the specificity and efficacy of the system.

References

1. Cancer, CNS, & Cardiovascular Biomarkers: Players, Products, and Prospects. Espicom Limited. 2008
2. Graber ML: The incidence of diagnostic error in medicine. *British Medical Journal Quality Safety* 2013; 22 Suppl 2:ii21–ii27
3. Raab SS, Grzybicki DM: Quality in cancer diagnosis. *A Cancer Journal for Clinicians* 2010; 60:139–65
4. Rosen S: *The Worldwide Market for Cancer Diagnostics.*, 4th edition. Kalorama Information, 2010, pp 25–54
5. *US Cancer Molecular Diagnostic Markers.* Frost & Sullivan. 2008
6. Hanahan D, Weinberg R: Hallmarks of cancer: the next generation. *Cell* 2011; 144:646–74
7. Charafe-Jauffret E, Ginestier C, Iovino F, Wicinski J, Cervera N, Finetti P, Hur M-H, Diebel ME, Monville F, Dutcher J, Brown M, Viens P, Xerri L, Bertucci F, Stassi G, Dontu G, Birnbaum D, Wicha MS: Breast cancer cell lines contain functional cancer stem cells with metastatic capacity and a distinct molecular signature. *Cancer Research* 2009; 69:1302–13
8. Almendro V, Marusyk A, Polyak K: Cellular heterogeneity and molecular evolution in cancer. *Annual Review of Pathology Mechanisms of Disease* 2013; 8:277–302
9. Cho RW, Clarke MF: Recent advances in cancer stem cells. *Current Opinions in Genetics & Development* 2008; 18:48–53
10. Marcato P, Dean C, Pan D, Araslanova R: Aldehyde dehydrogenase activity of breast cancer stem cells is primarily due to isoform ALDH1A3 and its expression is predictive of metastasis. *Stem Cells* 2011; 29:32–45
11. Balla MMS, Kusumbe AP, Vemuganti GK, Bapat SA: *Regenerative Medicine, Regenerative Medicine: From Protocol to Patient.* Edited by Steinhoff G. Dordrecht, Springer Netherlands, 2013, pp 387–412
12. Baccelli I, Trumpp A: The evolving concept of cancer and metastasis stem cells. *The Journal of Cell Biology* 2012; 198:281–93

13. Marie-Egyptienne DT, Lohse I, Hill RP: Cancer stem cells, the epithelial to mesenchymal transition (EMT) and radioresistance: Potential role of hypoxia. *Cancer Letters* 2013; 341:63–72
14. Foster R, Buckanovich RJ, Rueda BR: Ovarian cancer stem cells: Working towards the root of stemness. *Cancer Letters* 2013; 338:147–57
15. Visvader JE, Lindeman GJ: Cancer stem cells: current status and evolving complexities. *Cell Stem Cell* 2012; 10:717–28
16. Magee JA, Piskounova E, Morrison SJ: Cancer stem cells: impact, heterogeneity, and uncertainty. *Cancer Cell* 2012; 21:283–96
17. Li P, Stratton ZS, Dao M, Ritz J, Huang TJ: Probing circulating tumor cells in microfluidics. *Lab Chip* 2013; 13:602–9
18. Yoon HJ, Kim TH, Zhang Z, Azizi E, Pham TM, Paoletti C, Lin J, Ramnath N, Wicha MS, Hayes DF, Simeone DM, Nagrath S: Sensitive capture of circulating tumour cells by functionalized graphene oxide nanosheets. *Nature Nanotechnology* 2013; 8:735–42
19. Nagrath S, Sequist L V, Maheswaran S, Bell DW, Ryan P, Balis UJ, Tompkins RG, Haber DA: Isolation of rare circulating tumour cells in cancer patients by microchip technology. *Nature* 2007; 450:1235–9
20. Harris JL, Stocum M, Roberts L, Jiang C, Lin J, Sprott K: Quest for the ideal cancer biomarker: an update on progress in capture and characterization of circulating tumor cells. *Drug Development Research* 2013; 74:138–47
21. van de Stolpe A, Pantel K, Sleijfer S, Terstappen LW, den Toonder JMJ: Circulating tumor cell isolation and diagnostics: toward routine clinical use. *Cancer Research* 2011; 71:5955–60
22. Wirtz D, Konstantopoulos K, Searson P: The physics of cancer: the role of physical interactions and mechanical forces in metastasis. *Nature Reviews Cancer* 2012; 11:512–22
23. Yu M, Bardia A, Wittner BS, Stott SL, Smas ME, Ting DT, Isakoff SJ, Ciciliano JC, Wells MN, Shah AM, Concannon KF, Donaldson MC, Sequist L V, Brachtel E, Sgroi D, Baselga J, Ramaswamy S, Toner M, Haber DA, Maheswaran S: Circulating breast tumor cells exhibit dynamic changes in epithelial and mesenchymal composition. *Science* 2013; 339:580–4

24. Hung LY, Chuang YH, Kuo HT, Wang CH, Hsu KF, Chou CY, Lee GB: An integrated microfluidic platform for rapid tumor cell isolation, counting and molecular diagnosis. *Biomedical Microdevices* 2013; 15:339–52
25. Becker FF, Wang XB, Huang Y, Pethig R, Vykoukal J, Gascoyne PR: Separation of human breast cancer cells from blood by differential dielectric affinity. *Proceedings of the National Academy of Sciences* 1995; 92:860–4
26. Zou Y, Guo Z: A review of electrical impedance techniques for breast cancer detection. *Medical Engineering & Physics* 2003; 25:79–90
27. Abdolahad M, Janmaleki M, Taghinejad M, Taghnejad H, Salehi F, Mohajerzadeh S: Single-cell resolution diagnosis of cancer cells by carbon nanotube electrical spectroscopy. *Nanoscale* 2013; 5:3421–7
28. Keller PJ, Lin AF, Arendt LM, Klebba I, Jones AD, Rudnick JA, DiMeo TA, Gilmore H, Jefferson DM, Graham RA, Naber SP, Schnitt S, Kuperwasser C: Mapping the cellular and molecular heterogeneity of normal and malignant breast tissues and cultured cell lines. *Breast Cancer Research* 2010; 12:1–17
29. Holliday DL, Speirs V: Choosing the right cell line for breast cancer research. *Breast Cancer Research* 2011; 13:1–7
30. Lekka M, Gil D, Pogoda K, Dulińska-Litewka J, Jach R, Gostek J, Klymenko O, Prauzner-Bechcicki S, Stachura Z, Wiltowska-Zuber J, Okoń K, Laidler P: Cancer cell detection in tissue sections using AFM. *Archives of Biochemistry and Biophysics* 2012; 518:151–6
31. Zhang W, Kai K, Choi DS, Iwamoto T, Nguyen YH, Wong H, Landis MD, Ueno NT, Chang J, Qin L: Microfluidics separation reveals the stem-cell-like deformability of tumor-initiating cells. *Proceedings of the National Academy of Sciences* 2012; 109:18707–12
32. Suresh S: Biomechanics and biophysics of cancer cells. *Acta Biomaterialia* 2010; 3:413–38
33. Xu W, Mezencev R, Kim B, Wang L, McDonald J, Sulchek T: Cell stiffness is a biomarker of the metastatic potential of ovarian cancer cells. *PloS one* 2012; 7:1–12
34. Swaminathan V, Mythreye K, O'Brien E, Berchuck A, Blobe G, Superfine R: Mechanical stiffness grades metastatic potential in patient tumor cells and in cancer cell lines. *Cancer Research* 2011; 71:5075–80

35. Byun S, Son S, Amodei D, Cermak N, Shaw J, Ho J, Hecht VC: Characterizing deformability and surface friction of cancer cells. *Proceedings of the National Academy of Sciences* 2013; 110:7580–5
36. Shim S, Kim MG, Jo K, Kang YS, Lee B, Yang S, Shin S-M, Lee J-H: Dynamic characterization of human breast cancer cells using a piezoresistive microcantilever. *Journal of Biomechanical Engineering* 2010; 132:1–6
37. Li QS, Lee GYH, Ong CN, Lim CT: AFM indentation study of breast cancer cells. *Biochemical and Biophysical Research Communications* 2008; 374:609–13
38. Flanagan LA, Lu J, Wang L, Marchenko SA, Jeon NL, Lee AP, Monuki ES: Unique dielectric properties distinguish stem cells and their differentiated progeny. *Stem Cells* 2008; 26:656–65
39. Darling EM, Topel M, Zauscher S, Vall TP, Gullak F: Viscoelastic properties of human mesenchymally-derived stem cells and primary osteoblasts, chondrocytes, and adipocytes. *Journal of Biomechanics* 2010; 41:454–64
40. Titushkin I, Cho M: Modulation of cellular mechanics during osteogenic differentiation of human mesenchymal stem cells. *Biophysical Journal* 2007; 93:3693–702

CHAPTER SEVEN

INVESTIGATING THE CELLULAR SEPARATION MECHANISM OF WICKING FIBERS

Introduction

Technologies for CTC isolation and detection include macro-scale systems and microfluidics that use physical characteristics of the cells as well as antigen surface labels. Microfluidic devices have better specificity and isolation efficiency than macro-scale systems but are restricted to small volumes of sample and low yield of isolated CTCs^{1,2}. Many microfluidic devices and macro-scale systems use antibody-antigen interactions for binding epithelial markers to isolated CTCs. Many isolation methods use antibodies interacting with epithelial cell adhesion molecules (EpCAMs) and cytokeratins^{1,3}. These approaches assume CTCs are expressing epithelial markers, therefore limiting these approaches to a specific subpopulation of CTCs and missing aggressive CTC populations with mesenchymal phenotype⁴⁻⁸. Other microfluidic devices and chips use antigen-independent techniques to detect and separate cancer cells. These approaches use physical characteristics of the cancer cells, including size, deformability, and charge⁹. Methods that singularly use cell size to isolate CTCs, such as porous membrane cell filtration techniques, are limited due to the large variation in size of cancer cells¹⁰. Methods involving cell stiffness and impedance have established correlations between the biomechanical and electrical properties of cells and their metastatic state. Biomechanical measurements of cell stiffness confirm that cancer cells are significantly softer than normal cells, relating to the cancer cell's increased

deformability and metastatic potential^{11,12}. Cell-capture microfluidic devices or chips, based on the cell deformability or impedance, have higher capture efficiency and purity, but can only process small amounts of volume, therefore limiting the number of isolated cancer cells. Furthermore, most microfluidic approaches are complex and require a perfusion system with an optimum flow rate and shear stress that may alter or damage the isolated cells¹⁰. The current limitations of the both antigen-independent and -dependent microfluidic devices have motivated the simple, bundled fiber design that can rapidly analyze large volumes of sample and that may better capture different CTC subpopulations.

Similar limitations are found with progenitor stem cell isolation techniques. Adult tissue contains subpopulations of progenitor cells that are used widely in tissue engineering applications. Isolating progenitor cells from these tissues is challenging and inefficient due to the heterogeneity and lack of universal biomarkers that identify progenitor cells. Methods to isolate progenitor cells are costly, slow, and inefficient. Cell adherence assays, colony forming units-fibroblastic (CFU-F) assays, and methods of biomarker identification are most commonly used to isolate progenitor cells. The current isolation techniques isolate progenitor cells with different phenotypic and molecular differences that result in functional variability and different *in vitro* differentiation capabilities. Multiple epitopes or phenotypic biomarkers are used to identify progenitor cells. Mesenchymal stem cells (MSCs), also described as bone marrow derived cells, have the ability to differentiate into lineage-specific cell types including osteoblasts, chondrocytes, and adipocytes¹³. MSCs are routinely used in surgical procedures that

require tissue regeneration. Bone marrow aspirate containing MSCs is commonly used in orthopedic applications where the normal bone formation process is compromised to facilitate the regeneration of bone as well as other tissues. The outcomes of using isolated MSCs from patient or donor tissue have limited success in regenerative applications. MSC populations vary from donor-to-donor and contain intra-population heterogeneity affecting the functionality of the progenitor cells to differentiate and produce the appropriate tissue^{13,14}. The intrinsic heterogeneity of MSCs and other progenitor cells creates a challenge for researchers to develop efficient isolations techniques. The standard approach to identify MSCs uses expression of multiple biomarkers including CD29, CD44, and CD105¹⁴. This method can identify MSCs but does not predict the function of the MSCs or identify the differentiating potential of the MSC. Approximately 1 in 4 MSCs isolated have the ability to differentiate into three pathways. Most isolated MSC clones have potential to differentiate into one or two pathways¹⁴. There is a need for alternative methods to identify and isolate subpopulations of MSCs based on their potency and ability to differentiate toward specific lineages¹⁴.

In addition to providing a novel technique to identify and separate progenitor cells of varying differentiation potential and different cancer cell types, this work may provide more insight into the stem-cell hypothesis¹⁵. This theory proposes the metastatic cancer cells that disseminate from the tumor have stem-cell properties. Researchers have found that subpopulations within tumor cells contain stem-cell like functions have differentiating potential. This work further investigated similarities between progenitor and derived cell separation with cancer and normal cell separation.

The previous chapter investigated the potential use of the modified wicking bundle approach to separate varying cancer cell types and progenitor cells. In this chapter, the mechanisms for separation of varying cell types was explored. The physical properties of the cells such as size, shape, electrical charge, cell stiffness, and expression of epithelial adhesion molecules and mesenchymal proteins impact the vertical movement and distribution in the wicking fibers. Various cross-sectional geometries of the wicking fiber impact on cell separation were also explored. The first part of this chapter investigated cell size and the effect of different cross-sectional geometries on cell separation. The chapter further investigated cell mechanics of various cancer types and progenitor cells along the fibers. The final assessment evaluated the percentage of EpCAM expressed by the various cancer cell lines and changes in EpCAM expression along the wicking fiber bundle construct. Preliminary work was also conducted to investigate the mesenchymal phenotype of the cell lines by evaluating the expression of CD44.

Impact of Cell Size and Fiber Geometry on Cell Type Separation

Materials and Methods

Cell Size

Determining Cell Size of MCF-7 and MCF-10A Cells in Suspension

This procedure evaluated the diameter of cancer and benign epithelial cells while in cell suspension, prior to cell attachment, to mimic the cell behavior during the vertical test using the modified wicking bundle. Cells from a mammary epithelial cell line from

benign breast tissue, MCF-10A (ATCC), and human breast cancer cell line, MCF-7, (ATCC) were cultured in DMEM (Invitrogen) supplemented with 10% FBS (Gibco), 1% Fungizone, and MEGM single quotes (Lonza) and DMEM (Invitrogen) supplemented with 0.01 mg/mL human recombinant insulin (Gibco), 10% FBS, 1% Fungizone (Gibco), 10,000 U penicillin, and 10 mg streptomycin/mL (Sigma-Aldrich), respectively. Cells were cultured in a T-150 flask (Corning) and maintained in a humidified incubator at 37°C and 5% CO₂. Once confluent both cell types were removed with trypsin-EDTA solution (Sigma-Aldrich) and resuspended in culture medium. To determine the average cell diameter, MCF-10A and MCF-7 cells were fluorescently labeled with CellTracker™ Green CMFDA probe and CellTracker™ Red CMTPX probe (Invitrogen; Grand Island, NY, USA), respectively following manufacturer's protocol using a long-term labeling concentration of 25 µM for fluorescent imaging. Approximately 100,000 cells from each cell line were suspended in 1 mL of growth media in separate 1.5 mL Eppendorf microcentrifuge tubes (Sigma; St. Louis, MO USA).

The cells were mixed using the vortex to keep the cells homogeneously mixed in solution. To determine cell diameter 100 µL of the cell solution we pipette directly onto a microscope slide and imaged using a fluorescent microscope. Image J software was used to determine the average diameter of each sample (n=3) from both cell lines in suspension.

Determining Cell Size of D1 and MC3T3-E1 Cells in Suspension

We also investigated the average cell diameter of D1 and MC3T3E1 cells in solution prior to attaching to a surface. Mouse mesenchymal stromal cells, D1 (ATCC), and mouse pre-osteoblast cells, MC3T3E1 (ATCC) were cultured in growth media consisting of Dulbecco's Modified Eagle's Medium (DMEM, Invitrogen) supplemented with 10% fetal bovine serum (FBS, Gibco), 10,000 U penicillin, and 10 mg streptomycin/mL (Sigma-Aldrich), and Minimal Essential Medium α without ascorbic acid (Gibco) supplemented with 10% fetal bovine serum (Gibco), 10,000 U penicillin, and 10mg streptomycin/mL (Sigma), respectively. Cells were cultured in a T150 flask (Corning) and maintained in a humidified incubator at 37°C and 5% CO₂. Once cells were confluent, D1 and MC3T3E1 cells were detached using trypsin-EDTA solution (Sigma) and resuspended in growth media. D1 and MC3T3E1 cells were fluorescently labeled with CellTracker™ Green CMFDA probe and CellTracker™ Red CMTPX probe (Invitrogen; Grand Island, NY, USA), following manufacturer's protocol, respectively using the long-term labeling concentration of 25 μ M for both red and green cell tracker was used to label the cells. Following the same procedure above, fluorescent microscopy and Image J software were using to determine the average cell diameter for each cell line.

Cross-sectional Image of Single and Bundled Wicking Fibers

Wicking fiber bundles containing 3 individual extruded polylactide (Natureworks) fibers of non-circular cross-sectional dimensions of 0.72 mm x 0.55 mm were sectioned into 3 cm. The wicking fibers were dyed using a blue stain prior to embedding. Samples were placed vertically in boxed molds and infiltrated and embedded with Embed-it™

Low Viscosity Epoxy Resin (Polysciences, Inc.). The wicking fiber samples were embedded and sectioned following manufacture's protocol. Sections, 5 μm in thickness, were cut with a microtome and transferred to a microscope slide. The samples were imaged with a light microscope and imaging software was used to measure and characterize the inter- and intra- fiber spaces. To assess the cross-section of the single fibers containing cross-sectional dimensions of 0.72 mm x 0.55 mm or 0.51 mm x 0.33 mm, the samples were sectioned and placed vertically on a microscope slide. A light microscope was used to image the cross-section and imaging software was used to measure the groove sizes.

Investigating the Displacement of Microbeads

To evaluate the role cell size plays in the vertical displacement along the wicking fiber bundles, polystyrene beads of 6 and 20 μm were used to mimic cells of different sizes. The vertical wicking test was conducted with a bead solution containing beads of both sizes and using the modified wicking bundles. The vertical movement of beads was assessed in twisted polylactide wicking fiber bundles containing 10 individual fibers with cross-sectional dimensions of 0.72 mm x 0.55 mm ("large fiber bundle") or 10 individual fibers with cross-sectional dimensions of 0.51 mm x 0.33 mm ("small fiber bundle"). The bundles were formed by twisting the individual small or large fibers using a twisting apparatus at 11 rotations per centimeter twist. The bundles were sliced into 3 cm long sections to mimic the bundles used to separate cells. The alginate caps were formed on each twisted fiber bundle by dipping one end of the wicking fiber bundle in 100 μL of 5 M CaCl_2 solution (Fisher Scientific; Waltham, MA, USA) in a well of a 96-well plate and

pipetting 100 μ L of 1.4% (w/v) alginate solution comprised of alginic acid sodium salt from brown algae (Sigma; St. Louis, MO) in 155 mM NaCl (Sigma; St. Louis, MO) directly on the submerged fiber tip in the well. The alginate immediately adhered to the fiber end and solidified forming the modified wicking bundle.

Following the fabrication process, the modified wicking bundles were added vertically to a 12-well plate containing a custom-made lid to hold the samples vertical and 1 mL of bead solution was added to a 12-well plate containing 500,000 beads of each size. The samples were placed in the incubator at 37°C and 5% CO₂ for 2 hours. After the incubation period the samples were removed and beads were isolated from the top and bottom regions of the wicking fiber bundle as well as the alginate cap to analyze the amount of each bead type in each region using the flow cytometer. Similar to the cell removal process, the alginate caps were removed and transferred to 1.5 mL Eppendorf microcentrifuge tubes (Sigma; St. Louis, MO USA) containing 1 mL of the stock alginate dissolution buffer. The buffer was comprised of 100mM sodium citrate (Fisher Scientific; Waltham, MA USA), 10 mM HEPES buffer (Sigma; St. Louis, MO USA), and 27 mM NaCl (Sigma; St. Louis, MO USA) in 50 mL of distilled water. The alginate caps were dissolved for 30 minutes at 37°C and mixed vigorously using the vortex every 5 minutes. The wicking fiber bundle region was sectioned with a blade into top and bottom regions that were placed into microcentrifuge tubes containing 1 mL of PBS. The samples were mixed using the vortex and the fibers were removed. The amount of 6 μ m and 20 μ m beads in each fiber bundle region and the alginate cap were determined using Guava

easyCyte™ flow cytometer (Guava Technologies) and InCyte software (Guava Technologies).

Investigating Separation of MCF-10A and MCF-7 Cells in Large and Small Modified Wicking Bundles

To further explore the effects of size on the system. The vertical test method was conducted with benign and cancer cells using modified wicking bundles consisting of small or large wicking fibers. The wicking fiber bundles were constructed using 10 individual fibers with cross-sectional dimensions of 0.72 mm x 0.55 mm (“large fiber bundle”) or 10 individual fibers with cross-sectional dimensions of 0.51 mm x 0.33 mm (“small fiber bundle”). After the bundles were twisted the samples were cleaned by soaking in three changes of ethanol for 1 hour each, and placed under ultraviolet light for 6 hours. Samples were then soaked in a phosphate-buffered saline (PBS, Invitrogen) solution for 2 hours and air-dried overnight in a sterile hood. The 1.4% alginate cap was formed using the same methods previously described.

The benign breast epithelial cells, MCF-10A (ATCC), and breast cancer cells, MCF-7, (ATCC) were cultured in DMEM (Invitrogen) supplemented with 10% FBS (Gibco), 1% Fungizone, and MEGM single quotes (Lonza) and DMEM (Invitrogen) supplemented with 0.01 mg/mL human recombinant insulin (Gibco), 10% FBS, 1% Fungizone (Gibco), 10,000 U penicillin, and 10 mg streptomycin/mL (Sigma-Aldrich), respectively. Cells were cultured in a T-150 flask (Corning) and maintained in a humidified incubator at 37°C and 5% CO₂. Once confluent both cell types were removed with trypsin-EDTA solution (Sigma-Aldrich) and resuspended in culture medium to

prepare for vertical testing. MCF-10A and MCF-7 cells were fluorescently labeled with CellTracker™ Green CMFDA probe and CellTracker™ Red CMTPX probe (Invitrogen; Grand Island, NY, USA), respectively following manufacturer's protocol. To detect isolated cells from the modified wicking bundles with flow cytometer, MCF-7 cells were labeled with 5.0 μM cell tracker red and MCF-10A cells were labeled with the optimized cell tracker green concentration of 0.05 μM .

Both labeled cell types were seeded in each of the wells of a low attachment 12-well plate with a cell density of 500,000 cells per mL. The modified wicking bundles containing small or large fibers (n=6) were placed into each of the wells, as shown in the experimental set-up. The well plate containing the samples was placed on flattop shaker (VWR) at 100 rpm in a humidified incubator at 37°C and 5% CO₂. The vertical displacement of the human cancer and benign breast epithelial cells along the wicking were determined after 2 hours of incubation, with the initial time point being fiber placement into the cell solution.

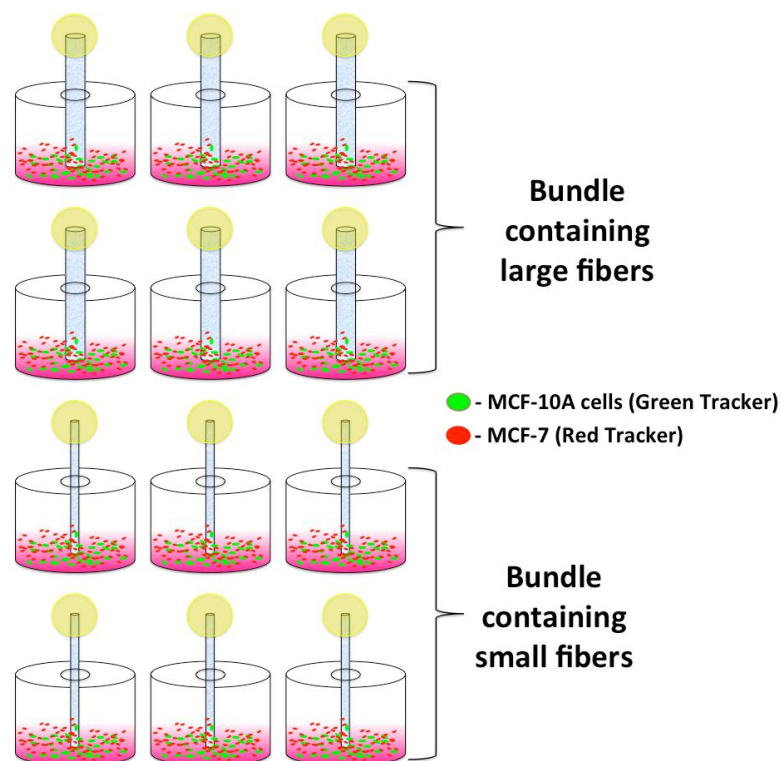


Figure 7.1: Experimental set-up investigating cell separation of benign and cancerous cells in modified wicking bundles containing small or large fibers

To quantify the cancer and normal cell separation, the construct was sectioned into top, bottom, and alginate regions and the cells were removed from each region, as illustrated in Figure 7.1. The alginate caps were first removed from the fiber bundles and transferred to a 1.5 mL Eppendorf microcentrifuge tubes (Sigma; St. Louis, MO USA) containing 1 mL of the stock dissolution buffer. The buffer was comprised of 100 mM sodium citrate (Fisher Scientific; Waltham, MA USA), 10 mM HEPES buffer (Sigma; St. Louis, MO USA), and 27 mM NaCl (Sigma; St. Louis, MO USA) in 50 mL of distilled water. The alginate caps were dissolved for 30 minutes at 37°C and mixed vigorously

using the vortex every 5 minutes. The wicking fiber bundle region was sectioned with a blade into top and bottom regions were placed into separate wells of a 24 well plate, Samples were rinsed with PBS and untwisted. Cells were removed by adding 500 μ L of trypsin-EDTA solution into the well with the fiber region and placing the plate on a flat-top (VWR) shaker at 200 rpm in a 37°C incubator. After 15 min the cells were diluted with 500 μ L of growth media and the number of red labeled MCF-7 and green labeled MCF-10A cells were determined from the alginate caps and top and bottom regions of the fiber bundles using a Guava easyCyte™ flow cytometer (Guava Technologies). The number of cancer and normal cells in each region was evaluated by following the manufacturer's instructions for InCyte software (Guava Technologies). MCF-7 and MCF-10A cells of known cell densities with and without red and green tracker, were used as positive and negative controls to calibrate the machine before measurements of the treatment groups were made.

Statistical Analysis

JMP 10 software was used to conduct an unpaired two-sample t-test to compare the average cell diameter of MCF-10A and MCF-7 cells, as well as, D1 and MC3T3E1 cells using a significance level of $p < 0.05$. The same analysis was used to compare the mean cell count of 6 μ m beads in each region of modified bundles of large fibers and modified bundles of small fibers using a significance level of $p < 0.05$. The mean cell count of 20 μ m beads in each region of the modified bundles containing large and small fibers was also analyzed using a two-sample t-test. The average percentage of MCF-10A

cells in each region of the modified bundles with small fibers was compared to modified bundles with large fibers using an unpaired two-sample t-test.

Results

Average Cell Diameter of MCF-7 and MCF-10A Cells

To determine the cell diameter, benign and cancerous cells were labeled with green and red cell tracker. The fluorescent label uniformly stains the cytoplasm as shown in Images A and B of **Figure 7.2**. The fluorescent images were processed using Image J software to determine the average cell diameter for each cell in the image. The average diameter of the MCF-10A cells ($\sim 16 \mu\text{m}$) was significantly larger than the average diameter of the MCF-7 cells ($\sim 11 \mu\text{m}$), shown in Image C. It is important to note within cancer cell lines there are variances in cell size and shape.

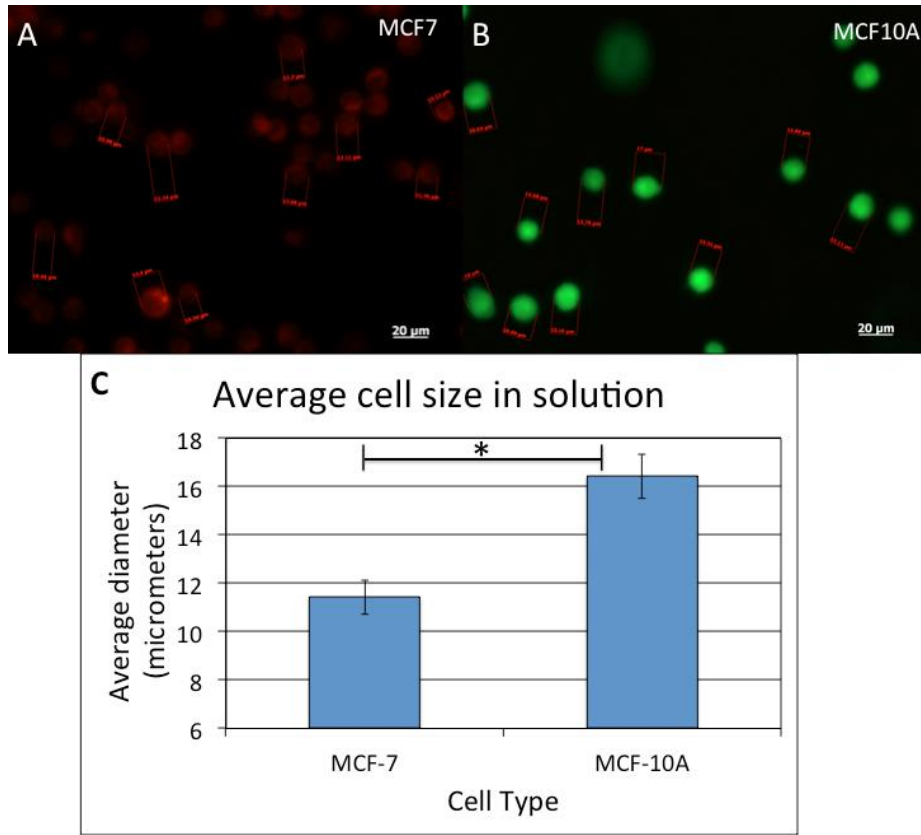


Figure 7.2: Fluorescently green labeled MCF-10A cells (A) and red labeled MCF-7 cells (B) suspended in growth media. (C) The average diameter of the benign MCF-10A cells is significantly larger than the cancerous MCF-7 cells, (*) indicate significant difference, $p < 0.05$

Average Cell Diameter of D1 and MC3T3E1 Cells

The average cell diameter of mesenchymal stromal cells and pre-osteoblasts were also analyzed and compared. The fluorescent images depict the MC3T3E1 cells labeled red (image A) have larger cell diameters than D1 cells labeled green (Image C). The semi-quantitative results showed the D1 cells with average diameter of 11 μm were significantly smaller than the MC3T3E1 cells with an average diameter of 14 μm.

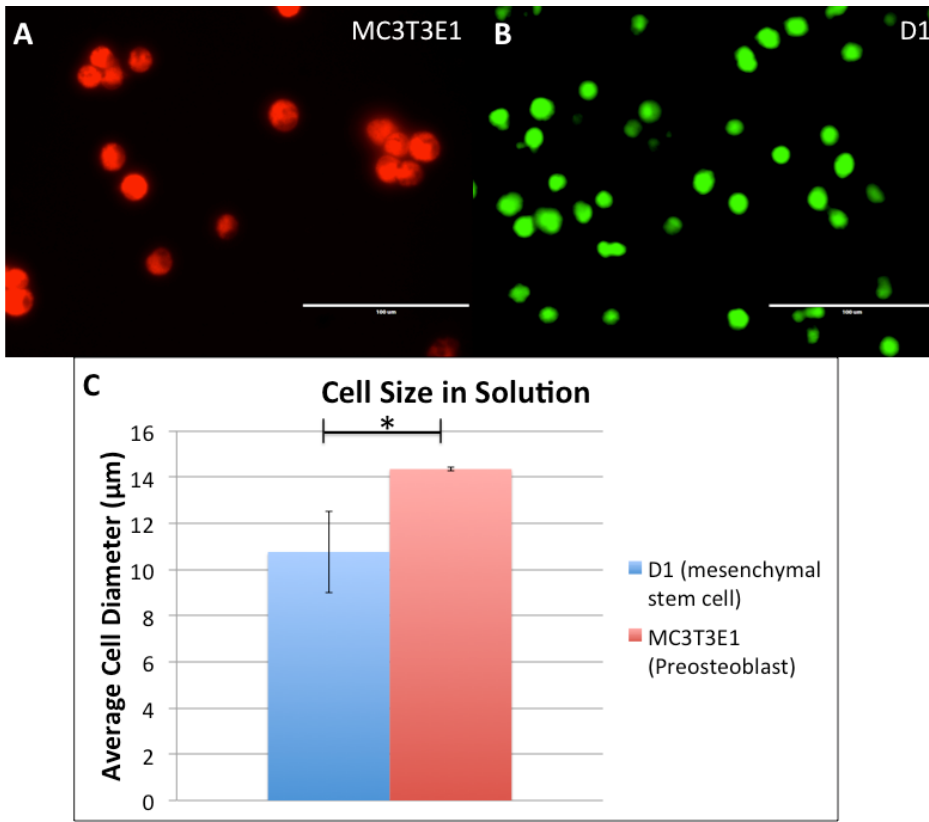


Figure 7.3: Fluorescently red labeled MC3T3E1 cell and green labeled D1 cells suspended in cell solution (C) The average cell diameter of D1 cells is significantly smaller than the MC3T3E1 cells

Cross-sectional Analysis of Wicking Fibers and Bundles

The cross-sectional images of the individual small and large fibers are depicted Images A and B of Figure 7.4. Using Image J software, the long and short axes of the small fiber were 0.51 mm and 0.33 mm and the large fiber were 0.72 mm and 0.55 mm, respectively. The groove sizes were also determined by measuring the length using Image J software. The groove sizes for the small fiber ranged from 20 µm to 82 µm and the large fiber groove sizes ranged from 34 µm to 150 µm. Histological processing was used

to evaluate the cross-section of the wicking fiber bundle. Prior to sectioning a blue dye was used to coat the fiber bundle. The cross-sectional image in Figure 7.4 shows blue dye in between the grooves of the fibers as well as the inter-fiber spaces between the wicking fibers. The image depicts a range in sizes of the micro channels along the bundle. The twisting configuration of the bundles distorts the grooves and spaces into channels smaller than along the single fiber. This suggests the small channels may prevent the large cell types from penetrating the top region of the fiber bundles.

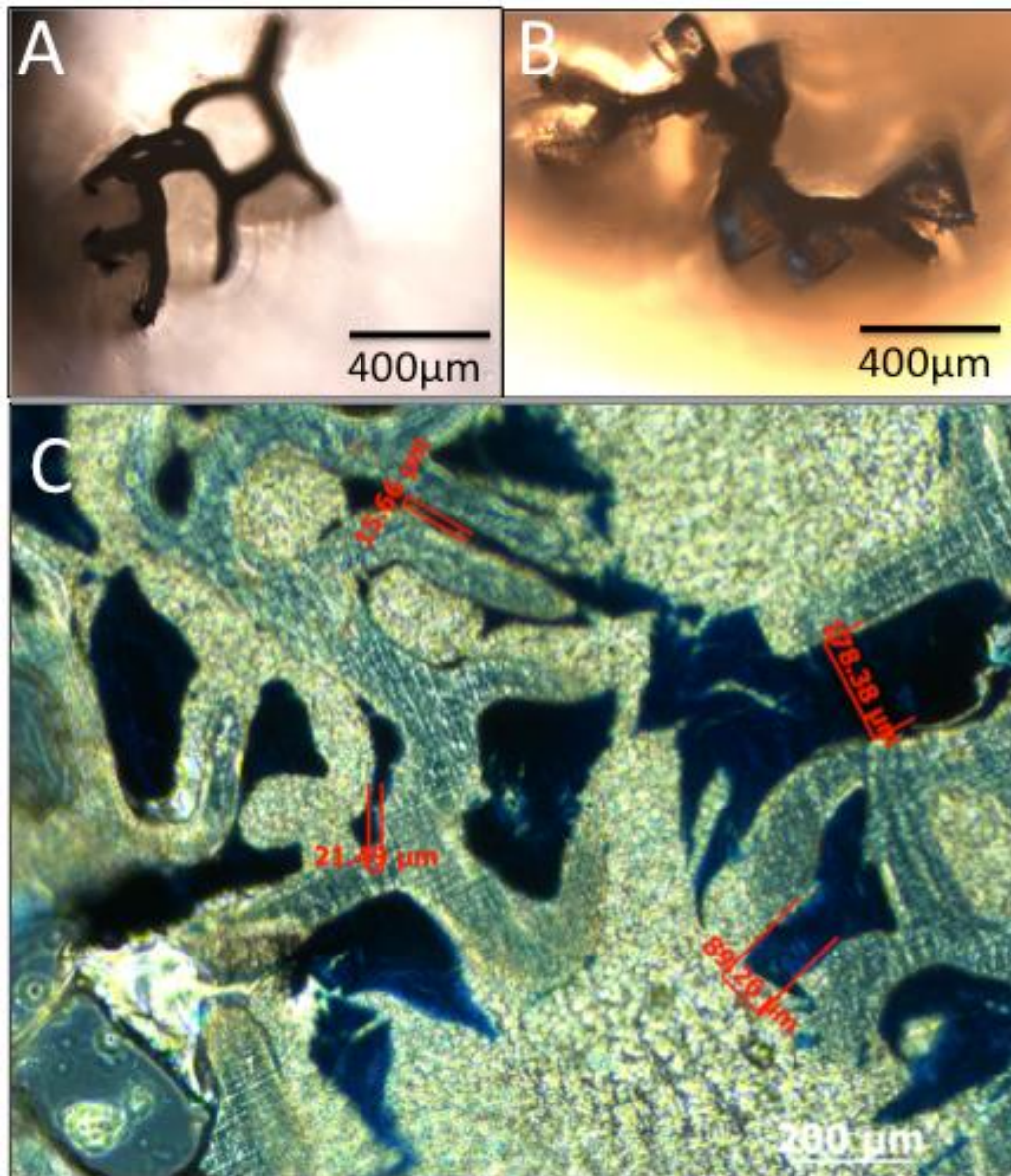


Figure 7.4: (A) Section of polylactide wicking fiber bundle depicts a range of inter- and intra- fiber spaces (B) and (C) depicts cross-sectional images of two different sized polylactide fibers

Bead Wicking Distribution in Modified Wicking Bundles

To investigate the role of size on the wicking behavior of cells through the system, beads of 6 and 20 μm were used to mimic cells of varying size. The distribution of the beads along the modified wicking bundles was investigated in bundles comprised of small or large cross-sectional fibers. The various bundles containing different sized fibers were used to explore the effect of fiber size on the bead movement. Beads were isolated from the top and bottom regions of the fibers and from the alginate cap. The results, Figure 7.5, show the forward scatter versus side scatter plot can be effectively used to quantify the number of each bead type. Since the beads are different sizes, the plots for each bead size were clearly distinguished (Image A). The scatter plots of the beads isolated from the bottom region depict significantly more 6 μm sized beads than 20 μm beads for both large and small modified wicking bundles. The alginate and top region showed more 6 μm beads in the modified constructs containing small fibers. Minimal 20 μm beads are detected in these regions for both fiber types.

The bead count was determined using the InCyte software and presented in the graph below, Figure 7.5. Both large and small modified wicking bundles show significantly more 6 μm beads in each region than the larger 20 μm beads (Image A). The top and bottom regions of the small wicking bundle contained significantly more 6 μm sized beads than the large wicking bundle. The percentage of the 6 μm beads in each region was similar for large and small fiber bundle constructs (Image B).

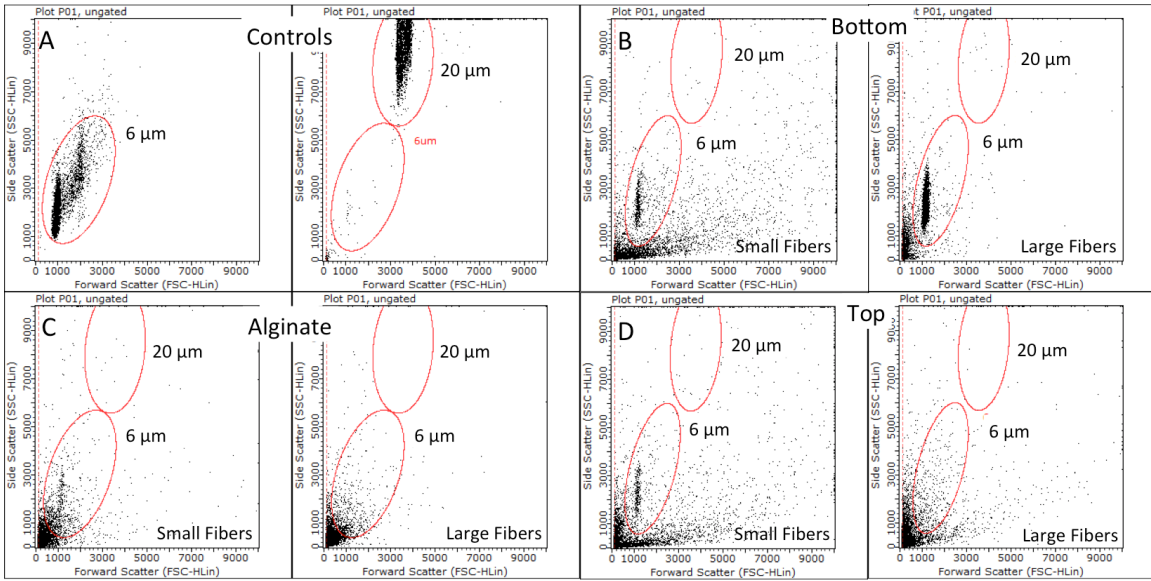


Figure 7.5: Bead wicking analysis with flow cytometry (A) Scatter plots showing the regions of the 6 μm (right) and 20 μm beads

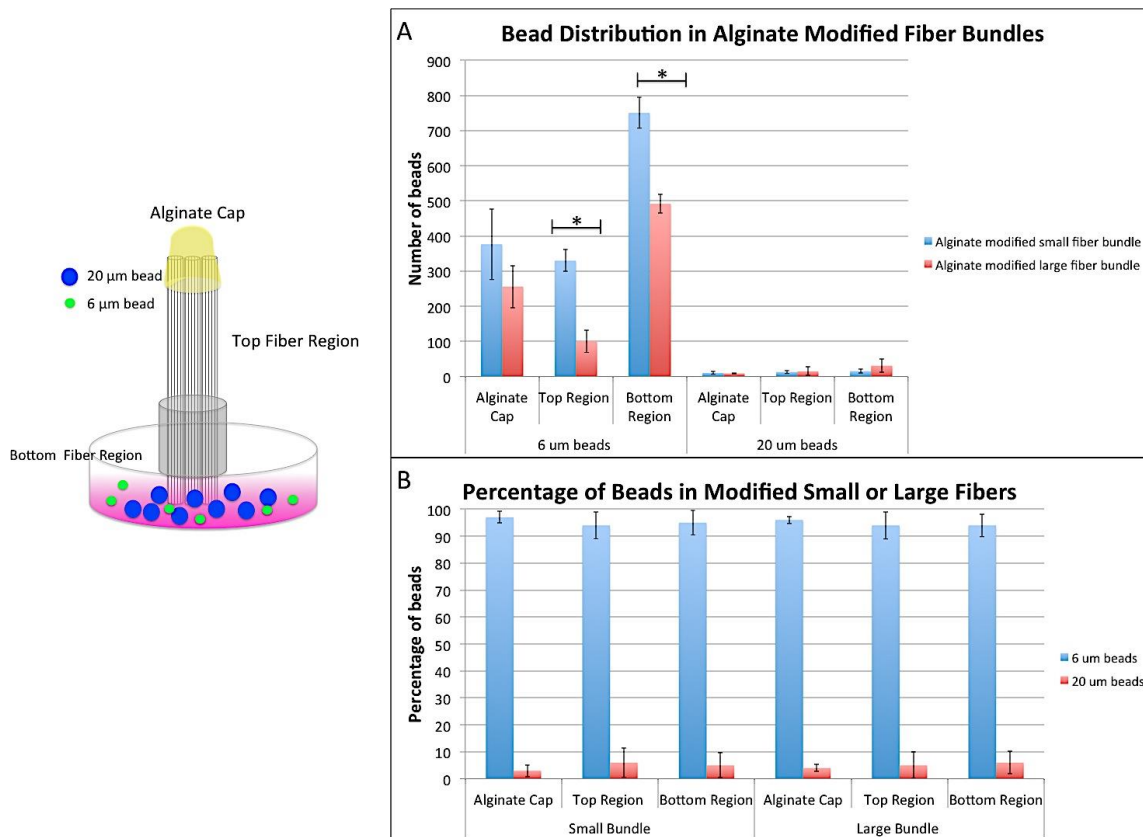


Figure 7.6: Flow cytometry analysis of 6 μm and 20 μm diameter beads in alginate modified fibers containing small or large individual fibers. (A) Both constructs showed significantly more 6 μm diameter beads in each region than the 20 μm beads. The modified fiber bundle containing the smaller bundles contained significantly more 6 μm beads in the top and bottom regions of the fiber bundle than the modified construct containing larger cross-sectional fibers. (B) The modified large and small fiber constructs showed comparable percentages of both bead types in each region of the fiber bundle and the alginate cap

Investigating Separation of MCF-10A and MCF-7 Cells in Large and Small Modified Wicking Bundles

This study investigated the effect of the cross-sectional size of the wicking fiber on the cell separation of benign and cancer cells. Modified wicking bundles of small and large individual fibers were used to test the vertical cell wicking of MCF-7 and MCF-

10A cells. The flow cytometry results, Figure 7.7, show comparable cell counts (Image A) and percentages (Image B) of cancerous and benign cells in the alginate cap and bottom region of the fiber for both modified wicking bundles containing large or small fibers. The top region of the bundles containing large wicking fibers showed significantly more MCF-10A cells than the bundles containing small wicking fibers. The scatter and fluorescent intensity plots from the flow cytometry analysis from each region presented in Figure 7.8 show for both large and small modified wicking bundles significantly less cells were removed from the top region of the fiber bundle and the alginate cap. The lack of cells in these regions is due to the cell removal processing methods. Further work needs to investigate alternate methods to improve the removal of cells.

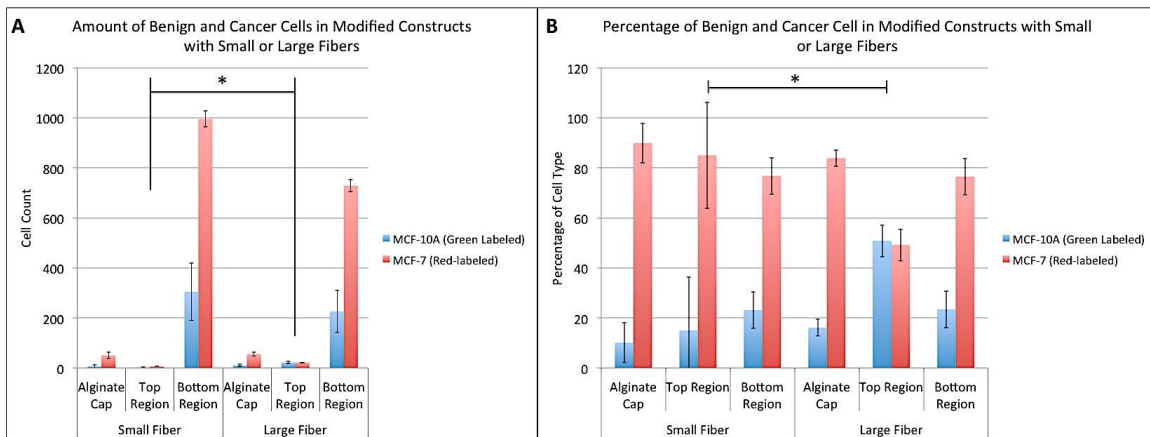


Figure 7.7 (A) Cell count in each region of the modified small and large wicking bundles. The alginate cap and bottom region of the wicking fiber bundle show similar cell counts of both cell types. The top region of the smaller fiber depicted significantly less MCF-10A and MCF-7 cells than the top region of the modified large fiber construct. (B) Percentage of each cell type in each region of the modified small and large wicking fiber constructs. The alginate cap and bottom fiber region show similar percentages of benign and cancer cells for both large and small fiber bundles. The percentage of MCF-10A cells in the top region of the large fiber bundle is significantly greater than the small fiber bundle.

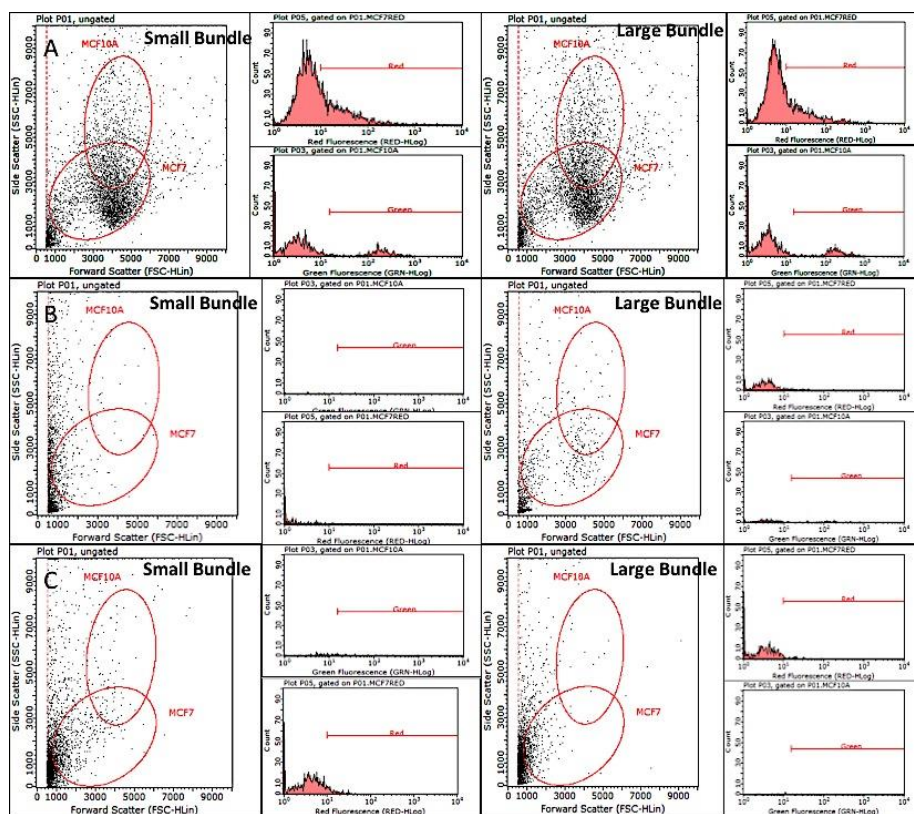


Figure 7.8: Scatter and fluorescent intensity plots of benign and cancer cells in each region of the alginate modified construct. (A) Bottom region of modified small bundles (left) shows comparable amounts of benign and cancer cells as the modified large bundles (right). (B) Top region of modified small bundles (Left) show less cell penetration and less green labeled benign cells than the modified large bundle construct (Right). (C) Alginate cap from modified small bundle construct shows comparable amounts of cancer and benign cell in large bundle construct.

Investigating Cytoskeletal Arrangement and Protein Expression along the Modified Wicking Bundles

Materials and Methods

Cell Culture

The cytoskeleton arrangement was investigated for various cancer types as well as mouse progenitor and pre-osteoblast cells. Benign epithelial cells, MCF-10A

(ATCC), and human breast cancer cells, MCF-7 (ATCC), were cultured in DMEM (Invitrogen) supplemented with 10% FBS (Gibco), 1% Fungizone, and MEGM single quotes (Lonza) and DMEM (Invitrogen) supplemented with 0.01 mg/mL human recombinant insulin (Gibco), 10% FBS, 1% Fungizone (Gibco), 10,000 U penicillin, and 10 mg streptomycin/mL (Sigma-Aldrich), respectively. Metastatic breast epithelial cells, MDA-MB-231 (ATCC) were cultured in DMEM (Invitrogen) supplemented with 10% FBS, 1% Fungizone (Gibco), 10,000 U penicillin, and 10 mg streptomycin/mL (Sigma-Aldrich). Mouse mesenchymal stem cells, D1 (ATCC), and mouse pre-osteoblast cells, MC3T3E1 (ATCC) were cultured in growth media consisting of Dulbecco's Modified Eagle's Medium (DMEM, Invitrogen) supplemented with 10% fetal bovine serum (FBS, Gibco), 10,000 U penicillin, and 10 mg streptomycin/mL (Sigma-Aldrich), and Minimal Essential Medium α without ascorbic acid (Gibco) supplemented with 10% fetal bovine serum (Gibco), 10,000 U penicillin, and 10mg streptomycin/mL (Sigma), respectively.

Immunofluorescence Staining for Actin Cytoskeleton and Vinculin

Staining for vinculin and actin cytoskeleton was performed on both the modified wicking bundles after conducting the vertical test with cell solutions, as well as cells seeded directly on a glass coverslip. Prior to staining along the wicking fiber bundles, 1 mL containing 500,000 cells from each cell line being investigated was seeded in a low-attachment 12-well plate. The modified wicking bundle was used to conduct the vertical test method as previously described. After two hours of incubation the modified wicking bundles were removed and prepared for staining. Cells were also seeded at a density of 100,000 cells per mL on a glass cover slip in a 24-well plate. The cytoskeleton

organization was evaluated for MCF-10A and MCF-7 cells along the modified wicking bundle after performing the vertical test with both cell lines mixed in each well.

Fluorescent images of the actin and vinculin were captured in the bottom, middle, and top regions of the bundle. This procedure was also performed to investigate cell mechanics of MCF10A and MDA-MB-231 along the fiber. D1 progenitor cells and the MC3T3E1 pre-osteoblast cells were analyzed, however, these cell lines were not mixed and each cell line was analyzed separately along the construct. The table below presents the different cell line groups that were used to investigate cell cytoskeletal arrangement. All cell lines investigated along the modified wicking bundle were also analyzed on a glass slide.

Table 7.1: Cell lines investigated

Cell lines assessed along the modified wicking bundle	Cell lines analyzed on glass slides
MCF-10A and MCF-7	MCF-10A
MCF-10A and MDAMB-231	MCF-7
D1	MDA-MB-231
MC3T3E1	D1
	MC3T3E1

Prior to the actin and vinculin staining, the samples were washed with PBS and fixed in 10% formalin for 20 minutes. Formalin was removed and samples were further rinsed in PBS. To stain for actin and vinculin, samples were blocked for 1 hour using blocking solution containing 2% BSA (Sigma; St. Louis, MO, USA), 5% goat serum (Sigma), and 0.1% triton X (ThermoScientific; Rockford, IL). The blocking solution was removed and the samples were washed with PBS. To prevent auto-fluorescence from the polylactide fibers, the samples were blocked in 1% (w/v) sodium borohydride (Sigma; St.

Louis, MO) in PBS and incubated at room temperature for 30 minutes. The sodium borohydride was removed and the samples were washed extensively with PBS for 30 minutes. Following the blocking step, the samples were incubated overnight at 4°C with the vinculin primary antibody (mouse anti-rabbit; Abcam; Cambridge, MA, USA) using a 1:200 dilution. After the overnight incubation, the primary was removed and stored for later use. The samples were gently washed with PBS and incubated in 500 µL of solution containing Alexa Fluor 488 phalloidin (Invitrogen; Grand Island, NY) using a 1:20 dilution, and Alexa Fluor 568 goat anti-rabbit antibody (Molecular Probes; Grand Island, NY, USA) using a 1:500 dilution for two hours at room temperature. Following the two hour incubation the phalloidin and secondary antibody solution was removed and 1 mL of a 2 mg/mL Hoechst 33342 solution (Thermo Scientific; Rockford, IL) was added to the samples and incubated for 5 minutes at room temperature. Samples were rinsed with PBS and stored at 4°C. To analyze cell cytoskeletal arrangement, images were obtained from each region of the fiber bundle using fluorescent microscopy (EVOS; Fluid Cell Imaging Station, Life Technologies); Image J imaging software was used to overlay images.

Immunofluorescence Analysis of EpCAM and CD44

EpCAM expression of the MCF-10A, MDA-MB-231, and MCF-7 cells was investigated along the modified wicking bundles. MCF-7, MCF-10A, and MDA-MB-231 cells were cultured and plated in low-attachment 12-well plate. Six wells were plated with MCF-7 and MCF-10A cells at a cell density of 500,000 cells per mL. The remaining six wells were seeded with MD-AMB-231 and MCF-10A cells at the same cell density.

The vertical test using the modified wicking bundles was performed. After 2 hours, the samples were removed and prepared for immunofluorescence staining. To investigate the amount of EpCAM and CD44 expressed by each cell type the cells were also individually plated at 20,000 cells per well on glass slides in a 24-well plate.

Immunofluorescence staining for EpCAM was performed on the modified wicking bundles. Both EpCAM and CD44 expression was investigated on the cancer cells plated on the glass slides. To stain for EpCAM and CD44 samples were blocked for 1 hour using blocking solution containing 2% BSA (Sigma; St. Louis, MO, USA), 5% goat serum (Sigma), and 0.1% triton X (ThermoScientific; Rockford, IL). The blocking solution was removed and the samples were washed with PBS. To prevent auto-fluorescence from the polylactide fibers, the samples were blocked in 1% (w/v) sodium borohydride (Sigma; St. Louis, MO) in PBS and incubated at room temperature for 30 minutes. The sodium borohydride was removed and the samples were washed extensively with PBS for 30 minutes. Following the blocking step, the samples were incubated overnight at 4°C with the primary antibody EpCAM (mouse anti-rabbit; Abcam; Cambridge, MA USA) using a 1:200 dilution or with the primary antibody CD44 (rabbit anti-human; Life Technologies; Grand Island, NY USA). After the overnight incubation, the primary was removed and stored for later use. The samples were gently washed with PBS and incubated in 500 µL of solution containing the secondary antibody Alexa Fluor 488 goat anti-rabbit antibody (Invitrogen; Grand Island, NY) using a 1:500 dilution, or Alexa Fluor 568 goat anti-rabbit antibody (Molecular Probes; Grand Island, NY, USA) using a 1:500 dilution for two hours at room temperature. Following the two hour

incubation, the secondary antibody solution was removed and 1 mL of a 2 mg/mL Hoechst 33342 solution (Thermo Scientific; Rockford, IL) was added to the samples at a and incubated for 5 minutes at room temperature. Samples were rinsed with PBS and stored at 4°C. Fluorescent images of EpCAM expression along the fibers were obtained from each region of the fiber bundle using fluorescent microscopy (EVOS; Fluid Cell Imaging Station, Life Technologies). Both EpCAM and CD44 expression was imaged for each cell line that was cultured on a glass cover slide. Image J imaging software was used to overlay images.

Flow Cytometry Analysis of EpCAM Expression along Fibers

Prior to EpCAM expression analysis by flow cytometry, the vertical test was conducted along the modified wicking bundles using a cellular mixture of MCF-10A and MDA-MB-231, or a mixture of MCF-10A and MCF-7 cells with all cell types seeded at 500,000 cells. Immediately after the vertical test, the samples were removed, transferred to a 6-well plate, and washed with PBS. The cells were stained for EpCAM prior to the removal from the modified wicking bundle. To stain for EpCAM, samples were incubated for 30 minutes at 4°C in 1 mL of primary antibody solution containing 5% goat serum (Sigma) and the primary antibody EpCAM (mouse anti-rabbit; Abcam; Cambridge, MA USA) using a 1:200 dilution. Following incubation, the samples were gently washed with PBS and incubated in 1 mL of solution containing the secondary antibody Alexa Fluor 488 goat anti-rabbit antibody (Invitrogen; Grand Island, NY) using a 1:500 dilution for 30 minutes at room temperature. Samples were rinsed in PBS and cells were removed from each region of the construct following previous procedures and

resuspended in 500 μ L of PBS for flow cytometry analysis. Positive and negative controls for each cell line were prepared by seeding 100,000 cells in microcentrifuge tubes. The positive controls from each cell line were rinsed with PBS and stained for EpCAM using the procedure described above. The negative controls were left unstained.

The amount of EpCAM expression in each region of the modified wicking bundle was analyzed using a Guava easyCyteTM flow cytometer (Guava Technologies) and by following the manufacturer's instructions for InCyte software (Guava Technologies). The green intensity plots were used to determine the amount of cells expressing EpCAM in each of the regions.

Results

Exploring Cell Mechanics of Cancer Cell Lines along Fibers

The actin and vinculin arrangement of each cancer line was investigated both on a 2-dimensional glass cover slide, as well as, along the modified wicking bundle. Figure 7.9 depicts the actin and vinculin arrangement of the cell lines tested along the wicking fibers. The MCF-7 cell lines (Image A) portray a rounded morphology with actin fibers primarily unorganized and circumferentially localized. MCF-10A show more aligned actin stress fibers along the periphery of the cell (Image B). MDA-MB-231 cells (image C) depict the fibril actin abundantly distributed around the cells with a more overall organized fiber arrangement. Both MCF-10A and MDA-MB-231 cells show less rounded morphology with more a more spindle shape appearance.

The morphology and cytoskeletal arrangement of benign, MCF-10A, and cancerous cells, MCF-7 was explored along the bottom, middle, and top regions of the

modified wicking bundles. Figure 7.10 depicts the cytoskeletal architecture of the cells after wicking through the bundle. The cancer cells present a rounded morphology with actin concentrated along the periphery in all regions of the bundle. This morphology suggests the cancer cells are tethered to the surface and are not spreading out on the fibers. The cell morphology of metastatic cancer, MDA-MB-231, and benign, MCF-10A, cells was also investigated along the wicking fibers after the cell mixture was wicked through the modified wicking bundle, Figure 7.11. The outcomes show similar rounded morphology in all regions of the fiber bundle. However, in comparison to the MCF-7 and MCF-10A separation, the MDA-MB-231 cell displacement through the fibers shows less cell-cell contact with more individual cell movement through the conduits.

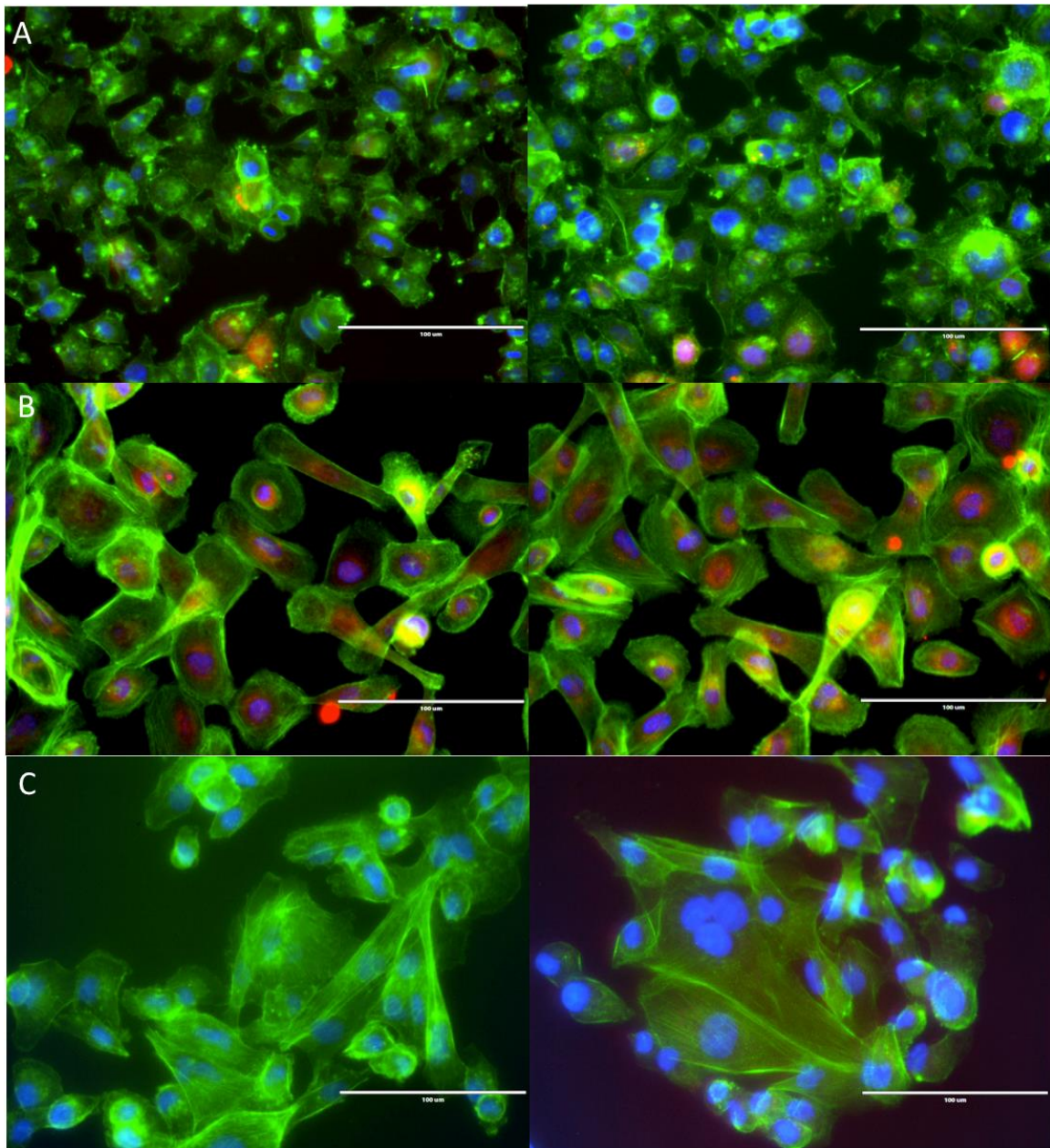


Figure 7.9: Actin cytoskeletal and vinculin arrangement of the various cancer types (A) MCF-7 non-metastatic cancer cells show weak actin cytoskeleton lacking fiber arrangement (B) MCF-10A benign cells show actin fibril arrangement with alignment along the periphery of the cell. Benign cells depict vinculin expression concentrated in central region of cells. (C) MDA-MB-231 cells depict more actin fiber arrangement compared to the other cell lines. Images show distinct actin fibers along the periphery and central regions of the cell.

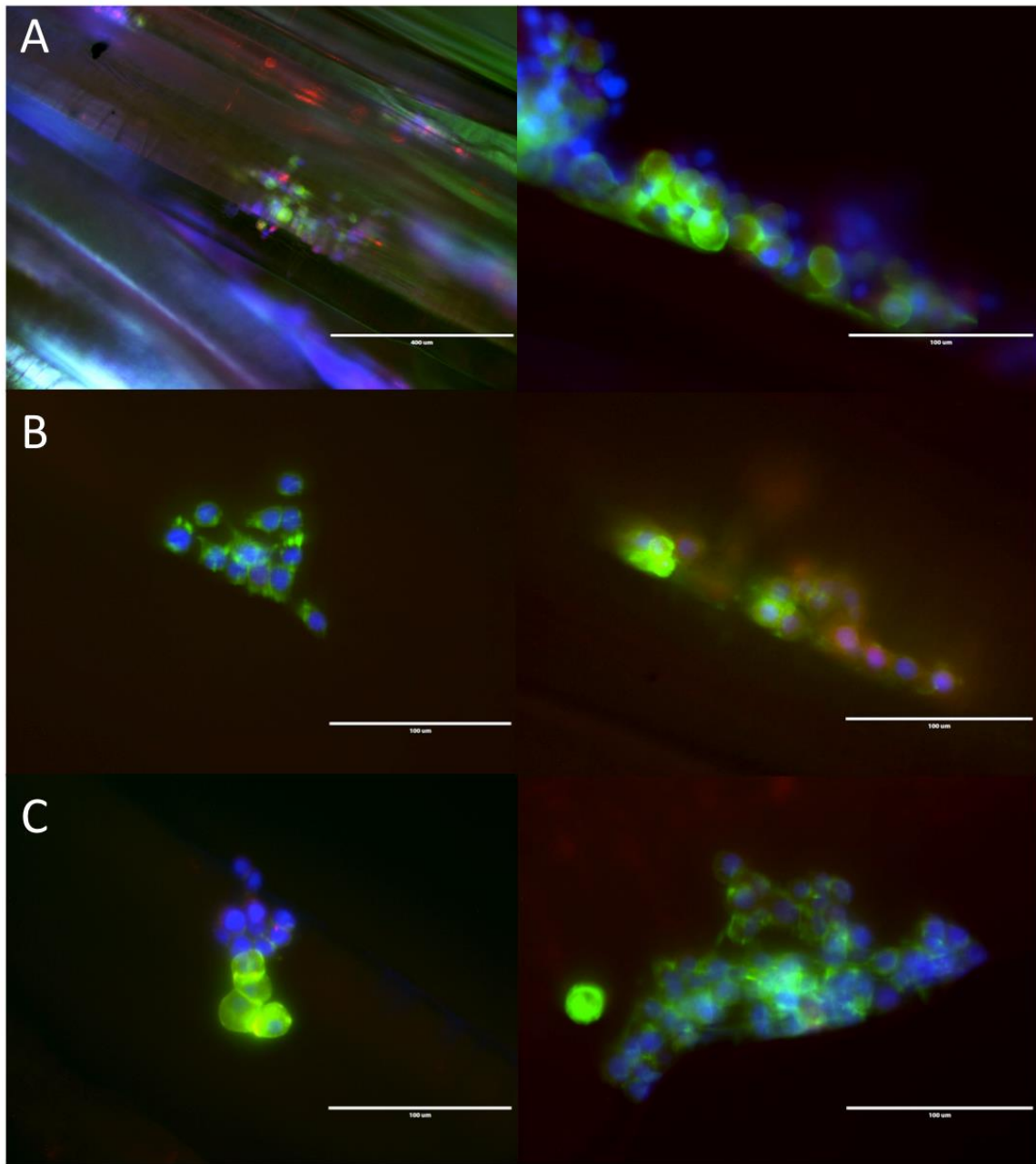


Figure 7.10: The actin and vinculin arrangement of MCF-7 and MCF-10A cells along the modified wicking fiber construct (A) Bottom region of the wicking fiber bundle shows the actin fibers are arranged along the periphery forming an outer shell. (B) Middle region of the wicking fiber bundle shows clumps of cells with round morphology (C) Top region of wicking fiber bundle depicts the same rounded morphology of the cells

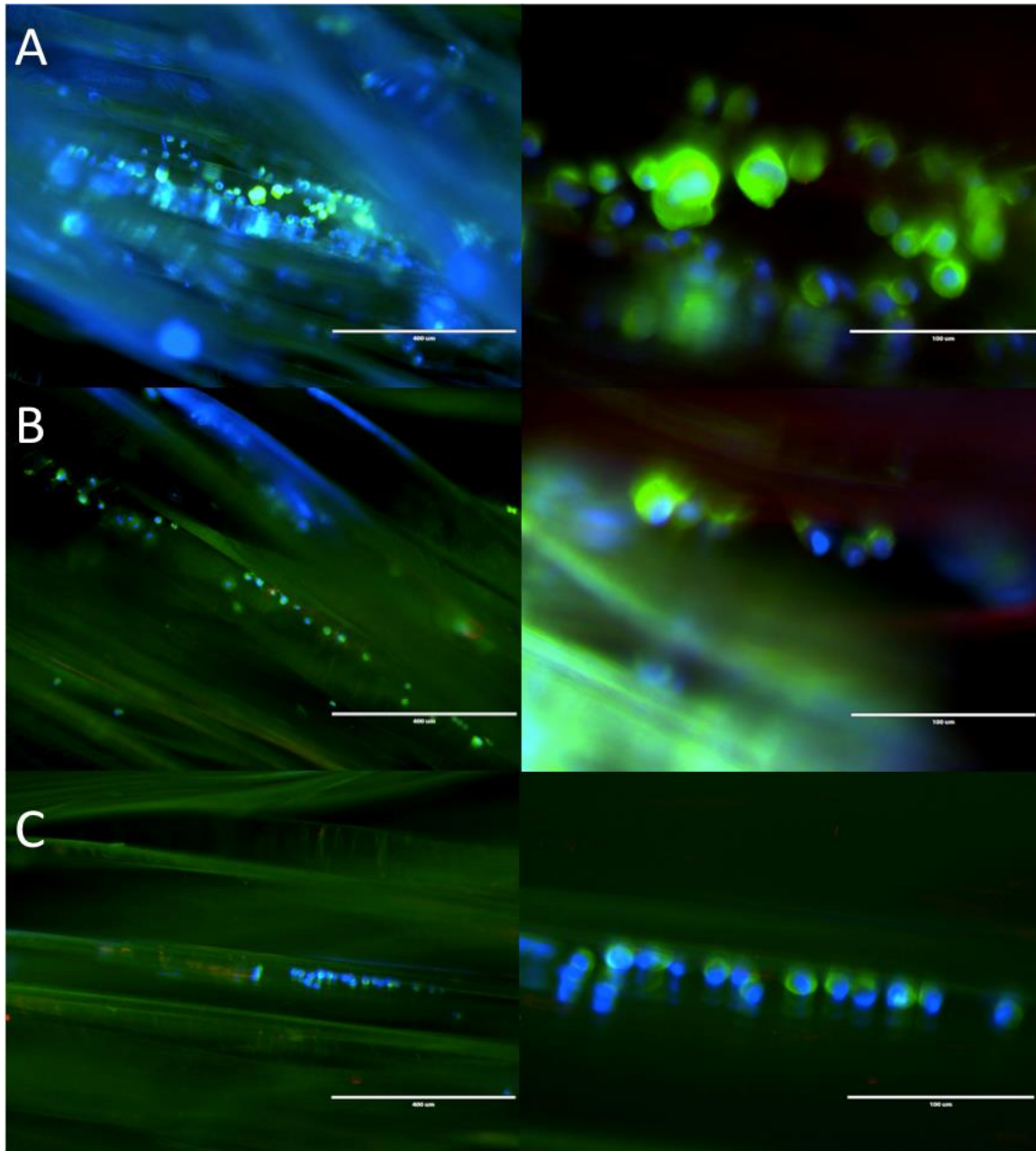


Figure 7.11: Cytoskeletal architecture of MDA-MB-231 cells along the modified wicking fiber construct. (A) Cells in bottom region of construct depict rounded morphology with actin concentrated along the periphery. The middle region (B) and top region (C) of the modified construct shows the same rounded morphology.

Exploring Cell Mechanics of Mesenchymal Stem Cells and Pre-Osteoblasts along the Fibers

The cell cytoskeletal architecture of mouse mesenchymal stem cells and mouse pre-osteoblasts was analyzed after attachment to a glass slide and wicking through the modified wicking bundle. Figure 7.12 depicts the fluorescent images of the actin cytoskeleton arrangement for D1 (Image A) and MC3T3E1 cells (Image B). The D1 cells depict a fibroblast-like morphology with a more spindle-like shape. In comparison, the MC3T3E1 cells also depict a more fibroblast morphology with greater actin fiber alignment, suggesting the pre-osteoblasts have a stronger cytoskeleton.

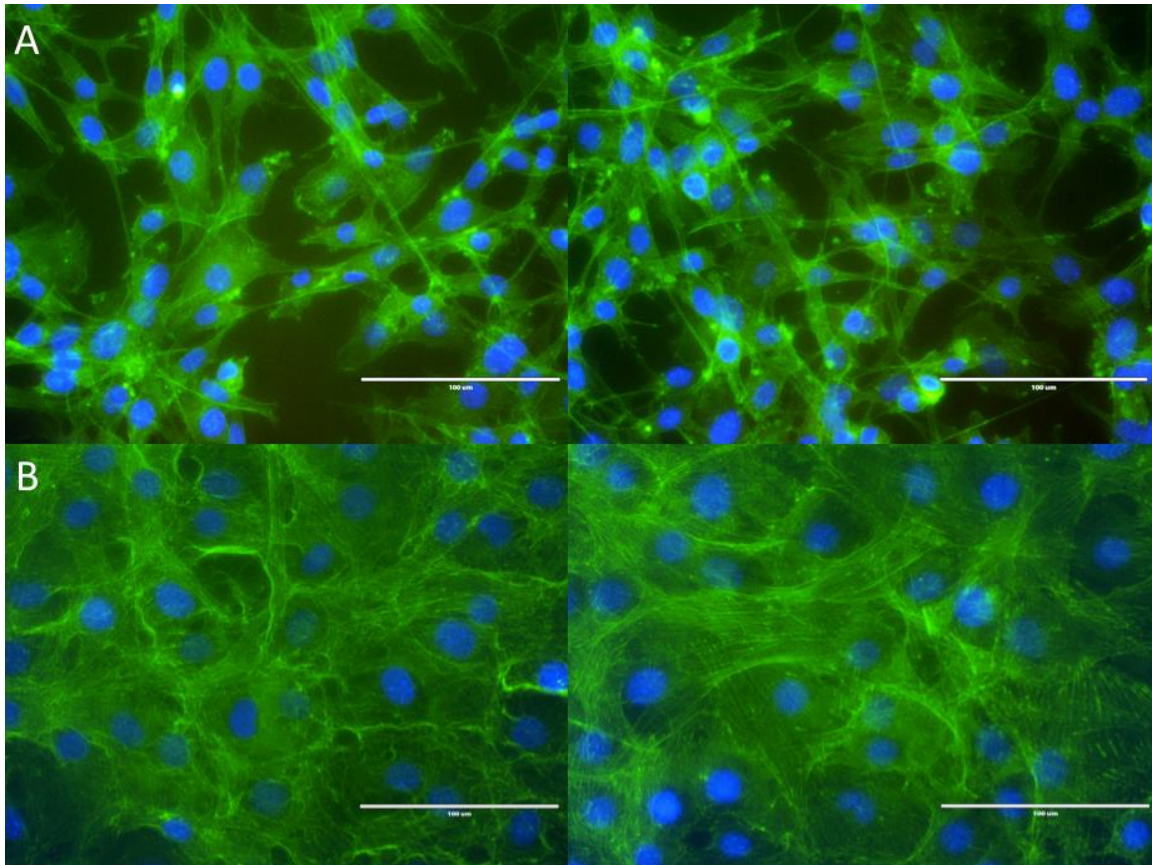


Figure 7.12: (A) Actin arrangement of D1 mouse mesenchymal stem cells show fibroblast-like morphology with actin fiber formation predominantly on the periphery of the cell. (B) MC3T3E1 pre-osteoblast cells depicts a less spindle shaped morphology with more actin fiber formation within the cell

The D1 and MC3T3E1 cell movement along the fibers after the vertical wicking test is depicted in Figure 7.13. The MC3T3E1 cells show greater cell attachment to the fibers with a more spread-out actin cytoskeleton along the bottom and middle regions of the fiber bundles. The D1 cells show a more rounded morphology along each of the regions with less cell attachment.

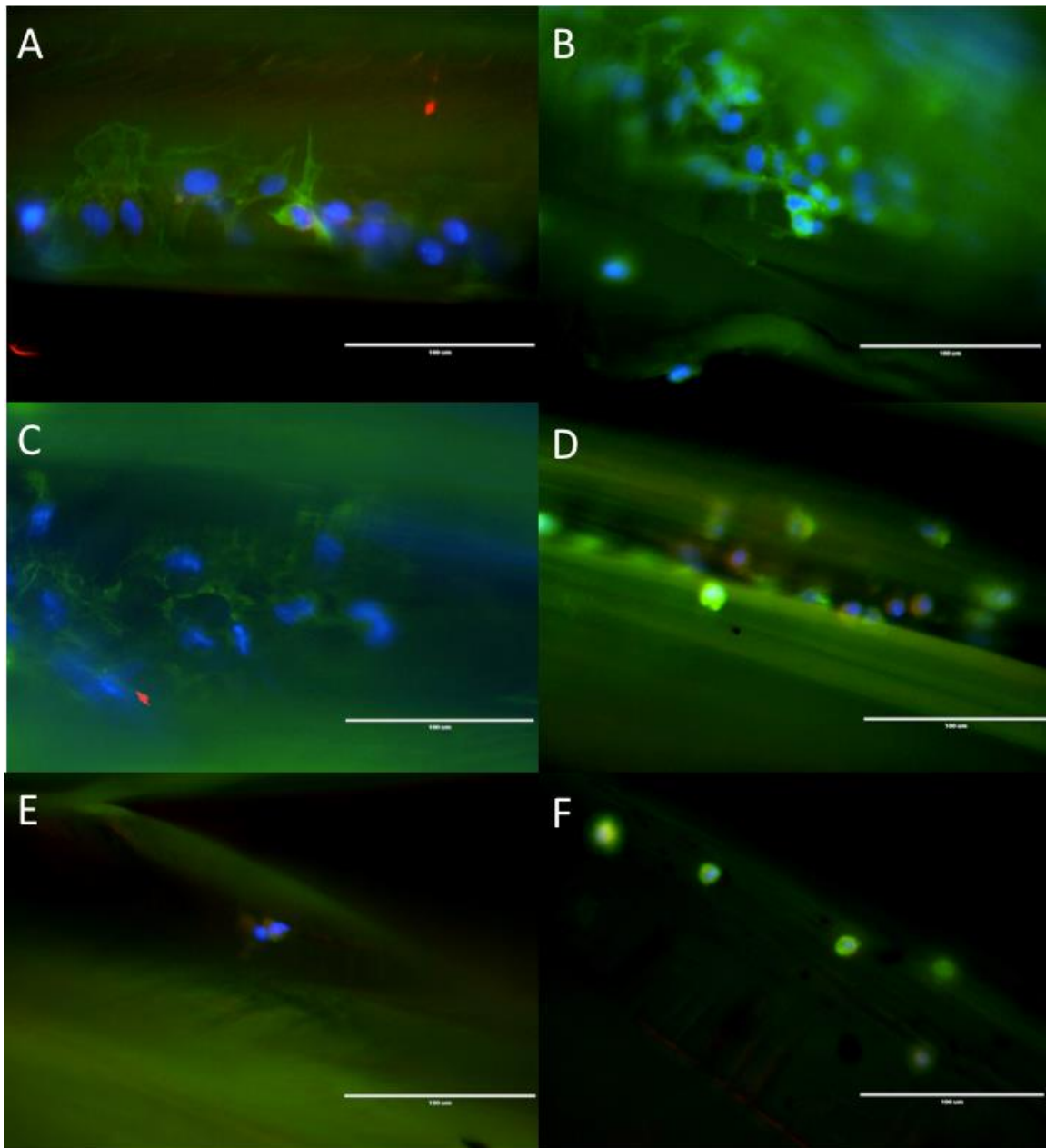


Figure 7.13: (A) Pre-osteoblast cells and (B) D1 cells along the top region of the wicking fiber bundle show the pre-osteoblasts have a less rounded morphology and more spread-out along the fiber. (C) Pre-osteoblast and (D) D1 cells in the middle region depict the pre-osteoblast have adhered more to the fiber compared to the rounded shape of the D1 cells. The pre-osteoblasts (E) and D1 cells (F) both show more rounded morphology in the top regions of the fiber

EpCAM Expression of Cancer Cell Lines along the Fibers

Each cancer cell line was cultured on a glass plate and analyzed for EpCAM expression using immunofluorescence. Figure 7.14 illustrates the levels of EpCAM expression for each cell line. MCF-7 cells showed high levels of EpCAM expression (Image A). Both MCF-10A (Image B) and MDA-MB-231 cells (Image C) demonstrated low levels of EpCAM.

A mixture of MCF-10A and MCF-7 were used to conduct the vertical wicking test. After the cells wicked into the modified wicking bundle, the EpCAM expression was investigated along each region of the fiber bundles using both immunofluorescence and flow cytometry. The immunofluorescence results show some expression of EpCAM in the bottom region of the fiber bundle, Figure 7.15. The middle (and top regions of the fiber bundles depict higher percentages of EpCAM expression. This is due to the greater penetration of MCF-7 cells to these regions. The flow cytometry results showed similar results, Figure 7.18. Higher percentages of cells expressing EpCAM were found in the top region of the wicking fiber bundle and alginate cap (Image A). The scatter and intensity plots depict EpCAM expression in each region of the construct (Image B). The higher percentage of EpCAM expression in the top region and alginate cap correlates to the greater number of MCF-7 cells that wick to these regions.

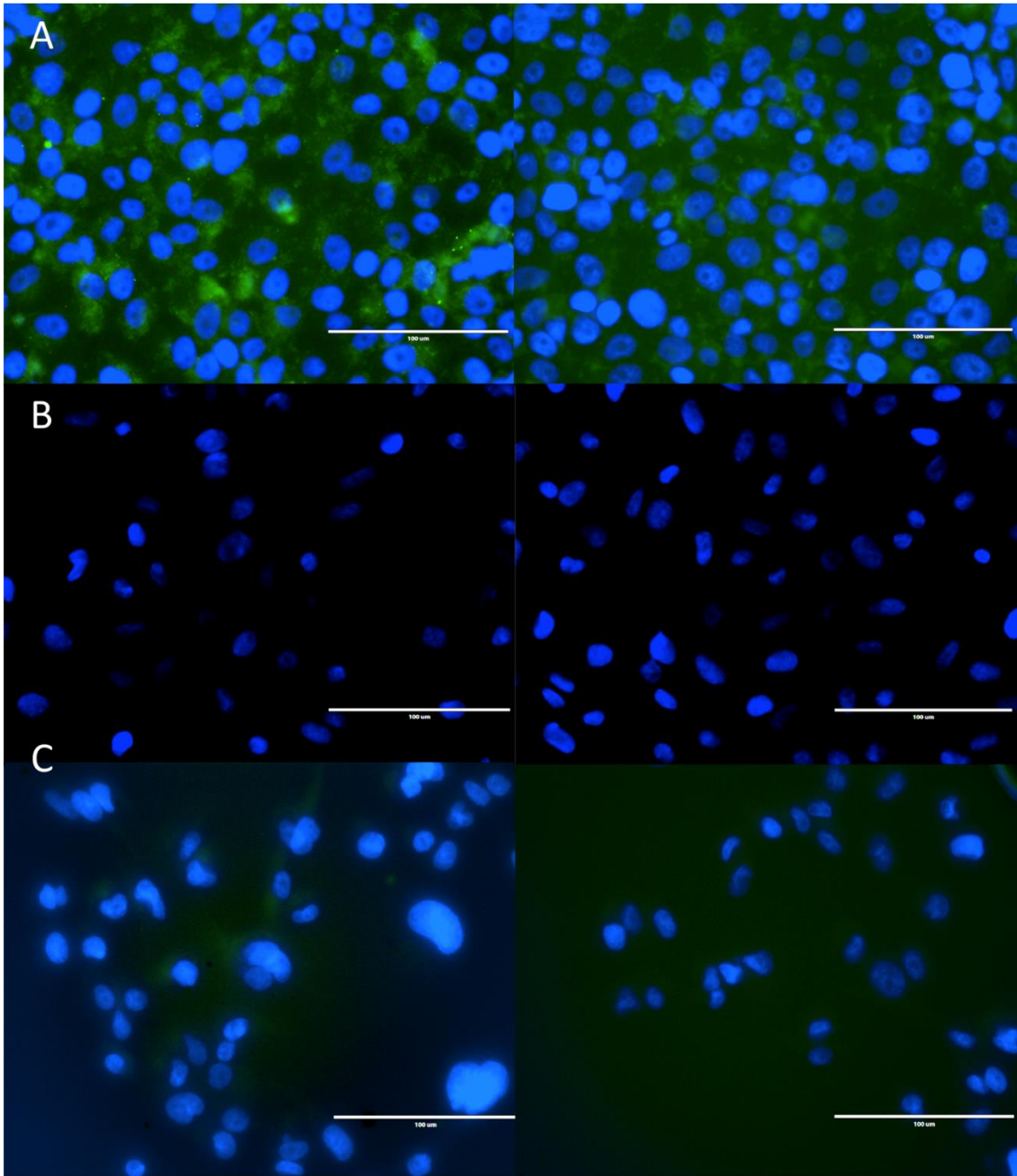


Figure 7.14: EpCAM expression (Green fluorescence) of each cancer cell line (A) MCF-7 cells show high expression of EpCAM (B) MCF-10A cells and (C) MDA-MB-231 show low expression of EpCAM

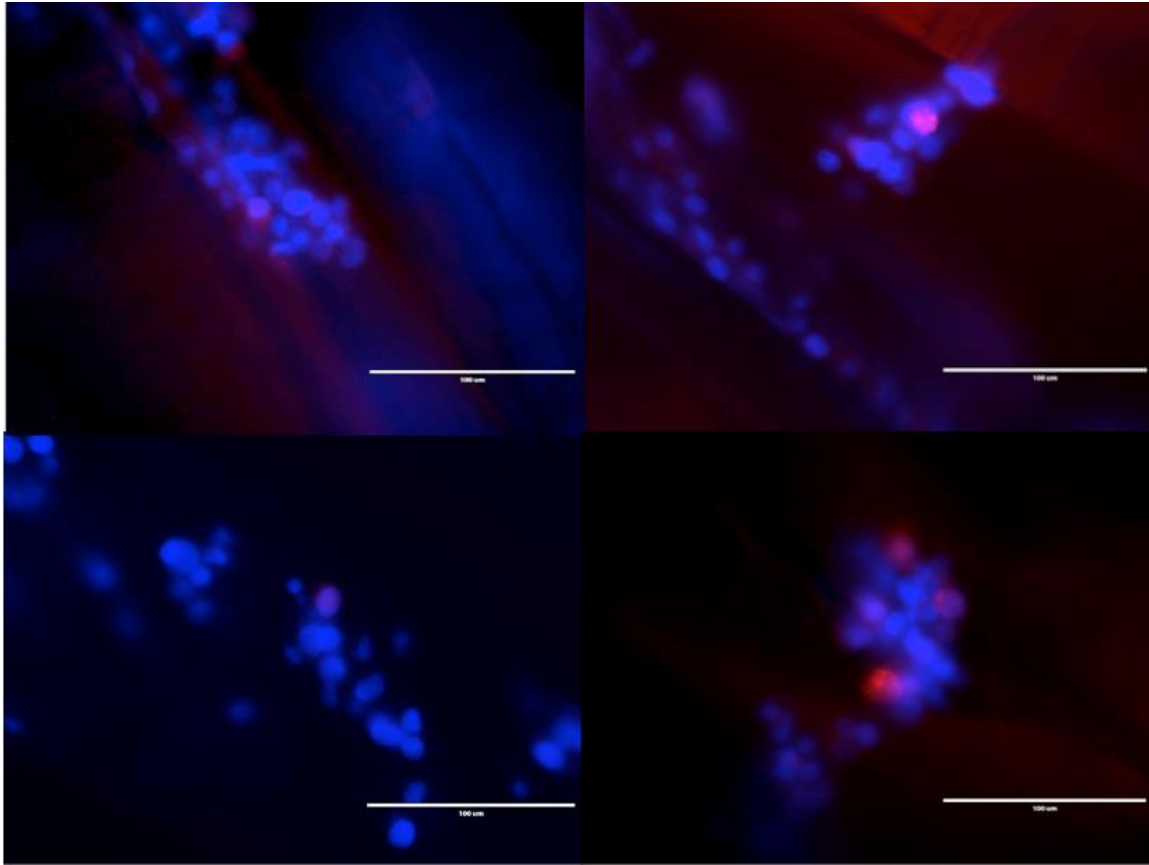


Figure 7.15: EpCAM expression (Tagged with red-fluorescent secondary antibody) of MCF-7 and MCF-10A cells in the bottom region of the wicking fiber bundle

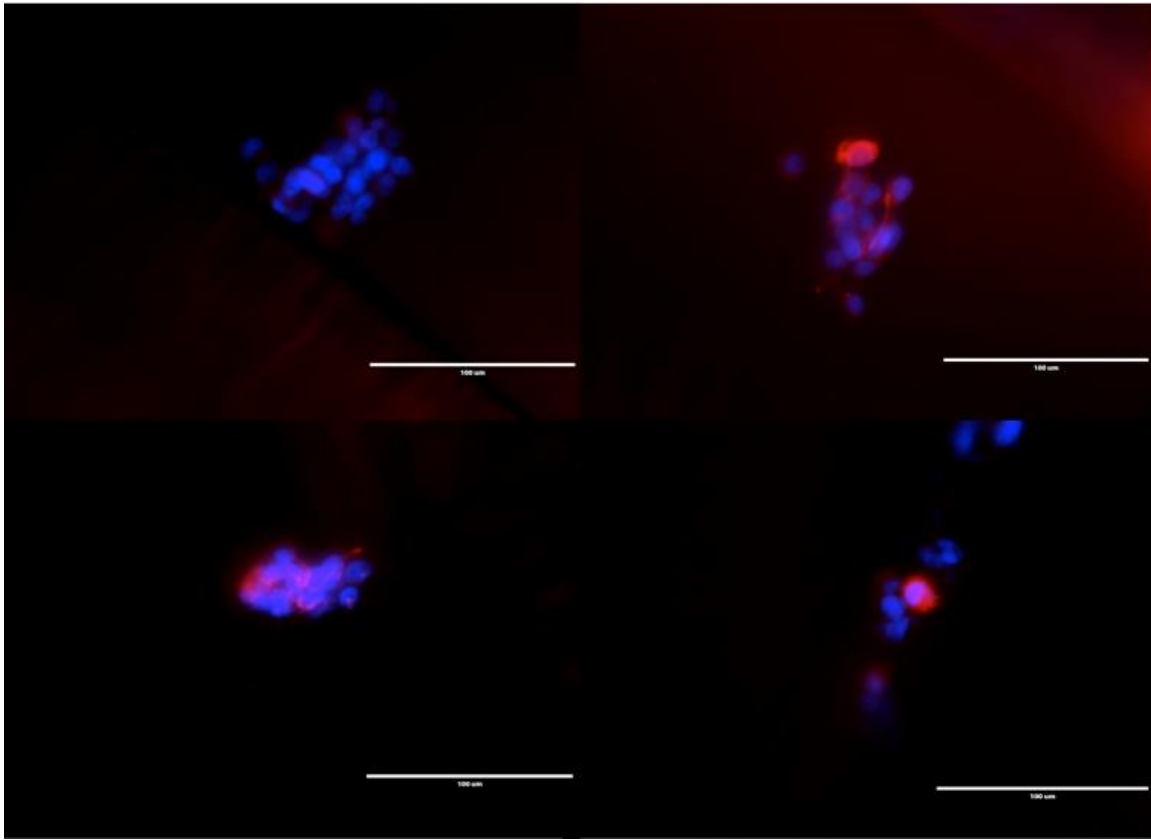


Figure 7.16: EpCAM expression of MCF-7 and MCF-10A cells along central region of wicking fiber bundle

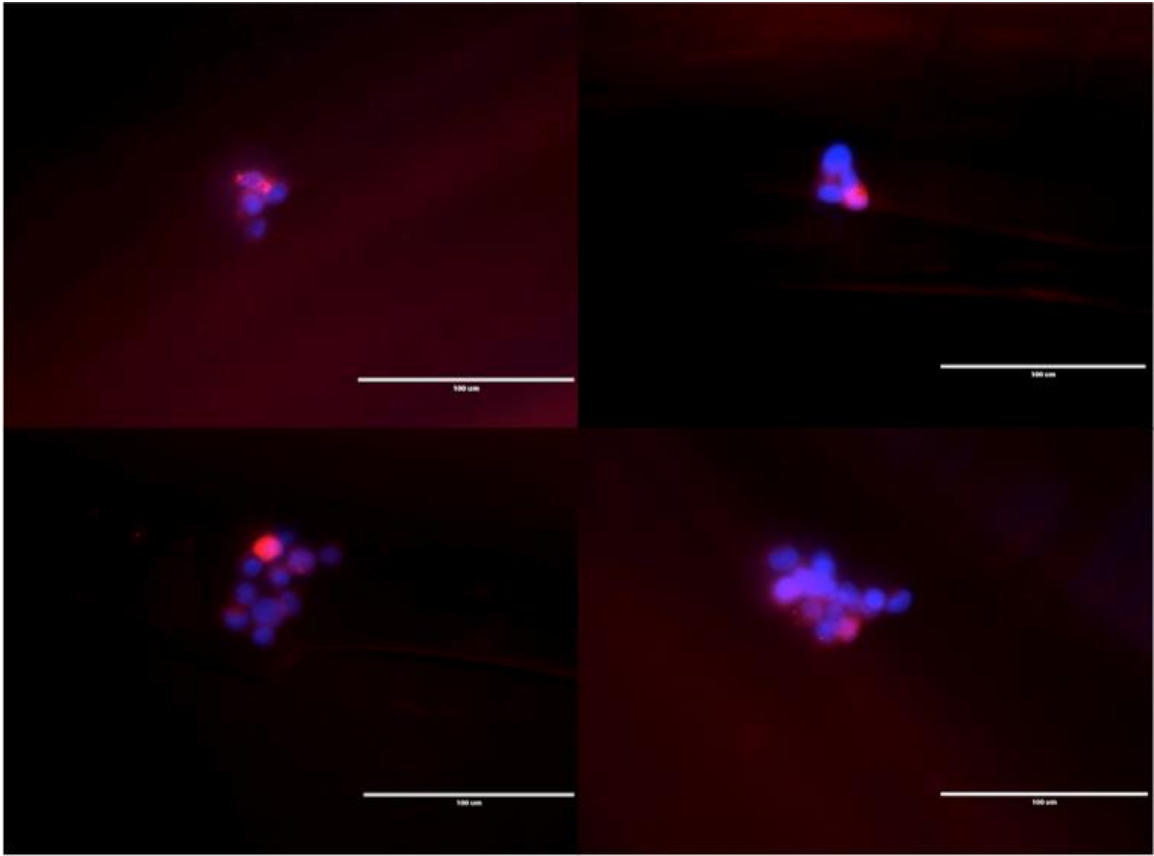


Figure 7.17: Depicts high percentage of EpCAM expression in top region of the wicking fiber bundle

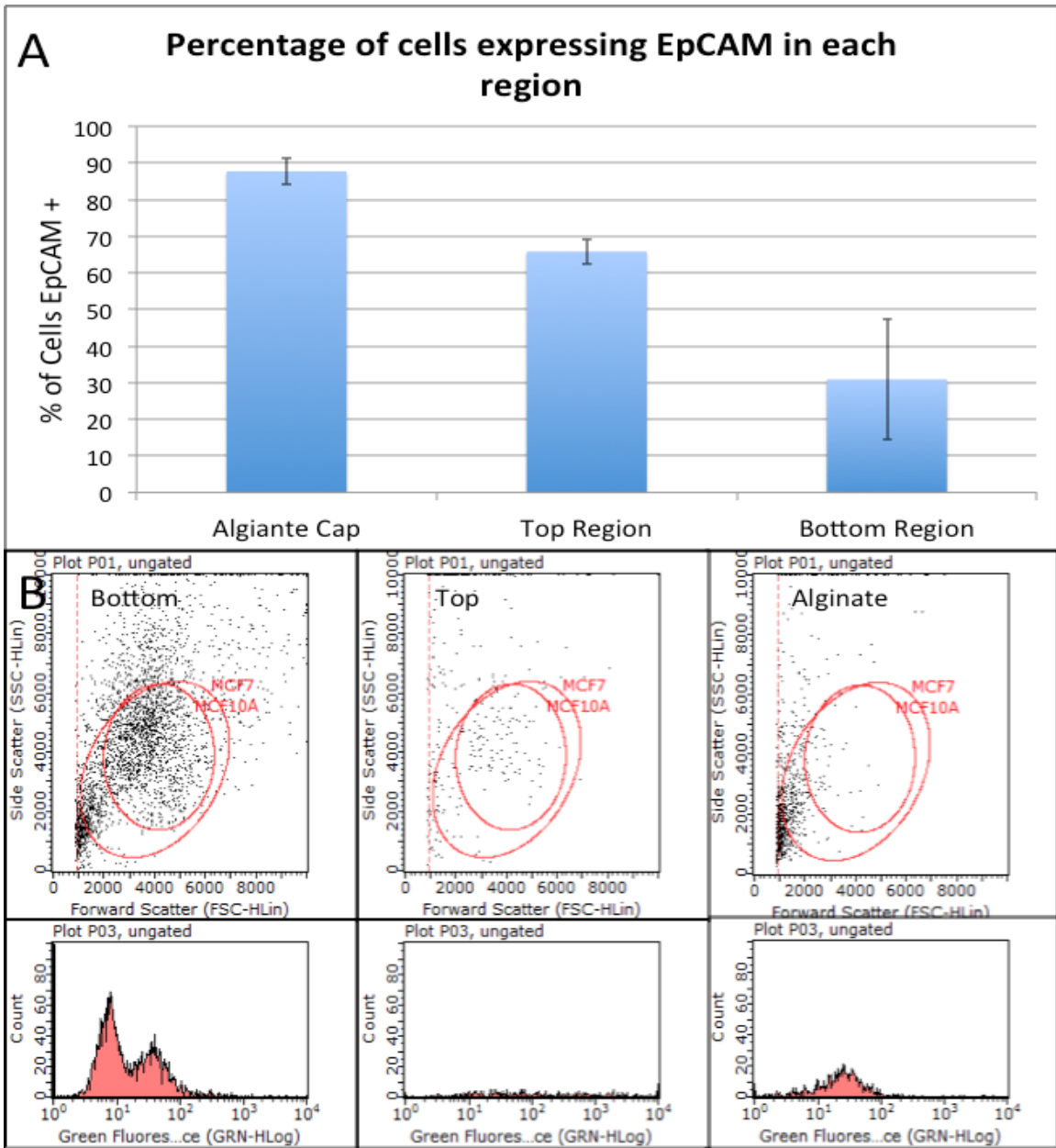


Figure 7.18: Flow cytometry analysis (A) Percentage of cells expressing EpCAM (B) Scatter and intensity plots of EpCAM expression from each region

The EpCAM expression was also investigated along modified wicking bundles after MCF-10A and MDA-MB-231 cells were processed through the vertical test. The fluorescent images of the modified wicking bundle (Figure 7.19) depict low EpCAM expression in all regions. As indicated previously both MCF-10A and MDA-MB-231 cell lines show minimal EpCAM expression. The EpCAM expression from the top and bottom regions of the modified wicking bundle was quantified using flow cytometry. The scatter and intensity plots of the control groups showed low EpCAM expression for both MCF-10A and MDA-MB-231 cells. Cell isolated from the top and bottom regions of the bundle showed low expression of EpCAM, approximately 10%. The EpCAM expression of MDA-MB-231 cells mixed with benign cells along the fiber bundles was significantly lower than MCF-7 mixed with benign. The results suggest the modified wicking bundle can separate cancer cells that expressing EpCAM, such as MCF-7 cells, into the top region of the wicking fiber bundle and alginate cap. Conversely, metastatic cancer cells often lack EpCAM expression and are still captured in the top region of the fiber bundle and the alginate cap. The outcomes imply EpCAM expression may play a role in cancer cell type separation along the fibers, but further investigation is needed. Preliminary works has also investigated expression of other proteins along the modified wicking bundle to determine if this separation device can be used to isolate subpopulations of cancer cells within cell lines. CD44 expression was assessed between each of the cell lines. High expression of this marker has been used to define metastatic cancer cells, as well as, breast cancer stem cells that are tumorigenic and can differentiate, propagating a heterogeneous tumor. Figure 7.21 depicts CD44 expression from benign, cancerous, and

metastatic cancer cell lines. The MDA-MB-231 and MCF-10A cells show high expression of CD44, and the MCF-7 cells show low expression. Future work involves investigating expression of CD44 and other tumorigenic protein markers along the fibers to optimize the system to distinguish cancer cells of varying phenotypic expression.

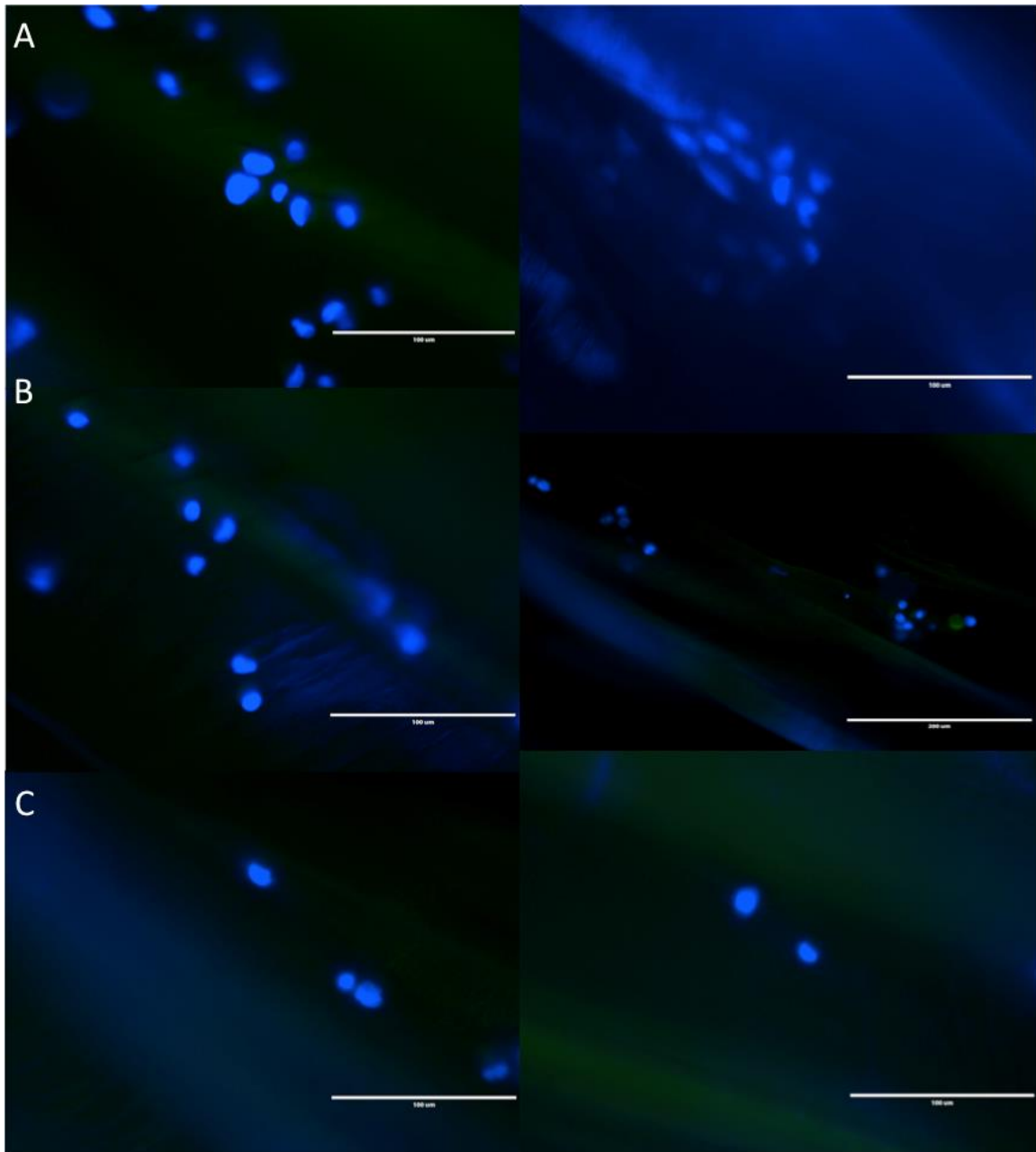


Figure 7.19: Depicts low EpCAM expression (tagged with green fluorescent secondary antibody) of MCF-10A and MDA-MB-231 cells in bottom (A), middle (B), and top regions (C) of the wicking fiber bundle.

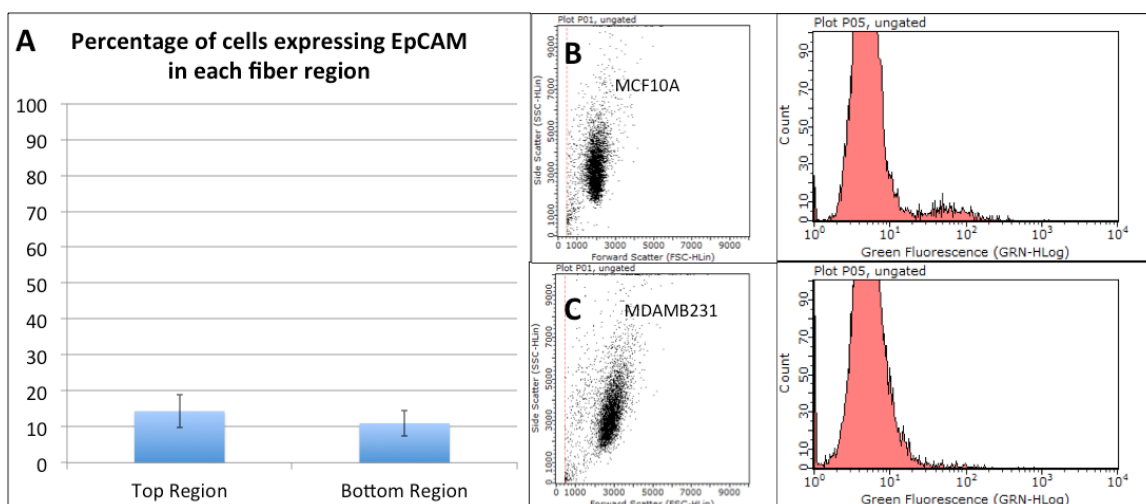


Figure 7.20: Flow cytometry analysis of EpCAM expression along top and bottom regions of wicking fiber bundle (A) Percentage of cells expressing EpCAM in top and bottom regions of wicking fiber (B) MCF10A control group shows low expression of EpCAM (C) MDA-MB-231 group depicts almost no EpCAM expression

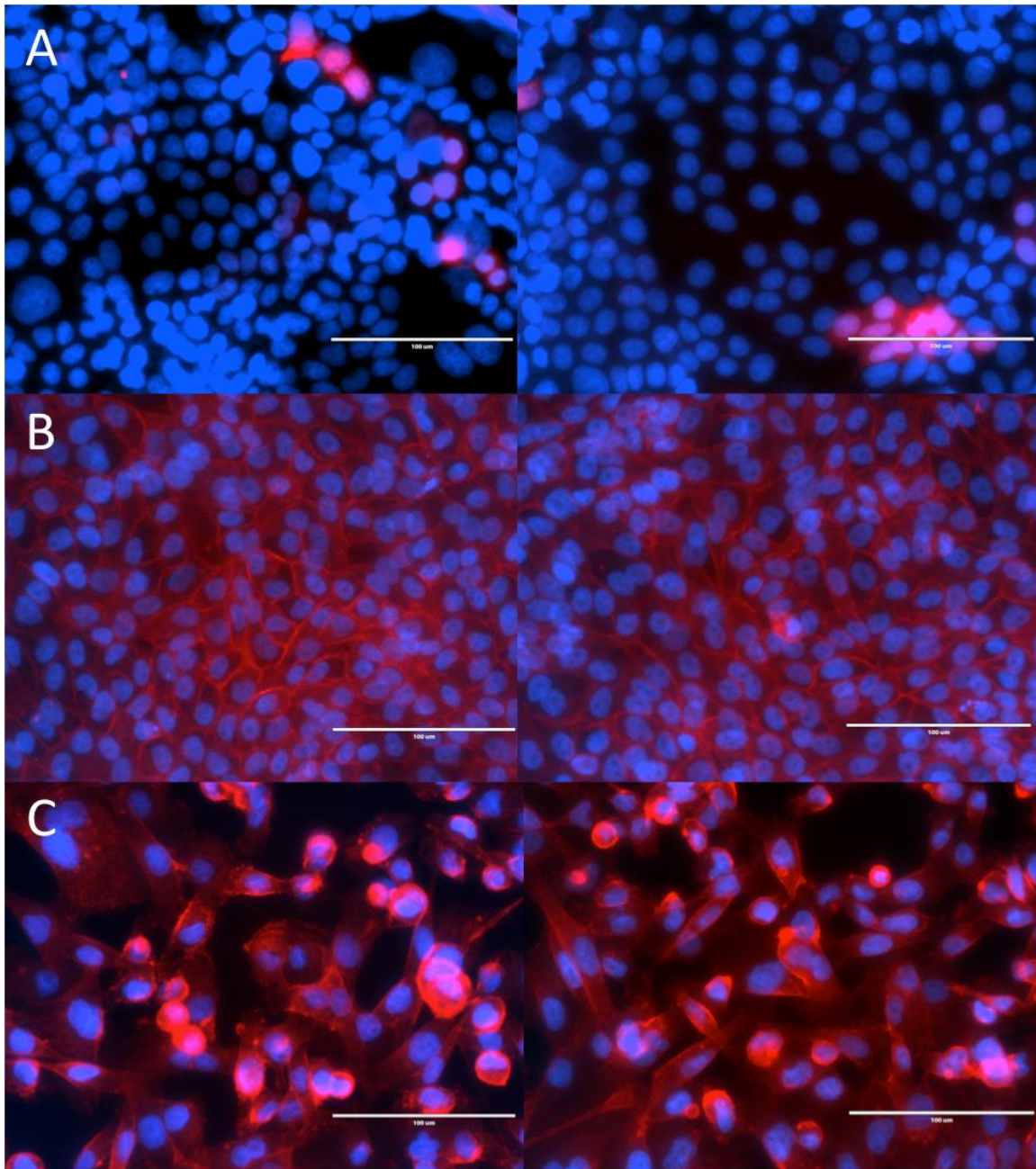


Figure 7.21: Levels of CD44 expression of the various cancer cell lines (A) MCF-7 show low CD44 expression (B) MCF10A and (C) MDA-MB-231 cells show high levels of CD44 expression

Discussion

The first part of this chapter explored the role of cell size as a major factor in cell separation between different cell types. The outcomes showed that there are differences in cell size of the various cell types that were separated along the modified wicking fiber construct. Interestingly, the MCF-7 cancer cells and D1 cells were both similar in cell size, and significantly smaller than the benign MCF-10A and MC3T3E1 pre-osteoblast cells. The increased travel of the smaller cell types, D1 and MCF-7 cells suggest cell size may play a major role in separation along the fiber construct. Beads of 6 and 20 μm were used to mimic cells of different sizes in modified wicking fiber constructs containing small or large wicking fiber bundles. The outcomes showed approximately 90% of the bead populations in each region were the 6 μm sized beads for both types of modified wicking fiber constructs.

The results confirm the size of the cell will play a role in the modified wicking fiber construct. It also reveals using bundles with individual wicking fibers of larger cross-section does not increase the amount of large beads into the system. The larger cross-sectional fibers consist of larger individual grooves along the fiber, providing conduits with larger diameters. Laplace equation, shown below, describes the capillary pressure generated in a capillary with a defined radius. According to Laplace equation the larger the diameter of the capillary the less capillary pressure is generated¹⁶.

Equation 7.1: Laplace Equation

$$P_{Capillary} = \frac{\gamma_{LV} \cos \theta}{Rc}$$

$\theta = \text{contact angle}$

$Rc = \text{Radius of the capillary}$

$\gamma_{LV} = \text{Surface tension between liquid and air}$

The maximum liquid height reached is also inversely proportional to the radius of the conduits. Jurin's law describes the maximum height reach along a capillary when the pressure reaches equilibrium¹⁷.

Equation 7.2: Jurin's Law

$$H_{Maximum} = \frac{2\gamma_{LV} \cos \theta}{\rho g Rc}$$

$\theta = \text{contact angle}$

$Rc = \text{Radius of the capillary}$

$\gamma = \text{Surface tension}$

$\rho = \text{Density of the liquid}$

The larger wicking fiber bundles consist of larger grooves or conduits with lower capillary pressure that will influence the vertical wicking behavior. The outcomes showed the modified wicking bundle containing the small groove sizes contained significantly more 6 μm beads than the bundles with larger groove sizes. The bundled fibers of smaller groove sizes create smaller capillaries that produce greater capillary pressure to transport

the bead solution vertically through the bundle. Although the modified wicking bundles contained different sized fibers, the amount of tension used to twist the fibers remained the same. The twist of the fibers will create pores or inter-fiber spaces between the fibers. The tension of the twist will result in different pore sizes. High tension can affect the continuity and reduce the radius of the capillaries between the fibers. Hajian and coworkers demonstrated twisted fibers of the same diameter with different twist rates exhibit different wicking behaviors. This group showed increased twisting results in smaller inter-fiber spaces reducing the effective radius as well as the continuity causing a reduction in the rate of capillary rise¹⁷. The twisting of the larger fibers in our system may have caused discontinuities along the fiber inhibiting the wicking action in some of the conduits. Although the larger conduits will decrease capillary pressure and the maximum height reached, increased pore size generated from the inter-fiber spaces will actually increase the rate of capillary action. This is described by the Lucas Washburn equation, which is determined by integrating the Hagen-Poiseuille equation that describes liquid capillary rise, shown below¹⁶⁻¹⁸.

Equation 7.3: Hagen-Poiseuille Equation

$$\frac{dh}{dt} = \frac{r^2}{8\eta h} \Delta P = \frac{r^2}{8\eta h} \left(\frac{2\gamma \cos\theta}{r} - \rho g h \right)$$

$\theta =$ Contact angle

$R_c =$ Radius of the capillary

$\gamma =$ Surface tension

$\rho =$ Density of the liquid

$\eta =$ Dynamic viscosity of the liquid

$h =$ Height reached by liquid by time t

$\Delta P =$ Pressure Difference

Equation 7.4: Lucas – Washburn Equation

$$h^2 = \frac{r\gamma \cos\theta}{2\eta} t = kt$$

$k =$ capillary rise rate coefficient

The Lucas-Washburn equation demonstrates the larger pore sizes between the fibers, the less resistance due to fiber and liquid interfaces increasing the liquid rate^{17,19}. The twisting of the bundles can control the pore size. The larger the pore size the faster the fluid can fill and the more fluid can be absorbed by the construct^{16,17}. The small and large modified wicking bundles were used to compare the wicking separation of MCF-10A and MCF-7 cells. The bundles showed similar cell counts and percentage of cell

types in each region. The larger fiber, however, showed increased MCF-10A cells in the top region. The increased number of cells in this region can be a result of the larger pore sizes. The benign cells were shown to be larger than the MCF-7 cells in a suspended solution. The larger pore sizes along the modified large fiber bundle has less liquid-fiber action allowing larger cells to fit through and travel with the liquid through the pores. Future work will investigate the various bundling configurations and tension rates to increase the wicking rate, as well as, the amount of capillary pressure generated to increase the amount of cells in the top regions of the fiber and with alginate cap. The system can be optimized to determine an effective cross-sectional size and twist rate to enhance the rate of separation and improve the separation and isolation of non-metastatic and metastatic cancer cell types.

This chapter also investigated the role of cell morphology and cytoskeletal arrangement of various cell types on their wicking behavior along the modified wicking bundles. The immunofluorescence staining of the cytoskeletal components on a 2-dimensional surface showed the cancer cell types had different morphology and actin arrangement. The non-metastatic cancer cells showed the least disorganized actin arrangement with a round morphology. Both the benign cells and metastatic cancer cells showed a more spindle shaped phenotype with more actin fiber arrangement. The difference in cell morphology is a factor of cell origin. MCF-10A and MDA-MB-231 cells are both basal epithelial cells and MCF-7 cells are luminal. Generally, basal type cells show a more spindle mesenchyme-like morphology and luminal cells show a more cobblestone appearance²⁰. Although the MCF-10A and MDA-MB-231 cells illustrated a

more spindle-like morphology the cytoskeletal arrangement will greatly impact the cell mechanics of the cell. The fibrous actin organization, as well as, microtubule structure will affect the cell stiffness or deformability of the cells. The metastatic cancer cells are shown to be more deformable than both cancerous and benign cells. Guck and coworkers measured optical deformability of MCF-7, MCF-10A, and MDA-MB-231 cells. The metastatic cancer cells deformed more than both non-metastatic cancer cells MCF-7 and benign MCF-10A cells²¹. The increased deformation and reduction of cytoskeletal strength of the metastatic cancer cells correlates to their ability to squeeze through tissue to reach the blood stream and penetrate other tissue^{21,22}. The cancerous cells, however, showed significantly more deformation than the MCF-10A cells. The degree of deformability of the cell has been correlated with metastatic potential. Other groups have developed microfluidic systems to isolate circulating tumor cells using the ability of cancer cells to deform. These systems include arrays, posts, or channels in combination with a hydrodynamic force to deform the cells through the size-limited barriers to isolate the more flexible cancer cells, which are also considered to have more metastatic potential¹². Biomechanical measurements from atomic force microscopy (AFM) and optical tweezer measurements confirm the cell stiffness of cancer cells are significantly softer than normal cells, relating to the cancer cell's increased deformability and metastatic potential^{11,12}. The ability of MCF-7 and MDA-MB-231 cells to deform may play a significant role in their ability to wick along the wicking fiber bundles. The cytoskeletal arrangement of the cancer cells along the wicking fiber bundles showed mostly round morphology. The images showed cancer cells tethered along the fibers with

very minimal cell spreading. This suggests cell morphology may play less of a role in cell separation in our system. The staining along the fibers containing MCF-7 and MCF-10A cells showed clusters of cells within the bundles of the fiber. The staining of MDA-MB-231 and MCF10A cells showed more individual cell movement with significantly less clusters. The clumping and moving of cells as clumps is characteristic migratory behavior of both MCF-10A and MCF-7 cells. Metastatic cancer cells, MDA-MB-231, migrate individually, which is characteristic for a mesenchyme-like cell. Regardless of the clusters shown, each of the cancer cell lines investigated showed a round phenotype along the fiber. In addition to cell morphology, cell adhesion can play a role. Chen and coworkers investigated cancer cell separation based on the cell adhesion to a substrate and found cancer cell types will adhere preferentially^{23,24}. Further work can investigate the cell adhesion strength along the wicking fibers of the various cell types and the effects of modifying surface topography on cell wicking behavior. The outcomes of this work show cell size and cell deformability may play greater roles in the mechanism for cell wicking than cell morphology.

The mouse mesenchymal stem cells and pre-osteoblast cells depicted morphological differences. The D1 stem cells showed weaker actin alignment and fiber formation compared to the more differentiated MC3T3E1 cells. Titushki and coworkers investigated cellular mechanic changes during cell differentiation. This group found changes in the cell mechanics of progenitor cells as they differentiate into bone cells²⁵. Furthermore, stem cells have been shown to be highly deformable¹². The thick bundle actin shown in the fluorescent image of the MC3T3E1 cells suggests the cells are less

deformable with higher cells stiffness. Further work will need to investigate the deformability of D1 cells and MC3T3E1 cells, but the outcomes suggest the D1 cells are more deformable and this characteristic may explain the high cell densities of D1 cells in the top region and alginate cap of the modified bundle. The D1 cells showed a similar round morphology as the cancer cells along the wicking fiber bundles. Interestingly, the MC3T3E1 cells depicted a more fibroblast morphology along the bottom and middle regions of the fibers. The pre-osteoblasts showed cell attachment and spreading along the grooves. The high actin fiber arrangement of the MC3T3E1 cells may limit deformability of the cell causing minimal penetration into the bundle. The pre-osteoblasts also show higher adhesion preference to the wicking fibers. The topography of the wicking fibers was shown to have a rough surface. The pre-osteoblasts may have a greater affinity to adhere to the rough surface than the D1 progenitor cells. This is reflected by the low amount of cells in the top regions of the fibers and the increased adherence and cell spreading of the pre-osteoblasts along the bottom regions of the fibers.

The standard for isolating CTCs involves isolating cells based on the expression of EpCAM and/or cytokeratin and the negative expression of CD45. The only FDA approved technology to isolate CTCs from blood biopsy samples is the CellSearch system (Verdex, USA). This system isolates cells expressing EpCAM using an immunomagnetic approach²⁶. The major limitation of these EpCAM based systems is the specificity for one type of cancer cell. Cancer cells of high metastatic potential have been defined with negative EpCAM expression and high expression of mesenchymal markers. Circulating tumor cells are transient and may transition into mesenchymal phenotypes by

a process called epithelial-mesenchymal transition (EMT)²⁷. In this conversion, cells lose epithelial markers, such as EpCAM, and express mesenchymal markers, resulting in a more aggressive, motile cell type. Aggressive CTC populations with mesenchymal phenotype in the bloodstream are missed by these conventional technologies⁴⁻⁸. Tumor-initiating cells with high metastatic potential are a small subpopulation of cancer cells that have been defined by CD44⁺ and CD24⁻. In this work we investigated EpCAM expression along the modified wicking bundle. EpCAM expression was analyzed in each region after separation of MCF-10A and MCF-7 cells. The results for this study showed higher percentages of EpCAM expression in the top region and alginate cap, because of high percentages of MCF-7 cells wicking to these regions. This suggests the construct can separate cancer cells expressing EpCAM. However, low expression of EpCAM was observed along the construct for cell separation of MCF-10A and MDA-MB-231. Since both cancer cell lines MCF-7 and MDA-MB-231 were observed in the top region of the fiber bundle and the alginate cap, EpCAM expression may not play a role in the mechanism for separation. However, the outcomes show cells expressing EpCAM are captured in the top region and alginate cap of modified fiber construct. Preliminary work investigated CD44 expression of each cancer cell line used. The results showed the different cancer types contain varying expression of CD44. Further work will investigate the expression of CD44 and CD24, markers of highly metastatic cancer cells along the fibers. The goal of the system is to isolate and distinguish between cancerous and metastatic cancer cells. We have shown the modified wicking bundle will separate both non-metastatic and cancerous cell types from benign cells. However, further work is

needed to enhance separation of cancer cells of varying metastatic potential. Due to the heterogeneity of tumors and CTC, there is a need for a CTC isolation technology that can capture and distinguish the heterogeneous phenotype.

This heterogeneity has also been translated to cell lines. Fillmore and coworkers has shown phenotypic and functional differences within cell lines and found that established breast cell lines contain a small subpopulation of tumorigenic self-renewing cells that can differentiate into various phenotypic cells²⁸. The results of this chapter show the mechanism of separation along the modified wicking fiber construct is due to functional and physical properties of the cancer cells, including cell size, deformability, and cell adhesion potential. Further work will optimize the system to separate subpopulations of highly metastatic cancer cells between cell lines.

Conclusions

This chapter investigated various factors that may contribute to the separation of various cell types along the modified wicking fiber bundles. The outcomes showed cell size, deformability, and ability to adhere to substrates play a major role in the cell wicking behavior. By understanding the mechanism of separation we can optimize the wicking fiber construct to not only separate cancer from benign cells but also cells of varying metastatic potential. Further work will optimize the tension and cross-sectional sizes of the wicking fiber bundles to increase efficiency of separation. Alterations to the topography of the grooves and the alginate cap will be explored to improve the separation of metastatic and non-metastatic cancer cells.

References

1. Hung LY, Chuang YH, Kuo HT, Wang CH, Hsu KF, Chou C-Y, Lee G Bin: An integrated microfluidic platform for rapid tumor cell isolation, counting and molecular diagnosis. *Biomedical Microdevices* 2013; 15:339–52
2. Nagrath S, Sequist LV, Maheswaran S, Bell DW, Ryan P, Balis UJ, Tompkins RG, Haber DA: Isolation of rare circulating tumour cells in cancer patients by microchip technology. *Nature* 2007; 450:1235–9
3. Yokobori T, Iinuma H, Shimamura T, Imoto S, Sugimachi K, Ishii H, Iwatsuki M, Ota D, Ohkuma M, Iwaya T, Nishida N, Kogo R, Sudo T, Tanaka F, Shibata K, Toh H, Sato T, Barnard GF, Fukagawa T, Yamamoto S, Nakanishi H, Sasaki S, Miyano S, Watanabe T, Kuwano H, Mimori K, Pantel K, Mori M: Plastin3 is a novel marker for circulating tumor cells undergoing the epithelial-mesenchymal transition and is associated with colorectal cancer prognosis. *Cancer Research* 2013; 73:2059–69
4. Harris JL, Stocum M, Roberts L, Jiang C, Lin J, Sprott K: Quest for the ideal cancer biomarker: an update on progress in capture and characterization of circulating tumor cells. *Drug Development Research* 2013; 74:138–47
5. Marie-Egyptienne DT, Lohse I, Hill RP: Cancer stem cells, the epithelial to mesenchymal transition (EMT) and radioresistance: Potential role of hypoxia. *Cancer Letters* 2013; 341:63–72
6. van de Stolpe A, Pantel K, Sleijfer S, Terstappen LW, den Toonder JMJ: Circulating tumor cell isolation and diagnostics: toward routine clinical use. *Cancer Research* 2011; 71:5955–60
7. Wirtz D, Konstantopoulos K, Searson P: The physics of cancer: the role of physical interactions and mechanical forces in metastasis. *Nature Reviews Cancer* 2012; 11:512–22
8. Yu M, Bardia A, Wittner BS, Stott SL, Smas ME, Ting DT, Isakoff SJ, Ciciliano JC, Wells MN, Shah AM, Concannon KF, Donaldson MC, Sequist L V, Brachtel E, Sgroi D, Baselga J, Ramaswamy S, Toner M, Haber DA, Maheswaran S: Circulating breast tumor cells exhibit dynamic changes in epithelial and mesenchymal composition. *Science* 2013; 339:580–4
9. Alix-Panabières C, Pantel K: Circulating tumor cells: liquid biopsy of cancer. *Clinical Chemistry* 2013; 59:110–8
10. Hyun KA, Jung H: Advances and critical concerns with the microfluidic enrichments of circulating tumor cells. *Lab Chip* 2013; 14:45–56

11. Byun S, Son S, Amodei D, Cermak N, Shaw J, Ho J, Hecht VC: Characterizing deformability and surface friction of cancer cells. *Proceedings of the National Academy of Sciences* 2013; 110:7580–5
12. Zhang W, Kai K, Choi DS, Iwamoto T, Nguyen YH, Wong H, Landis MD, Ueno NT, Chang J, Qin L: Microfluidics separation reveals the stem-cell-like deformability of tumor-initiating cells. *Proceedings of the National Academy of Sciences* 2012; 109:18707–12
13. González-Cruz RD, Fonseca VC, Darling EM: Cellular mechanical properties reflect the differentiation potential of adipose-derived mesenchymal stem cells. *Proceedings of the National Academy of Sciences* 2012; 109:E1523–9
14. Phinney DG: Functional heterogeneity of mesenchymal stem cells: implications for cell therapy. *Journal of Cellular Biochemistry* 2012; 113:2806–12
15. Pantel K, Alix-Panabières C: Detection methods of circulating tumor cells. *Journal of Thoracic Disease* 2012; 4:446–7
16. Chen X, Vroman P, Lewandowski M, Perwuelz a., Zhang Y: Study of the Influence of Fiber Diameter and Fiber Blending on Liquid Absorption Inside Nonwoven Structures. *Textile Research Journal* 2009; 79:1364–70
17. Hajjani F, Ghareaghaji a. a., Jeddi A a. a., Amirshahi SH, Mazaheri F: Wicking properties of polyamide 66 twisted nanofiber yarn by tracing the color alteration in yarn structure. *Fibers and Polymers* 2014; 15:1966–76
18. Rengasamy RS, Kothari VK, Bele VS, Khanna R: Liquid sorption behaviour of nonwovens. *Journal of the Textile Institute* 2011; 102:1019–30
19. Washburn E: The Dynamics of Capillary Flow. *The Physical Review* 1921; 17:273–83
20. Holliday DL, Speirs V: Choosing the right cell line for breast cancer research. *Breast Cancer Research* 2011; 13:1–7
21. Guck J, Schinkinger S, Lincoln B, Wottawah F, Ebert S, Romeyke M, Lenz D, Erickson HM, Ananthkrishnan R, Mitchell D, Käs J, Ulvick S, Bilby C: Optical deformability as an inherent cell marker for testing malignant transformation and metastatic competence. *Biophysical Journal* 2005; 88:3689–98
22. Fritsch A, Höckel M, Kiessling T, Nnetu KD, Wetzel F, Zink M, Käs JA: Are biomechanical changes necessary for tumour progression? *Nature Physics* 2010; 6:730–2

23. Chen W: Nanoroughned Surfaces for Efficient Capture of Circulating Tumor Cells without Using Capture Antibodies. *ACS Nano*. 2013; 7:566–75
24. Bussonni A, Miron Y, Baudoin M, Bou-matar O, Grandbois M, Charette P, Renaudin A: Cell detachment and label-free cell sorting using modulated surface acoustic waves (SAW) in droplet-based microfluidics. *Lab on a Chip* 2014;31–3
25. Titushkin I, Cho M: Modulation of cellular mechanics during osteogenic differentiation of human mesenchymal stem cells. *Biophysical Journal* 2007; 93:3693–702
26. Hyun K-A, Kwon K, Han H, Kim S-I, Jung H-I: Microfluidic flow fractionation device for label-free isolation of circulating tumor cells (CTCs) from breast cancer patients. *Biosensors & Bioelectronics* 2013; 40:206–12
27. Martowicz A, Spizzo G, Gastl G, Untergasser G: Phenotype-dependent effects of EpCAM expression on growth and invasion of human breast cancer cell lines. *BMC Cancer* 2012; 12:1–15
28. Fillmore CM, Kuperwasser C: Human breast cancer cell lines contain stem-like cells that self-renew, give rise to phenotypically diverse progeny and survive chemotherapy. *Breast Cancer Research* 2008; 10:R25

CHAPTER EIGHT

DEVELOPMENT OF A BONE TISSUE ENGINEERING LEARNING MODULE FOR MIDDLE SCHOOL STUDENTS

Introduction

The National Academy of Sciences has reported that the United States educational system is lagging in the production of students in STEM (Science Technology Engineering Mathematics) fields compared to other countries¹. Due to the lack of interest in STEM careers there is a shortage of professionals to fill STEM positions^{1,2}. To encourage STEM participation there is a major push for STEM education, especially for elementary school students, who during this time develop perceptions and interests in STEM related fields. STEM education also strives to increase the lack of diversity, as well as, the low interest of women involvement. The American Society for Engineering Education has reported the percentage of women earning a bachelor's degree in engineering was 18.4% in 2011³. Lower female participation in STEM fields reflects a need to increase awareness and involvement of female students at an earlier age. Howard and coworkers describe middle school as critical years where students begin to consider careers and develop personal career goals, which is reflected in their class choices and activities in high school⁴. Educational researchers have shown introducing and emphasizing STEM activities to middle school students, especially women, can impact student interest in STEM fields⁴.

The purpose of STEM education is to not only increase numbers and awareness of the field, but to provide students a foundation for life problem-solving skills and critical

thinking². This chapter focuses on the development and testing of a biomedical engineering learning module to effectively teach concepts focused on bone tissue engineering to young female students in middle school. The activities introduced the engineering design process involving systematic critical thinking. The student's knowledge of engineering and tissue engineering concepts were assessed before and after the learning module. Additionally, interest in student educational and career path towards engineering was evaluated.

The educational program was conducted in coordination with ProjectWise summer camp for young girls in middle school. This camp provides experiences and hands-on learning activities in the field of science and engineering. During the camp the girls participated in six different mini courses of different engineering and science disciplines. The developed bioengineering mini course was held on two different days for an hour and fifteen minutes long each day. Each day consisted of an interactive lecture introducing bone tissue engineering concepts followed by a hands-on activity to reinforce the concepts of the lecture and further introduce the engineering design process. The bone tissue engineering concepts presented to the students focused primarily on transport phenomena in tissues of the human body and how this applies to tissue engineering applications. The module on the first day specifically focused on diffusion concepts and the second day presented another transport phenomena in the body, capillary action. Pre- and post- quizzes were implemented before and after the teaching module to investigate the effectiveness of the module. Pre- and post- surveys were also implemented to assess if the students interest in engineering was affected by the teaching module. Fifty middle

school girls participated in the bioengineering teaching modules. An Institutional Review Board (IRB) was approved prior to implementation of the module to collect and publish the survey and quiz data from the students. The Clemson University Office of Research Compliance (ORC) reviewed and approved the IRB exempt protocol submitted, IRB2013-202: IBIOE-Project WISE Perception by Female Students. Parental permission and child agreement forms were implemented as part of the IRB for consent from both parents and students to participate in study.

Teaching Modules

Day 1 – Diffusion Concepts Related to the Human Body

Interactive Teaching Module

The first day provided an interactive presentation that introduced the students to bioengineering and how the field impacts them and the field of medicine. The presentation showed the young girls how bioengineering can be both a rewarding and an exciting career. The presentation further introduced the tissue engineering segment of bioengineering and demonstrated the impact and significance of this field in their lives. This segment of the presentation described design criteria for tissue engineered scaffolds and how different tissues require different design specs. The second part of the presentation specifically focused on transport concepts in the body including diffusion and osmosis and how these concepts relate to designing tissue engineered constructs. Demos, shown Figure 8.1, were conducted during the presentation to show diffusion in various applications and what parameters affect the rate of diffusion.

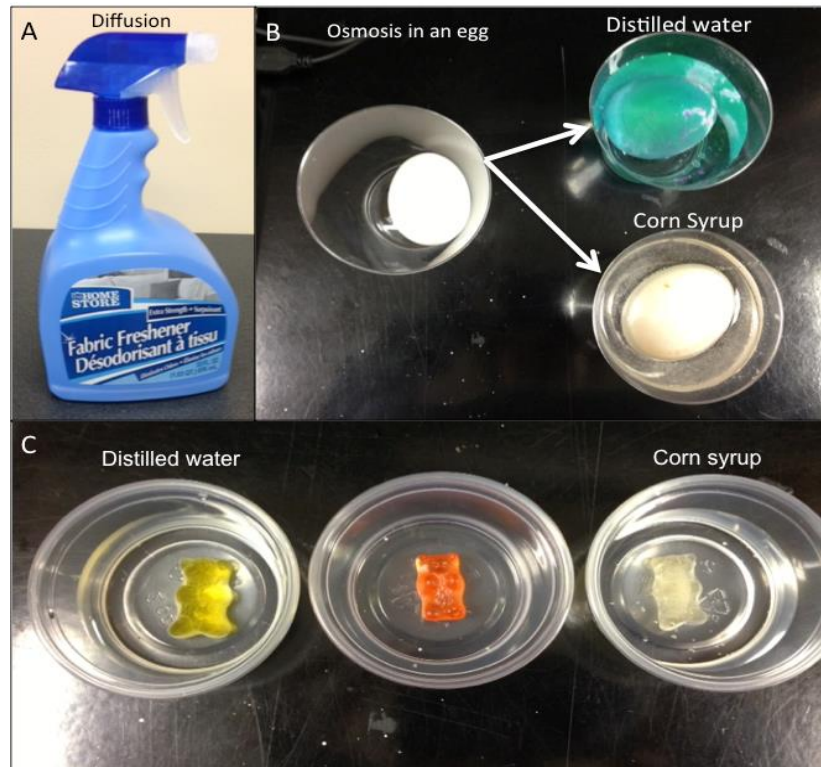


Figure 8.1: Demos presented to students to illustrate diffusion and osmosis (A) Diffusion of smell (B) Osmosis in an egg in a hypertonic or hypotonic solution after the shell is removed with vinegar (C) Osmosis in gummy bears in hypertonic or hypotonic solutions

The remaining half of the teaching module, the students participated in a hands-on group activity, adapted by Hove and coworkers, investigating diffusion in materials representing tissues of different stiffness⁵. The students were first given three different materials that simulated three different tissues of varying stiffness, depicted in image A of *Figure 8.2*. The students worked in groups to determine which material best represented the mechanical properties of fat, bone, or muscle⁵.

To further demonstrate diffusivity of tissues the students worked in groups to hypothesize how stiffness might affect diffusion. The group activity involved exploring

diffusion of a dye solution on hydrogels of varying stiffness. The hydrogels were pre-made using varying concentrations of agarose (0.5%, 1%, and 2% agarose) to represent the three different tissues consisting of different stiffness. Students first predicted how the stiffness would affect the movement of a colored solution. Prior to conducting the experiment, students were given worksheets to record their predictions, as well as track their measurements and results. To begin the study, students used transfer pipettes to pipette one drop of dye solution on each of the agarose gels, Image B of Figure 8.2. The students measured the diameter of spread on each agarose gel every 3 minutes for a 15 minutes.



Figure 8.2: (A) Different materials with varying stiffness to represent muscle, fat, and bone tissues (B) The group activity where students determine the rate of movement of the dye solution in various agarose stiff gels

Following the recording of measurements the students made a plot of diameter of the colored solution over time. The worksheets used for this group activity are shown in Appendix B. The students explored any differences in diffusion rates between samples and determined if stiffness of tissue would influence the rate of diffusion. As a group, the outcomes of the study were discussed and the students learned that diffusivity changes

with different tissue types causing the colored solution to move faster in less stiff tissues such as fat.

Day 2 – Transport Phenomena in Tissue Engineered Scaffolds

Interactive Teaching Module

The second day provided another interactive presentation focusing on the lack of vascularity in tissue-engineered scaffolds and the need for vascularity. The presentation introduced capillary action and provided a demonstration using celery stalks with food coloring.



Figure 8.3: Demonstration of water moving through capillaries or xylem in the celery stalks by capillary action

A group activity was developed to show the students the various factors that influence capillary action. The students were shown how to conduct a vertical test with

fabric and assess the movement of the colored solution over time. Students were provided yarns of various sizes and materials. The students were allowed to bundle the yarns and use various blends to increase capillary action. The students worked together in groups to follow the engineering design process to optimize the capillary action in a yarn system. The students followed the engineering design process by first brainstorming, developing ideas, choosing a solution, testing the solution, communicating the problems with that particular solution, and as a group going back and redesigning. Worksheets were developed to help students work through the engineering design process and record measurements of the testing (Appendix B).

The final demo evaluate vertical test of dye-solution with various types of paper towel brands. The students predicted which paper towel brand would perform the best based on the porosity, strength, weaves, and patterns. These activities illustrated how the architecture of a tissue-engineered scaffold can affect the diffusion and transport, which can affect cell survival.

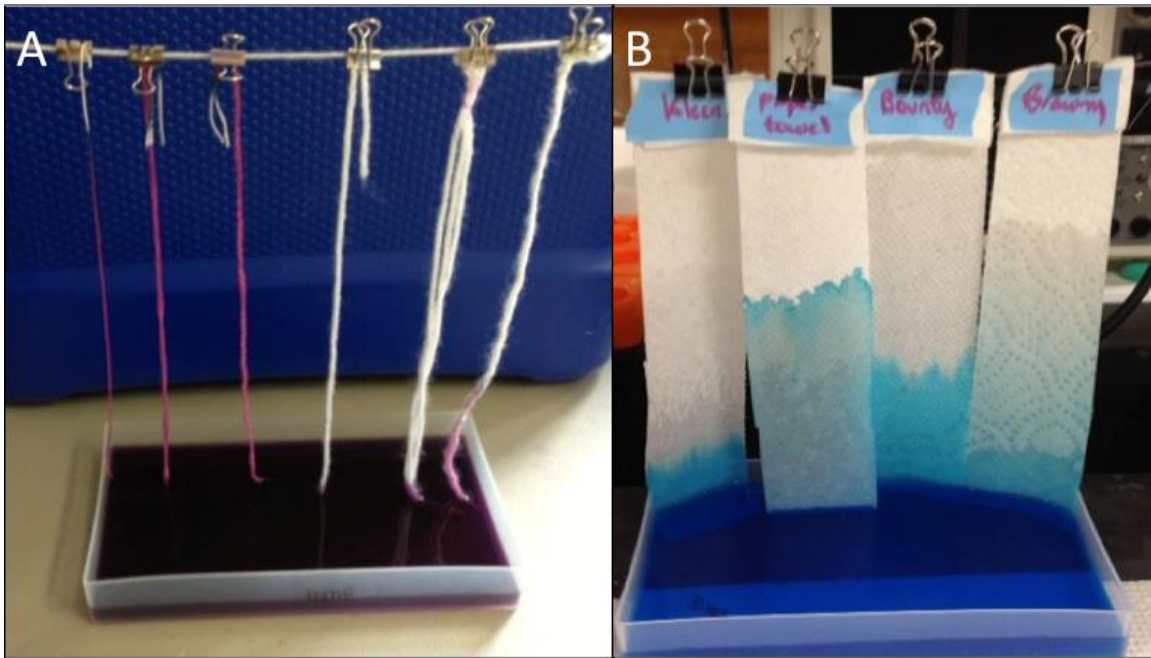


Figure 8.4: (A) Designing and testing capillary action in various yarn materials (B) Architecture of the paper towel will affect capillary action

Assessment of Modules

Pre- and post- surveys (Appendix B) were conducted using a likert ranked system, open-ended questions, and a drawing question to assess any change in interest in the field of science and engineering after the modules. The first part of the survey investigated interest and attitude of the students towards STEM (Science, Technology, Engineering, and Mathematics) fields. This part of the survey included 21 questions with Likert scale responses. The questions were adapted from existing established STEM interest surveys developed by Lyons and colleagues, and previous work conducted by IBIOE lab members^{6,7}. To further investigate the student's attitude and perception of engineering two open-ended questions and a "Draw an Engineer test" (DAET) were also included in

the assessment. The open-ended questions asked the students to describe engineering and what engineers do. To analyze the responses for the open-ended questions, categories were established to code the responses and the frequency of each category was analyzed. The DAET was adapted from Knight and colleagues⁸. This test was developed to investigate student's perceptions of engineering. To assess the drawings various categories were created and the pictures were coded for each category. The frequency of activities drawn, common objects, and images were assessed.

Pre- and post- quizzes (Appendix B) were used to evaluate the effectiveness of the modules to evaluate if the students have an improved understanding of bioengineering and related transport phenomena. The quizzes consisted of four open-ended questions each worth 3 points. A grading scale was developed for each question based on the student responses. The table below describes the grading scale used to determine the percentage grade of the pre- and post- quizzes.

Statistical Analysis

Statistical analysis was conducted in JMP 10 using Wilcoxin Signed-Rank Test to determine significant change of the student responses to the likert scale survey questions. The data distribution was assumed non-parametric and tested with a significance level of 0.05. The Wilcoxin Signed-Rank Test was also used to investigate changes in grade percentages for each question as well as the total score because data distribution was assumed without a normal distribution. The purpose of the quizzes was to investigate if the module positively affected the students understanding of bioengineering, tissue engineering scaffolds, as well as transport phenomena that occurs in scaffolds,

specifically diffusion and capillary action. The table below describes the questions and the grading scale used to determine the percentage scores for each student. The total number of students who participated in the WISE module was n=50. Due to lost surveys and lack of interest to participate in the study, the number of students who participated in the sample size for the surveys and quizzes was n=44.

Table 8.1: Grading Scale

	Score 0	Score 1	Score 2	Score 3
What does a bioengineer do?	No Response “I don’t know” “I forgot”	Connects biology and life with engineering	Understands bioengineering can improve medicine and the well-being of people	Understands bioengineering is a broad field with the goal to improve the field of medicine
What is diffusion?	No Response “I don’t know” “I forgot”	Describes some relation to spreading or moving	Describes change in concentrations and balancing of substances	Describes the movement of particles from high concentrations to lower concentration
What is the length of your thumb in cm?	No Response “I don’t know” “I forgot”	>15 cm or use of different units	10-14 cm 1-2 cm	3-9 cm
What is capillary action?	No Response “I don’t know” “I forgot”	Describes movement	Understands the vertical movement of water in a tube is caused by capillary action	Understands capillary action occurs in pores or tubes based on adhesion and cohesion of water molecules

Results

Both pre- and post- survey questions assessing student interest in STEM using Likert scale questions showed high percentages of students interested in STEM fields. Table 8.2 shows the frequency of student responses as percentages for each question.

Table 8.2: Pre Survey responses. Table depicts the percentage of students who agree or disagree for each survey question

Survey Questions	Strongly Disagree (%)	Somewhat Disagree (%)	Not sure (%)	Somewhat Agree (%)	Strongly Agree (%)
I like engineering	2.3	4.5	13.6	54.5	27.3
I like math	4.5	6.8	6.8	40.9	40.9
I like science	2.3	4.5	6.8	29.5	36.4
Boys are better at being engineers than girls	84.1	11.4	4.5	0.0	0.0
Engineering has nothing to do with our lives	81.8	11.4	6.8	0.0	0.0
Engineering and science help make people's lives better	0.0	0.0	4.5	20.5	75.0
I find it boring to hear new ideas	65.9	15.9	11.4	6.8	0.0
I would like to join a science club	6.8	13.6	34.1	20.5	25.0
I dislike science lessons	38.6	29.5	18.2	6.8	6.8
I get bored watching science programs on TV	29.5	25.0	18.2	25.0	2.3
I am good at solving problems	0.0	0.0	18.2	63.6	18.2
I am nervous to take an engineering class	25.0	31.8	36.4	6.8	0.0
I would like to join an engineering club	2.3	4.5	52.3	20.5	20.5
Boys know more about engineering and technology than girls	79.5	9.1	9.1	2.3	0.0
I like doing experiments	0.0	4.5	4.5	15.9	75.0
I like reading and thinking about science	2.3	13.6	20.5	43.2	22.7
I find engineering boring	34.1	31.8	18.2	11.4	4.5
I am smart enough to be an engineer	6.8	2.3	15.9	25.0	50.0
Being an engineer is more fun than other jobs	4.5	22.7	40.9	22.7	9.1

Table 8.3: Post survey questions depicts similar responses to pre survey questions

Survey Questions	Strongly Disagree	Somewhat Disagree	Not sure	Somewhat Agree	Strongly Agree
I like engineering	2.3	6.8	4.5	50.0	36.4
I like math	0.0	9.1	6.8	34.1	50.0
I like science	2.3	2.3	6.8	20.5	68.2
Boys are better at being engineers than girls	84.1	11.4	4.5	0.0	0.0
Engineering has nothing to do with our lives	81.8	4.5	9.1	2.3	2.3
Engineering and science help make people's lives better	4.5	2.3	2.3	9.1	81.8
I find it boring to hear new ideas	68.2	20.5	6.8	4.5	0.0
I would like to join a science club	6.8	13.6	29.5	25.0	25.0
I dislike science lessons	47.7	31.8	18.2	2.3	0.0
I get bored watching science programs on TV	27.3	27.3	15.9	22.7	6.8
I am good at solving problems	0.0	0.0	15.9	50.0	34.1
I am nervous to take an engineering class	43.2	25.0	11.4	15.9	4.5
I would like to join an engineering club	11.4	9.1	22.7	22.7	34.1
Boys know more about engineering and technology than girls	88.6	4.5	6.8	0.0	0.0
I like doing experiments	0.0	0.0	9.1	15.9	75.0
I like reading and thinking about science	4.5	13.6	20.5	31.8	29.5
I find engineering boring	59.1	15.9	9.1	9.1	6.8
I am smart enough to be an engineer	2.3	0.0	15.9	22.7	59.1
Being an engineer is more fun than other jobs	9.1	6.8	38.6	31.8	13.6

Table 8.4: Significant positive change between pre and post survey responses, no negative changes were seen

Survey Questions	Significant Positive Change
I like engineering	p=0.0366
I like math	
I like science	
Boys are better at being engineers than girls	
Engineering has nothing to do with our lives	
Engineering and science help make people's lives better	
I find it boring to hear new ideas	p=0.0217
I would like to join a science club	
I dislike science lessons	
I get bored watching science programs on TV	
I am good at solving problems	
I am nervous to take an engineering class	
I would like to join an engineering club	p=0.0388
Boys know more about engineering and technology than girls	
I like doing experiments	
I like reading and thinking about science	
I find engineering boring	
I am smart enough to be an engineer	
Being an engineer is more fun than other jobs	

Most of the questions showed no significant difference between the pre- and post-surveys responses, shown in tables below. The results showed significantly more students liked math and science lessons; as well as did not find engineering boring.

The first open-ended question on the pre- and post- surveys asked the students to describe engineering. The students' responses to this question were similar for the pre and post surveys, as illustrated in the frequency chart below. No significant difference was observed in the responses to this question. The most common engineering themes

described to this question were helping people, as well as, solving, improving, and building.

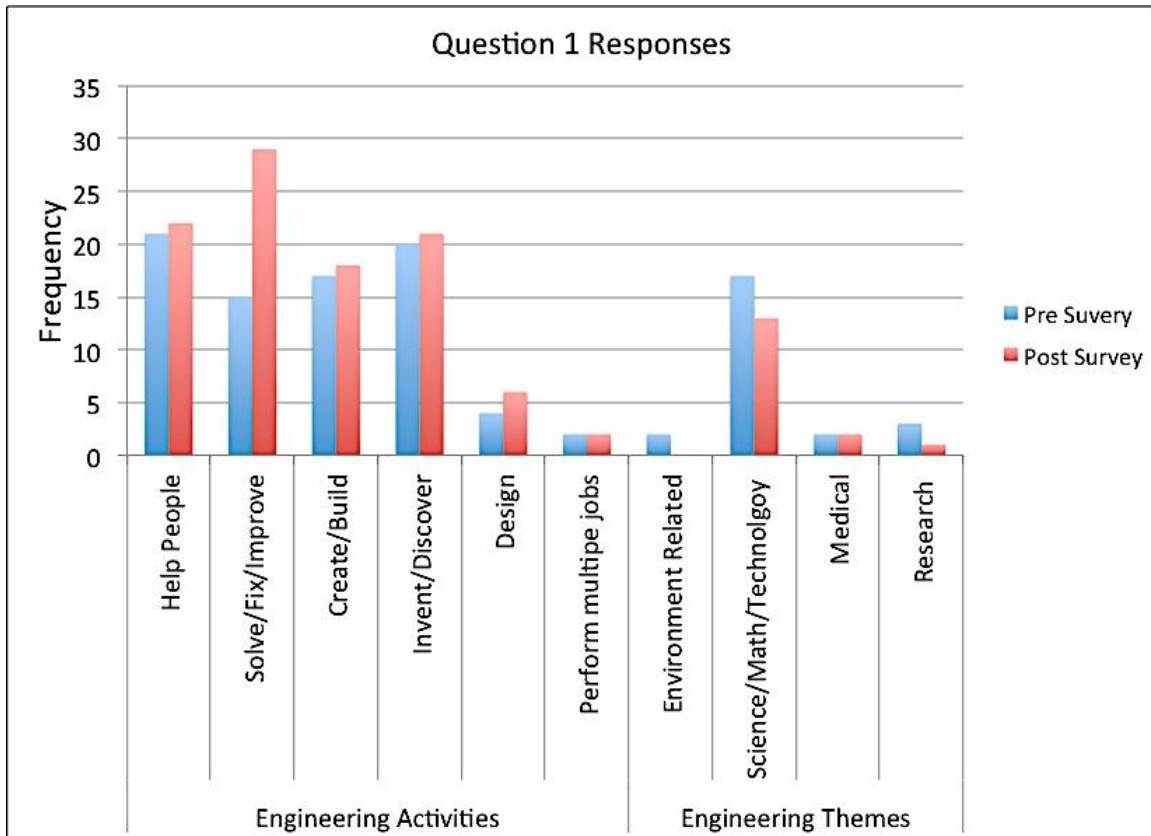


Figure 8.5: Student responses to the open-ended question "What is engineering?"

The second open-ended question asked the students to describe what engineers do. The post survey responses to this question were similar to the pre survey responses, as shown in the figure below. The most common engineering activities described were similar to those mention in question one. The common responses include helping people,

building, creating, and solving problems. The most common engineering theme described was medical related for both pre and post surveys.

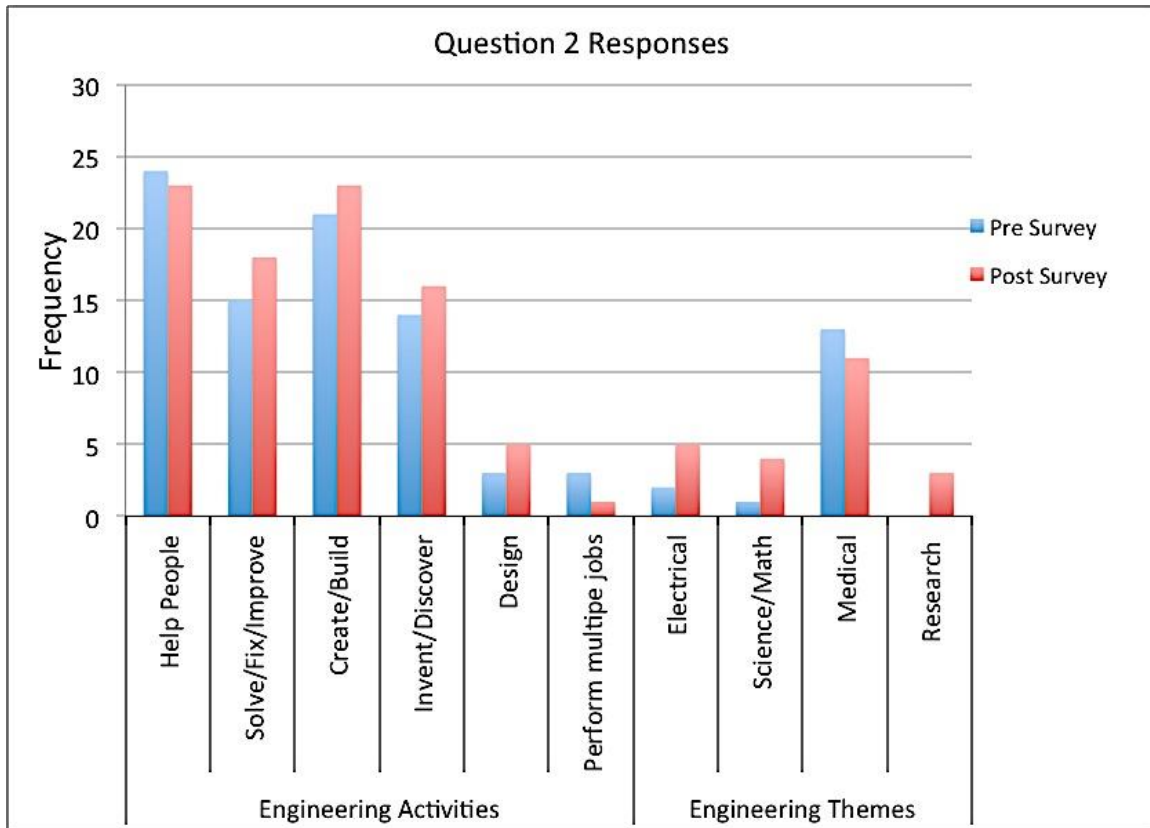


Figure 8.6: Student responses to second open-ended question: "What does an engineer do?"

The final assessment analyzed the student's perception of an engineer before and after the module. The students drew a picture of an engineer at work. The drawings were characterized based on common themes found in the drawings. The chart below summarizes the frequency of each of the categories. The frequency plot shows under the people category more male engineers were drawn than females on both pre and post surveys. Most of the drawings from the pre surveys showed actions of building and

fixing. Interestingly, the post survey drawings showed an increase in pictures related to lab and research and less related to fixing. The related themes described by the pre and post surveys were also different. Drawings of robots and computers were higher for the pre survey than the post survey. The post survey showed a significant increase in the amount of tissue engineering related pictures compared to the pre survey. These outcomes show drawing pictures as an assessment may provide educators and researchers a tool to determine perception and attitude of students.

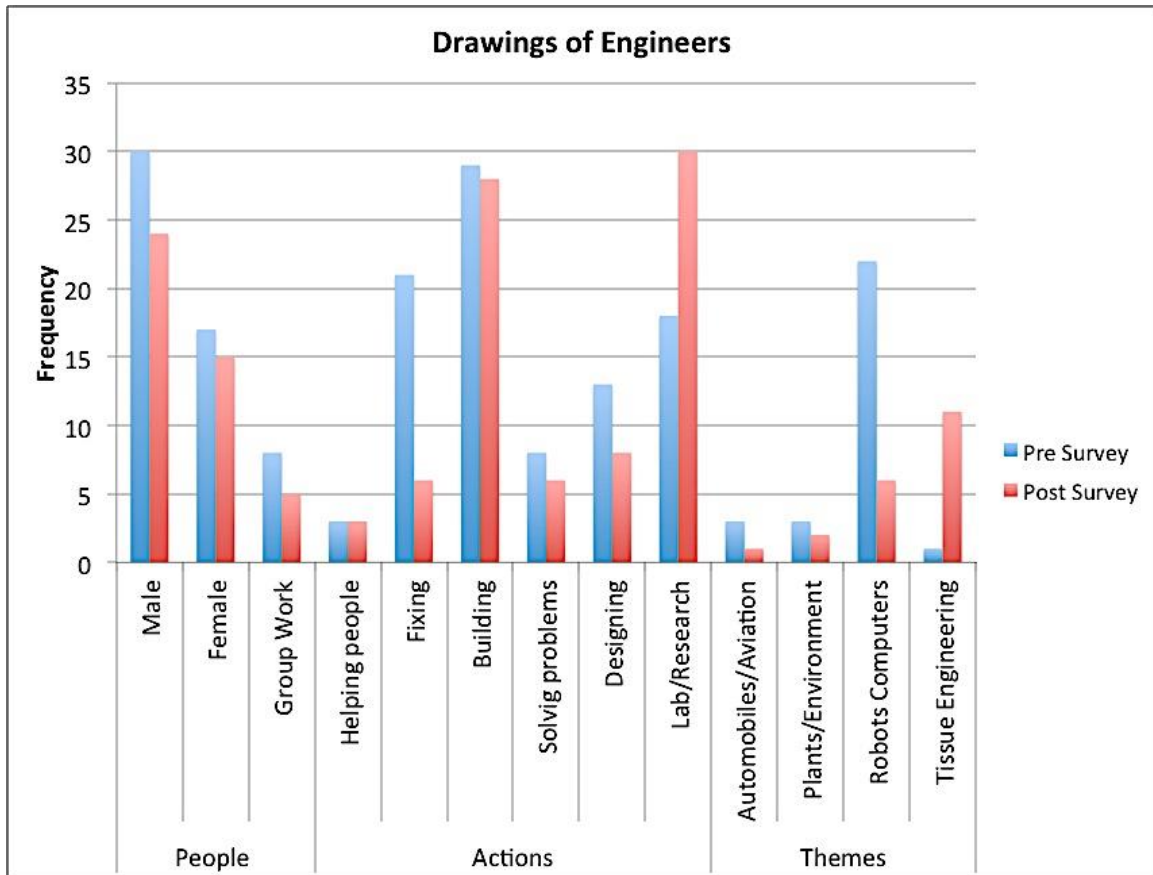


Figure 8.7: Categorizes the drawings of pre and post surveys. The categories include people, actions, and themes

The pre and post quizzes were implemented to determine the effectiveness of the teaching module. The outcomes of the post quiz showed improvement in the students understanding of bioengineering, measurements, and transport phenomena including diffusion and capillary action. The figure below shows there was a significant increase in grade percentage for the post quiz for all post quiz questions, $p < 0.05$. Question 1 responses showed improved understanding of bioengineering ($p = 0.0001$). Question 2, 3, and 4 responses reflected a better understanding of diffusion, measurements, and capillary action ($p = 0.0001$, $p = 0.0254$, $p = 0.0001$ respectively). The overall average test score for the post quizzes was significantly higher than the average pre quiz scores ($p = 0.0001$). The post quiz scores showed a 30 % increase in grade percentage. The outcomes suggest the module was effective in teaching students tissue engineering related concepts.

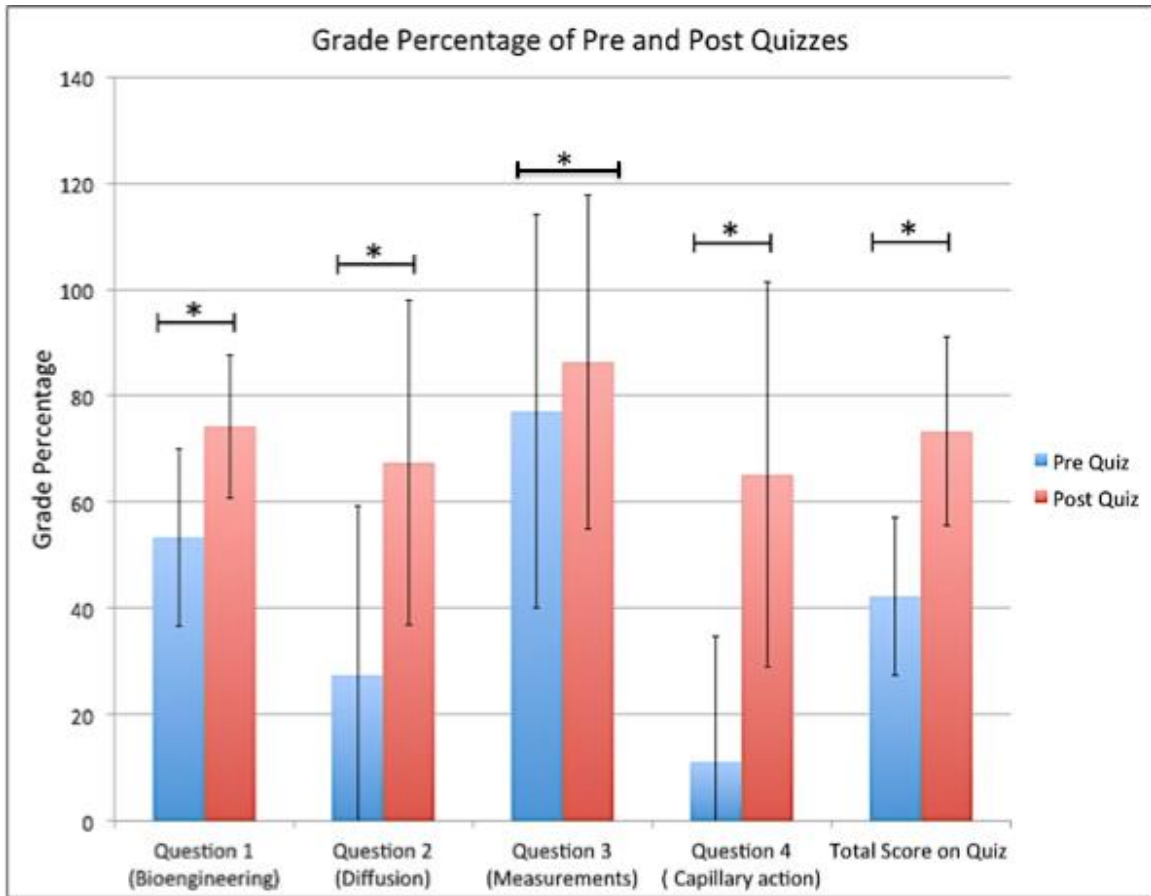


Figure 8.8: The post quiz grade percentages were significantly greater than the pre quiz grade percentages, (*) signifies $p < 0.05$.

Discussion

The outcomes revealed this module did not influence the student's interest in STEM fields. The post survey responses of the Likert style questions showed no significant difference compared to the pre survey responses. The results from the questionnaire showed high interest in STEM prior to the module. This may be a factor of the ProjectWise summer camp. Most of the students participating in this camp express interests in STEM fields prior to attending. The post survey of the open-ended question

responses also showed no difference. Interestingly, the DAET of the post survey depicted different trends in responses than the pre survey. The pre survey showed a majority of the students drew pictures related to building and robots or computers. The post survey showed a number of students drew pictures related to tissue engineering and research. This variety of pictures can also be influenced by the other engineering related activities the students are participating in. Prior to attending this module students participated in electrical computer science engineering activities related to robots and computers. The additional activities of the camp may influence the student's perceptions and attitudes of engineering. However, the DAET analysis suggests students may have a greater understanding of what an engineers can do. The outcomes also indicate the DAET can capture more information about student's perceptions and attitudes through the drawings than open-ended questions or the Likert-scale questions

The interactive modules improved their understanding of tissue engineering and how the field impacts them as well as the medical field. The responses on the post-quiz reflected greater understanding of what bioengineering is and the concepts involve in developing a tissue-engineered scaffold. The post-quiz showed the module was effective in providing the students a better understanding of transport phenomena that occurs in the body and tissue engineered scaffolds. This module was developed for students in grades 6-8th. Future work will tailor the activities and presentation for students in high school or in lower grades.

Conclusion

The assessment showed the module had no effect on the interest of the students in STEM fields. However, the outcomes from the pre and post quizzes demonstrate the module was effective in teaching the students tissue engineering concepts. The post quiz results showed a significant increase in grade percentages than the results of the quiz prior to student participation in the module. This module can be an effective tool for teachers in the classroom to introduce students to bioengineering.

References

1. Wyss VL, Heulskamp D, Siebert CJ: Increasing middle school student interest in STEM careers with videos of scientists 2012; 7:501–22
2. Brown R, Brown J, Reardon K, Merrill C: Understanding STEM: Current Perceptions. *Technology and Engineering Teacher* 2011:5–10
3. Yoder BL: *Engineering by the Numbers*. 2011, pp 11–47
4. Howard KAS, Wendt A, Hagness S, Cramer S: *Work in Progress : Grand Challenges for Engineering in the Middle School Classroom : Preliminary Results*. Institute of Electrical and Electronics Engineers 2012:1–2
5. Hove A Van, Hoffman MD, Barranello M, Vats K, Benoit DSW: *Biomaterials for Controlled Delivery of Cells and Drugs : The Helpful Hydrogel*. Society for Biomaterials Education Challenge 2013
6. Lyons J, Carolina S, Fralick B, Kearn J: *A survey of Middle-School Students' Attitudes Toward Engineers and Scientists*. American Society for Engineering Education 2009
7. Nguyen D: *In Vitro Simulation of Pathological Bone Conditions to Predict Clinical Outcome of Bone Tissue Engineered Materials*. All Dissertations 2013; Paper 1233
8. Knight M, Cunningham C: *Draw an Engineer Test (DAET) : Development of a Tool to Investigate Students ' Ideas about Engineers and Engineering*. American Society for Engineering Education 2004; Session 25

CHAPTER NINE

CONCLUSIONS AND RECOMMENDATIONS FOR FUTURE WORK

Conclusions

This work developed and tested the ability of a wicking bundle system to (1) improve mass transport and cellular distribution in large bone tissue engineered scaffolds and (2) separate cell types based on their wicking behavior. A major limitation of large bone defects is the vascularity to support all regions of the defect site to provide homogeneous bone regeneration. Conventional approaches to improving transport of tissue engineered grafts involving incorporated angiogenic factors or vascular-promoting cells have shown very limited success. The survival and success of large tissue engineered constructs are dependent on the vascularity of surrounding tissue and sufficient mass transport. We developed and tested a new approach to provide a synthetic vascular like system within a large bone graft to improve mass transport and cell infiltration.

The second application of the wicking fiber system involved cell separation and isolation based on signature cell wicking characteristics for both cancer and progenitor cell identification applications. A major challenge of cancer diagnostics is the heterogeneity and transient properties of the tumor, and subsequently cancer cells that have detached from the tumor (CTCs). Tumors and CTCs have been reported to have different subpopulations of cancer cells with varying phenotypes and degrees of tumor-initiating capabilities. The inherent dynamic heterogeneity of cancer cells limits the ability molecular biomarker detection, typically gene and protein expression. Molecular biomarker detection

can be unreliable, lack specificity, and provide limited information regarding cancer cell stage. We developed a cell identification based on the signature wicking profiles of various cell types. This work showed a proof-of-concept identification system using cancer cell types with varying metastatic potential and progenitor cells of varying differentiation potential. This work further explored the mechanisms of cell separation along the wicking fiber system. The following conclusions were drawn from each of the aims investigated:

Characterization of Fluid, Biomolecule, and Cellular Transport by Wicking Fibers

1. The fluid transport tests showed the wicking fibers significantly enhanced the wicking rate and maximum height reach of fluid compared to round fibers. The twisted configuration of the wicking fibers showed superior wicking behavior compare to the braided configuration.
2. The wicking fibers enhanced the transport rate of FITC conjugated albumin into a collagen-agarose hydrogel compared to round fibers, suggesting the fibers provide conduits that can enhance and facilitate biomolecule movement.
3. The wicking fibers can recruit and distribute cells by wicking and providing conduits for cell travel. Progenitor cell vertical displacement along wicking fibers was significantly greater than round fibers. The wicking fibers showed enhanced distribution of progenitor cells in collagen gel compared to round fibers.

Assessment of Wicking Fibers in ChronOS Strip Bone Scaffolds

1. The wicking fiber bundles enhanced the fluid retention and distribution in the chronOS strip scaffolds.

2. The wicking fiber bundles improved cell viability, proliferation, and distribution by increasing the porosity of the scaffold and providing conduits to facilitate diffusion and enhanced capillary action.
3. The osteogenic differentiation of pre-osteoblast cells in modified chronOS strip scaffolds showed earlier and increased bone forming related protein expression compared to the unmodified scaffolds. Higher gene expression and ALP was observed earlier in the differentiation study compared to unmodified scaffolds suggesting the wicking fiber may augment osteogenic differentiation.
4. The major limitation of the differentiation study was the scaffold size used. Due to the small geometry of the scaffolds used and the *in vitro* set-up, mass transport may not have been limited in the scaffolds.

Characterizing Modified Wicking Bundles and Their Effect on Cell Seeding

1. The wicking fiber bundles were successfully modified with an absorbent cap. The wicking rate and fluid absorbed were significantly increased by the modification of the wicking bundle. The enhanced wicking rate was a result of the greater change in pressure generated by the transpiration of fluid from the alginate cap. The transpiration pressure primes the system leading to an increased wicking rate and fluid height.
2. The modified wicking bundles increased the recruitment of progenitor cells and the rate of FITC conjugated albumin into a hydrogel compared to the unmodified

bundles. In a submerged system the alginate enhanced the transport of cells and biomolecules until the hydrogel reached swollen capacity.

3. The modified wicking bundles significantly improved the cell viability, proliferation, and distribution of the chronOS strip scaffolds following cell seeding with a perfusion pack system. The modified wicking bundles provide an intrinsic cell seeding approach for scaffolds to initially improve the recruitment and distribution of cells that could be easily implemented for clinical use.

Investigation of Modified Wicking Bundles as an Antibiotic Release System

1. Three loading mechanisms of gentamicin antibiotic into polylactide fibers were developed and tested. The third mechanism, mixing the gentamicin with the polylactide pellets prior to extrusion, showed elution levels above the minimal inhibitory concentration for the duration of the study. The first mechanism, wicking the antibiotic solution into the bundles, and second mechanism, incorporating the antibiotic in the water bath, were not loaded initially with enough antibiotic solution to sustain release.
2. The cross-section of the polylactide fiber affects the amount of antibiotic loaded and the release profile. The wicking fibers loaded by mechanism 2, incorporated a higher concentration of antibiotic, and showed increased elution compared to the round fibers. The single large fiber loaded by mechanism 3 showed significantly faster release of the antibiotic compared to the small fiber bundle. The bundle incorporated more antibiotic and showed a slower constant release profile.

3. The release from the alginate cap showed sustained release of gentamicin above the MIC for 7 days. The results suggest higher initial loading concentration may improve the duration of release.
4. The DSC results suggest the incorporation of gentamicin may affect the crystallinity of the polylactide and alter the degradation of the polymer.

Cell Separation and Isolation using Modified Wicking Bundles

1. Cell separation of cancer and normal cells was observed along unmodified wicking bundles. A mixture of mesenchymal stem cells and monocytes was also separated using the unmodified wicking fibers.
2. The modified wicking bundles increased the amount of cells separated along the system and provided a mechanism for isolating cancer cells by the absorbent cap.
3. The modified wicking bundles showed separation of non-metastatic cancerous and benign breast epithelial cells. The cancer cells were observed and isolated from the top region of the fiber bundles and alginate cap.
4. Metastatic cancer cells were also separated and isolated from benign cells using the modified wicking bundle.
5. The modified wicking bundle showed greater densities of metastatic cancer cells than non-metastatic cancer cells, however, more work is needed to more efficiently separate metastatic for non-metastatic cancer cells.
6. Mesenchymal stem cells were separated and isolated from a more differentiated pre-osteoblast cells using the modified bundles.

7. Stem cells and cancer cells showed similar wicking behaviors along the modified fiber bundles

Investigation of Cell Separation Factors of the Wicking Fibers

1. The cell types (D1, mouse mesenchymal stem cells, and MCF-7, human epithelial cancer cells) that displace to the top regions of the bundle and alginate cap showed smaller size cell diameters than the cells that remain in the bottom region of the bundle (MC3T3E1, mouse pre-osteoblast cells, and MCF-10A, human benign epithelial cells). Cell size may play a role in cell separation along fibers.
2. The beads used to mimic cell size in the modified wicking fibers showed very limited penetration of the larger beads into the system. The smaller beads were isolated from the top region of the fiber and alginate cap.
3. The modified wicking bundles containing smaller fibers increased the number of beads isolated in the alginate cap and the fiber bundles. The smaller conduits of the fiber bundle generated greater capillary pressure increasing the fluid height and subsequently the amount of beads in the system.
4. The inter-fiber spaces created by the tension of fiber bundle influence the wicking rate of the fluid and affect the cell wicking behavior.
5. The cancer cell types differed in cell morphology and cytoskeletal arrangement, which influenced the deformability of the cell. Cell deformation also plays a role in the ability of different cell types to move through the system. Cancer cells of high metastatic potential are more deformable than non-metastatic cancer and benign cells.

Additionally, the mesenchymal stem cells have less actin stress fibers than the pre-osteoblast, which may contribute to the increased deformability of stem cells.

6. The cytoskeletal arrangement of cancer cell types along the fibers showed a rounded morphology with limited cell spreading. Uniquely, the pre-osteoblasts adhered to the fibers and illustrated spread morphology along the grooves. This suggests the surface topography and cell adherence properties may also contribute to varying levels of cell separation.
7. The modified bundle fibers separated and isolated both non-metastatic cancer cells expressing EpCAM and metastatic cancer cells that show very limited expression of EpCAM. This suggests the system can isolate cancer cells of varying phenotypic expression but further work investigate optimizing the separation of the various phenotypes.

Bone Tissue Engineering Teaching Module for Middle School Students

1. The outcomes of the pre and post surveys showed the module had no effect on the students interest in engineering. This is a factor of the type of students surveyed. Most of the students who participated were already interested in engineering and chose to participate in the Women in Science and Engineering (WISE) summer camp.
2. The drawings reflecting the student's perception of engineering showed a difference between the pre and post quizzes. The outcomes of this assessment were influenced by the other engineering related activities the students participated in during the camp.

3. The post quizzes showed a significant increase in grading percentages compared to the pre quiz results. This indicates the module was effective in improving the students understanding of tissue engineering and related transport phenomena.

Future Work

1. Further work can investigate the effects of bundle tension and architecture on the wicking behavior of the bundle. A twisting apparatus should be developed that can incrementally adjust the tension and provide a bundle with homogenous tension across it. Other bundling configurations can also be explored, such as various braided and weaved configurations.
2. Further work can investigate the transpiration pressure generated from the alginate cap. Hydrogels of varying stiffness and swelling potential can also be investigated to experimentally determine the effect of different hydrogels on the wicking behavior of the fluid.
3. To further our understanding of the fluid transport phenomena in the system permeability measurements can be performed. A micro CT scanner could also be used to better quantify the biomolecule and cellular movement.
4. A COMSOL model can also be developed to investigate transport of fluid, biomolecules, and cells within the modified wicking fiber system to optimize the system for the different applications. The model can investigate the effects of changing the hydrophobicity of the polymer, as well as the effects of bundles of various tensions and fiber sizes.

5. The oxygen levels of the unmodified and modified chronOS strip samples in the central and peripheral regions of the scaffold can be quantified using fiber-optic oxygen microsensors. A model can be developed using this data to determine the oxygen gradients in modified and unmodified chronOS strip scaffolds. This data can provide information to help determine ideal fiber arrangement and placement in the scaffolds.
6. Test the mechanical properties of the chronOS strips with and without modified wicking bundles.
7. The differentiation of pre-osteoblast cells on the alginate modified polylactide fiber bundles should also be investigated to assess if the alginate caps should be removed prior to implantation.
8. Further work can test the modified chronOS strip scaffolds in an *in vitro* test system to better simulate the vascular limitations of the specific implant site for the bone graft.
9. A rabbit posterolateral fusion animal model can be used to compare the modified and unmodified chronOS strip samples *in vivo*.
10. Future work can also consider functional modifications to the fiber and coatings to the alginate to direct and sustain transport
11. Future work will investigate long-term release of antibiotic from the wicking bundles. The initial loading concentration and fiber size and bundle should be optimized to provide antibiotic release ideally for six weeks to a year based on application.

12. Bacterial studies should also be performed to verify the gentamicin was not altered from the processing of the fibers and the concentration is high enough to prevent bacterial growth. Other studies need to determine the toxicity of the gentamicin and any effect on bone differentiation.
13. The DSC results indicated the gentamicin may alter the crystallinity of the polylactide. Further work should investigate changes in degradation and mechanical properties of the polylactide.
14. Future work should improve the efficiency of the modified wicking bundles to separate and isolate cancer cells. Modifications to the fibers, such as tapering the top region of the bundles and altering the fiber tension may improve the separation of non-metastatic and metastatic cancer cells.
15. More physiologically relevant cell densities should be tested to determine the efficiency of the system. Circulating tumor cells (CTCs) are found in the blood typically at a density of 10-100 cells per mL. Future work would determine if the modified wicking bundle can recover cancer cells seeded at this density.
16. To further prove the efficacy of the modified bundle system metastatic and non-metastatic cancer cells, spiked volunteer blood at the physiologically relevant concentration of 10 cells per mL should be evaluated. Determine if erythrocytes and/or leukocytes will effect cell movement along fibers.
17. Future work should also investigate the mesenchymal and epithelial phenotypes of the cells recovered by the system.

18. A statistical model could be developed to further investigate interactions of different fiber configurations as well as variations of cell lines.

APPENDICES

Appendix A

Educational Surveys and Activities

Pre-Survey Questions for Project WISE (26 June 13)

Name: _____ Age: _____

Grade: _____

What is engineering?

What does an engineer do?

Draw a picture of an engineer at work:




Figure A-1: Survey questions evaluating perception of engineering.

Pre-Survey Questions for Project WISE (26 June 13)

Name: _____ Age: _____

Grade: _____

	Strongly Disagree	Somewhat Disagree	Not Sure	Somewhat Agree	Strongly Agree
I like engineering					
I like math					
I like science					
Boys are better at being engineers than girls					
Engineering has nothing to do with our lives					
Engineering and science help make people's lives better					
I find it boring to hear new ideas					
I would like to join a science club					
I dislike science lessons					
I get bored watching science programs on TV					
I am good at solving problems					
I am nervous to take an engineering class					
I would like to join an engineering club					
Boys know more about engineering and technology than girls					
I like doing experiments					
I like reading and thinking about science					
I find engineering boring					
I am smart enough to be an engineer					
Being an engineer is more fun than other jobs					

Figure A-2: Survey questions evaluating interests in engineering.

Prediction:

Time (minutes)	Distance, diameter (centimeters)	Rate (cm/min)
Initial		
3		
6		
9		
12		
15		

Graph Area:

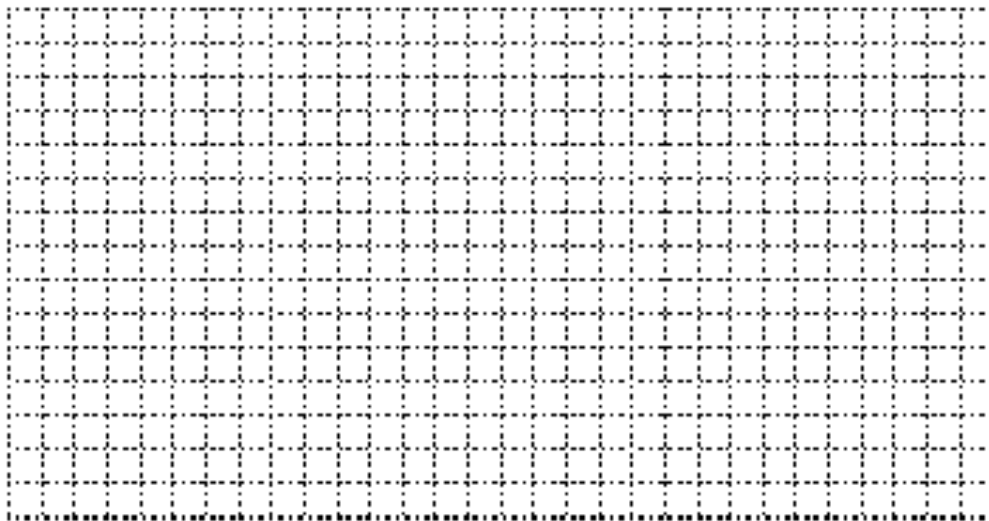


Figure A-3: Activity worksheet for exploring diffusion.

Prediction:

Time (minutes)	Distance dye traveled from bottom (centimeters)	Rate (cm/min)
Initial		
3		
6		
9		

Graph Area:

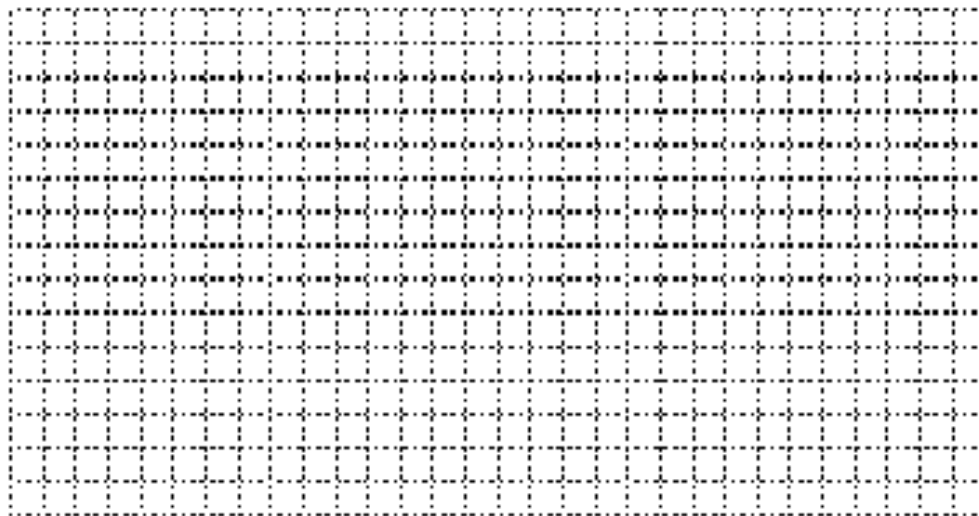


Figure A-4: Activity worksheet for exploring capillary action.